Technical University of Denmark

DTU

Emission of SO2 from Cement Production

Hu, Guilin; Dam-Johansen, Kim; Wedel, Stig; Hansen, Jens Peter

Publication date:
2007

Document Version
Publisher's PDF, also known as Version of record

[Link back to DTU Orbit](#)

Citation (APA):
Hu, G., Dam-Johansen, K., Wedel, S., & Hansen, J. P. (2007). Emission of SO2 from Cement Production.

DTU Library
Technical Information Center of Denmark

Emission of SO$_2$ from Cement Production

A Study of Pyrite Transformation and Direct Sulfation of Limestone

Ph. D. Thesis

By

Guilin Hu

31. January 2007

CHEC Research Group
Department of Chemical Engineering
Technical University of Denmark
Lyngby, Denmark

Preface

This thesis presents the main results obtained in my three–year long Ph. D. study in the period February 1st 2004 to January 31, 2007 at the CHEC (Combustion and Harmful Emission Control) research center, Department of Chemical Engineering, Technical University of Denmark. The study was supervised by Prof. Kim Dam–Johansen, associate Prof. Stig Wedel and Ph. D. Jens Peter Hansen.

First of all, I am very grateful to my main supervisor Prof. Kim Dam–Johansen for his efforts to make this Ph. D. study possible. I sincerely thank him for the many very inspiring discussions and comments, his precious time spent on the supervision, and nevertheless the generous financial support which makes it possible to achieve the fruitful results in this study.

I would like to thank associate Prof. Stig Wedel for the many valuable discussions, comments and suggestions during the study, and Jens Peter Hansen and Kent Thomsen from FLSmidth A/S, Denmark for their cooperation and support to the project.

I would like to thank technician Carsten Nørby, Jørn Hansen and Thomas Wolfe in CHEC for their help to establish experimental facilities; Ole Johnsen of the Geological Museum, University of Copenhagen, Denmark, for supplying the sample of Iceland Spar for the experiments; Lise Lotte Berring and Astrid Schøneberg from the Department of Chemistry for their help on performing X–ray powder diffraction analysis.

Finally, I would like to thank FLSmidth A/S in Denmark and the Technical University of Denmark for their financial support to the project.

Guilin Hu
2007-01-31

Abstract

This thesis presents theoretical and experimental research results concerning pyrite (FeS_2) oxidation at elevated temperatures and direct sulfation of limestone ($CaCO_3$) obtained in my Ph. D. project concerning SO_2 emission from cement production. Pyrite oxidation which releases SO_2 and limestone sulfation which absorbs SO_2 are the two important reactions that determine SO_2 emission from the cyclone preheater used in the dry process—the current dominant process for cement production in the world.

An extensive literature study indicates that in an oxygen–containing atmosphere pyrite can be oxidized directly or after it is first decomposed to form pyrrhotite (a two–step process). The actual mechanism by which pyrite is oxidized is determined by reaction conditions such as temperature, oxygen concentration, particle size and gas flow. The direct oxidation of pyrite usually takes place under the conditions of relatively lower temperatures (usually lower than about 800 K), higher oxygen concentrations and smaller particle sizes, whereas the two–step process usually takes place under the opposite conditions.

The direct oxidation of pyrite is usually accompanied by the formation of iron sulfates which significantly hinder the oxidation process because of the pore–blocking effect by the relatively larger molar volume of the sulfates. In practice at temperatures higher than about 800 K, the transformation of pyrite may start with direct oxidation and then shift to the two–step process. In the two–step process, decomposition of pyrite and oxidation of the formed pyrrhotite may take place simultaneously.

The direct sulfation of limestone was studied in a cyclone preheater–like environment concerning its mechanism and kinetics. The experimental results show that the direct sulfation of limestone involves oriented nucleation and crystal grain growth of the solid product—anhydrite. This finding reveals the mechanism by which the product layer is formed and explains various phenomena related to this reaction.

An important subject in this Ph D. study is the initial kinetics of the direct sulfation of limestone which is particularly important for SO_2 absorption on limestone in the cyclone preheater. The intrinsic sulfation kinetics was studied in a specially designed pilot reactor that simulates conditions in the cyclone preheater. The results show that the direct sulfation of limestone has a relatively fast intrinsic rate. The intrinsic sulfation rates determined in this

study is a couple of orders of magnitude higher than the rates predicted by the earlier published intrinsic rate equations in the literature.

During the sulfation process, the sulfation rate usually decreases rapidly with increasing conversion most likely caused by the deactivation by the shielding effect of the nucleation and crystal grain growth of the solid product and the significant influence of solid–state diffusion. The kinetic behaviors of the direct sulfation of limestone in the initial stage and after longer reaction time are quite different most likely because of the occurrence of nucleation and crystal grain growth of the solid product after longer reaction time.

The direct sulfation of limestone is usually significantly restricted by the slow solid–state diffusion which is a necessary process to facilitate the continuation of the sulfation reaction due to the formation of a solid product. The complicated influences of various gases such as CO_2, O_2 and H_2O on the sulfation process are most likely related to their influence on solid–state diffusion.

It was demonstrated in this study by a combination of the apparently observed kinetic behaviors and corresponding SEM (scanning electron microscope) images that the sulfation process can be significantly enhanced by increasing solid–state diffusion in the solid reactant (limestone) or in both the solid reactant and solid product by addition of various additives such as different Li^+, Na^+ and K^+ containing inorganic salts, $CaCl_2$ and HCl.

Based on the found sulfation mechanism, mathematical models for the initial sulfation of limestone and for the growth stage were developed. The model for the initial sulfation stage is a theoretical model which describes the reaction and diffusion process at the surface of the limestone, while the model for the growth stage is an empirical model which describes the kinetics in the growth period. These two models give good simulations of the experimental results and form a better basis for future process simulation and optimization.

Resumé

Ph. D. afhandlingen omhandler problemstillinger af speciel relevans for cementproduktion med lave emissioner af svolvdioxid. Afhandlingen omfatter dels pyritoxidation – dvs. dannelse af SO_2, dels direkte sulfatering af kalksten – dvs. absorptionen af SO_2 på $CaCO_3$ under oxiderende betingelser i temperaturområdet 723–973 K. De to parallelle reaktioner er tilsammen ansvarlige for hovedparten af SO_2 emissionen fra cementproduktion.

Et omfattende litteraturstudium viser at pyrit i en oxidativ atmosfære kan blive oxideret direkte eller via en to–trinsproces hvor der først dannes pyrrhotit. Den præcise oxidationsmekanisme bestemmes af en række faktorer som temperatur, iltkoncentration, partikelstørrelse og gas flow. Direkte oxidation af pyrit er normalt dominerende ved lave temperaturer, høje iltkoncentrationer og med små partikler.

Ved direkte oxidation af pyrit, er jernsulfater normalt dannet i små mængder, hvilket kan forsinke eller stoppe oxidationsprocessen på grund af jernsulfats høje molære voluminer – og dermed langsomme diffusion af oxygen. I praksis ved temperaturer omkring 800 K, starter transformation af pyrit tit ved direkte oxidation efterfulgt af den nævnte to–trinsproces.

Direkte sulfatering af kalksten er studeret i et reaktorsystem, der simulerer en cyklonforvarmer. De eksperimentale resultater viser at direkte sulfatering af kalksten involverer orienteret kernedannelse efterfulgt af krystalvækst. Eksperimentelle resultater viser at initialkinetikken for den direkte sulfatering er afgørende for SO_2 absorption på kalksten i en cyklonforvarmer. Initialkinetikken er således op til 100 gange hurtigere end tidligere målinger præsenteret i litteraturen.

Sulfaterinshastigheden falder hurtigt med omsætningsgraden af kalkstenen sandsynligvis på grund af dækning af kalkstensoverfladen med produktkrystaller – og hermed en signifikant indflydelse af faststofdiffusion. Den direkte sulfatering er ved højere omsætningsgrader normalt begrænset af den langsomme faststofdiffusion, der kan påvirkes af forskellige gasser såsom CO_2, O_2 og H_2O.

Det er demonstreret med en kombination af kinetiske data og SEM (scanning elektron mikroskopi) billeder at sulfateringsprocessen kan fremmes ved at øge faststofdiffusion i både

kalksten og det dannede faste produkt ved at tilsætte additiver som f.eks. alkalimetalsalte, $CaCl_2$ og gasformig HCl.

Baseret på de eksperimentelle observationer er matematiske modeller opbygget for både den initiale sulfatering og den videre sulfatering med vækst af produktkrystaller. Modellen for den initiale sulfatering er i høj grad en teoretisk model som beskriver sulfateringsreaktion og faststofdiffusionsproces ved kalkstensoverfladen. Modellen for den videre sulfatering er en empirisk model som beskriver væksten af produktkrystaller. De to modeller beskriver de eksperimentelle data med god præcision – og danner et godt udgangspunkt for en videre optimering af cyklonforvarmerprocessen ved cementproduktion.

Table of contents

APPENDIXES:

1   Particle distribution of Faxe Bryozo used for experiments in the pilot entrained flow reactor.

2   Porosity of Faxe Bryozo particles.

3   Estimation of intra–particle diffusion resistance.

4   EDS X–ray microanalysis results.

5   Published and submitted articles.

Chapter 1   Introduction

1.1   Cement production process

The commercial cement products are usually powder mixtures of ground Portland cement clinker and various additives. (The name "Portland cement" is originated from a British patent which was filed by Joseph Aspdin in 1824 for his invention of a new hydraulic cement.) The production of Portland cement clinker is thus the most important step for cement manufacturing. Portland cement clinker mainly consists of tricalcium silicate (Ca_3SiO_4, normally called alite), dicalcium silicate (Ca_2SiO_5, normally called belite), tricalcium aluminate ($Ca_3Al_2O_6$, normally called aluminate) and aluminoferrite ($Ca_2(Al_xFe_{(1-x)})_2O_5$, 0<x<0.7, normally called ferrite) which are formed by burning calcareous materials (normally different types of limestone) and argillaceous materials (normally different types of clay or shale) together at high temperatures (Taylor 1997, Hewlett 1998) . The production process may consist of the following units:

- Raw meal preparation: grinding and mixing of the raw materials
- Preheating of raw meal
- Pre–calcination: calcination of limestone particles contained in the raw meal before burning
- Burning: converting the calcinated raw meal to cement clinker by high temperature burning, often in a rotary kiln
- Cooling of cement clinker
- Cement grinding: grinding cement clinker to produce commercial cement products

Depending on how the raw materials are prepared, the current commercially applied process technologies for cement production can generally be divided into four categories, i.e. the wet process, the semi–wet process, the dry process and the semi–dry process.

In the wet and semi–wet processes, raw materials are ground in a wash mill. The slurry is usually pumped directly into the rotary kiln and burned to form cement clinker. In such a process, evaporation of water, preheating, calcination and burning all take place in the rotary kiln. The wet process has a relatively high energy consumption because of the energy needed to evaporate the water in the slurry. The semi-wet process is principally the same as the wet

process except that a filter press is used to remove part of the water in the slurry in order to reduce the energy needed for the evaporation of water. Today, both the wet and the semi-wet processes get little application due to the drawback of high energy consumption. However, in the case of wet raw materials (with water content > about 20%), the wet process is still preferred.

In the dry process, raw materials are crushed, ground and mixed in dry condition. Before burning, raw meal is normally preheated through a preheating system, usually a multi–stage cyclone preheater, to recover waste heat contained in the flue gas. The raw meal is then pre–calcinated in a separate calciner to increase efficiency of the burning process. The burning usually takes place in a rotary kiln as in the wet process. Because of the efficient recovery of waste heat from the hot flue gas, the energy efficiency of the dry process is much higher than the wet process. The total energy needed for the production of 1 kilogram clinker in the dry process is typically about 3300 kJ, only approximately half of that needed in the wet process. Today, the dry process is the dominant process in the world owing to its superior energy efficiency.

Figure 1.1 is an illustration of the core part of a modern dry process consisting of preheating, pre–calcination, burning and clinker cooling. Preheating of the raw meal takes place in the multi–stage cyclone preheater. The raw meal is introduced into the cyclone preheater at the top stage by dispersing it in the hot flue gas in the cyclone inlet. After direct heat exchange between the hot flue gas and the cold raw meal particles, the raw meal particles are separated in the cyclone and fed into the next stage. The same process as in the top stage repeats until the last stage cyclone where the separated raw meal particles are fed into the calciner. After the generally counter current (though co–current in each cyclone stage) heat exchange through the cyclone preheater the raw meal particles are heated from around 373 K to around 1073 K, while the flue gas temperature has dropped from around 1160 K to around 570 K. In the calciner, the limestone particles in the raw meal decompose to form CaO because of the relatively high temperature in the calciner about 1123–1173 K. Extra heat is provided for the endothermic decomposition of the limestone in the calciner by firing fuels. After calcination, the calcinated raw meal enters the rotary kiln where it is burnt to form cement clinker at a temperature up to 1670–1770 K. The rotary kiln is heated by firing fuels. The formed cement clinker is cooled in a clinker cooler.
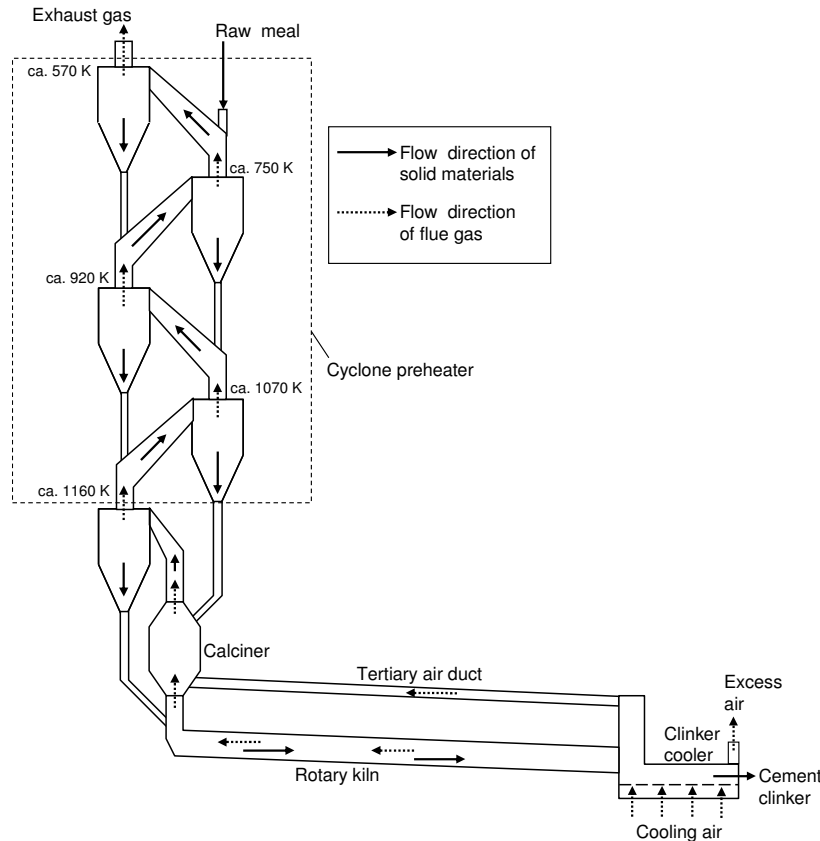
Figure 1.1 Illustration of the core part of a modern dry process for the production of Portland cement clinker

The semi–dry process (also called Lepol process) is similar to the dry process except that raw meal is nodulised by spraying water on it before it is fed into the kiln. The nodulised raw meal is then dried and calcinated on a moving grate by flue gas from the kiln. The main purpose of nodulising the raw meal is to avoid the dust collecting problem associated with preheating and pre–calcination process. However, modern exhaust cleaning technologies have made this process obsolescent.

1.2   SO$_2$ emission from cement production by the dry process

Production of cement uses limestone, clay and shale as raw materials. These materials are minerals and contain usually a small fraction of pyrite (FeS_2). In the dry process cyclone preheater, these materials are stepwise heated from less than 373 K to about 1070 K in the flue gas from the calciner and rotary kiln. The flue gas formed by combustion of fuels and decomposition of limestone usually contains a few percent of oxygen. In the hot and oxygen–

containing environment in the cyclone preheater, part of the sulfur contained in pyrite is converted to SO_2. The formed SO_2 is partly absorbed on the limestone particles—one of the main constituents of the raw meal, whereas the rest is emitted from the system.

The SO_2 emission from cement production by the dry process depends very much on the properties of the raw materials such as pyrite concentration. The emission of SO_2 usually increases with increasing concentration of pyrite in the raw materials. The SO_2 emission level can therefore vary from a few hundred ppm in one cement plant to several thousand ppm in another plant determined by their locations and raw material sources. SO_2 emission is harmful to both environment and human beings and is strictly limited by legislations in many developed countries. For example, in the European Union (EU), an emission limit of about 200–600 mg/Nm^3 at 10 % O_2 is generally imposed on new plants by national laws in the different member countries (EC reference document on best available techniques in the cement and lime manufacturing industries, IPPC, EC, 2001). This forces cement manufacturers in the EU to take extra measures to comply with the legislations. The effective abatement of SO_2 emission from cement production is thus an issue for both environment protection and cement manufacturer's compliance to the legislations.

1.3   Project objectives and scope

The emission of SO_2 from the cyclone preheater in cement production is mainly influenced by two reactions, i.e. the oxidation of pyrite that is responsible for the formation of SO_2 and the sulfation of limestone that is responsible for the desulfurization of the flue gas. The high SO_2 emission level from cement production despite of the tremendous excess of limestone is mainly caused by the relatively low temperatures in the top two cyclone stages. The temperature there is high enough for a fast oxidation of pyrite contained in the raw meal but too low for an efficient absorption of the formed SO_2 on the limestone. In order to get effective reduction of SO_2 emission from the cyclone preheater, it will be helpful to get better knowledge about these two reactions, such as their reaction mechanisms and kinetic behaviors in a cyclone preheater–like environment.

For pyrite oxidation, Hansen (2003) has performed a rather extensive study on the kinetics of pyrite oxidation in a cyclone preheater–like environment. In this project, only a literature survey concerning the transformation of pyrite at elevated temperatures is made. The mechanism and kinetic behavior of pyrite oxidation is assessed based on the literature survey.

For the sulfation of limestone, experimental work is performed in order to clarify the reaction mechanism and kinetic behavior of the sulfation of limestone at relatively low temperatures and low conversions—typical conditions in a cyclone preheater. Mathematical models are suggested to simulate the sulfation process at low conversions.

Chapter 2   Pyrite transformation at elevated temperatures

This chapter presents the results of an extensive literature survey about pyrite transformation at elevated temperatures. The mechanism of pyrite transformation is discussed and assessed based on facts presented in the literature. The contents of this chapter are published in the article "Decomposition and Oxidation of Pyrite" by Guilin Hu, Kim Dam–Johansen, Stig Wedel and Jens Peter Hansen, Progress in Energy and Combustion Science, 2006, Vol. 32, pp295-314. The article is appended to this thesis.

2.1   Introduction

Pyrite (FeS_2, M=120) is a naturally occurring crystalline material. It has a density of 5 and usually has a metallic and golden look. The crystallographic structure of pyrite is cubic as rock salt (NaCl). Pyrite is widely spread in nature and can be found in concentrated form or as impurities in coal and many other minerals. When pyrite is oxidized in oxygen–containing atmospheres, part of the sulfur contained in pyrite is usually converted to SO_2. The wide occurrence of pyrite in different minerals and coals makes it one of the main sources of SO_2 emission from various industrial activities, such as the metallurgical industry, power production and cement production.

In cement production, different kinds of limestone, clay and shale are used as raw materials. These materials are minerals which usually contain a small fraction of pyrite. During preheating of the raw meal (powder mixture of the raw materials) in the cyclone preheater used in the dry process—the current dominant process technology for cement production— the pyrite is oxidized to form SO_2 in the hot and oxygen–containing flue gas from the rotary kiln and calciner. The transformation of pyrite in an oxygen–containing atmosphere is a complicated process, and may proceed by different mechanisms under different conditions. Parameters such as temperature, particle size, flow condition and properties of the surrounding atmosphere can all affect the transformation process, and consequently the SO_2 emission from the system as well.

In the past decades, much research has been carried out to clarify the mechanisms and kinetics of pyrite transformation under different conditions. The following is a survey of the

literature on the mechanisms and kinetics of pyrite transformation at elevated temperatures in inert and oxygen–containing atmospheres. The transformation of pyrite in inert atmospheres is relevant here simply because, in some situations, it is part of the whole transformation process of pyrite in oxygen–containing atmospheres.

2.2   Pyrite transformation in an inert atmosphere

2.2.1 Transformation process and products

When heated in an inert atmosphere, pyrite (FeS_2) will decompose to release sulfur gas and form iron sulfides of lower sulfur content (FeS_X, here $1 \leq x \leq$ ca. 1.2) which are named pyrrhotite. Pyrrhotite is crystalline and magnetic, and can also be found in nature. The composition and crystallographic structure of pyrrhotite vary with reaction conditions such as temperature and sulfur gas partial pressure (Jellinek 1968). Restricted by crystal structures, x in the formula for pyrrhotite, FeS_X, can only take certain values.

The thermodynamic properties of the transformation of pyrite in inert atmospheres have been studied by a number of researchers (Bog et al. 1959, Kullerud et al. 1959, Arnold 1962, Dickson et al. 1962, Toulmin et al. 1964, Scott et al. 1971, Chuang et al. 1985, Barker et al. 1986 and Hong et al. 1998). One of the most comprehensive and representative investigations was performed by Toulmin et al. (1964). The phase diagram of the Fe–S system (Figure 2.1) that they presented gives a good illustration of the transformation process of pyrite at elevated temperatures and shows the equilibrium relationship between pyrite, pyrrhotite and other related decomposition products. In the diagram, pyrrhotite is expressed as $(FeS)_N(S_2)_{1-N}$ because pyrrhotite was supposed to be a solid solution of sulfur in troilite (FeS). Troilite is FeS_X with x = 1, and is also called pyrrhotite by some authors. N and x are related by the equation x = (2–N)/N.
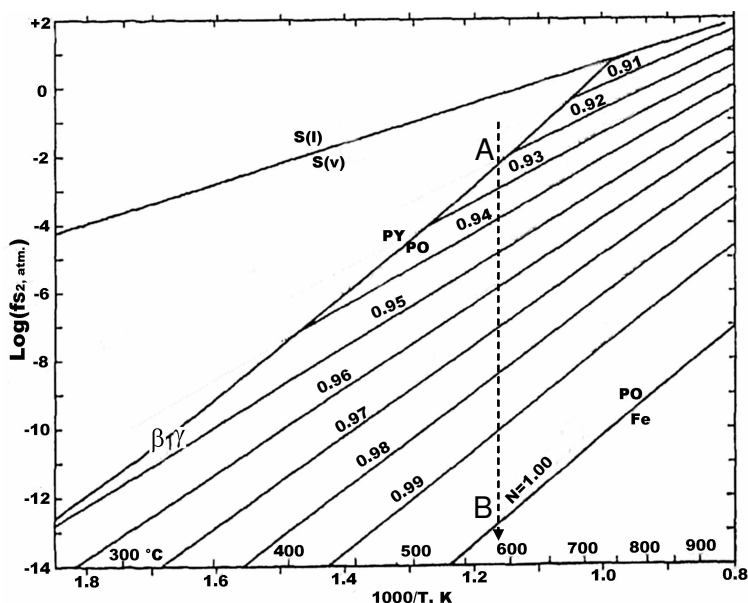
Figure 2.1 Phase diagram of the Fe–S system (modified from Toulmin et al. 1964).
In the figure: f_{S_2}: the fugacity of sulfur gas; S(l): liquid sulfur; S(v):   sulfur
vapor; PY: pyrite; PO: pyrrhotite; Fe: iron; N: fraction of FeS in pyrrhotite when
pyrrhotite is expressed as $(FeS)_N(S_2)_{1-N}$. The line marked with   PY/PO is the
equilibrium line between pyrite and pyrrhotite. The line marked   with PO/Fe is the
equilibrium line between troilite and elemental iron. The lines   between the
equilibrium lines PY/PO and PO/Fe represent isopleths of pyrrhotite of different
N values. β/γ is the transition point of the crystal   structure of pyrrhotite from
the β form to the γ form. The dashed line illustrates   the transformation process of
pyrite at a fixed temperature.

.

The diagram shows that at a fixed temperature pyrite will start to decompose to form
pyrrhotite and sulfur gas when the sulfur gas pressure is lowered to the corresponding
equilibrium pressure (at the point A where the dashed line crosses the line marked PY/PO).
This process can be represented by the following overall reaction:

$$FeS_2(s) \rightleftarrows FeS_x(s) + (1-0.5x)S_2(g) \qquad\qquad (2.1)$$
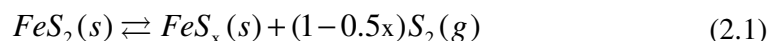
Under equilibrium conditions, sulfur content in the formed pyrrhotite (x in FeS_x) is
determined by the temperature. Figure 2.2, created by using the empirical equation obtained
by Lambert et al. (1998), shows the correlation between x and the decomposition temperature.
The correlation is valid in the temperature interval from 523 to 1016 K.
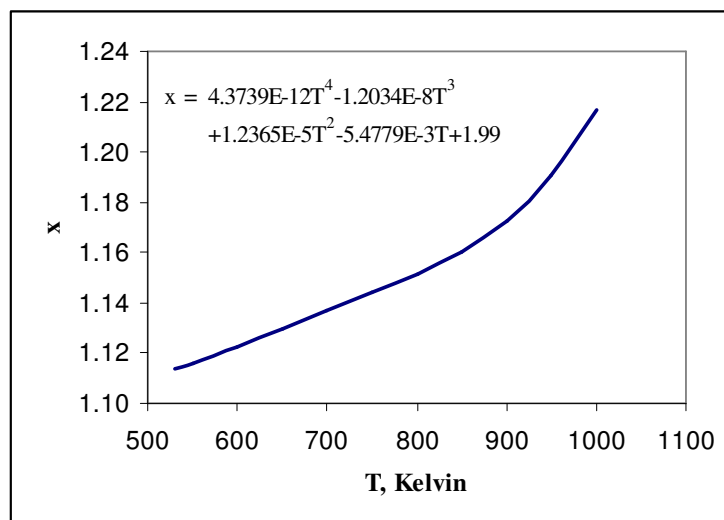
Figure 2.2 Dependence of x (moles of S per mole of Fe in pyrrhotite FeS_x) on the decomposition temperature of pyrite (created by using the equation shown in the figure obtained by Lambert et al. (1998)).

The primary pyrrhotite formed from the decomposition of pyrite will continue to release sulfur gas if the sulfur gas pressure in the system is lowered further. This process will result in pyrrhotite of lower sulfur content. In a practical decomposition process, there will be a gradient of the partial pressure of sulfur gas across the formed pyrrhotite layer due to the outgoing diffusion of the formed sulfur gas. The existence of this gradient means that the partial pressure of sulfur gas in the pyrrhotite layer will deviate from the equilibrium state, and thus cause further decomposition of the primary pyrrhotite before pyrite is completely decomposed. Fegley et al. (1995) and Lambert et al. (1998) identified two different pyrrhotite phases in partially decomposed pyrite particles. A reasonable explanation for their observations is the further decomposition of the primary pyrrhotite due to the deviation of the partial pressure of sulfur gas from the equilibrium pressure.

If this process continues, the stoichiometric iron sulfide FeS will be formed (at the point B where the dashed line crosses the line marked PO/Fe in Figure 2.1). This process can be represented by the following overall reaction:

$$FeS_x(s) \rightleftarrows FeS(s) + 0.5(x-1)S_2(g) \qquad (2.2)$$
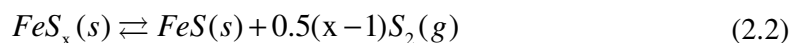
If the sulfur gas pressure is lowered further, FeS will decompose to form elemental iron (the line marked by PO/Fe in Figure 2.1). This can be represented by the following overall reaction:

$$FeS(s) \rightleftarrows Fe(s) + 0.5S_2(g) \qquad\qquad (2.3)$$
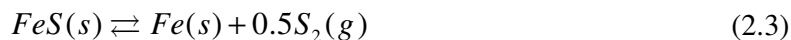
The thermal decomposition of pyrite should be a reversible process in light of the fact that pyrite/pyrrhotite can be readily synthesized by the sulfidation reaction between elemental iron and sulfur gas under fairly mild conditions (Ferrer et al. 1991, de las Heras et al. 1996 and Meng et al. 1999, 2002, 2003).

Pyrite has an incongruent melting point of 1016 K, with a total equilibrium sulfur gas pressure of around 1 MPa (Kullerud et al. 1959). The incongruent melting point of pyrite increases slightly with increasing total sulfur gas pressure — for example, 1021 K at 33.5 MPa (Kullerud et al. 1959). At the incongruent melting point, pyrite melts to form pyrrhotite and a sulfur-rich liquid. This point is the invariant point of the system. The incongruent melting point is also the maximum decomposition temperature of pyrite, as pyrite can not exist at a temperature that is higher than its incongruent melting point. Under normal conditions, this maximum temperature should be around 1016 K.

During the thermal decomposition of pyrite, sulfur gas is released. Sulfur gas normally consists of a number of allotropic species (West 1950, Meyer 1968) and should be considered as a mixture rather than a pure gas. These allotropic species can be represented by S_z, with z varying from 1 to 8 or higher. Under equilibrium conditions, the fraction of each species in the mixture is determined by the chemical equilibrium. Low temperatures and high total sulfur gas pressures are favorable to the formation of large allotropic species, whereas high temperatures and low total sulfur gas pressures are favorable to the formation of small allotropic species, especially S_2. However, under equilibrium conditions, the fraction of the large allotropic species increases with the temperature. This is because the effect of the total sulfur gas pressure, which increases exponentially with the temperature, surpasses the effect of the temperature increase. Figure 2.3 shows the molar fractions of the different allotropic species in the temperature interval that is relevant to pyrite decomposition under equilibrium conditions.
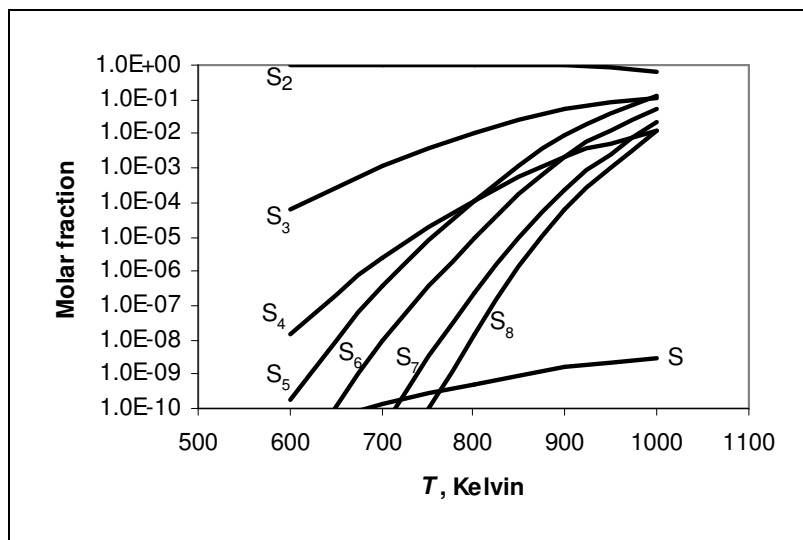
Figure 2.3 Molar fractions of allotropic species of sulfur gas over pyrite under
equilibrium conditions (the diagram is calculated by using data from Gurvich et al.
(1989) and Hong et al. (1998)).

The figure is constructed by using the equilibrium constants compiled by Gurvich et al.
(1989) and the equation presented by Hong et al. (1998) (as shown below) for the calculation
of the total equilibrium sulfur gas pressure over pyrite (valid from 598 to 1016 K):

$$log_{10}P = 16.2(\pm 0.21) - 15700(\pm 150)/T \qquad\qquad (2.4)$$

(Here, P: total sulfur gas pressure over pyrite in bar (1 bar = 0.1 MPa), T: temperature in
Kelvin)

It is assumed in the calculation that allotropic species with an n that is larger than 8 are
negligible. The figure shows that under equilibrium conditions, S_2 is the absolutely dominant
species in the decomposition of pyrite at temperatures lower than about 800 K (the molar
fraction of S_2 is around 99 %; the total equilibrium sulfur gas pressure is approximately 38
Pa). At higher temperatures, the molar fractions of the larger allotropic species (mainly S_3, S_5
and S_6) begin to increase to a significant level. The total molar fraction of these large
allotropic species is around 6 % at 900 K (the total sulfur gas pressure is approximately 5700
Pa) and 35 % at 1000 K (the total equilibrium sulfur gas pressure is approximately 0.3 MPa).
It is clear that under equilibrium conditions, the formation of the larger allotropic species may
need to be considered at a temperature higher than about 900 K.

According to Meyer (1968), the establishment of equilibrium between the different
allotropic species can be slow when the temperature is lower than about 673 K, and the sulfur

gas composition can deviate from the equilibrium values and be dependent on the sources from which the sulfur gas is generated.

Reactions (2.1)–(2.3) are endothermic. The existence of non-stoichiometric pyrrhotite makes the individual calculation of enthalpy change of Reaction (2.1) and (2.2) difficult. Hong et al. (1997) summarized the enthalpy change of Reaction (2.1) that was obtained by different authors. The values ranged from 234 to 449 kJ per mole sulfur gas (S_2) formed. Hong et al. (1997) calculated it to be 284.5 kJ per mole S_2 formed in the temperature interval from 600 to 900 K. The enthalpy change for Reaction (2.3) can be readily calculated by using thermodynamic data of the relevant substances (166 kJ per mole of FeS at 298 K, calculated by using data from NIST-JANAF Thermochemical Tables, Fourth Edition, by M. M. Chase, 1998).

2.2.2 Kinetics of pyrite decomposition

The kinetics of the thermal decomposition of pyrite (Reaction (2.1)) has been studied by a number of authors. As observed by Hoare et al. (1988), Fegley et al. (1995) and Hong et al. (1997), the thermal decomposition of pyrite (Reaction (2.1)) always progresses with a clear boundary between the unreacted pyrite and the formed product layer of pyrrhotite. This is well demonstrated by the SEM (Scanning Electron Microscope) image of a partially decomposed pyrite particle taken by Hong et al. (1997) (Figure 2.4):
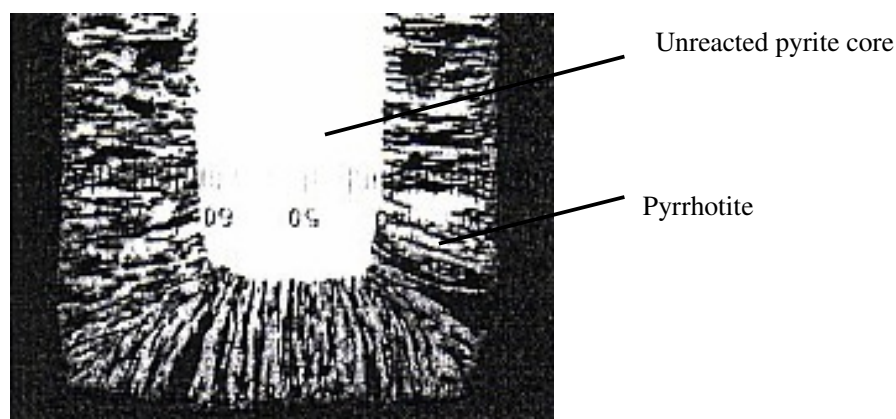

Figure 2.4 SEM image of a partially decomposed pyrite particle
(particle size: length × width × thickness = 1–2 cm × 1 cm × 0.05 cm)
(modified from Hong et al. 1997).

This is a typical behavior when the reaction proceeds with a shrinking unreacted core. For the purpose of modeling the kinetics of pyrite decomposition, the simplified shrinking unreacted core model (Levenspiel 1962, Szekely et al. 1976) was frequently used. This model assumes that the reaction occurs at the interface of the shrinking unreacted core of the solid reactant. There is a clear reaction front between the shrinking unreacted core and the formed product layer. The physical properties of the product layer are the same across the whole product layer. Gaseous reactants diffuse from the main gas phase to the reaction front through the gas film and the product layer, while gaseous products diffuse away from the reaction front to the main gas phase through the product layer and the gas film. The whole reaction process can be controlled by gas film/product layer diffusion when the reaction involves gaseous reactants and/or gaseous products and when the diffusion process is slow, or by chemical reaction when the reaction is slow compared with the diffusion, or by a combination of these steps (mixed control) when none of them is dominant.

For endothermic gas–solid reactions, the reaction is more or less influenced by heat transport through the gas film and/or product layer due to the requirement of energy balance between the heat needed for the reaction and the heat transferred to the reaction interface. The consequence of large heat transport resistance is the occurrence of a significant temperature gradient across the gas film and the product layer. This means that the reaction is proceeding at a lower temperature than that of the main gas phase. This can be shown by performing an energy balance for the reaction.

The following Equation (2.5) for the heat transport can be established by assuming that:

a) Quasi–steady–state approximation is applicable (the temperature is assumed always to be in an equilibrium state in the particle due to the much faster heat transfer rate than the shrinking rate of the core)

b) Heat transport by radiation is negligible

c) Heat transport by convection in the product layer is negligible

d) The heat capacity of the particle is negligible when compared to the reaction heat

$$(T_\text{f} - T_c) = \frac{\Delta H_r \rho_B}{3 M_B} \left(\frac{R}{h} + \frac{R^2}{\lambda} \left((1 - x_B)^{-\frac{1}{3}} - 1 \right) \right) \frac{dx_B}{dt} \qquad (2.5)$$

Equation (2.5) shows that a significant temperature difference across the gas film and the product layer (T_f-T_c) can occur at a high reaction rate and/or for a large particle size. Flow conditions, gas properties and properties of the product layer can also affect this temperature difference by influencing the heat transfer coefficient h and the thermal conductivity λ. When

an endothermic reaction is significantly influenced by heat transport, the effect of an increase of the main gas temperature on the reaction is expected to be weaker than under true isothermal conditions (i.e. the main gas phase and the particles have the same temperature). This is because the core temperature will not increase proportionally with the increase of the main gas temperature due to the fact that reaction rate increases exponentially with the temperature, whereas heat transport increases linearly with the temperature difference.

The thermal decomposition of pyrite is an endothermic reaction with both solid and gaseous products but without gaseous reactants. A number of authors, based on the obtained experimental results such as apparent activation energy (Schwab et al. 1947) and kinetic rate data (Coats et al. 1966, Hoare et al. 1988, Lambert et al. 1998, Fegley et al. 1995 and Hong et al. 1997), concluded that the decomposition of pyrite is controlled by chemical reaction and that the reaction is a zero order surface reaction (i.e. $r = k$).

However, under unfavorable flow conditions, the thermal decomposition of pyrite may as well be significantly influenced by the diffusion, as shown by the studies of Boyabat et al. (2003).

Boyabat et al. (2003) studied the thermal decomposition of pyrite in a horizontal tube furnace in the temperature interval from 673 to 1073 K in nitrogen. Different particle sizes ranging from 0.5 to 1.3 mm were used. The conversion rate was observed to be significantly influenced by the gas flow rate, the temperature and the particle size. Based on the bent form of the conversion versus time curves, they concluded that the process was controlled by heat transport through a gas film at the initial stage of the reaction, and by product layer diffusion at the later stage of the reaction. The conclusion of heat transport control at the low conversions was based on the observation that there was a linear relationship between the conversion and the reaction time. The conclusion of product layer diffusion control at the high conversion stage was based on the fact that the model for product layer diffusion control (Levenspiel 1962) fitted the experimental data well. They determined the apparent activation energy to be approximately 113 kJ/mol for the heat transport control and approximately 96 kJ/mol for the product layer diffusion control.

However, the conclusion of product layer diffusion control as suggested by Boyabat et al. (2003) is questionable, as the activation energy of 96 kJ/mol is much higher than the apparent activation energy of about 10–15 kJ/mol for gas phase diffusion in the relevant temperature interval for pyrite decomposition. The activation energy that they measured at the start of the decomposition is only 17 kJ/mol higher than the activation energy that was measured at high

conversions. This difference seems to be too small to justify the supposed shift of the controlling mechanisms. Boyabat et al. (2003) observed in their experiments that the conversion rate was significantly affected by gas flow rate even at the initial stage. This clearly indicates that the decomposition process was significantly influenced by diffusion, most likely gas-film diffusion at the start and product-layer diffusion at high conversions. The decomposition process was, therefore, probably a case of mixed control by both chemical reaction and diffusion. This also explains the relatively low activation energies that they obtained.

The influence of the diffusion observed by Boyabat et al. (2003) also indicates that the apparent reaction order of the decomposition reaction is non-zero with respect to the sulfur gas under conditions, in which the reaction is significantly influenced by the diffusion. Otherwise, the diffusion is not supposed to influence the reaction. However, under chemical reaction control, the reaction was observed by Coats et al. (1966), Hoare et al. (1988), Fegley et al. (1995), Hong et al. (1997) and Lambert et al. (1998) to be zero order. The discrepancy may be explained by the reversibility of the decomposition reaction of pyrite. As discussed earlier, the decomposition reaction of pyrite is reversible. The decomposition reaction can, therefore, be influenced by the sulfur gas pressure due to its effect on the reverse reaction. In the case of chemical reaction control, the diffusion resistance for the dissipation of the formed sulfur gas should be insignificant. The influence of the reverse reaction will thus be negligible due to the insignificant sulfur gas partial pressure at the reaction front. The observed apparent reaction order of zero is, therefore, the reaction order of the forward reaction.

"Heat transport control", as suggested by Boyabat et al. (2003), seems to be an ambiguous concept. As discussed earlier, for an endothermic reaction, the significant influence of heat transport will cause the particle temperature to be significantly lower than that of the main gas phase. However, there is not a natural limit of this temperature drop by which the controlling point can be defined. Heat transport is not a natural step of the reaction process (gas phase diffusion → product layer diffusion → reaction), but a parallel process which is connected with the reaction. It is, therefore, more accurate to say that the reaction is influenced by heat transport rather than controlled by heat transport.

The activation energy is an important kinetic parameter that indicates the sensitivity of reaction rate towards temperature. Activation energy is also useful for the judgment of the

controlling mechanism. Table 2.1 lists the apparent activation energies obtained by different authors.

Table 2.1 Apparent activation energies obtained by different authors for the thermal decomposition of pyrite.

Author	Temperature	Atmosphere	Particle size	Apparent activation energy, kJ/mole	Suggested controlling mechanism
Udintseva et al. (1941)*	673–1023 K	Vacuum		110	
Schwab et al. (1947)	873–923 K	CO_2	0.01–0.1 mm (crushed, irregular particles)	121–138	Chemical reaction
Pannetier et al. (1961)*	724–749 K	Vacuum		310	
Zhukovskii et al. (1965)*	723–963 K	N_2, vacuum		110	
Samal (1966) *	759–827 K	Vacuum		120	
Coats et al. (1966)	873–926 K	Ar	$\varnothing 6.25 \times 6.25$ mm (cylindrical form)	281	Chemical reaction
Hoare et al. (1988)	(TGA with heating rate 3 K/min.)	Nitrogen	Irregular single particle of 0.5–10 mg (estimated to be 0.6–0.8 mm in diameter)	286	Chemical reaction
Fegley et al. (1995)	663–804 K	CO_2, Ar	$10–20 \times 10 \times 1$ mm (slice form)	150	Chemical reaction
Hong et al. (1997)	673–863 K	He, N_2, CO_2	$10–20 \times 10 \times 0.5$ mm (slice form)	297	Chemical reaction
Lambert et al. (1998)	626–973 K	Vacuum, N_2, Ar He	0.21–0.25 mm (crushed, irregular particles)	200 (vacuum and 0.1 MPa) 275–294 (0.8 MPa)	Chemical reaction
Boyabat et al. (2003)	673–1073 K	N_2	1.3–0.46 mm (crushed, irregular particles)	96–113	Heat transport at the start Product layer diffusion at high conversions

*References in Hong et al. (1997).

The activation energies that were obtained by the different authors vary in a wide range from the lowest value of 96 kJ/mol to the highest value of 310 kJ/mol. The variation may be caused by the varying relative significance of the diffusion process under different reaction conditions, as in the case of Boyabat et al. (2003). It may also be caused by a shift of the

controlling reaction step in a multi–step reaction mechanism, as suggested by Hong et al. (1997) and Lambert et al. (1998).

Heat transport is another important factor that can affect the determination of the apparent activation energies. According to Equation (2.5), a higher reaction rate will cause a significant temperature difference between the main gas phase and the unreacted core. At a low temperature, the influence of heat transport may be limited, as the reaction proceeds relatively slowly and the temperature difference between the main gas phase and the unreacted core will be small. At a high temperature (for example > 873 K), the decomposition of pyrite will proceed quickly. This can cause a significant temperature difference between the main gas phase and the unreacted core if the conditions for heat transport are not optimal.

For example, by using data from Boyabat et al. (2003), it can be calculated that the temperature of the pyrite core may be about 19 K lower than that of the main gas phase at the start of the decomposition process for a pyrite particle of 1.3 mm in diameter in a nitrogen atmosphere of 923 K (the reaction heat (ΔH_r) of 284.5 kJ per mole S_2, calculated by Hong et al. (1997), is used for the calculation). 19 K is significant for the decomposition of pyrite at such a temperature level. It can be expected that this temperature difference will be much larger at higher temperatures. The reaction will, therefore, be observed to proceed more slowly than expected due to the fact that the reaction is actually proceeding at a lower temperature than that measured in the main gas phase. When the activation energy of the reaction is determined, a lower value will be obtained. It can, therefore, be expected that the activation energy obtained at low temperatures will be higher than that obtained at higher temperatures if the effect of the heat transport is not accounted for. This may be part of the reasons for the relatively low activation energies of around 100 kJ/mol that were obtained by Udintseva et al. (1941), Zhukovskii et al. (1965) and Boyabat et al. (2003), as listed in Table 2.1. It needs to be noted that pyrite has an incongruent melting point of 1016 K. The true temperature of the pyrite must be much lower than the main gas temperature when the activation energy is determined beyond 1016 K, as in the cases of Udintseva et al. (1941) and Boyabat et al. (2003). For those cases with activation energies of around 300 kJ/mol, as listed in Table 2.1, the influence of heat transport is probably limited.

2.3   Pyrite transformation in an oxygen-containing atmosphere

2.3.1 Transformation processes and products

In an oxygen-containing atmosphere, pyrite will be oxidized to form a series of final products, such as hematite (Fe_2O_3), magnetite (Fe_3O_4), iron (ferric or ferrous) sulfate ($Fe_2(SO_4)_3$, $FeSO_4$) and sulfur dioxide (SO_2). The transformation process and the formation of these products are influenced by the reaction conditions, such as temperature, oxygen concentration, flow condition and particle size.

2.3.1.1   Transformation processes

It was observed by a number of authors that the transformation of pyrite in an oxygen–containing atmosphere can take place in two ways, depending on the reaction conditions. One is the direct oxidation of pyrite, and the other is a two–step process that involves thermal decomposition as in an inert atmosphere and then subsequent oxidation of the formed pyrrhotite. The observations made by Jorgensen et al. (1982) and Dunn et al. (1989a, b) are good illustrations of these two transformation processes.

Jorgensen et al. (1982) performed pyrite oxidation in air with simultaneous DTA (differential thermal analysis) and TGA at a heating rate of 10 K/min. The pyrite particles were 0.053–0.074 mm in diameter. They observed by X–Ray powder diffraction and SEM examination that the pyrite was directly oxidized to form hematite at a temperature lower than about 803 K. At a higher temperature, pyrrhotite was observed to be formed as an intermediate, which was successively oxidized to form hematite. Figure 2.5 illustrates this process.
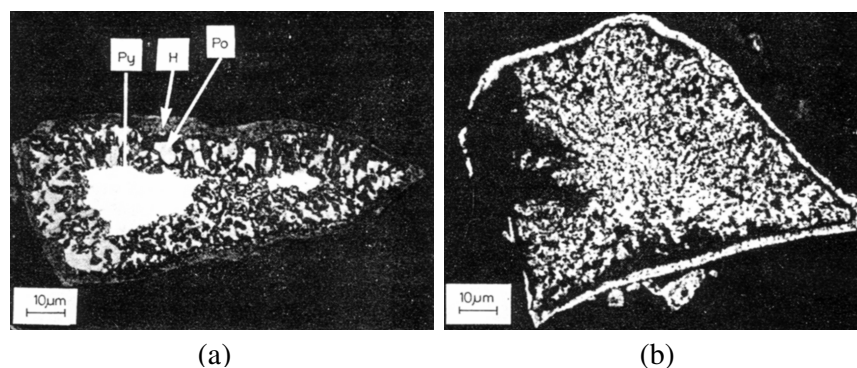
(a)   (b)

Figure 2.5 SEM images of pyrite particles oxidized in air (Jorgensen et al. 1982)   (Py–
pyrite, Po–pyrrhotite, H–hematite).

Figure 2.5a shows a partially reacted particle with an unreacted pyrite core (PY), a porous
pyrrhotite layer (PO) in the middle and a rim of hematite (H) surrounding the particle. The
texture of the pyrrhotite is similar to that observed by Hong et al. (1997) under inert
conditions (see Figure 4). Figure 2.5b shows a completely oxidized pyrite particle with two
parts of different textures: the rim surrounding the particle from direct oxidation of the pyrite
at the earlier heating stage and the inner part from the oxidation of the pyrrhotite, which has
maintained the texture of the pyrrhotite that was formed from the thermal decomposition of
the pyrite.

Dunn et al. (1989a, b) studied the oxidation of pyrite at different oxygen concentrations
with simultaneous DTA and TGA at different heating rates. The reaction products were
analyzed by X–ray powder diffraction. The experiments were performed with two different
particle sizes. With the smaller particle size (< 0.045 mm), it was observed that pyrite was
directly oxidized to form hematite at a low heating rate (2.5 K/min.) in air atmosphere. The
oxidation was completed at a temperature of around 776 K. With the larger particle size
(0.09–0.12 mm) and at a heating rate of 2.5 K/min in air, they observed that pyrite was
directly oxidized to form hematite at a temperature lower than about 788 K. At a higher
temperature, a porous oxide layer was observed to be formed in the inner part of the particles.
A similar phenomenon was observed with small particles (< 0.045 mm) that were heated at a
high heating rate (40 K/min). Figure 2.6 shows SEM images of cross–sections of the reacted
particles.

<div align="center">(a)   (b)</div>
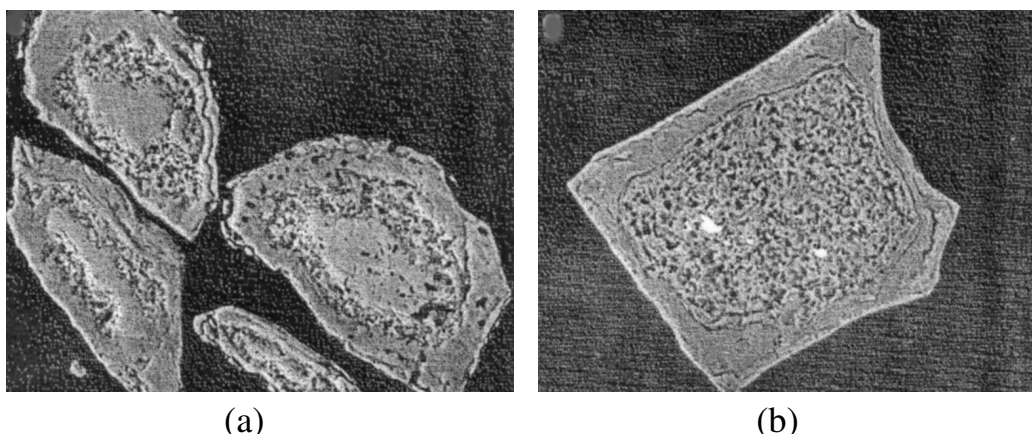
Figure 2.6 SEM images of oxidized pyrite particles (particle size
about 0.09–0.125 mm) (Modified from Dunn et al. 1989b).

Figure 2.6a shows partially reacted particles with an oxide rim formed at the lower
temperatures (< about 788 K), a porous oxide layer in the middle formed at a temperature
higher than about 788 K and an unreacted core of the pyrite. The porous oxide layer in the
inner part was supposed to be formed by the oxidation of the porous pyrrhotite that was first
formed as an intermediate by the thermal decomposition of the pyrite at temperatures higher
than about 788 K. Figure 2.6b shows a particle after completed oxidation that consists of
mainly hematite with two different textures, similar to the observations by Jorgensen et al.
(1982).

As observed by Jorgensen et al. (1982) and Dunn et al. (1989a, b), the texture of the
product layer that was formed by direct oxidation of the pyrite is different from that formed
by the successive oxidation of the pyrrhotite formed by the thermal decomposition of the
pyrite. During the direct oxidation of the pyrite, sulfates were observed to be formed
(Jorgensen et al. 1982 and Dunn et al. 1989a,b). The formation of sulfates makes the product
layer less porous due to the large molar volume of the sulfates (there will be more detailed
discussion about this later). However, the fact that the texture difference remains after the
sulfates were decomposed (Jorgensen et al. 1982 and Dunn et al. 1989a,b) indicates that the
porous appearance of the inner part is probably related to the special morphology of the
pyrrhotite phase. The dense appearance of the rim formed by the direct oxidation of the pyrite
may not be related to the formation of sulfates.

The two–step process explains very well the observation of pyrrhotite formation during the oxidation of pyrite by Schorr et al. (1969), Prasad et al. (1985), Hong et al. (1997) and Hansen (2003)

Hong et al. (1997) studied pyrite transformation in a tube furnace in a CO_2 atmosphere containing 100–1000 ppm O_2 in the temperature interval from 665 to 811 K and with a single pyrite particle. The particle was in slice form and with a dimension of 10–20 mm × 10 mm × 0.5 mm. They observed that in 100 and 1000 ppm O_2 atmospheres and at temperatures from 757 to 811K, only pyrrhotite was formed. The activation energy obtained under these conditions was almost the same as that obtained in inert atmospheres. At lower temperatures (from 665 to 733 K), both pyrrhotite and hematite were observed, which indicates simultaneous thermal decomposition of the pyrite and oxidation of the formed pyrrhotite.

Hansen (2003) studied the transformation of pyrite in an entrained flow reactor in an atmosphere containing 5% oxygen and at 798 K. The particle size was 0.032–0.064 mm. The residence time of the particles in the reactor was about 3 seconds. Figure 2.7 shows a partially reacted particle with an unreacted pyrite core, a porous pyrrhotite layer (determined by EDAX (energy dispersive X–Ray microanalysis)) and a rim of hematite at the particle surface.

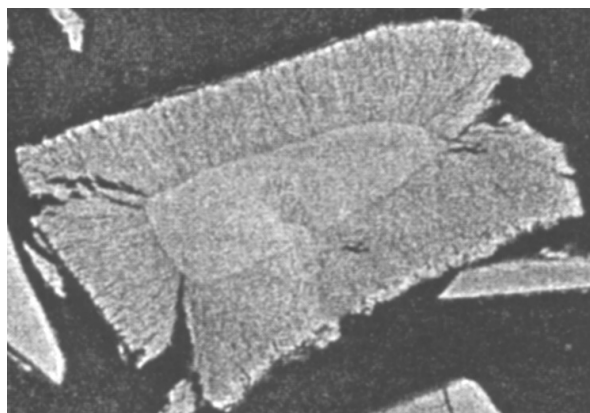Figure 2.7 SEM image of a partially reacted pyrite particle (particle
size about 0.06 mm) (modified from Hansen 2003).

This is clear evidence for the thermal decomposition, instead of the direct oxidation, of the pyrite. The hematite rim at the surface of the particle may be formed by direct oxidation during the heating–up stage, but may also be formed by the simultaneous oxidation of the pyrrhotite.

The above observations by the different authors show that the way by which pyrite is transformed in an oxygen-containing atmosphere is influenced by parameters such as temperature, particle size, oxygen concentration, heating rate and flow condition. As illustrated in Figure 2.8, three different situations can be generalized from the above observations:
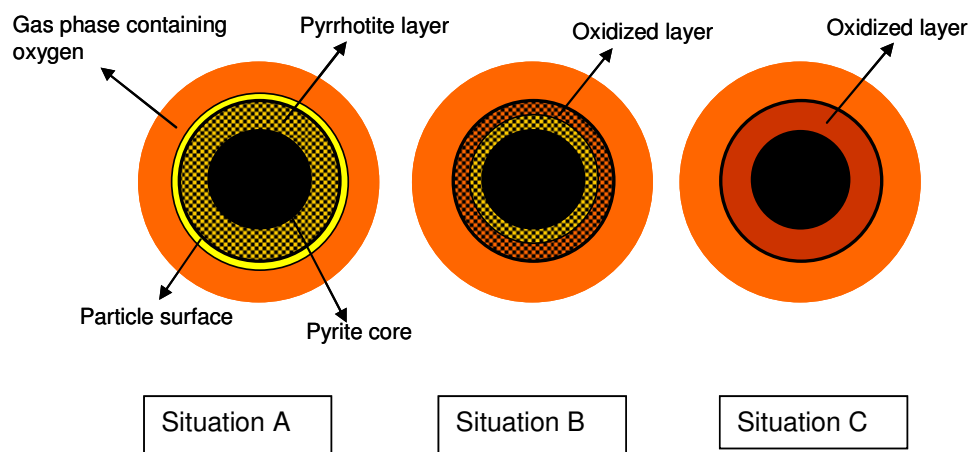

Figure 2.8 Illustration of pyrite transformation in an oxygen-containing atmosphere.

In situation A, oxygen has no contact with the particle. Pyrite undergoes thermal decomposition just like in an inert atmosphere, as observed by Hong et al. (1997). This situation can occur when the oxidation of the sulfur gas is able to consume all oxygen during its diffusion to the particle surface. This is normally the case when the reaction temperature is high and/or the oxygen concentration is low. The pyrrhotite will not be oxidized until the pyrite is fully decomposed.

In situation B, oxygen has contact with the particle, but is not in contact with the pyrite core. The pyrite undergoes thermal decomposition as in an inert atmosphere, but part of the formed pyrrhotite is oxidized alongside the gas phase oxidation of sulfur to SO_2. The observations made by Prasad et al. (1985), Dunn et al. (1989a,b), Hong et al. (1997) and Hansen (2003) may be such cases. This situation can occur when the reaction temperature is not very high and the oxygen concentration is relatively high.

In situation C, oxygen is in direct contact with the pyrite core. The pyrite is now oxidized directly. This situation can occur when the reaction temperature is low and the oxygen concentration is high. The hematite layer that is formed at lower temperatures in the TGA experiments by Jorgensen et al. (1982) and Dunn et al. (1989a,b), and the observation made by Schorr et al. (1969), are probably due to this process. The direct oxidation could, in

practice, occur to a high or low degree in situations A and B during the earlier period of the heating–up. Slow heating-up can cause significant oxidation of the pyrite. During the direct oxidation, small amounts of iron sulfates may be formed. This will result in a denser product layer since the molar volumes of iron sulfates are much higher than those of iron oxides (this will be discussed in detail later). This dense layer will restrict the inward diffusion of the oxygen and the outward diffusion of the sulfur gas, and then influence the overall transformation process. With fast heating–up, this direct oxidation will be greatly limited.

Which kind of situation occurs in practice will depend on the relative rates of the transport of oxygen to and into the particle and the thermal decomposition of pyrite under given conditions (the oxidation of sulfur gas can be assumed to be infinitively fast). Thermal decomposition of pyrite will take place if the rate of the oxygen transport through the gas film and the product layer toward the interface of the unreacted pyrite core is slower than what is needed for the oxidation of the sulfur gas generated by the decomposition of the pyrite. In this case, the oxygen will be consumed before it reaches the interface of the unreacted pyrite core. Direct oxidation of pyrite will take place if the rate of oxygen transport through the gas film and the product layer is faster than that needed for the oxidation of the released sulfur gas. In this case, the oxygen is able to reach the interface of the unreacted pyrite core.

The thermal decomposition of the pyrite will be the dominant process at a high temperature due to the high activation energy — for example, when the temperature is higher than about 800 K (Jorgensen et al. 1982, Dunn et al. 1989a,b and Hansen 2003). At a much higher temperature — for example, higher than about 923 K — the high thermal decomposition rate of the pyrite will cause a significant temperature difference between the main gas phase and the pyrite particle, as discussed earlier. A number of authors (Srinivasachar et al. 1990, Tuffrey et al. 1995, ten Brink et al. 1996, Vuthaluru et al. 1998 and McLennan et al. 2000) observed that the pyrite particles remained solid until they were fully decomposed in combustion environments with temperatures up to 1700 K. This means that the pyrite particles never exceeded their incongruent melting point of 1016 K even at such high gas temperatures. Therefore, the melting of pyrite will, normally not take place in an oxygen–containing atmosphere, because the high decomposition rate at temperatures close to the melting point of pyrite and the large endothermic enthalpy change of this process will keep the core temperature below the melting point.

The subsequent oxidation of the formed pyrrhotite in the case of situations A and B can be vigorous at high O_2 concentrations and at high temperatures (Dunn et al. 1991, 1992a, 1993a).

Melting of the pyrrhotite can take place even though the main gas temperature is lower than pyrrhotite's melting point of around 1261–1460 K (Kubaschewski 1982). This phenomenon was observed by Hansen (2003) in the oxidation of pyrite in an entrained flow reactor at 798 K in a 21 % oxygen atmosphere. Figure 2.9 shows the molten and partially oxidized pyrrhotite particles from his experiment.
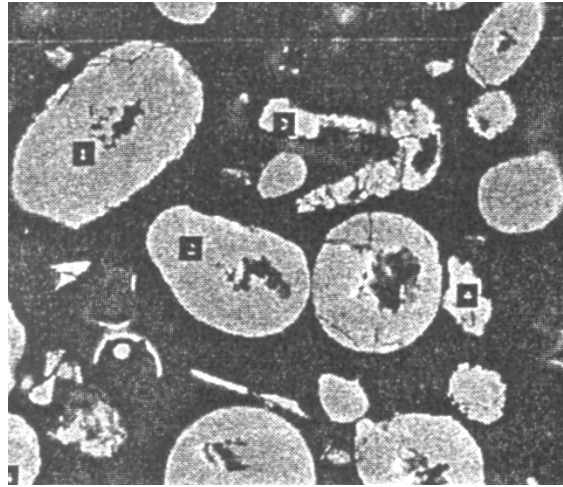
Figure 2.9 Molten and partially oxidized pyrrhotite particles (the large particle is approximately 0.05 mm in diameter) (modified from Hansen 2003)

2.3.1.2   Formation of iron oxides

Iron oxides are the main final products of pyrite oxidation. According to the phase diagram of the Fe–O_2 system presented by Darken et al. (1946) (Figure 2.10), hematite will be the stable iron oxide up to about 1600 K in an atmosphere containing a low percentage of oxygen. In a pure oxygen atmosphere (0.101 MPa), hematite can exist as the stable iron oxide up to about 1730 K.

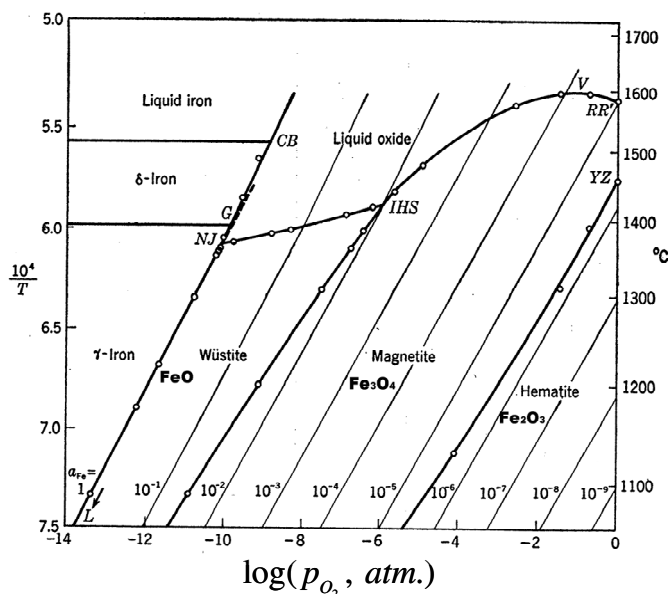Figure 2.10 Phase equilibrium between iron oxides and oxygen (1 atm. = 0.101 MPa) (modified from Darken et al. 1946)

Investigations by a number of authors showed that the final oxide formed from pyrite/pyrrhotite oxidation was hematite at the highest temperature of up to about 1473 K (Schwab et al. 1947, Kopp et al. 1958, Schorr et al. 1969, Jorgensen et al. 1982, Cole et al. 1987, Dunn et al. 1989a,b, Gao et al. 1989, Dunn et al. 1992b, Dunn et al. 1993b, Hong et al. 1997, Vuthaluru et al. 1998, Pelovski et al. 1999, Eneroth et al. 2003, Hansen 2003 and Hansen et al. 2003) and magnetite at a temperature higher than about 1773 K (Hubbard et al. 1984 and ten Brink et al. 1996). This is in good accordance with Figure 2.10.

However, there are also investigations (Nishihara et al. 1959, Hubbard et al. 1984, Prasad et al. 1985, Groves et al. 1987, Huffman et al. 1989, Helble et al. 1990, Komraus et al. 1990, Srinivasachar et al. 1990, ten Brink et al. 1994 and McLennan et al. 2000) which showed that magnetite was present with hematite and, in some cases, magnetite was even the dominant oxide under the conditions where hematite should be the stable oxide, according to Figure 2.10. Wustite was observed to form as an intermediate in a few cases (Huffman et al. 1989, Vuthaluru et al. 1998, McLennan et al. 2000). Further more, it was observed by a number of authors (Nishihara et al. 1959, Huffman et al. 1989, Helble et al. 1990, Srinivasachar et al. 1990) that the ratio between hematite and magnetite increased significantly with increasing oxygen concentration and reaction time.
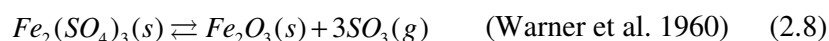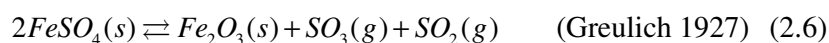
The discrepancy between the experimental observations and the equilibrium state and the dependency of hematite– magnetite ratio on oxygen concentration and reaction time can probably be explained by the fact that, in practical situations, there may be oxygen deficiency at the reaction front caused by the relatively fast reaction rate of the oxidation of pyrite/pyrrhotite and the slow diffusion rate of oxygen under certain reaction conditions. The deficiency of oxygen at the reaction front favors the formation of magnetite and, in some cases, even wustite.

Thus, the formation of iron oxides (hematite or magnetite/wustite) is determined by the oxygen concentration at the reaction front and not by the oxygen concentration in the main gas phase. Parameters such as temperature, flow condition, particle size and residence time that can affect the oxygen concentration at the reaction front will all affect the formation of iron oxides. In practice, as observed by the above authors, the formation of magnetite as the main phase usually took place at temperatures higher than about 1173–1273 K under conditions of sufficient oxygen supply in the main gas phase. This is often related to the oxidation of pyrrhotite. The formation of magnetite during the direct oxidation of pyrite is expected to be limited, as the oxidation of pyrite can only take place at temperatures lower than about 800 K.

2.3.1.3   Formation of sulfates

During the oxidation of pyrite, sulfates (mainly ferrous sulfate ($FeSO_4$) and ferric sulfate ($Fe_2(SO_4)_3$)) was observed to form as minor products at temperatures up to about 923 K (Schwab et al. 1947, Jorgensen et al. 1982, Komraus et al. 1990, Dunn et al. 1992b, 1993b, Allen et al. 1995 and Eneroth et al. 2003). At temperatures lower than about 520 K, ferrous sulfate monohydrate was observed to form (Cole et al. 1987 and Eymery et al. 1999).

For a better understanding of the formation of the two major sulfates (ferrous and ferric sulfates) during the oxidation of pyrite at elevated temperatures, it is helpful to look at the thermal stability of these two sulfates. Ferrous and ferric sulfates will decompose according to the following overall reactions when heated:

$$2FeSO_4(s) \rightleftarrows Fe_2O_3(s) + SO_3(g) + SO_2(g) \qquad \text{(Greulich 1927)} \quad (2.6)$$

$$SO_3(g) \rightleftarrows SO_2(g) + 0.5O_2(g) \qquad (2.7)$$

$$Fe_2(SO_4)_3(s) \rightleftarrows Fe_2O_3(s) + 3SO_3(g) \qquad \text{(Warner et al. 1960)} \quad (2.8)$$

$$SO_3(g) \rightleftarrows SO_2(g) + 0.5O_2(g) \tag{2.9}$$

The further decomposition of SO_3 to SO_2 and O_2 (Reaction (2.7) and (2.9)) and the reverse reaction (oxidation of SO_2 to SO_3) at temperatures lower than about 923 K are limited by the thermodynamics and reaction kinetics, respectively (Greulich 1927, Schenk et al. 1968).

Figure 2.11 shows the total equilibrium gas pressures by the decomposition of ferrous sulfate and ferric sulfate. The figure is constructed by using data from Greulich (1927) for the decomposition of ferrous sulfate and Warner et al. (1960) for the decomposition of ferric sulfate.
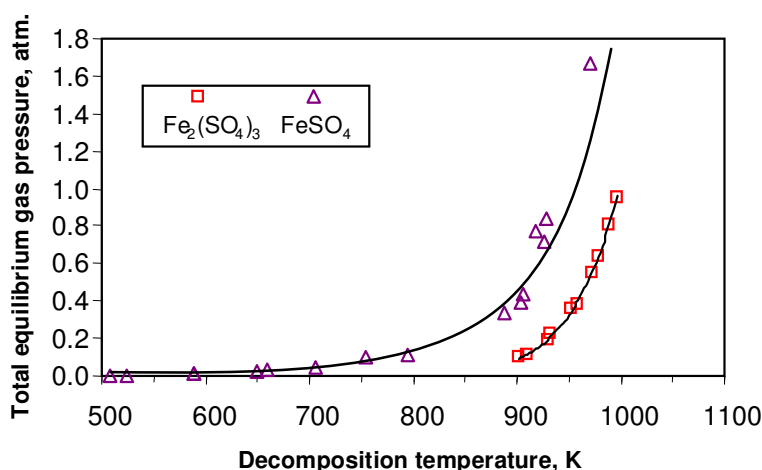

Figure 2.11 Equilibrium decomposition pressures of ferric sulfate and ferrous sulfate (1 atm. = 0.101 MPa) (Data from Greulich 1927 and Warner et al. 1960)

The existence of these two sulfates depends on the surrounding gas composition and temperature. It may be incorrect to say that ferric sulfate is more stable than ferrous sulfate during the oxidation of pyrite, just based on the lower equilibrium decomposition pressure of ferric sulfate, as the gases in balance with these two sulfates are different. The gas in balance with ferric sulfate is SO_3, whereas the gases in balance with ferrous sulfate are SO_2 and SO_3. It is well known that SO_2 is normally the dominant gaseous species from the oxidation/combustion of diverse sulfur–containing substances, including pyrite, and that the establishment of equilibrium between SO_2 and SO_3 is slow at low temperatures without a catalyst (Schenk et al. 1968). Ferric sulfate can be less stable than ferrous sulfate during the oxidation of pyrite if the formed SO_2 in the gas is not readily converted to SO_3. This may be

the explanation for the many observations of the formation of ferrous sulfate, especially the observation of the existence of ferrous sulfate up to about 873 K that was made by Dunn et al. (1992b, 1993b).
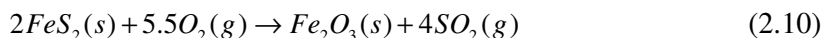
Both sulfates decompose at temperatures higher than about 823–923 K, as observed by Jorgensen et al. (1982), Dunn et al. (1989a,b, 1992b and 1993b), most likely because the partial pressures of SO_2 and SO_3 during pyrite oxidation at such temperatures were lower than the equilibrium pressures.

Thus, during the oxidation of pyrite, the temperature and the gas composition close to the solid surface are probably the two most important parameters that determine whether sulfate can be formed and which sulfate will be formed. The relatively high SO_2 concentration in the gas phase under normal reaction conditions seems to favor the formation of ferrous sulfate over the formation of ferric sulfate. The formation of ferric sulfate may, to a high degree, depend on whether there are conditions for the ready conversion of SO_2 to SO_3.
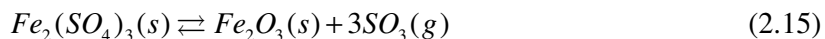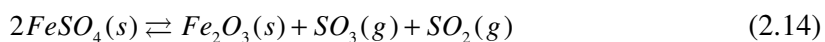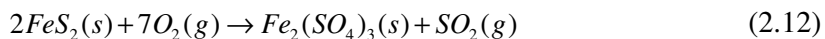
As shown above, the transformation of pyrite in an oxygen–containing atmosphere is a complicated process, which involves many reactions and products. By considering only the main reactions and the related final products, the transformation of pyrite may be generalized and represented by the following overall reactions:

In the case of direct oxidation:

- Oxidation of pyrite:

$$2FeS_2(s) + 5.5O_2(g) \rightarrow Fe_2O_3(s) + 4SO_2(g) \qquad (2.10)$$

$$SO_2(g) + 0.5O_2(g) \rightleftarrows SO_3(g) \qquad (2.11)$$

- Formation and decomposition of sulfates:

$$2FeS_2(s) + 7O_2(g) \rightarrow Fe_2(SO_4)_3(s) + SO_2(g) \qquad (2.12)$$

$$FeS_2(s) + 3O_2(g) \rightarrow FeSO_4(s) + SO_2(g) \qquad (2.13)$$

$$2FeSO_4(s) \rightleftarrows Fe_2O_3(s) + SO_3(g) + SO_2(g) \qquad (2.14)$$

$$Fe_2(SO_4)_3(s) \rightleftarrows Fe_2O_3(s) + 3SO_3(g) \qquad (2.15)$$

$$SO_2(g) + 0.5O_2(g) \rightleftarrows SO_3(g) \qquad (2.16)$$

In the case of thermal decomposition and subsequent oxidation:

- Thermal decomposition of pyrite and oxidation of the formed sulfur gas:

$$FeS_2(s) \rightarrow FeS_x(s) + (1 - 0.5x)S_2(g) \tag{2.17}$$

$$S_2(g) + 2O_2(g) \rightarrow 2SO_2(g) \tag{2.18}$$

$$SO_2(g) + 0.5O_2(g) \rightleftarrows SO_3(g) \tag{2.19}$$
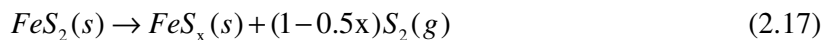
- Oxidation of pyrrhotite at temperatures lower than about 1173–1273 K and possible formation and decomposition of sulfates at temperatures up to about 923 K:

$$2FeS_x(s) + (1.5 + 2x)O_2(g) \rightarrow Fe_2O_3(s) + 2xSO_2(g) \tag{2.20}$$

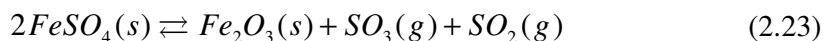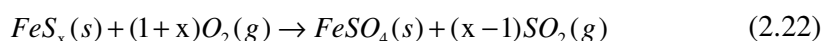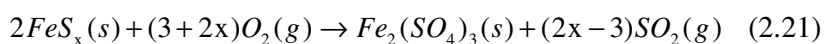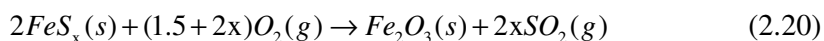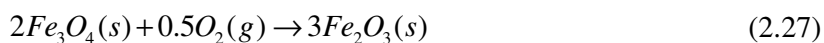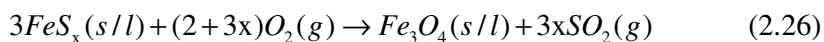$$2FeS_x(s) + (3 + 2x)O_2(g) \rightarrow Fe_2(SO_4)_3(s) + (2x - 3)SO_2(g) \tag{2.21}$$

$$FeS_x(s) + (1 + x)O_2(g) \rightarrow FeSO_4(s) + (x - 1)SO_2(g) \tag{2.22}$$

$$2FeSO_4(s) \rightleftarrows Fe_2O_3(s) + SO_3(g) + SO_2(g) \tag{2.23}$$

$$Fe_2(SO_4)_3(s) \rightleftarrows Fe_2O_3(s) + 3SO_3(g) \tag{2.24}$$

$$SO_2(g) + 0.5O_2(g) \rightleftarrows SO_3(g) \tag{2.25}$$

- Oxidation of pyrrhotite at temperatures higher than about 1173–1273 K:

$$3FeS_x(s/l) + (2 + 3x)O_2(g) \rightarrow Fe_3O_4(s/l) + 3xSO_2(g) \tag{2.26}$$

$$2Fe_3O_4(s) + 0.5O_2(g) \rightarrow 3Fe_2O_3(s) \tag{2.27}$$
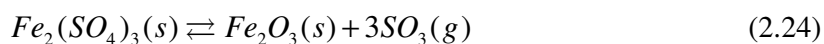
2.3.2 Kinetics of pyrite oxidation

As shown earlier, the transformation of pyrite in an oxygen–containing atmosphere can proceed by direct oxidation or by a two–step process: first, thermal decomposition of the pyrite and, second, subsequent oxidation of the formed pyrrhotite. The reaction kinetics of these different transformation processes are different.

2.3.2.1   Direct oxidation

In the case of direct oxidation, the reaction proceeds following a shrinking unreacted core model. Under the condition for the direct oxidation (relatively low temperatures and high oxygen concentrations), sulfate is usually favored to form as a (minor) solid product. Sulfates have a much larger molar volume than iron oxides (as shown in Table 2.2). The formation of sulfates causes mass gain and volume increase because of the much higher molar weights and molar volumes of both ferrous and ferric sulfates than those of pyrite and iron oxides. The

volume increase caused by the formation of sulfates may significantly influence the oxidation process because of probable blocking of pores in the product layer.

Table 2.2 Molar volume and molar weight of different substances

Substance	Molar volume, cm^3/(mole Fe)	Molar weight, g/(mole Fe)
FeS	18.2 (Perry et al. 1997, 2–15)	87.9
FeS$_2$	24.0 (Perry et al. 1997, 2–16)	119.9
Fe$_2$O$_3$	15.6 (Perry et al. 1997, 2–14)	79.9
Fe$_3$O$_4$	14.8 (Perry et al. 1997, 2–14)	77.2
FeO	12.6 (Perry et al. 1997, 2–14)	71.9
Fe$_2$(SO$_4$)$_3$	64.6 (Perry et al. 1997, 2–14)	199.9
FeSO$_4$	41.6 (David et al. 2003, 4–63)	151.9
FeSO$_4$.H$_2$O	56.7 (David et al. 2003, 4–63)	170

As shown in Table 2.2, the mass increase per mole oxidized pyrite will be 26.7 % for the formation of ferrous sulfate and 66.7 % for the formation of ferric sulfate, which corresponds to volume increases of 73 % and 169 %, respectively. The formation of sulfates during the oxidation of pyrite may therefore partially or totally block the pores in the product layer, depending on the fraction of the formed sulfate. By assuming that the product layer consists of only Fe$_2$O$_3$ and Fe$_2$(SO$_4$)$_3$, the volume increase by the formation of ferric sulfate will be equal to the total porosity formed by oxidizing pyrite to Fe$_2$O$_3$ just if 18 % (by mass) of the oxidized pyrite is converted to ferric sulfate.

Schwab et al. (1947) performed pyrite oxidation experiments by the thermogravimetric method in air at 673–773 K. The oxidation started with a relatively fast conversion rate, but slowed down quickly at higher conversions. It was observed that the achieved final conversions were lower at lower temperatures than at higher temperatures. The oxidation process was probably direct oxidation of the pyrite judged by the reaction conditions (in air and at a temperature lower than 783 K). The oxidation process was suggested to be controlled by the diffusion of oxygen through the product layer, based on the observed insensitivity of the reaction rate to the change of temperature and the low apparent activation energy of a few kcal/mol (1 cal = 4.186 J) evaluated by using the rate data at the initial stage of the oxidation.

The following empirical equation was proposed to fit the experimental data:

$$1-(1-x_B)^{1/2} = \frac{t}{\tau} \tag{2.28}$$

The gradual pore–blocking effect that was caused by the formation of ferric sulfate was suggested to be part of the reasons why the following theoretical equation for product layer diffusion control for spherical particles (Levenspiel 1962) did not fit the experimental data and the difficulties to get a full oxidation of the pyrite particles:

$$\frac{t}{\tau} = 1 - 3(1-x_B)^{2/3} + 2(1-x_B) \tag{2.29}$$

Hansen et al. (2003) performed oxidation experiments with shale particles containing pyrite in a fixed-bed reactor. The gas flow was forced through the sample bed. The influence of gas film diffusion was verified to be negligible by varying the gas flow. It was observed that the transformation process proceeded in a two–stage pattern: a fast initial stage and a subsequent slow stage. It was also observed that lower temperatures and higher oxygen concentrations caused a lower final conversion, as shown in Figure 2.12a, b, c. These observations were quite similar to those by Schwab et al. (1949). A reasonable explanation could be that direct oxidation of pyrite had occurred, and the formation of sulfate blocked the pores, which then caused the observed phenomena.
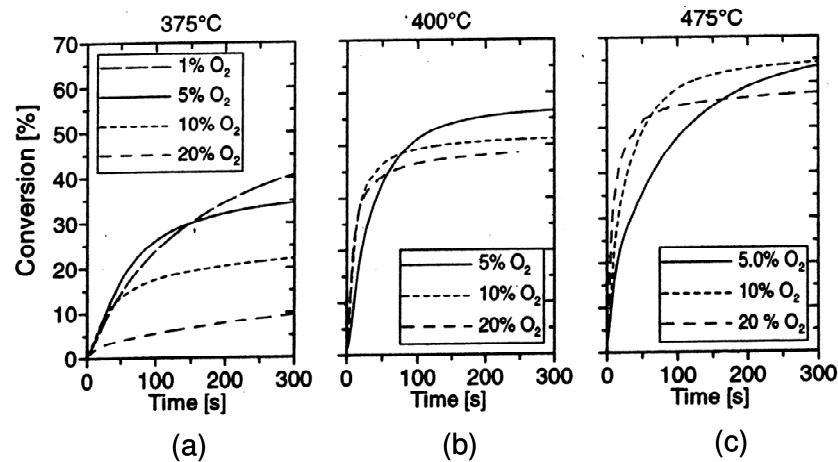

Figure 2.12 Influence of oxygen concentration and temperature on the conversion of pyrite contained in shale particles (modified from Hansen et al. 2003).

Hansen et al. (2003) used the following empirical equation to model the oxidation process of the pyrite contained in shale particles. The model consists of two parts. The first term on the right represents the fast process. The second term on the right represents the slow process.

$$\frac{dx_B}{dt} = fk_1(1-x_{B,1}) + (1-f)k_2(1-x_{B,2}) \qquad (2.30)$$

Here, f is the fraction with fast reaction rate.

2.3.2.2   The two-step process

In the case of the two–step process, the kinetic models for the thermal decomposition of pyrite in an inert atmosphere should be applicable to the first step. However, compared to the same reaction in an inert atmosphere, the thermal decomposition of pyrite in an oxygen–containing atmosphere may proceed much faster due to the extra heating effect from the oxidation of the formed sulfur gas and the reduction of eventual diffusion resistance of the outgoing sulfur gas through the product layer and/or the gas film. This effect may be significant in the case of the pyrite oxidation experiments performed by Hansen (2003) in an entrained flow reactor. The conversion reached approximately 60–80 % at 823 K, with approximately 3 seconds of residence time and with a particle size of around 0.03–0.06 mm. The reaction is about two orders of magnitude faster than the calculated rate by using the following equation for reaction control for spherical particles (Levenspiel (1962)) and the rate constants obtained by Hong et al. (1997) and Lambert et al. (1998).

$$\frac{t}{\tau} = 1 - (1-x_B)^{1/3} \qquad (2.31)$$

This may be caused by the possibly under–estimated rate constants for the thermal decomposition of pyrite in an inert atmosphere (as discussed earlier) or by the erroneous assumption of equal temperatures of the particles and the main gas phase or by a combination of these two.

For the second step — that is, the oxidation of pyrrhotite — there are two different situations: one with pyrrhotite in a solid state at lower temperatures (<1261–1460 K); and another with pyrrhotite in a molten state at higher temperatures (>1261–1460 K). Kinetic data and models related to this process are limited in the literature. Srinivasachar et al. (1989) proposed the following 7–stage model for the transformation of pyrite in a combustion environment:

1) Heating up of pyrite to 870 K.

2) Decomposition of pyrite to pyrrhotite. This stage is assumed to be controlled by heat transport.

3) Oxidation and heating up of solid pyrrhotite. The oxidation of solid pyrrhotite is assumed to be a surface reaction with first–order dependence on the oxygen concentration.

4) Melting of pyrrhotite. The rate of melting is assumed to be determined by heat generated by the oxidation reaction and heat exchanged with the surrounding environment.

5) Oxidation of molten pyrrhotite. This stage is assumed to be controlled by the diffusion of oxygen through gas and liquid film.

6) Cooling of the particle and crystallization of magnetite.

7) Oxidation of solid magnetite to hematite. This stage is assumed to be controlled by chemical reaction with first–order dependence on the oxygen concentration.

In this model, two general equations were used. One is an equation for the energy balance accounting for the heating up of the particle, heat released/needed by the reaction, heat transferred to the particle by convection and heat transferred to the particle by radiation. The second is an overall rate equation for surface reaction based on external particle surface area. It is assumed that the intrinsic oxidation reaction is of first–order dependence on the oxygen concentration.

The oxidation of pyrrhotite in a molten state was thought to be controlled by the diffusion of oxygen through gas and liquid film in this model, due to the relatively fast oxidation reaction at such high temperatures. ten Brink et al. (1996) used a similar model for the transformation of pyrite in a flame environment. It was observed that the resistance of the liquid boundary layer was negligible. This was explained by the so–called 'surface renewal mechanism' with melts of lower viscosity which improves the mass transport efficiency.

2.4   Conclusions

An assessment of the mechanisms and a short discussion of the kinetics of pyrite transformation in inert and oxygen–containing atmospheres at elevated temperatures have been given based on a literature review.

The transformation of pyrite in an inert atmosphere proceeds through a multi–step sequential process (pyrite → pyrrhotite → troilite → iron) depending on the temperature and

the total sulfur gas pressure in the system. Pyrite has an incongruent melting point of 1026 K, which is also the maximum temperature for the decomposition of pyrite.

The composition and crystallographic structure of the pyrrhotite formed by pyrite decomposition varies with reaction conditions such as temperature and sulfur gas partial pressure. The sulfur content in pyrrhotite generally increases with increasing temperature and sulfur gas partial pressure.

The thermal decomposition of pyrite to pyrrhotite follows a shrinking unreacted core model. The decomposition reaction is reversible. Under the condition of negligible gas film and product layer diffusion resistances, the decomposition reaction can be closely described by a zero–order surface reaction. Under bad flow conditions, the decomposition reaction may be significantly influenced by gas film/product layer diffusion because of the slow dissipation of the formed sulfur gas.

The decomposition of pyrite is highly endothermic. At high decomposition rates, the decomposition process is usually significantly influenced by the heat transport from main gas phase to the particle, which results in a much lower particle temperature than the surrounding environment.

In an oxygen–containing atmosphere, pyrite can be oxidized directly or oxidized after it is first decomposed to pyrrhotite (the two–step process) determined by the relative rates between oxygen diffusion to the pyrite core and the thermal decomposition of the pyrite under given reaction conditions. The direct oxidation of pyrite usually takes place at temperatures lower than about 800 K and at higher oxygen concentrations, whereas the two–step process normally takes place under the opposite conditions.

The direct oxidation of pyrite proceeds following a shrinking unreacted core model. The oxidation process may be significantly hindered by the formation of iron (II, III) sulfates because of the probable pore–blocking effect caused by the large molar volume of the sulfates.

In the two–step process, pyrite first decomposes to form pyrrhotite. The formed pyrrhotite is subsequently oxidized. The oxidation of the formed pyrrhotite may take place after the pyrite is decomposed completely or simultaneously with pyrite decomposition depending on the actual reaction conditions such as temperature, oxygen concentration, gas flow and particle size. The first step, the decomposition of pyrite, may be enhanced by the faster dissipation of the formed sulfur gas caused by the oxidation of the sulfur gas outside or inside

the particle and the heat produced by the oxidation of the sulfur gas, and pyrrhotite as well in case of simultaneous oxidation. The second step, the oxidation of the pyrrhotite, may proceed with pyrrhotite in a solid or a molten state, depending on the particle temperature. The pyrrhotite will be melted at temperatures higher than about 1261–1460 K. The melting of pyrrhotite can normally only take place after the highly endothermic decomposition of pyrite is completed. The oxidation of pyrrhotite in a molten state may be controlled by oxygen diffusion through the gas film and the liquid boundary layer.

Iron oxides (mainly hematite Fe_2O_3 and magnetite Fe_3O_4) are the main final products of the oxidation of pyrite. The formation of iron oxides is determined by the temperature and the oxygen concentration. Hematite usually forms at lower temperatures (<1173–1273 K) and at higher oxygen concentrations, whereas magnetite usually forms at higher temperatures and/or at lower oxygen concentrations. Magnetite may be formed at temperatures significantly lower than the equilibrium temperature for the $Fe–O_2$ system probably due to the significantly lower oxygen concentration at the reaction front that is caused by the relatively high reaction rate of the oxidation of pyrite/pyrrhotite and the low diffusion rate of oxygen under certain reaction conditions.

Sulfates (mainly ferrous sulfate $FeSO_4$ and ferric sulfate $Fe_2(SO_4)_3$) may be formed as minor products of the oxidation of pyrite at temperatures lower than about 873–923 K. The formation of sulfates is probably determined by the gas composition at the reaction front. Ferrous sulfate may be favored to form in a gas that is rich in SO_2, whereas ferric sulfate may be favored to form in a gas that is rich in SO_3.

Chapter 3   Direct sulfation of limestone

This chapter presents the results of an extensive literature survey and experimental work about the direct sulfation of limestone. Based on experimental results, the mechanism for the direct sulfation of limestone is assessed; mathematical models are developed to describe the sulfation kinetics at low conversions. The contents in this chapter are presented in the following four articles/manuscripts: 1) "Review of the Direct Sulfation Reaction of Limestone" by Guilin Hu, Kim Dam–Johansen, Stig Wedel and Jens Peter Hansen, Progress in Energy and Combustion Science, 2006, Vol. 32, pp386-407; 2) "Direct sulfation of limestone" by Guilin Hu, Kim Dam–Johansen, Stig Wedel and Jens Peter Hansen, AIChE J., 2007, Vol. 53, No. 4, pp948-960; 3) "Initial Kinetics of the Direct Sulfation of Limestone" by Guilin Hu, Lei Shang, Kim Dam–Johansen, Stig Wedel and Jens Peter Hansen, which has been submitted to AIChE J., 2007; 4) "Oriented Nucleation and Growth of Anhydrite during Direct Sulfation of Limestone" by Guilin Hu, Kim Dam-Johansen and Stig Wedel, which has been submitted to Crystal Growth and Design, 2007. These articles/manuscripts are appended to this thesis.

3.1   Introduction of the direct sulfation of limestone

The sulfation of limestone at high temperatures can proceed via two different routes depending on whether calcination of the limestone takes place under given reaction conditions. The dissociation of limestone is normally determined by the temperature and CO_2 partial pressure in the system. At a given temperature, limestone decomposes to form CaO and CO_2 when the partial pressure of CO_2 in the system is lower than the corresponding equilibrium CO_2 pressure over limestone. The equilibrium CO_2 pressure over limestone is temperature–dependent. The dependence has been investigated by a number of authors (Johnston 1910, Mitchell 1923, Smyth et al. 1923, Hill et al. 1956 and Baker 1962). Figure 3.1 shows the variation of equilibrium CO_2 pressure over limestone with temperature determined by Hill et al. (1956) and Baker (1962).
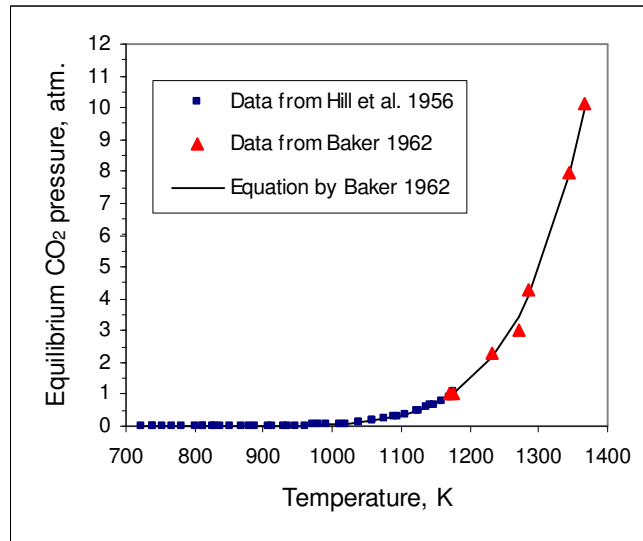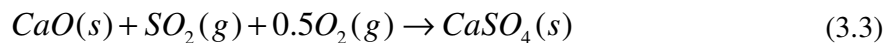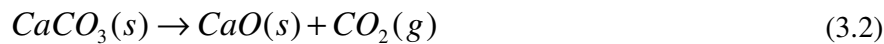
Figure 3.1 Equilibrium CO_2 pressure over limestone

The experimental data in the figure can be described well by the following equation (Baker 1962):

$$\log_{10} p_{CO_2}^e = -\frac{8308}{T} + 7.079 \qquad (3.1)$$

Here, $p_{CO_2}^e$ is given in atmospheres (1atm.= 0.101MPa), and T is given in Kelvin.

If calcination of limestone takes place (the CO_2 partial pressure in the system is lower than the equilibrium CO_2 pressure over limestone), the limestone first decomposes to form CaO, which subsequently reacts with SO_2. This process is often called the indirect sulfation of limestone and is expressed by the following overall reactions:

$$CaCO_3(s) \rightarrow CaO(s) + CO_2(g) \qquad (3.2)$$

$$CaO(s) + SO_2(g) + 0.5O_2(g) \rightarrow CaSO_4(s) \qquad (3.3)$$

If calcination of limestone does not take place (the CO_2 partial pressure in the system is higher than the equilibrium CO_2 pressure over limestone), the limestone may react directly with SO_2. This process is often called the direct sulfation of limestone and is expressed by the following overall reaction:

$$CaCO_3(s) + SO_2(g) + 0.5O_2(g) \rightarrow CaSO_4(s) + CO_2(g) \qquad (3.4)$$
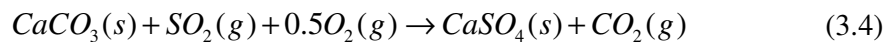
In the cyclone preheater used in the dry process for cement production, the CO_2 partial pressure is normally around 0.03 MPa, which is higher than the equilibrium CO_2 pressure

over limestone at the highest temperature of about 1073 K in the equipment. The sulfation of limestone in the cyclone preheater is thus the direct sulfation. This reaction is also relevant in the application of direct dry limestone injection for the reduction of SO_2 emission during pressurized fluid-bed combustion (PFBC). In PFBC, due to the high operating pressure, the partial pressure of CO_2 in the combustor is normally sufficiently high to prevent the calcination of the limestone.

3.2   Literature survey

The direct sulfation of limestone has been studied extensively in the past decades, mainly because of its relevance for the desulfurization of flue gas by direct dry limestone injection in PFBC for power production. In the following sections, the major findings in the literature related to the kinetics and mechanism of the direction sulfation of limestone are presented.

3.2.1 Kinetic properties of the direct sulfation of limestone

3.2.1.1   Influence of SO_2, O_2, CO_2 and H_2O

The direct sulfation of limestone was observed to be affected by SO_2, O_2, CO_2 and H_2O in varying degrees depending on their concentrations and other reaction conditions. The degree of influence of each of these gases is normally measured in terms of their apparent reaction orders. Table 3.1 lists the apparent reaction orders of these gases determined by various authors.

Table 3.1 Apparent reaction orders of SO_2, O_2, CO_2 and H_2O determined by different authors

Author	Experimental Equipment	Experimental conditions	Observed apparent reaction order
SO_2:			
Yang et al. 1975	Gravimetric method	T: 1023 K; P: 0.1MPa Gas composition: SO_2: 0.1-3.1%; O_2: 5%; CO_2:15%, H_2O: 0-2.9% Particle size: 1.1 mm	1 (with water) 0.76 (without water)
Spatinos et al. 1991	Fixed-bed	T: 573-873 K; P: 0.1MPa Gas composition: SO_2: 0.5-3%; O_2: 10%; CO_2:NA Particle size: 2-4 mm	> 1
Iisa et al. 1992a	PTGA*	T:1073 K; P: 1.5 MPa Gas composition: SO_2: 0.1-0.5%; O_2: 4%; CO_2: 15% Particle size: 125-180 μm	0.49
Krishnan 1993	TGA*	T: 1023 K; P: 0.1 MPa Gas composition: SO_2: 0.15-0.6%; O_2: 6%; CO_2: 70% Particle size: 53-350 μm	0.4 (evaluated by initial reaction rate)
Zhong 1995	TGA	T: 1073 K; P: 0.1 MPa Gas composition: SO_2: 0.1-0.5%; O_2: 10%; CO_2: 70% Particle size: 4-5.4 μm	1
Liu et al. 2000	Fixed-bed	T: 883-1123 K; P: 0.1 MPa Gas composition: SO_2: 0-0.24%; O_2: 10%; CO_2: 20-80% Particle size: 8.4-54 μm	1
Qiu et al. 2000	PTGA*	T: 1123 K; P: 1.3 MPa Gas composition: SO_2: 0.16-0.45%; O_2: 5%; CO_2: 14% Particle size: 125-180 μm	0.58 (evaluated by initial reaction rate)
O_2:			
Yang et al. 1975	Gravimetric method	T: 1023 K; P: 0.1MPa; Gas composition: NA Particle size: 1.1 mm	0.22 (with water)
Dam-Johansen 1987	Fixed-bed	T: 873 K; P: 0.1 MPa Gas composition: SO_2: 0.15%; O_2: 0-4%; CO_2: 1.8% Particle size: 0.327-2.0 mm	>0 and <1
Iisa et al. 1990	PTGA	T: 1123 K; P: 1.5 MPa Gas composition: SO_2: 0.3%; O_2: 1-6%; CO_2: 15% Particle size: 125-180 μm	0
Alvarez et al. 1999	PTGA	T: 1123 K; P: 1.2 MPa Gas composition: SO_2: 0.5%; O_2: 3-7%; CO_2: 12-15% Particle size: 100-595 μm	0
Liu et al. 2000	Fixed-bed	T: 883-1123 K; P: 0.1 MPa Gas composition: O_2: > ca. 5%; others: NA Particle size: 8.4-54 μm	0
CO_2:			
Ulerrich et al. 1980	PTGA	T: 1088 K; P: 1 MPa Gas composition: SO_2: 0.5%; O_2: 10.5-14%; CO_2: 5.8-8.7% Particle size: 125-180 μm	< 0
Dam-Johansen 1987	Fixed-bed	T: 873 K; P: 0.1 MPa Gas composition: SO_2: 0.15%; O_2: 0-4%; CO_2: 0-10% Particle size: 0.327-2.0 mm	< 0
Snow et al. 1988	TGA	T: 298-1373 K; P: 0.1 MPa Gas composition: SO_2: 0.3%; O_2: 5%; CO_2: 2-95% Particle size: 2-106 μm	0
Iisa et al. 1990	PTGA	T: 1123 K; P: 1.5 MPa Gas composition: SO_2: 0.3%; O_2: 4%; CO_2: 15-90% Particle size: 125-180 μm	0
Illerup et al. 1993	Fixed-bed	T: 1123 K; P: 1 MPa Gas composition: SO_2: 0.15%; O_2: 4%; CO_2: 10% Particle size: 0.85-1 mm	No influence on the final conversion.
Tullin et al. 1993	TGA	T: 1023-1048 K; P: 0.1 MPa Gas composition: SO_2: 0.3%; O_2: 4%; CO_2: 30-80% Particle size: 9-37 μm (consisting of 1-5 μm primary particles)	< 0
H_2O:			
Yang et al. 1975	Gravimetric method	T: 1023 K; P: 0.1MPa Gas composition: SO_2: 0.1-3.1%; O_2: 5%; CO_2:15%, H_2O: 1-40% Particle size: 1.1 mm	0
Hajaligol et al. 1988	TGA	T: 1173 K; P: 0.1 MPa Gas composition: SO_2: 0.3%; O_2: 5%; CO_2:95%, H_2O: 6-12% Particle size: 10-12 μm	> 0

* TGA = thermal gravimetric analysis; PTGA = pressurized thermal gravimetric analysis.

The observed apparent reaction order of SO_2 varied from 0.4 to greater than 1. No clear trend is evident for the variation of the reaction order with the reaction conditions. Few authors tried to explain the reaction order(s) they observed. Iisa et al. (1992a) suggested that the low reaction order of SO_2 that they observed at high conversions is related to solid–state diffusion control. Spatinos et al. (1991) believed that the high reaction order they observed was due to a possible increase of the micro-porosity of the product layer with the increase of the SO_2 concentration caused by the faster evolution of the CO_2 gas at higher SO_2 concentrations.

For O_2, the general trend is that the reaction order becomes zero at high O_2 concentrations. The reason is not clear. No explanations were given by those authors who observed this phenomenon.

The rate of the direct sulfation reaction can be significantly reduced by higher CO_2 concentrations under certain conditions, as observed by Ulerrich et al. (1980), Dam–Johansen (1987) and Tullin et al. (1993). Ulerrich et al. (1980) believed that the lower sulfation rates caused by higher CO_2 concentrations were related to slower diffusion of the formed CO_2 away from the limestone particles. However, no explanation of how the sulfation reaction is actually affected by the slow diffusion of the CO_2 is given. Tullin et al. (1993) suggested that the negative effect of higher CO_2 concentrations was related to the reverse reaction of the dissociation of the limestone.

The direct sulfation of limestone was observed to be significantly enhanced by the presence of water in the gas phase. Yang et al. (1975) observed that water in the gas phase increased the apparent reaction order of SO_2. Hajaligol et al. (1988) observed a higher sulfation rate in the presence of water. Water is clearly not inert for the direct sulfation of limestone. However, no explanations of the observed phenomena were given in these two papers.

3.2.1.2   Influence of system pressure

The direct sulfation reaction can be significantly hindered by higher system pressures under certain conditions, as observed by Qiu et al. (2000) and Bulewicz et al. (1987). Qiu et al. (2000) investigated the effect of the system pressure in a PTGA by maintaining constant partial pressures of SO_2 and CO_2. The oxygen content in the gas was 5 %. It was observed that the rate of the sulfation reaction at 1123 K was significantly lower at higher system pressures despite the increase of oxygen concentration at higher pressures. The effective

diffusivity in the product layer was also evaluated to be lower at higher system pressures. The authors suggested that the effect of the higher system pressures was caused by possible structure variation of the product layer or increased resistance of the outward diffusion of the formed CO_2.

Bulewicz et al. (1986) investigated the effect of the system pressure at constant gas composition (volume percentage). In this case, the gas concentrations were increased with the increase of the system pressure. The authors did not give an explanation of the observed phenomenon.

3.2.1.3   Influence of temperature

The influence of temperature is reflected by the apparent activation energy of the sulfation process. Table 3.2 lists the apparent activation energies evaluated directly by using sulfation rate data or by using mathematical models by different authors. The apparent activation energies measured at very low conversions were often assumed to represent the activation energies of the intrinsic kinetics of the sulfation reaction, while those measured at higher conversions were often assumed to represent the activation energies of the diffusion process in the product layer.

Table 3.2 Apparent activation energies determined by different authors

| Author | Temperature (K) | Apparent Activation Energy (kJ/mol) | | | |
| | | For Intrinsic kinetics or at low conversions | | For product layer diffusion or at high conversions | |
		Value	Evaluation method	Value	Evaluation method
Hajaligol et al. 1988	773-1213	68.7	model	146.5	model
Snow et al. 1988	298-1373	64	model	NA*	model
Iisa et al. 1992a	923-1123	NA		92 - 130	rate data
Iisa et al. 1992b	923-1223	77	model	133	rate data
Fuertes et al. 1993	1023-1173	96	model	NA	
Krishnan 1993	1023-1123	110 – 138	rate data	NA	
Tullin et al. 1993	773-1123	70 – 160	rate data at low conversions	170-390	rate data at high conversions
Fuertes et al. 1994	1023-1173	NA	model	148	model
Zhong 1995	773-1073	35.9	model	66.5	model
Zevenhoven et al.	1123-1223	9.14 - 82.2	model	(-70.7) - 338	model
Alvarez et al. 1999	1073-1198	87.2	model	NA	
Qiu et al. 2000	1023-1173	96.8	rate data at low conversions	144	model
Liu et al. 2000	883-1123	80 – 90	rate data at low conversions	83.1	model

* NA = not available.

As shown in Table 3.2, the influence of temperature on the direct sulfation of limestone is quite strong judged by the relatively high apparent activation energies. There is, however, no consistency in the apparent activation energies determined by the different authors. Zevenhoven et al. (1998a) suggested that the influence of temperature on the physical properties (such as pore structure and total surface area) of limestone particles may be a reason for the wide variation of the activation energies they determined with different limestones.

3.2.1.4   Influence of additives

Studies performed by Fuertes and Fernandez (1996) and Partanen et al. (2005) showed that the direct sulfation of limestone can be significantly enhanced by various Li^+, Na^+ and K^+ containing inorganic salts and HCl in the gas phase.

Fuertes and Fernandez (1996) studied the influence of a number of inorganic salts containing Li^+, Na^+, K^+, Cs^+, Al^{3+}, Zn^{2+} and Ca^{2+} on the direct sulfation of ultra–pure calcium carbonate in a TGA in the temperature interval from 973 K to 1148 K. It was observed that all the salts containing Li^+, Na^+ and K^+ enhanced the sulfation reaction, whereas the rest showed negative effects to different degrees. Based on the observation of increasing enhancement with increasing conversion for Na_2CO_3 doped samples, it was concluded that the enhancement of the direct sulfation of limestone by the alkali metal salts was due to an increased solid–state diffusion by the additives. The apparent activation energy determined with Na_2CO_3 doped sample (about 96 kJ/mol) was significantly lower than that determined with the undoped sample (about 140 kJ/mol). Based on this observation, Fuertes and Fernandez (1996) concluded further that the sulfation was controlled by chemical reaction for Na_2CO_3 doped samples.

Partanen et al. (2005) studied the simultaneous absorption of SO_2 and HCl on limestone in a TGA at 923 K and 1123 K. It was observed that the sulfation of $CaCO_3$ formed by recarbonation of calcinated limestone in CO_2 containing atmosphere was significantly enhanced by the presence of HCl in the gas phase. The enhancement was suggested to be related to the formation of a eutectic between $CaCO_3$, $CaSO_4$ and $CaCl_2$. $CaCl_2$ was formed by the simultaneous chlorination of $CaCO_3$.

3.2.1.5   Reactivity of limestone

Different limestones often show different reactivities as demonstrated by the studies of Zevenhoven et al. (1998a) and Alvarez et al. (1999). Zevenhoven et al. (1998a) studied the kinetics of the direct sulfation of 5 different limestones at 1123 K and 1223 K. The measured rate constants of these limestones varied from 0.00071 to 0.0013 m/s, an approximately 2–fold variation. Alvarez et al. (1999) performed similar studies on 5 different limestones at 1123 K. The measured initial sulfation rates of these limestones varied from 0.00038 to 0.0012 $g/(m^2s)$, an approximately 3–fold variation. Limestones are minerals which usually differ significantly in both physical and chemical properties (Dam-Johansen et al. 1991a, Yrjas et al. 1995 and Alvarez et al. 1999). Borgwardt et al. (1987), in their study of the influence of additives on the indirect sulfation of limestone, suggested that limestones containing a higher percentage of impurities may be more reactive because of higher solid–state diffusivity in the product layer caused by formation of more point defects by the impurities (West 1999). However, it is not clear whether the same conclusion can be made for the direct sulfation of limestone.

3.2.2   Kinetic modeling

The shrinking unreacted core model (Szekely et al. 1976 and Levenspiel 1962) has been the most frequently used mathematical model for description of the kinetics of the direct sulfation of limestone (Snow et al. 1988, Hajaligol et al. 1988, Iisa et al. 1992a, b, Krishnan et al. 1993, Tullin et al. 1993, Fuertes et al. 1994, Zhong 1995, Zevenhoven et al. 1998a, Alvarez et al. 1999, Liu et al. 2000, Qiu et al. 2000). Only a few authors have tried other approaches such as the parallel pore model (Szekely et al. 1976, Spartinos et al. 1991) and the changing internal surface (CIS) model (a model similar to the parallel pore model) (Zevenhoven et al. 1998b).

Although the different mathematical models differ in their way of describing the sulfation process, the basic steps included were generally the same, including gas film diffusion, pore diffusion, product layer diffusion and chemical reaction. To model the sulfation process by using these models, chemical reaction kinetics—the intrinsic sulfation rate— and diffusion kinetics in gas film/pores and product layer are usually needed.

3.2.2.1   Intrinsic kinetics

The intrinsic rate expressions used by different authors were empirical and included often only the influence of SO_2 as shown below:

$$r = k\ C_{SO_2}^{m} \quad (mol/(m^2 s)) \tag{3.5}$$

The influence of other gases were either incorporated in the rate constant or assumed to be zero order. The intrinsic kinetic parameters such as rate constants, reaction order and activation energy were usually evaluated directly by using rate data or by fitting rate data to a mathematical model. Table 3.3 shows the intrinsic rate expressions applied by the different authors and the corresponding rate constants they evaluated. As shown in the table, most of the authors assumed a reaction order of one with respect to SO_2. No consistency can be seen in the rate constants. Considering the different reaction conditions and limestone types used for their experiments, the inconsistency seems to be a natural result.

Table 3.3 Rate expressions for the direct sulfation of limestone applied by different authors

Author	Experimental condition	Rate expression $(mol/(m^2s))$	Rate constant, k
Snow et al. 1988	T: 773-1373 K; P: 0.1 MPa Gas composition: SO_2: 0.3%; O_2: 5%; CO_2: 2-95% Particle size: 2-106 µm	$k\,C_{SO_2}$	$0.72e^{(-64046/(8.314T))}$, m/s
Hajaligol et al. 1988	T: 773-1213 K; P: 0.1 MPa Gas composition: SO_2: 0.3%; O_2: 5%; CO_2:95% Particle size: 2-106 µm	$k\,C_{SO_2}$	$1.5e^{(-68650/(8.314T))}$, m/s
Fuertes et al. 1993	T: 923-1173 K; P: 0.1 MPa Gas composition: SO_2: 0.25%; O_2: 3.6%; CO_2:96.4% Particle size: 2-106 µm	$k\,p_{SO_2}$	$104e^{(-95700/(8.314T))}$, $mol/(m^2\ s\ atm)$
Krishnan 1993	T: 1123 K; P: 0.1 MPa Gas composition: SO_2: 0.15-0.6%; O_2: 6%; CO_2: 70% Particle size: 53-350 µm	$k\,C_{SO_2}^{0.4}$	$0.00031-0.0015$, $mol^{0.6}/(m^{0.8}s)$
Zhong 1995	T: 1073K; P: 0.1 MPa Gas composition: SO_2: 0.1-0.5%; O_2: 10%; CO_2: 70% Particle size: 4-5.4 µm	$k\,C_{SO_2}$	0.0049, m/s (E_a=35.9 kJ/mol)
Zevenhoven et al. 1998a	T: 1123 K; P: 1.5 MPa Gas composition: SO_2: 0.3%; O_2: 4%; CO_2: 20% Particle size: 250-300 µm	$k\,C_{SO_2}$	$0.0007-0.0014$, m/s
Alvarez et al. 1999	T: 1073-1198 K; P: 1.2 -2.5MPa Gas composition: SO_2: 0.5%; O_2: 3-7%; CO_2: 12-15% Particle size: 100-595 µm	$k\,C_{SO_2}$	0.00011 m/s at 1073 K 0.0003 m/s at 1198K (E_a=87.2 kJ/mol)
Liu et al. 2000	T: 883-1123 K; P: 1.5 MPa Gas composition: SO_2: 0-0.24%; O_2: 10%; CO_2: 20-80% Particle size: 8.4-54 µm	$k\,C_{SO_2}$	$19e^{(-90000/(8.314T))}$, m/s
Qiu et al. 2000	T: 1123K; P: 0.6 MPa Gas composition: SO_2: 0.35%; O_2: 5%; CO_2: 30% Particle size: 125-180 µm	$k\,C_{SO_2}^{0.58}$	0.00015, $kmol^{0.42}/(m^{0.26}s)$

3.2.2.2   Diffusion in the product layer

The direct sulfation of limestone is a gas–solid reaction with the formation of a solid product layer. Calcium sulfate ($CaSO_4$) is normally the final product (Murthy et al. 1979 and Ljungström et al. 1982). The formed $CaSO_4$ is of the type anhydrate II (Dam–Johansen et al. 1991b) and has a molar volume of about 46 cm^3, which is 24.7 % higher than the molar volume of limestone (calculated as calcite with a molar volume of 36.9 cm^3). The percentage of the volume increase when calcite is converted to $CaSO_4$ is much higher than the porosity of most of the limestones. Despite the high molar volume of the product, the product layer formed by the direct sulfation of limestone was observed to be porous (Snow et al. 1988,

Hajaligol et al. 1988 and Liu et al. 2000). The porosity and pore sizes were observed to increase with increasing temperature and to decrease with increasing conversion (Hajaligol et al. 1988 and Liu et al. 2000). The measured pore size in the product layer varied from a few nm to over 100 nm depending on the reaction conditions and the conversion (Hajaligol et al. 1988 and Liu et al. 2000).

Diffusion in the product layer, which has frequently been discussed in the literature, is important for the modeling of the direct sulfation of limestone. It appears to be a common belief in the literature that at high conversions the sulfation process is controlled by diffusion in the product layer. There were mainly two different views concerning the type of diffusion in the product layer that controls the sulfation process.

One view was gas phase diffusion in the pores of the product layer, suggested by Hajaligol et al. (1988), Krishnan et al. (1993) and Liu et al. (2000) mainly based on the porosity of the product layer.

The other view was solid–state diffusion, as suggested by Hepola et al. (1990), Iisa et al. (1992a, b), Tullin et al. (1993), Fuertes et al. (1994) and Alvarez et al. (1999), mainly based on the relatively high apparent activation energy of the sulfation process at high conversion (as listed in Table 3.2) and the relatively low effective diffusivities in the product layer. Table 3.4 lists the effective diffusivities determined via model simulations by different authors.

Table 3.4 Effective diffusivity in the product layer determined by different authors

Author	Experimental condition	Model used for evaluation of the effective diffusivity	Effective diffusivity at 1123 K (m^2/s)
Hajaligol et al. 1988	T: 773-1213 K; P: 0.1 MPa Gas composition: SO_2: 0.3%; O_2: 5%; CO_2:95% Particle size: 2-106 µm	Shrinking unreacted core model	1.5×10^{-6} ($D_e = 9.96e^{(-146510/(8.314T))}$)
Iisa et al. 1990	T: 1123 K; P: 1.5 MPa Gas composition: SO_2: 0.3%; O_2: 4%; CO_2:15% Particle size: 125-180µm	Shrinking unreacted core model	$0.6\text{-}4 \times 10^{-10}$
Iisa et al. 1991	T: 1133 K; P: 0.8-2 MPa Gas composition: SO_2: 0.3%; O_2: 4%; CO_2:15% Particle size: 150 µm	Shrinking unreacted core model	$2\text{-}4 \times 10^{-10}$ (at 1133K)
Fuertes et al. 1994	T: 923-1173 K; P: 0.1 MPa Gas composition: SO_2: 0.25%; O_2: 3.6%; CO_2:96.4% Particle size: 2-106 µm	Shrinking unreacted core model	1.3×10^{-9} ($D_e = 0.0086e^{(-146500/(8.314T))}$)
Zhong 1995	T: 1073K; P: 0.1 MPa Gas composition: SO_2: 0.1-0.5%; O_2: 10%; CO_2: 70% Particle size: 4-5.4 µm	Shrinking unreacted core model	$2.1 \times 10^{-9}*$
Zevenhoven et al. 1998b	T: 1123-1223 K; P: 1.5 MPa Gas composition: SO_2: 0.3%; O_2: 4%; CO_2: 20% Particle size: 250-300 µm	Shrinking unreacted core model	$6.6\text{-}102 \times 10^{-10}$
		Changing internal surface model	$1.8\text{-}16.8 \times 10^{-15}$
Alvarez et al. 1999	T: 1073-1198 K; P: 1.2 -2.5MPa Gas composition: SO_2: 0.5%; O_2: 3-7%; CO_2: 12-15% Particle size: 100-595 µm	Shrinking unreacted core model	6×10^{-13}
Liu et al. 2000	T: 883-1123 K; P: 1.5 MPa Gas composition: SO_2: 0-0.24%; O_2: 10%; CO_2: 20-80% Particle size: 8.4-54 µm	Shrinking unreacted core model	9.1×10^{-10} ($D_e = 6.71 \times 10^{-6}e^{(-10000/T)}$)
Qiu et al. 2000	T: 1023-1123K; P: 1.3 MPa Gas composition: SO_2: 0.16%; O_2: 5%; CO_2: 14% Particle size: 125-180 µm	Shrinking unreacted core model	$0.1\text{-}1.0 \times 10^{-9}$

* Calculated by using the activation energies obtained by the respective authors.
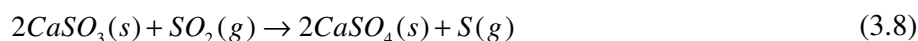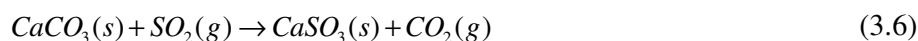
As shown in the above table, except for the values obtained by Alvarez et al. (1999), Hajaligol et al. (1998) and Zevenhoven et al. (1998b) with the changing internal surface (CIS) model (a model considering the internal surface area as well), the effective diffusivities obtained by the other authors are generally of the same order of magnitude, in the range of 10^{-9} to 10^{-10} m^2/s.

In order to clarify whether the diffusion was controlled by gas phase diffusion or by solid–state diffusion, Iisa et al. (1992a) investigated the influence of temperature on the further sulfation of pre–sulfated limestone particles. They observed an apparent activation energy of approximately 120 kJ/mol, which seems to support the arguments for solid–state diffusion control.

However, the diffusion kinetics in the product layer apparently is more complicated than imagined. Based on model simulations, it was observed by a number of authors (Hajaligol et al. 1988, Krishnan et al. 1993, Alvarez et al. 1999 and Qiu et al. 2000) that the effective diffusivity in the product layer decreased with increasing conversion or increasing SO_2 concentration. Tullin et al. (1993) and Qiu et al. (2000) also observed that the apparent activation energy of the effective diffusivity increased significantly with increasing conversion. No satisfactory explanation of these phenomena was given in these papers.

3.2.3 Sulfation mechanism

The mechanism of the direct sulfation of limestone was not explored as much as the overall kinetics in the past. There are only a few suggestions presented in the literature. Van Houte et al. (1979, 1981) suggested that the direct sulfation reaction takes place according to the following reaction steps at low temperatures (in the range of 573–900 K):

$$CaCO_3(s) + SO_2(g) \rightarrow CaSO_3(s) + CO_2(g) \qquad (3.6)$$

$$2CaSO_3(s) + O_2(g) \rightarrow 2CaSO_4(s) \qquad (3.7)$$

$$2CaSO_3(s) + SO_2(g) \rightarrow 2CaSO_4(s) + S(g) \qquad (3.8)$$

$$S(g) + O_2(g) \rightarrow SO_2(g) \qquad (3.9)$$

In this mechanism, Reaction (3.6) and (3.7) were assumed to be the main reactions. The sulfation process was suggested to be controlled by Reaction (3.6) or Reaction (3.7) depending on reaction conditions.

Tullin et al. (1993) suggested the following reaction mechanism to explain their experimental observations, in particular the depressing effect of higher CO_2 partial pressures on the direct sulfation reaction:
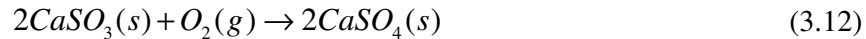
Step 1   dissociation of $CaCO_3$:

$$CaCO_3(s) \rightleftarrows CaO(s) + CO_2(g) \qquad (3.10)$$

Step 2   Formation of sulfite:

$$CaO(s) + SO_2(g) \rightleftarrows CaSO_3(s) \qquad (3.11)$$

Step 3   Oxidation of sulfite:

$$2CaSO_3(s) + O_2(g) \rightarrow 2CaSO_4(s) \tag{3.12}$$

In this suggested mechanism, Step 2, the sulfitation of CaO, was considered to be the rate–limiting step under the reaction conditions used in their study. The depressing effect of higher CO_2 partial pressures was believed to be caused by the influence of CO_2 on Step 1, the dissociation of the limestone.

Solid–state diffusion was suggested by a number of authors (Hepola et al. 1990, Iisa et al. 1992a, b, Tullin et al. 1993, Fuertes et al. 1994, Alvarez et al. 1999) to be the limiting step for the direct sulfation of limestone at high conversions. Fuertes et al. (1994) proposed the following reaction mechanism to illustrate the process:

Interchange of sulfate and carbonate ions at the interface between the product (CaSO$_4$) layer and the solid reactant (CaCO$_3$):

$$SO_4^{2-} + CaCO_3 \rightarrow CaSO_4 + CO_3^{2-} \tag{3.13}$$

Diffusion of carbonate ions through the product layer to the surface of the product layer and successive dissociation at the surface:

$$CO_3^{2-} \rightarrow (CO_2)_{ads} + O^{2-} \tag{3.14}$$

Formation of sulfate at the surface:

$$O^{2-} + SO_3 \rightarrow SO_4^{2-} \tag{3.15}$$

Desorption of CO_2 from the surface:

$$(CO_2)_{abs} \rightarrow CO_2(g) \tag{3.16}$$

In general, the above suggested mechanisms of the direct sulfation of limestone were not well supported by direct or indirect evidence and are therefore highly speculative. The details of these suggested mechanisms were not sufficient to give satisfactory explanations of the many experimental observations.

3.2.4 Summary

The above literature survey shows that the direct sulfation of limestone may be significantly influenced by a number of factors such as gas composition, temperature, system pressure and additives. The sulfation rate usually increases with increasing SO_2 and O_2 concentrations, but decreases with increasing CO_2 concentration. Water in the gas phase may

promote the sulfation reaction as well. The degree of influence of these gases depends on reaction conditions. The influence of O_2 may become negligible at high concentrations.

The influence of reaction temperature on the direct sulfation of limestone is usually strong, and can be both positive and negative. The negative influence of the temperature is mainly caused by sintering of limestone particles and the product layer at high temperatures.

The direct sulfation of limestone can be significantly enhanced by various additives such as Li^+, Na^+ and K^+ containing inorganic salts and HCl. The enhancements by the additives are most likely related to their capabilities in increasing ionic movement in the solid phases via formation of more point defects and eutectics.

Although the many investigations in the past have given us much factual information about the direct sulfation of limestone, our understanding of this reaction is still incomplete, reflected by the many unexplained or unsatisfactorily explained experimental observations, such as:

- Concerning the influence of gases: what is the reason for the variations of the apparent reaction orders of SO_2 and O_2 with the reaction conditions, and why does CO_2 have negative influence on the sulfation rate?

- Concerning the influence of water: how is the sulfation promoted by water in the gas phase, and why does the apparent reaction order of SO_2 increase in the presence of water?

- Concerning the product layer: how is the porosity of the product layer formed, and why does the porosity increase with increasing temperature and decrease with increasing conversion?

- Concerning product layer diffusion: why does the effective diffusivity decrease with increasing conversion, whereas its apparent activation energy increase with increasing conversion?

- Concerning the enhancement of the sulfation reaction by additives: where and how is solid–state diffusion increased and what are the diffusing species?

To answer the above questions, it is absolutely necessary to improve our understanding of the mechanism of the sulfation process.

3.3   Scope of the experimental work

The direct sulfation of limestone was studied with focus on the sulfation mechanism and kinetics. Experiments were performed with three different limestones of different morphological properties. The influence of various gases (SO_2, O_2, CO_2 and H_2O), temperature and additives were investigated. Efforts were especially put on investigations of the intrinsic kinetics and kinetics at relatively low conversions which are practically important for SO_2 absorption on limestone with short limestone particle residence time such as in the cyclone preheater used in cement production. The influence of various additives such as different kinds of alkali metal salts, $CaCl_2$ and HCl was studied for their potential application in enhancing the sulfation reaction at relatively low temperatures around 773–973 K which are typical temperatures in the cyclone preheater as well.

The experimental work includes three major subjects: the initial (intrinsic) sulfation kinetics, sulfation kinetics at low conversions and sulfation kinetics with addition of additives. The results with additives are presented in a separate chapter considering the significantly different kinetic behaviours compared to without additives.

3.4   Experimental

3.4.1 Reactor set-ups

To investigate the kinetics of the direct sulfation of limestone, two different reactors were used. One is a bench–scale quartz fixed–bed reactor which was practical for the study of the reaction kinetics with prolonged reaction time and higher limestone conversions. The other is a pilot entrained flow reactor for studying intrinsic kinetics of the direct sulfation of limestone. The following is descriptions of these two reactor systems.

3.4.1.1   Fixed–bed reactor

The fixed–bed reactor, as illustrated in Figure 3.2, was originally developed by Dam–Johansen et al. (1987, 1991a–d) for studying the sulfation of limestone in another context. The reactor consists of a quartz shell and a removable inner tube that contains the sample bed; the inner diameter of the inner tube is 16 mm. The reactor is electrically heated by three separate heating sections. Each of the heating sections has its own temperature controlling system. The reaction temperature is measured by a thermocouple located immediately beneath

the sample bed. Temperature mapping of the reactor showed that the temperature variation was less than 2 degrees between the measuring point and the point that is about 10 cm over the bed. It was observed during each experiment that the temperature increased no more than about 0.5–1 degree after SO_2 was introduced. The isothermal reaction condition is thus considered to be approximately fulfilled.

The required gases (SO_2, O_2, CO_2 and N_2) are supplied from gas cylinders with the flow of each gas controlled by a mass flow controller. Water vapor is added into the gas mixture by passing the CO_2 or N_2 gas through liquid water in a heated container. The container is specially designed to secure saturation of the passing gas. The gas mixture enters the reactor either at the bottom or at the top and is preheated to the required temperature before it reaches the sample bed. After reaction, the gas mixture flows out of the bottom of the reactor and is cooled to approximately 278 K to remove water from the gas. The gas is then analyzed for SO_2, O_2, and CO_2 by on–line gas analyzers. The concentrations of SO_2, O_2m and CO_2, temperature and pressure up–stream of the bed are continuously measured and logged via a data acquisition system.
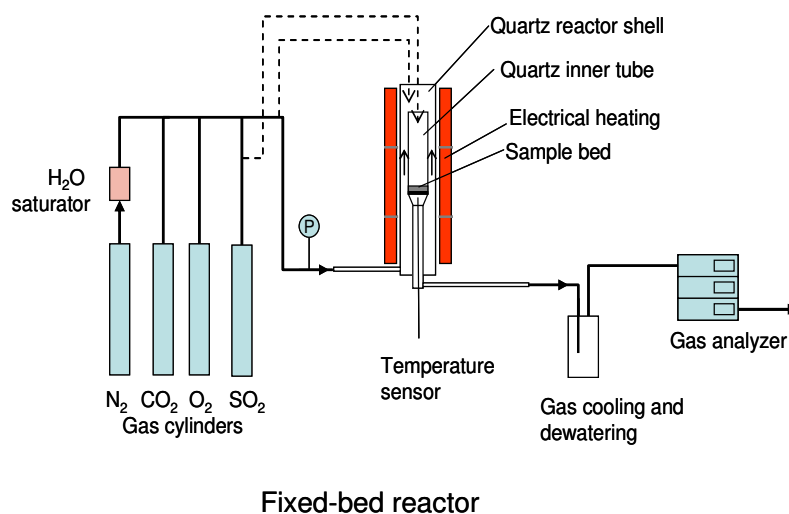
Fixed-bed reactor

Figure 3.2 Illustration of the fixed–bed reactor set-up

To perform experiments, the reactor was preheated to the required temperature. The gases were mixed to the required composition, which was verified by the gas analyzers. The inner tube was taken out and a weighed sample of limestone particles was poured into the bed. The surface of the sample bed was leveled by gently knocking the tube. The tube with the sample

was then put back in the reactor and was heated again. All the gases except SO_2 were mixed and admitted into the reactor. The heating-up generally took 5–8 minutes. After the temperature reached the set point, SO_2 gas was added to the gas stream. The reaction then started, and continued for a period from 5 minutes to a couple of hours depending on the purposes.

For each experiment, a sample weight of 0.25–2.8 g was used depending on the reaction temperatures. Large sample weights were used for experiments at lower temperatures and small sample weights for experiments at higher temperatures to obtain a concentration drop of SO_2 around 10 % at higher SO_2 concentrations (> ca. 1000 ppm) and 10-30 % at lower SO_2 concentrations (< ca. 500 ppm), which corresponds to a SO_2 concentration drop of ca. 20–200 ppm. The uncertainty of SO_2 measurement by the online gas analyzer is less than ± 2.5 ppm at high SO_2 concentrations (> 500 ppm) and less than ± 0.5 ppm at low SO_2 concentrations (< 500 ppm). The concentration drop range encountered during the experiments ensures reliable measurements and nearly differential reaction conditions in the reactor. It was verified that the variation in sample weight had no noticeable influence on the sulfation rate under the reaction conditions used.

3.4.1.2   Pilot entrained flow reactor

The pilot entrained flow reactor is illustrated in Figure 3.3.
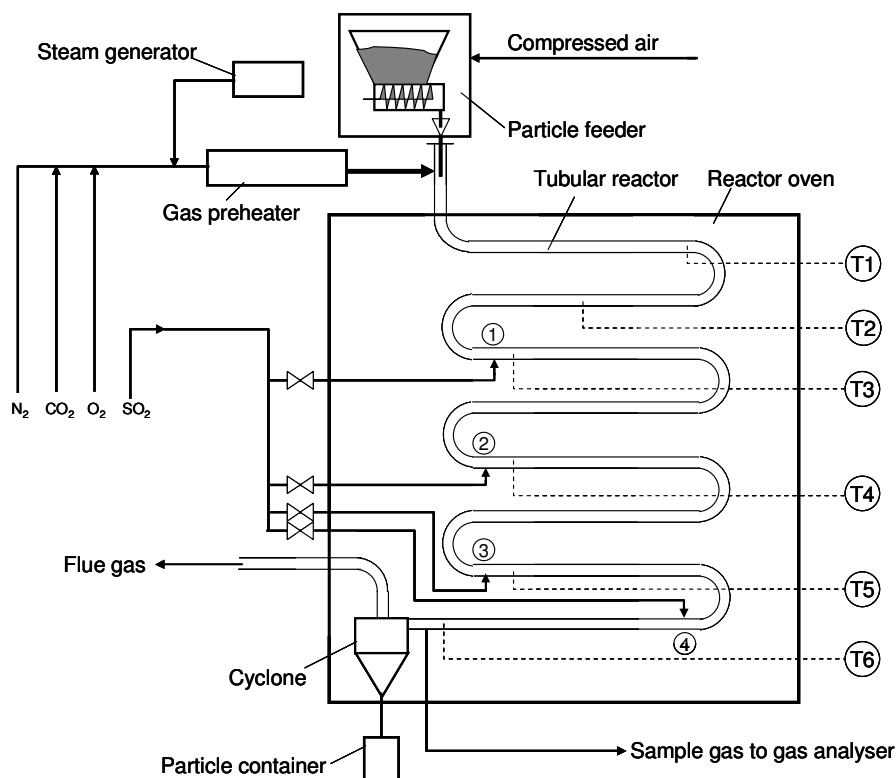
Figure 3.3 Illustration of the pilot entrained flow reactor

The main equipments of the pilot entrained flow reactor system include a gas supply unit, an electrically heated gas preheater, a steam generator, a particle feeder, a tubular reactor and a data acquisition system. The required amounts of gases (SO_2, CO_2, O_2, N_2 and compressed air) are supplied by the gas supply unit. SO_2, CO_2 and O_2 are from gas cylinders. Compressed air is from the utility supply net. The flow rate of each gas is controlled by a mass flow controller. Water vapor is supplied by the steam generator. The flow rate of the steam is controlled by a water dosing pump. Before entering the reactor, the mixed gases (CO_2, O_2, N_2 and H_2O) are preheated in the preheater to the required temperature (usually a couple of hundred degrees higher than the reaction temperature). The limestone particles are fed by the automatic particle feeder at set feeding rate into the reactor. Compressed air is used as the carry gas for the particles and a source of O_2 for the reaction as well. The preheated gases and the limestone particles meet at the inlet of the reactor. The limestone particles suspended in the gas stream are heated up by the preheated gas and further heated in the reactor. After reaction the particles are separated in a cyclone that is directly connected to the reactor. The separated particles fall down into the container outside the reactor oven. The gas is sampled

just before the cyclone and is analyzed for the concentration of SO_2, O_2 and CO_2 in online gas analyzers.

The reactor is made of Fe–Cr–Ni based high temperature resistant alloy tube (AVESTA 235MA, DIN 1.4893-X8CrNiN21-11) with an outer diameter of 26.7 mm and a wall thickness of 2.11 mm. The total length of the reactor is about 15 meter. SO_2 from the gas supply unit is injected at one of the 4 injection points along the length of the reactor. The dosing head are specially designed with small holes to ensure even distribution of SO_2 in the main gas flow. By shifting between the injection points, conversions at different residence times under identical flow and temperature conditions can be measured.

The temperature in the reactor is monitored at six points along the reactor length as shown in Figure 3.3. Figure 3.4 shows the temperature distribution without and with particle feeding at the three reaction temperatures applied in the experiments. This figure shows that temperature in the reactor is quite close to the set point from after the first SO_2 injection point (about 2–3 K lower than the set point) and is equal to the set point from after the second SO_2 injection point.
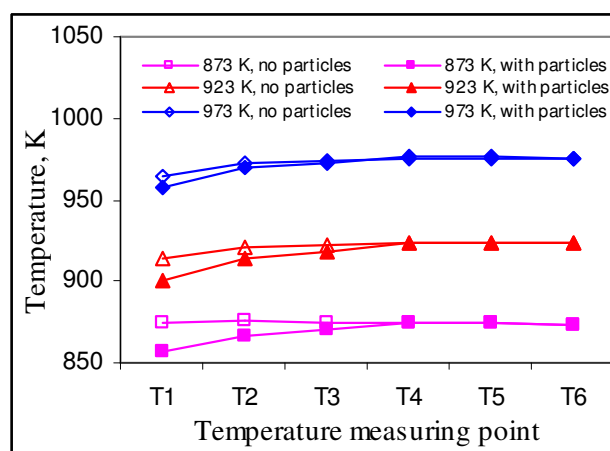
Figure 3.4 Temperature distributions in the reactor with and without particle feeding

The reactor has two major features:

1) Preheating of limestone particles to the required reaction temperature, which ensures an isothermal reaction condition.

2) Performing experiments with different residence times under identical flow conditions.

To perform experiments, the gas preheater, steam generator and the reactor oven are first heated to their temperature set points. After the temperature in the reactor is stabilized, CO_2, O_2, N_2 and H_2O of the required amounts are introduced into the reactor by first passing through the gas preheater, while SO_2 gas is introduced into the reactor directly at one of the injection points. The gas sampling is started. The concentrations of CO_2, O_2 and SO_2 are analyzed in the online gas analyzers. The gas concentrations, the 6 temperatures in the reactor and the pressure at the outlet of the reactor are logged into a data file in the data acquisition system. The concentrations of CO_2, O_2 and SO_2 without the addition of limestone particles are adjusted according to the desired values and then recorded. Limestone particles are then fed into the reactor according to the desired feeding rate. The SO_2 concentration at the outlet of the reactor is recorded. The difference between the stabilized SO_2 concentrations with and without the limestone particles in the reactor is used to calculate the conversion of the limestone.

3.4.2 Limestone samples

Limestone is a sedimentary rock consisting of mainly calcite ($CaCO_3$). In this study, three types of limestone were used for the experiments: a soft and porous bryozoan limestone from Faxe Kalk in Denmark (referred to hereafter as Faxe Bryozo), a hard and dense limestone from Obajana, Nigeria, provided by FLSmidth A/S in Denmark (referred to hereafter as Obajana Limestone), and Iceland Spar (a naturally occurring and pure crystalline calcite) provided by the Geological Museum, Copenhagen University, Denmark. Faxe Bryozo was in powder form when purchased. The structure of this type of limestone has been thoroughly studied by Dam–Johansen et al. (1991a–d) in relation to their extensive study of sulfation of various limestones. Particles of Faxe Bryozo are agglomerates of primary grains of a few micrometers in size. The three limestones were ground and sieved. The limestone particles prepared for the experiments were dried in an oven at 393 K for about 12 hours. Table 3.5 shows the properties of these limestones and the particle sizes used for the experiments.

All the three limestones were used for experiments in the fixed–bed reactor. Most of the experiments were performed with Faxe Bryozo. A few experiments were performed with Obajana Limestone and Iceland Spar for the purpose of comparison. For experiments in the pilot entrained flow reactor, only Faxe Bryozo was used.

Table 3.5 Properties of limestones used for the experiments

Limestone	Faxe Bryozo	Obajana Limestone	Iceland Spar
Composition*:			
CaCO$_3$ (w %)	97	94	> 99.5
Elemental analysis (w %):			
Na	< detection limit of 0.001	0.026	< detection limit of 0.001 %
Mg	0.26	0.64	0.005
Al	0.026	0.31	< detection limit of 0.001 %
Si	0.23	1.2	< detection limit of 0.001 %
P	0.014	0.005	< detection limit of 0.001 %
S	0.03	0.03	0.04
K	0.0054	0.15	< detection limit of 0.001 %
Ca	39	38	40
Ti	0.002	0.019	< detection limit of 0.001 %
V	0.002	0.002	< detection limit of 0.001 %
Cr	< detection limit of 0.001	0.001	< detection limit of 0.001 %
Mn	0.02	0.004	0.006
Fe	0.047	0.19	0.02
Zn	0.0014	< detection limit of 0.001	< detection limit of 0.001 %
Sr	0.042	0.27	0.02
Particle size (mm)	0.18–0.25 for fixed–bed reactor	0.2–0.3	0.18–0.25
	0.063–0.18 for entrained flow reactor		
	(particle distribution see appendix 1)		
Total surface area** (m^2/g)	0.79 for both	0.19	NA
Porosity***	ca. 0.3 for both (see appendix 2)		

* Determined by Wavelength Dispersive X-Ray (Philips PW2400).

**Determined by BET with nitrogen absorption (Micrometrics ASAP 2000).

***Determined by mercury intrusion (Micromeritics, MicroAutopore II 9220)

3.4.3 General experimental conditions

The general experimental conditions used in the fixed–bed reactor and the pilot entrained flow reactor are listed in Table 3.6. For the pilot entrained flow reactor, a gas speed of 20 m/s was used in order to ensure turbulent flow in the reactor. The temperature, pressure and gas concentrations are relevant values in the cyclone preheater used in cement production.

Table 3.6 Reaction conditions in the fixed–bed reactor and the pilot entrained flow reactor

Reaction condition	Fixed–bed reactor	Pilot entrained flow reactor
Temperature	723–973 K	873–973 K
Pressure	0.11 MPa	0.1 MPa
SO_2 concentration	50–1800 ppm	900–1800 ppm
O_2 concentration	0.5–45 vol. %	3–6 vol. %
CO_2 concentration	5–52 vol. %	8–15 vol. %
H_2O concentration	0–7.5 vol. %	0, 8 vol. %
Gas flow rate	1 l/min. (0.1 MPa, 298 K)	Gas speed: about 20 m/s at reaction temperature
Limestone particle load	Bed weight: 0.25–2.8 g	Feeding rate: 1.5–2.5 kg/h

3.5   Results

To evaluate the kinetic properties of the sulfation reaction, three rate–related concepts are used. One is limestone conversion (x) which is dimensionless and defined as the fraction of the solid reactant in the particles that is reacted. The second is conversion rate (dx/dt) which has the unit of s^{-1} and is defined as limestone conversion achieved per unit time (second). The third is sulfation rate (r) which has the unit of $mol/(m^2 s)$ and is defined as the amount of solid reactant (in mol) reacted per unit time (second) and square meter total surface area of the particles.

3.5.1 Initial sulfation

3.5.1.1   Data treatment

The initial sulfation kinetics of Faxe Bryozo was investigated in the entrained flow reactor, which allowed measuring of conversion rates at relatively low conversions because of the very short residence time (less than 1 second) in the reactor. In the entrained flow reactor, the conversion of the limestone was calculated based on the difference between outlet SO_2 concentrations without and with particle feeding by using the following equation:

$$x = \frac{P\,V(y_{SO_2, no\ particle\ feeding} - y_{SO_2, with\ particle\ feeding})M_{CaCO_3}}{\Re\,T\,w\,\eta} \tag{3.17}$$

The outlet SO_2 concentrations were the stabilized SO_2 concentrations with and without particle feeding. Figure 3.5 shows a typical case for the variation of outlet SO_2 concentration

during an experiment. The SO_2 outlet concentration without particle feeding was shown to increase slightly with decreasing residence time due to the absorption of SO_2 by a small amount of fine limestone particles which deposited on the tube wall. To minimize measuring errors, the outlet SO_2 concentration without particle feeding was measured during each experiment at each injection point just before or after the measuring of SO_2 outlet concentration with particle feeding. Before performing experiments at a higher temperature gas with the same compositions as for the experiments was passed through the reactor without particle feeding until SO_2 concentration became stable to deactivate small amount of fine limestone particles on the tube wall. Due to the fast deactivation of the limestone particles and the relatively fast initial absorption rate, the influence of the small amount of limestone particles that may deposit on the tube wall during the experiments was estimated to be insignificant based on the fact that SO_2 outlet concentrations at each stabilized state were quite constant without noticeable decrease or increase as illustrated in Figure 3.5.
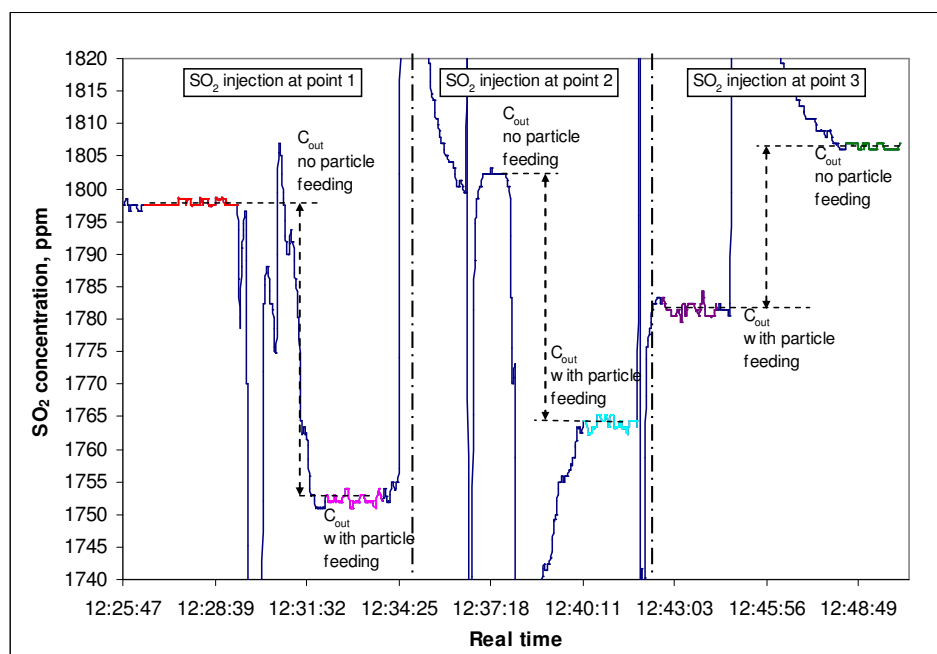
Figure 3.5 A typical example of the variation of outlet SO_2 concentrations with and without limestone particle feeding with SO_2 injected at different injection points (reaction conditions: T: 873 K; P: 0.1 Pa; SO_2: 1800 ppm; O_2: 3 %; CO_2: 15 %; N_2: balance)

Conversion of SO_2 to SO_3 at elevated temperatures and especially with a steel reactor is often a concern for the study of kinetics of limestone sulfation. To investigate the degree of the conversion of SO_2 to SO_3 in the pilot entrained flow reactor, SO_2 containing gas with similar composition as for the experiments was passed the reactor without limestone particle feeding. The reactor temperature was increased gradually. Figure 3.6 shows the variations of SO_2 outlet concentration and reactor temperature with the time. This figure demonstrates that at temperatures up to 973 K the conversion of SO_2 to SO_3 was negligible as the end SO_2 concentration at 973 K was approximately the same as the start concentration. The SO_2 concentration drop during heating–up from 873 K to 973 K was caused by SO_2 absorption on the small amount of fine limestone particles on the tube wall left during earlier experiments at lower temperatures. The SO_2 concentration increased to the start concentration after longer time.
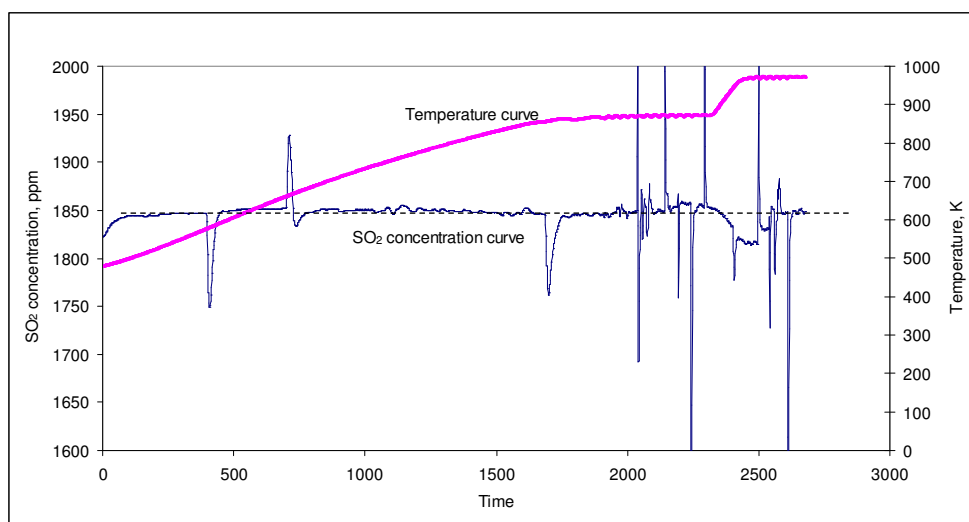
Figure 3.6 Variation of SO_2 concentration with temperature without limestone particle feeding

The insignificant conversion of SO_2 to SO_3 during the experiments was also confirmed by the insensitivity of outlet SO_2 concentrations on residence time and variation in O_2 concentration without particle feeding as illustrated in Table 3.7 with two consecutive experiments at 973 K.

Table 3.7 Outlet SO_2 concentrations at different residence time and O_2 concentrations at 973 K

Experiment	O_2 concentration, %	Outlet SO_2 concentration, ppm	
		Residence time = 0.17 s	Residence time = 0.08 s
a	3	1807	1810
b	6	1804	1808

Due to the relatively small difference between the SO_2 concentrations without and with limestone particle feeding (generally in the interval from 30–70 ppm), the main error source of the calculated conversion of the limestone was from the measuring errors of the SO_2 concentrations and gas flow rates. It was estimated that a maximum deviation of approximately ± 2 ppm existed for SO_2 concentration measurements and 1 % of the total gas flow rates for gas flow measurements. The standard deviations of the calculated conversions of the limestone (indicated by the "I" bars in the figures) are calculated based on these two estimated errors. The standard deviations are generally in the range 5–8 %.

3.5.1.2   Influence of SO_2, O_2, CO_2 and H_2O

To see the influence of gases such as SO_2, O_2, CO_2 and H_2O, the initial sulfation of Faxe Bryozo was studied at two different SO_2, O_2 and CO_2 concentrations with and without addition of water in the gas. Figures 3.7–3.11 show the results.

The initial conversion rate of Faxe Bryozo was significantly promoted by higher SO_2 concentrations and low CO_2 concentrations as shown in Figure 3.7 and 3.9, but not by higher O_2 concentrations as shown in Figure 3.8. At a longer reaction time, the sulfation reaction seems to be hindered by higher O_2 concentrations. The negative effect of higher O_2 concentrations was more evident at 973 K as shown in Figure 3.8. Water in the gas phase seems to significantly hinder the initial sulfation reaction as shown in Figure 3.10.
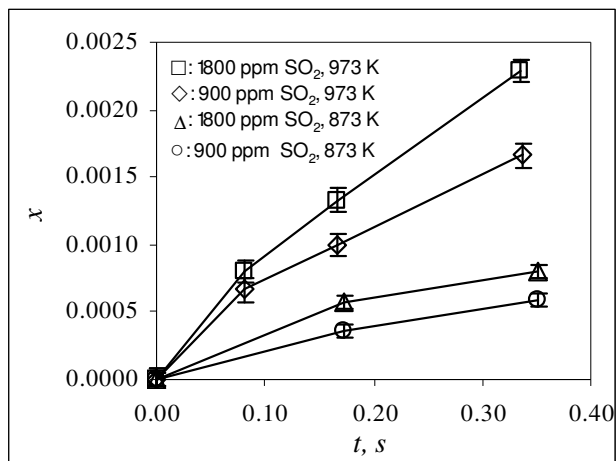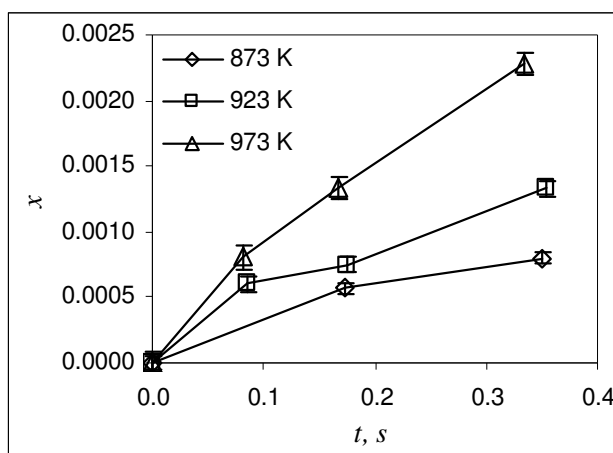
Figure 3.7 Variation of conversion of Faxe Bryozo with reaction time at different SO_2 concentrations (standard conditions if not specified: P: 0.1 MPa; SO_2: 1800 ppm; O_2: 3 %; CO_2: 15 %; N_2: balance)
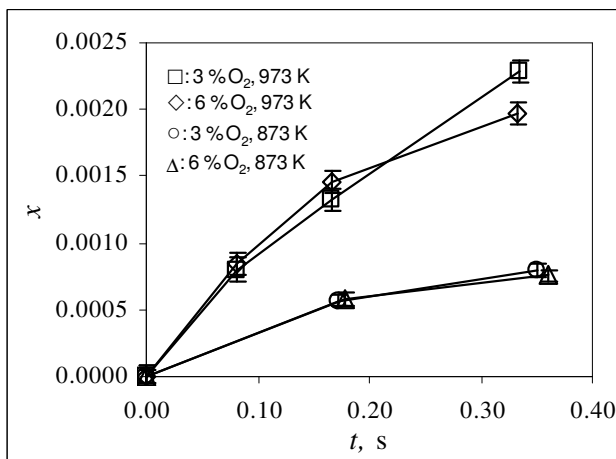
Figure 3.8 Variation of conversion of Faxe Bryozo with reaction time at different O_2 concentrations (standard conditions if not specified: P: 0.1 MPa; SO_2: 1800 ppm; O_2: 3 %; CO_2: 15 %; N_2: balance)
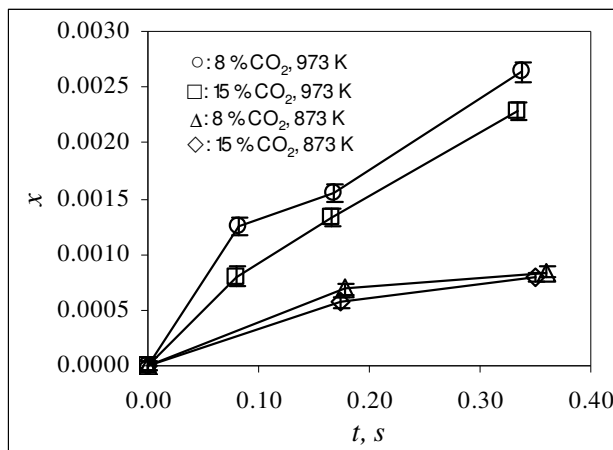
Figure 3.9 Variation of conversion of Faxe Bryozo with reaction time at different CO_2 concentrations (standard conditions if not specified: P: 0.1 MPa; SO_2: 1800 ppm; O_2: 3 %; CO_2: 15 %; N_2: balance)
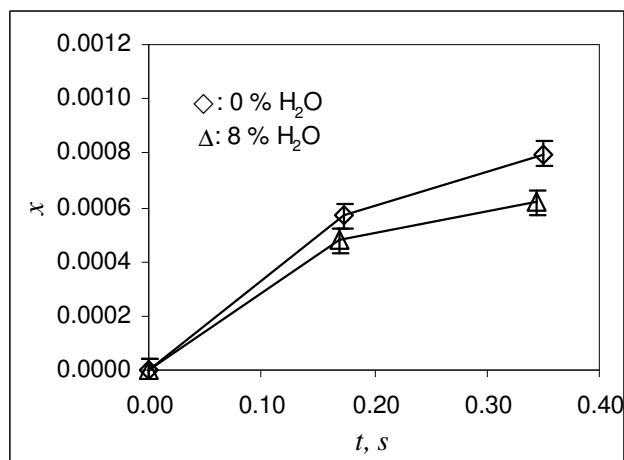
Figure 3.10 Variation of conversion of Faxe Bryozo with reaction time at 873 K with and without water addition in the gas (standard conditions if not specified: P: 0.1 MPa; SO_2: 1800 ppm; O_2: 3 %; CO_2: 15 %; N_2: balance)

The initial sulfation kinetics seems to be quite different from that observed in earlier studies at higher conversions. This is reflected in the special effect of O_2 and the negative effect of H_2O. No earlier studies have observed negative effect of higher O_2 concentrations. The negative effect of H_2O observed here contradicts the observation by Hajaligol et al. (1988).

3.5.1.3   Influence of temperature

The influence of temperature on the initial sulfation of Faxe Bryozo was studied at three different temperatures. As shown in Figure 3.11, the initial sulfation reaction was significantly promoted by higher temperatures.

Figure 3.11 Variation of conversion of Faxe Bryozo with reaction time at different temperatures (standard conditions if not specified: P: 0.1 MPa; SO_2: 1800 ppm; O_2: 3 %; CO_2: 15 %; N_2: balance)

The initial sulfation rate $(mol/(m^2s))$ (obtained by dividing conversion rate (s^{-1}) with the molar total surface area of the limestone sample) observed with Faxe Bryozo was significantly higher than the predicted rates by using the intrinsic rate expressions presented in the literature. Figure 3.12 shows the comparison between the predicted rates and the average sulfation rates at the shortest residence time shown in Figure 3.11. The sulfation rates obtained with Faxe Bryozo were about 15–100 times higher than the predicted rates by using the intrinsic rate expressions presented in the literature.
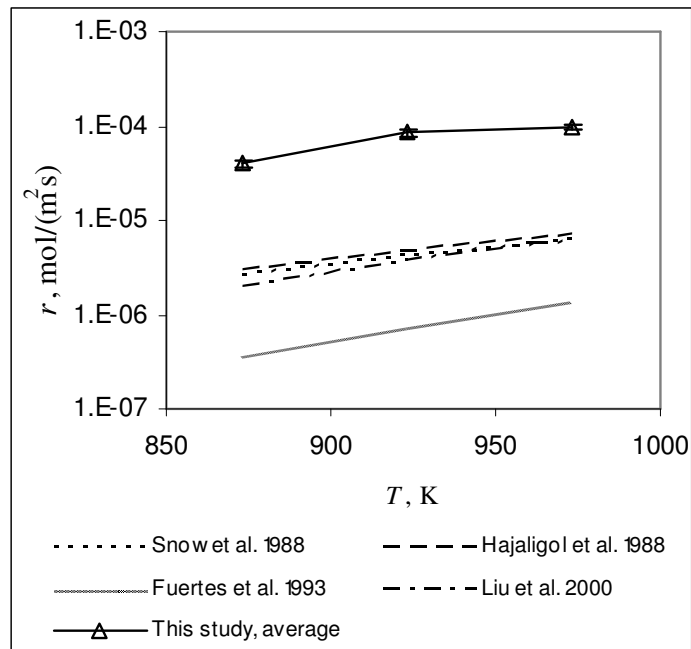
Figure 3.12 Comparison between the initial (average) sulfation rates measured in this study with Faxe Bryozo and the intrinsic rates predicted by rate expressions presented in the literature (Conditions: P: 0.1 MPa; SO_2: 1800 ppm; O_2: 3 %; CO_2: 15 %; N_2: balance)

Though the conversions of the limestone achieved in the pilot entrained flow reactor were relatively low because of the short residence time, the sulfation process was most likely already significantly influenced by the formation of the solid product, as none of the conversion vs. time data sets in Figures 3.7–3.11 can be closely represented by a linear line through the origin, which is otherwise expected at this low conversion stage if the influence of the solid product was negligible. The mechanism by which the sulfation reaction was influenced by the solid product at the initial sulfation stage will be discussed in the discussion section.

By using the average conversion rates at different temperatures obtained in the shortest residence times shown in Figure 3.11, an apparent activation energy of about 79 kJ/mol is obtained. This relatively high apparent activation energy indicates that the intra–particle diffusion resistance during the experiments was not significant. According to calculations (see appendix 3) the intra–particle diffusion may begin to become significant at a rate constant of about $5 \ 10^{-3}$ m/s for a particle size of 0.2 mm. The highest conversion rate (average rate at the shortest residence time) measured in the pilot entrained flow reactor at 973 K was about $8 \ 10^{-3}$

s^{-1}. This rate corresponds to a rate constant of about $4.5 \ 10^{-3}$ m/s at the used SO_2 concentration when the reaction is assumed to be first order with respect to SO_2. Based on this it can also be concluded that the intra–particle diffusion resistance was not significant.

3.5.2 Sulfation at low conversions

3.5.2.1   Data treatment

For experiments carried out in the fixed-bed reactor, the conversion rate and conversion of the limestone sample were calculated based on the difference of SO_2 concentrations before and after the bed by using the following equations:

Conversion rate at any time:

$$\frac{dx}{dt} = \frac{P \ V (y_{SO_2, before the bed} - y_{SO_2, after the bed}) M_{CaCO_3}}{\Re \ T \ W \ \eta} \qquad (s^{-1}) \qquad (3.18)$$

Conversion increase during the sampling interval Δt:

$$\Delta x = \frac{P \ V (y_{SO_2, before the bed} - y_{SO_2, after the bed}) M_{CaCO_3} \ \Delta t}{\Re \ T \ W \ \eta} \qquad (3.19)$$

Conversion at time t is obtained by summing Δx from the start to time t.

However, in the first half minute of the sulfation reaction, the outlet SO_2 concentration measured by the online gas analyzer deviates significantly from the true SO_2 concentration just after the bed because of residence time distribution in the reactor system. To assess the true SO_2 concentration just after the bed, the obtained experimental data were deconvoluted by using Fourier Transform. The following is a short introduction of this method (Levevspiel 1999, Jensen 1999).

Figure 3.13 illustrates the effect of RTD to outlet concentration. For a vessel with a RTD function of $E(t)$, the outlet concentration profile deviates from the inlet concentration profile in the form of a more flat curve and wider time distribution. The outlet concentration is said to be the convoluted signal of the inlet concentration. The inlet concentration and the outlet concentration are related by the following equation according to the convolution theorem (Varma and Morbidelli 1997):

$$C_{out}(t) = \int_0^t C_{in}(t - t^*) E(t^*) dt^* \qquad (3.20)$$

This equation means: the outlet concentration at time t is the integrated contribution of that part having a residence time of t^* in the input at the inlet at time t^* earlier than t. Equation 3.21 can be denoted by the following equation:

$$C_{out} = C_{in} * E \tag{3.21}$$
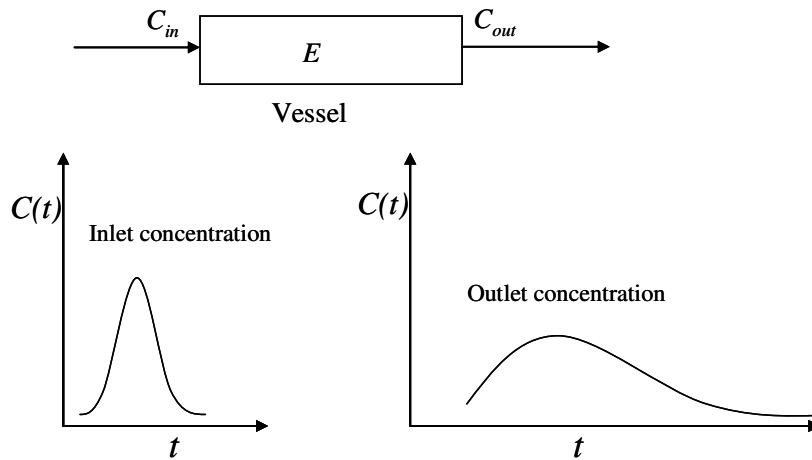
Figure 3.13 Illustration of the influence of RTD on gas concentration

For the sulfation experiments, the vessel can be considered as the volume from the point just after the bed to the gas analyzer as illustrated in Figure 3.14. C_{out} is the measured concentration. What needed is C_{in}, the concentration just after the bed without the influence of RTD. The calculation of C_{in} from known C_{out} and E is called deconvolution, which can be done by discrete Fourier transform, as C_{out} and E are usually discrete data series. By performing Fourier transform that is normalized with $N^{-0.5}$ (N: total data points in C_{out} or E) at both sides of Eq. 3.21 and rearrangement, the transformed C_{in} can be calculated by the following equation:

$$\mathbb{F}[C_{in}] = \frac{\mathbb{F}[C_{out}]}{N^{0.5} \times \mathbb{F}[E]} \tag{3.22}$$

C_{in} can then be calculated by perform inverse Fourier transform:

$$\mathbb{F}^{-1}\left[C_{in}\right] = \mathbb{F}^{-1}\left[\frac{\mathbb{F}\left[C_{out}\right]}{\mathbb{F}\left[E\right]}\right] \times N^{-0.5} \qquad\qquad (3.23)$$
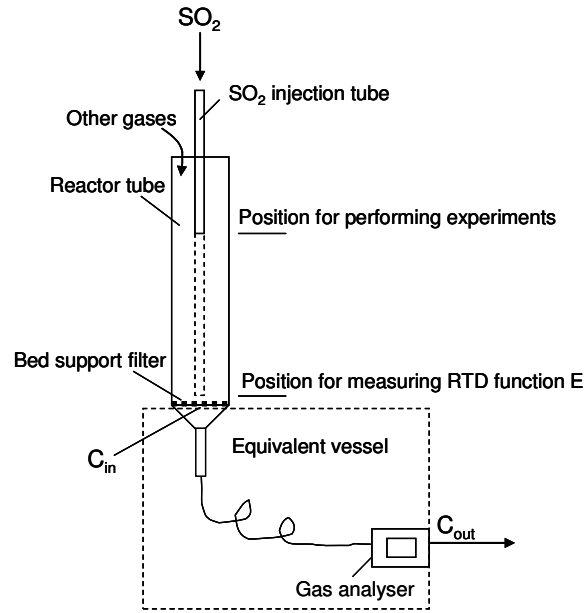
Figure 3.14 Illustration of the application of deconvolution method in experiments with the fixed–bed reactor

The RTD function of the equivalent vessel illustrated in Figure 3.14 was determined by a step injection of SO_2 gas at the position very close to the bed support filter, which ensures the same vessel properties for the sulfation experiments. Due to the existence of a short period (a few seconds) with full SO_2 absorption at the start of each experiment, stead state above the sample bed was supposed to be established at the moment SO_2 break through the bed. No influence of RTD in the volume from SO_2 injection point to the bed is expected. All experiments were performed with a sampling rate of 2 times per second. Fourier transform calculations were carried out by using Discrete Fourier Transform package in Maple 10 (a mathematical software from MapleSoft).

To check the reliability of the method, the deconvolution was performed with one representative sulfation experiment and the step signal for determining the RTD function by varying the cut frequency (components in Fourier transform with frequencies higher than a certain value is set to zero for avoiding severe fluctuation). Figure 3.15 shows the

deconvoluted step signal used to construct the *E* function. With increasing cut frequency, the deconvoluted signal approaches more and more to the step signal shape but with increasing fluctuation as expected. Figure 3.16 shows the deconvoluted SO_2 concentration just after the bed in the first 20 seconds of a representative experiment. With increasing cut frequency, the deconvoluted SO_2 concentration just after the bed stayed at the same position though with increasing fluctuation. These two figures demonstrate that the applied method was reliable. 0.25 was shown to be the optimal cut frequency for reducing the influence of high frequency noise. The cut frequency was thus set to 0.25 in all the calculations.
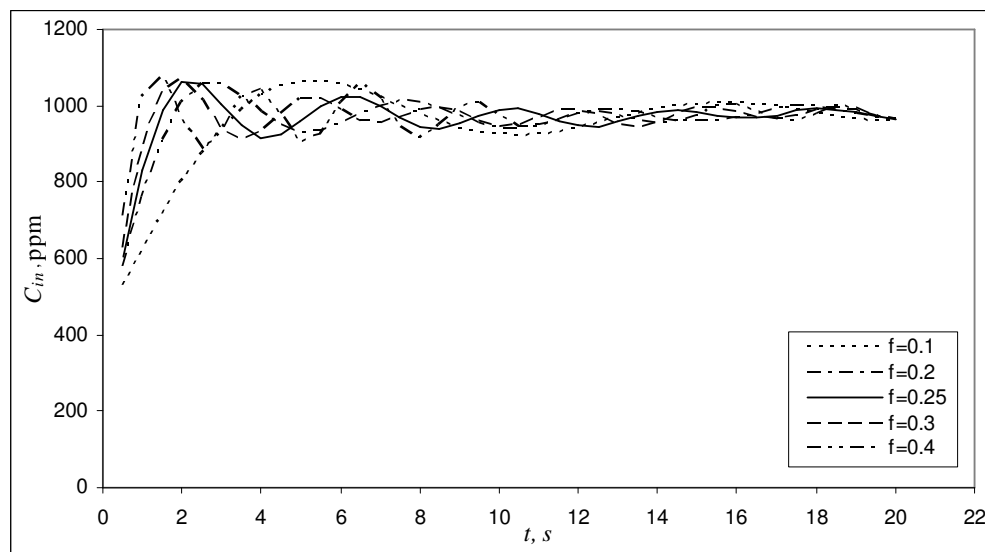
Figure 3.15 Deconvoluted step signals with different cut frequencies
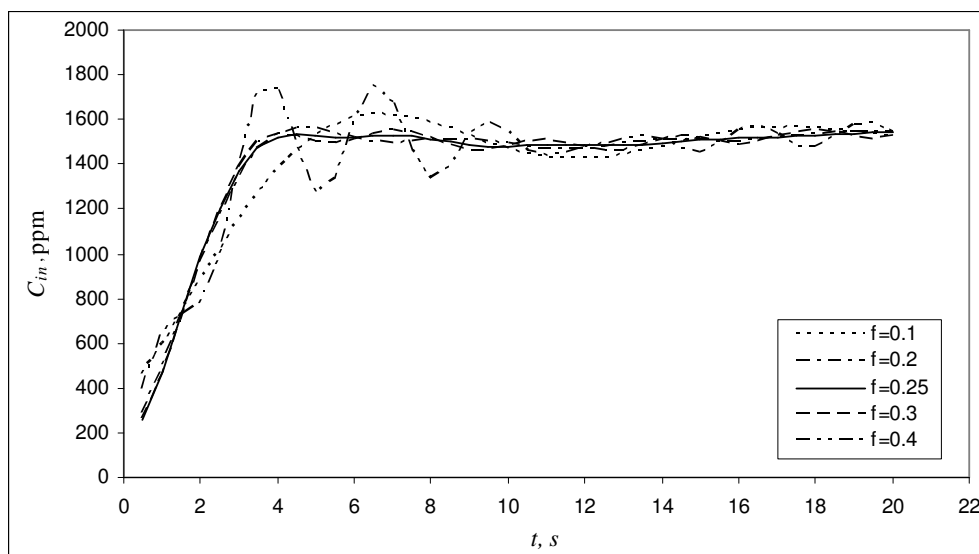
Figure 3.16 Deconvoluted SO_2 outlet concentration of a representative experiment with different cut frequencies (Reaction conditions: limestone: Faxe Bryozo; T: 823 K; P: 0.11 MPa; SO_2 inlet: 1800 ppm; O_2: 3%; CO_2: 30%; N_2: balance)

The sulfation in the fixed–bed reactor was observed to have a short period of a few seconds with full absorption. The actual time span for this period depended on the reaction conditions such as bed weight, gas flow, gas composition and temperature. After this full absorption period, there was a period of a few seconds with sharp decrease in the measured conversion rate of the limestone, which was then followed by a period with relatively slow and almost linear decrease in the conversion rate. Figure 3.17 is a typical example of the deconvoluted conversion rate vs. time curves of Faxe Bryozo which illustrates the above described variation pattern of the conversion rate. The time scale here is t' —the time from the point where SO_2 is detected by the SO_2 analyzer—in stead of the true reaction time t because of the existence of the short period with full SO_2 absorption.
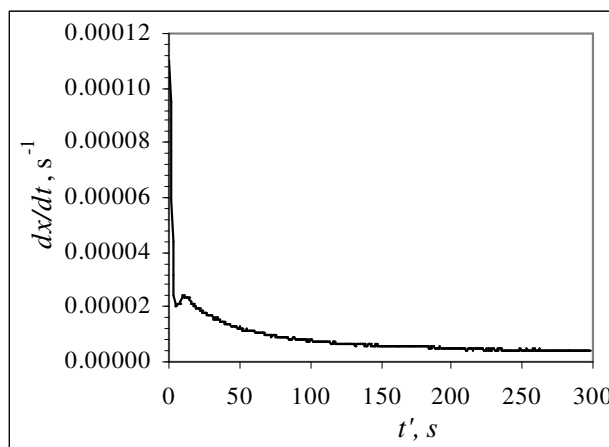
Figure 3.17 Illustration of the variation of conversion rate of Faxe Bryozo with reaction time (reaction conditions: limestone: Faxe Bryozo; T: 823 K, P: 0.11 MPa; SO_2 (inlet): 1830 ppm SO_2; O_2: 3%; CO_2: 30 %; N_2: balance)

The presented conversion rate data is estimated to have a standard deviation of about $\pm$ 2.5% which was evaluated by using the rate data of two set experiments repeated under identical reaction conditions (900 data pairs). The "I" bars in some of the figures represents the standard deviation evaluated by error propagation, which is generally around $\pm$ 5 %, twice as large as the value evaluated by data of repeated experiments. The standard deviation evaluated by error propagation may be taken as an indication for the possible maximum deviation.

Because of the dramatic variation of the conversion rate in the first half minute and the closely linear variation thereafter, the kinetic properties of the sulfation reaction at reaction time longer than 3 minutes are presented by average conversion rates calculated by the following equation:

$$(dx/dt)_{av} = \Delta x / \Delta t = (x_{480s} - x_{180s})/300 \qquad (\text{s}^{-1}) \qquad\qquad (3.24)$$

3.5.2.2   Influence of gases

3.5.2.2.1 SO_2
The influence of SO_2 on the conversion rate of Faxe Bryozo was investigated in the fixed–bed reactor by varying SO_2 concentration while keeping the other gas concentrations constant. Figure 3.18 shows the conversion rate vs. time curves at different SO_2

concentrations in the first few minutes, which demonstrates that the influence of SO_2 decreased significantly with reaction time. Figure 3.19 shows the variation of the average conversion rates with SO_2 concentrations after a longer reaction time. The influence of SO_2 on the average conversion rate corresponds to an average apparent reaction order of about 0.22 at 3 % oxygen and about 0.17 at 0.5 % oxygen, which are significantly lower than the values of 0.76 observed by Yang et al. (1975), 0.49 by Iisa et al. (1992a), 0.4 by Krishnan (1993) and 0.58 by Qiu et al. (2000), probably because of the much lower temperatures used in this study.

The influence of SO_2 on the direct sulfation reaction seems to be affected by the presence of water in the gas, as an addition of 7.5 % water in the gas increased the average apparent reaction order of SO_2 to approximately 0.4 in the SO_2 concentration interval from 500 to 1800 ppm. This phenomenon is principally in agreement with the observation by Yang et al. (1975). Oxygen seems to affect the apparent reaction order of SO_2 as well. Lower O_2 concentrations apparently results a lower apparent reaction order of SO_2 as shown in Figure 3.19.
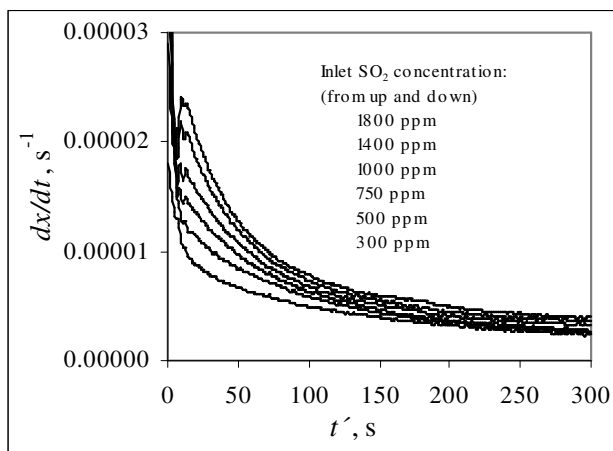
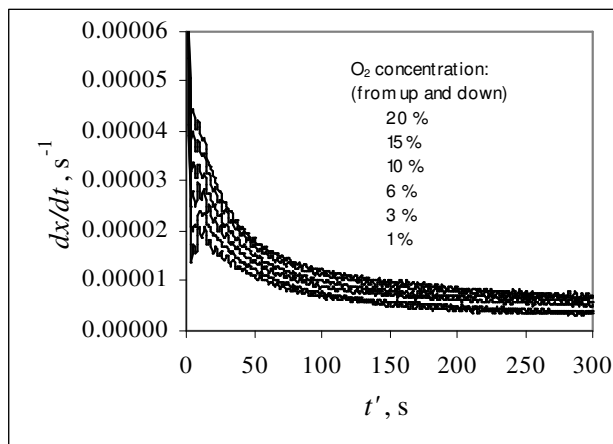

Figure 3.18 Conversion rate vs. time curves obtained with Faxe Bryozo at 823 K at different SO_2 concentrations (other conditions: P: 0.11 MPa; O_2: 3 %; CO_2: 30 %; N_2: balance)
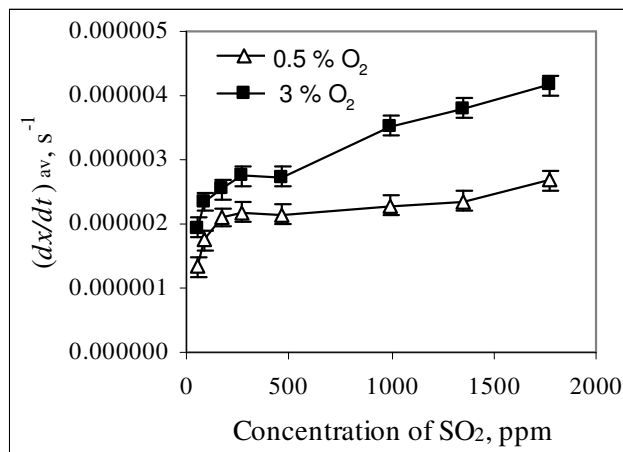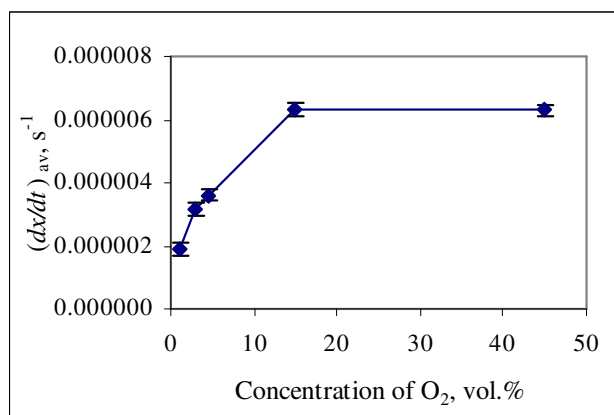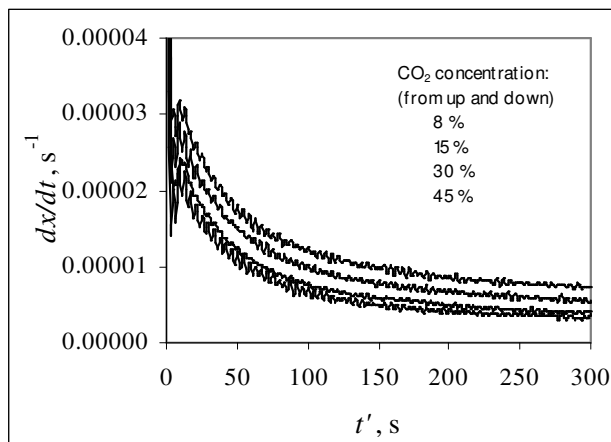
Figure 3.19 Variation of the average conversion rate of Faxe Bryozo with SO_2 concentrations at 823 K (other conditions: P: 0.11 MPa; CO_2: 30 %; N_2: balance)

3.5.2.2.2 O_2

The direct sulfation of Faxe Bryozo was observed to be promoted by higher O_2 concentrations in the fixed–bed reactor as shown in Figures 3.19, 3.20 and 3.21. Figure 3.20 shows the conversion rate vs. time curves at different O_2 concentrations without water addition in the first few minutes. At longer reaction time, the apparent reaction order of O_2 at low O_2 concentrations (0.5–3 %) was evaluated (by using data presented in Figure 3.19) to be about 0.2.

Figure 3.21 shows the variation of the average conversion rate with O_2 concentrations in the presence of 7.5 % water in the gas. This figure demonstrates that the average conversion rate increased with increasing O_2 concentration up to approximately 15 % O_2. The effect of O_2 corresponds to an apparent reaction order of around 0.4. At higher O_2 concentrations the conversion rate did not increase further, giving an apparent reaction order of zero. This phenomenon is principally in agreement with observations by Iisa et al. (1990), Alvarez et al. (1999) and Liu et al. (2000). The presence of water seems to create a higher reaction order for O_2 as for SO_2.

Considering the negligible influence of O_2 on the sulfation reaction in the initial stage, the promoting effect of O_2 observed in the fixed–bed reactor indicates that the sulfation mechanism is changed after prolonged reaction time.

Figure 3.20 Conversion rate vs. time curves obtained with Faxe Bryozo at 823 K at different O_2 concentrations (other conditions: P: 0.11 MPa; inlet SO_2: 1800 ppm; CO_2: 30 %; N_2: balance)
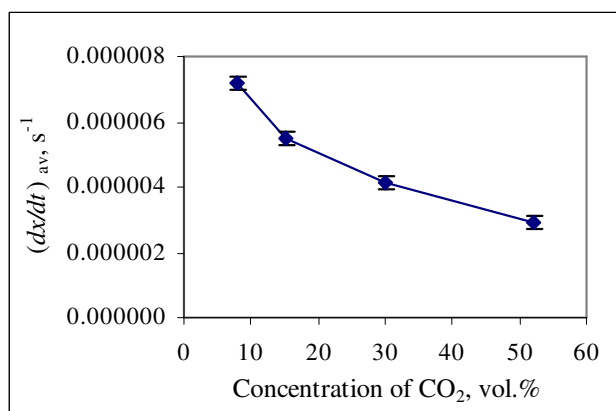

Figure 3.21 Variation of the average conversion rate of Faxe Bryozo with O_2 concentrations at 823 K (other conditions: P: 0.11 MPa; inlet SO_2: 1800 ppm; CO_2: 30 %; H_2O: 7.5 %; N_2: balance)

3.5.2.2.3 CO_2

The direct sulfation of Faxe Bryozo in the fixed–bed reactor was observed to be significantly hindered by higher CO_2 concentrations as shown in Figures 3.22–3.23. The influence of CO_2 on the average conversion rate corresponds to an apparent reaction order of approximately –0.5. The observed negative influence of higher CO_2 concentrations is in agreement with the observations in the pilot entrained flow reactor and previous observations by Ulerrich et al. (1980), Dam–Johansen (1987), and Tullin et al. (1993).

Figure 3.22 Conversion rate vs. time curves obtained with Faxe Bryozo at 823 K at different CO_2 concentrations (other conditions: P: 0.11 MPa; inlet SO_2: 1800 ppm; O_2: 3 %; N_2: balance)

Figure 3.23 Variation of the average conversion rate of Faxe Bryozo with CO_2 concentrations at 823 K (other conditions: P: 0.11 MPa; inlet SO_2: 1800 ppm; O_2: 3 %; N_2: balance)

3.5.2.2.4 H_2O

In contrary to the negative effect of H_2O on the initial sulfation as observed in the pilot entrained flow reactor, H_2O was observed to promote the direct sulfation of Faxe Bryozo at prolonged reaction time. Figure 3.24 shows the conversion rate vs. time curve at 923 K with and without water in the gas. Initially water was not added to the gas. The conversion rate decreased with the reaction time. At the reaction time of about 600 seconds, water was added to the gas at a concentration of about 7.5 %. The addition of water resulted in an abrupt

increase in the conversion rate. The conversion rate continued to decrease with the reaction time at almost the same rate as before the addition of water. At the reaction time of about 950 seconds, the addition of water was ceased; this caused an abrupt drop in the conversion rate. A similar experiment performed at 823 K yielded similar results. The promoting effect of water on the direct sulfation of Faxe Bryozo in the fixed–bed reactor is in agreement with the observation by Hajaligol et al. (1988). The presence of water seems to cause changes in the sulfation behavior of the limestone, which is reflected by the almost constant conversion rate after the stop of water addition.
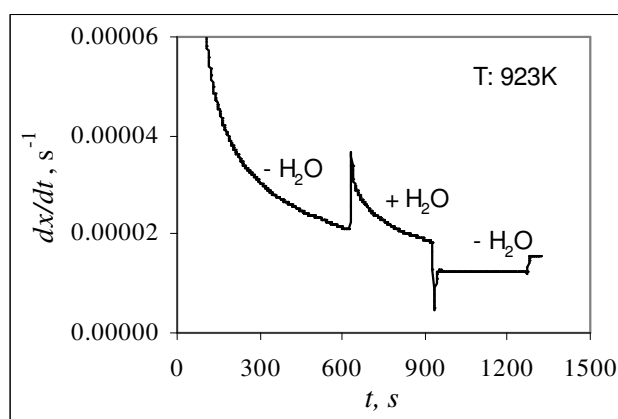
Figure 3.24 Influence of water addition on the conversion rate of Faxe Bryozo at 923 K (other conditions: P: 0.11 MPa; inlet SO_2: 1800 ppm; O_2: 3 %; CO_2: 30 %; H_2O: 0-7.5 %; N_2: balance).

3.5.2.3   Influence of temperature

The influence of temperature on the direct sulfation of Faxe Bryozo in the fixed–bed reactor was observed to be strong as in the pilot entrained flow reactor. Figure 3.25 shows the conversion rate vs. time curves at different temperatures in the first few minutes. For the period with closely linear decrease in the conversion rate, the apparent activation energy is evaluated in the temperature interval from 723 K to 973 K by using the average conversion rate for both Faxe Bryozo and Obajana Limestone. The conversion rates at different temperatures were measured at the same inlet gas concentrations (vol. %). Due to the differential reaction conditions in the reactor, the low reaction orders of SO_2 and O_2 and the negative reaction order of CO_2, the contributions from the small variations of the gas concentrations caused by the different temperatures to the conversion rates were estimated to

be insignificant. The activation energies are thus directly evaluated by plotting $\ln((dx/dt)_{av})$ againt $1/T$.

As shown in Figure 3.26, the apparent activation energy is evaluated to be about 104 kJ/mol for Faxe Bryozo and about 103 kJ/mol for Obajana Limestone. These two values are essentially equal despite the very different morphologies of these two limestones. The values are quite close to those obtained by Fuertes et al. (1993) (96 kJ/mol), Krishnan et al. (1993) (110–138 kJ/mol) and Qiu et al. (2000) (96.8 kJ/mol) at low conversions.
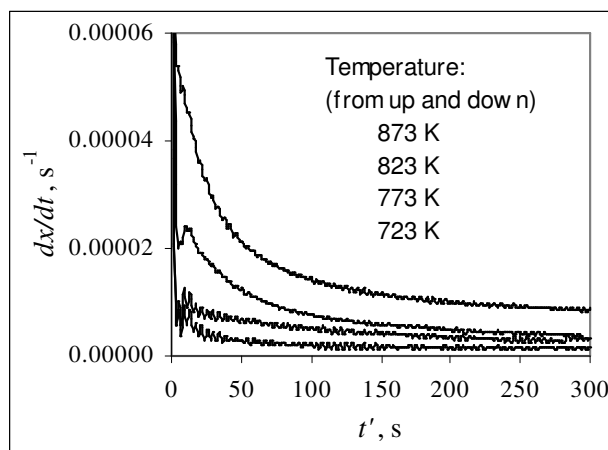
Figure 3.25 Conversion rate vs. time curves obtained with Faxe Bryozo at different temperatures (other conditions: P: 0.11 MPa; inlet SO_2: 1800 ppm; O_2: 3 %; CO_2: 30 %; N_2: balance)
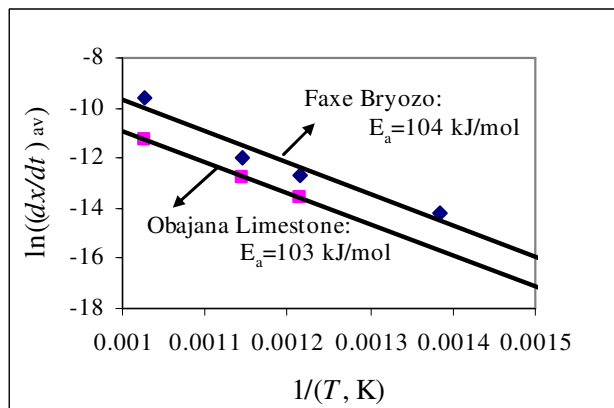
Figure 3.26 Variation of the average conversion rate with reaction temperature (other conditions: P: 0.11 MPa; inlet SO_2: 1800 ppm; O_2: 3 %; CO_2: 30 %; H_2O: 7.5 %; N_2: balance)

The relatively high activation energies and the significantly (a couple of orders of magnitude) lower conversion rates in the fixed–bed reactor than in the pilot entrained flow reactor ensure that the intra–particle diffusion resistance during the experiments was not significant.

3.5.2.4   Final product

Faxe Bryozo particles sulfated at 823, 873, 923 and 973 K with conversions around 1 %, 1.4 %, 11% and 4.5 % were analysed by X–ray powder diffraction. Figure 3.27 shows the powder patterns. Anhydrite ($CaSO_4$) was the only identified solid product. For samples sulfated at 823 and 873 K, only the strongest peak at $2\theta=25.5°$ for anhydrite is visible because of too low conversions. The formation of anhydrite is in good agreement with the findings by Murthy et al. (1979), Ljungström and Lindqvist (1982), Dam–Johansen et al. (1991c) and Tullin et al. (1993).
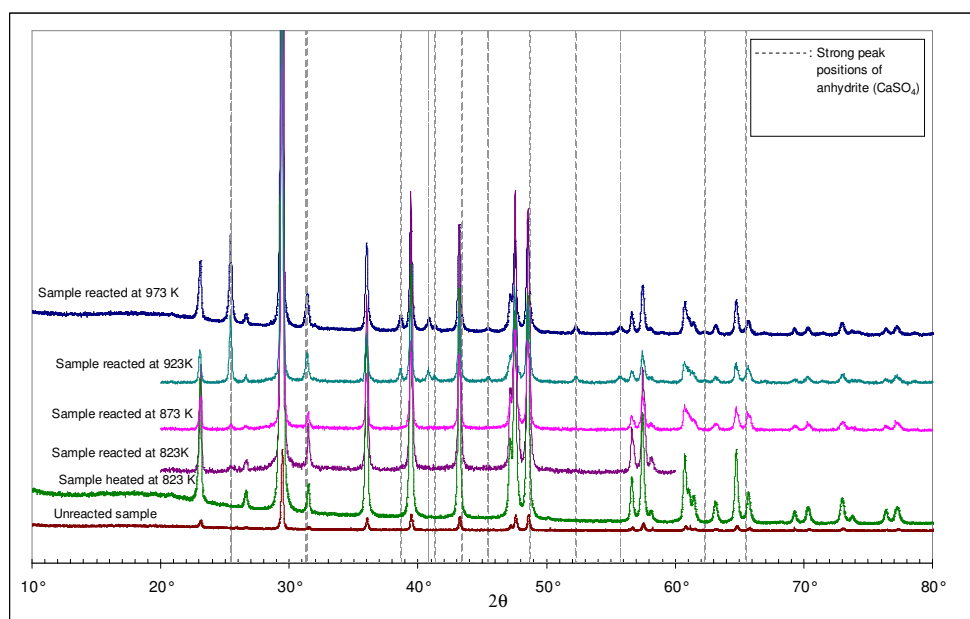
Figure 3.27 Powder patterns of X–ray diffraction of sulfated and unsulfated Faxe Bryozo particles

3.5.2.5   Morphological change of sulfated limestone particles

The surface morphologies of the limestone particles before and after the sulfation were examined by SEM (scanning electron microscope). The SEM examinations revealed that the

direct sulfation of limestone involves nucleation and crystal grain growth of the solid product (anhydrite), which is well demonstrated in Figures 3.28–3.36.

Figures 3.28–3.31 show SEM images of Faxe Bryozo particles before and after the sulfation reaction at 823–973 K. The particle sulfated at 823 K (Figure 3.29) looks apparently slightly smoothened and rounded compared to the unreacted particles (Figure 3.28). Individual crystal grains of the solid product are not visible, though powder patterns of X–ray diffraction of the same sample used for Figure 3.29 indicates the existence of anhydrite crystals. It is most likely that the magnification of the SEM image is insufficient in this case to show the very small crystal grains. At 873 K, the formation of product crystal grains is visible (Figure 3.30) after 10 minutes sulfation. At 973 K, the particle surfaces are covered by product crystal grains after 10 minutes sulfation (Figure 3.31).

Figures 3.32–33 and Figures 3.34–36 show particle surfaces of Obajana Limestone and Iceland Spar, respectively, before and after sulfation at 973 K. The formation of crystal grains of the solid product is clearly shown.

To confirm that the crystals shown in Figures 3.35–3.36 are $CaCO_3$, the same samples used for the SEM images are analyzed by EDS (energy dispersive spectrum) X–ray microanalysis. The results showed that the crystals contain high percentage of sulfur, oxygen and calcium (see appendix 4–1), which in conjunction with the results of the powder pattern of X–ray diffraction confirms that the crystal grains shown in the above SEM images are anhydrite grains.
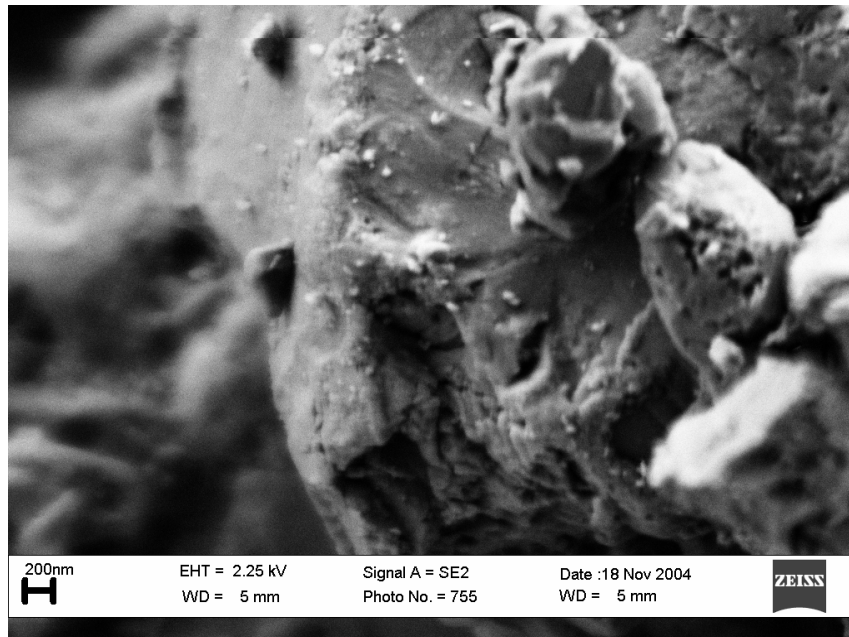
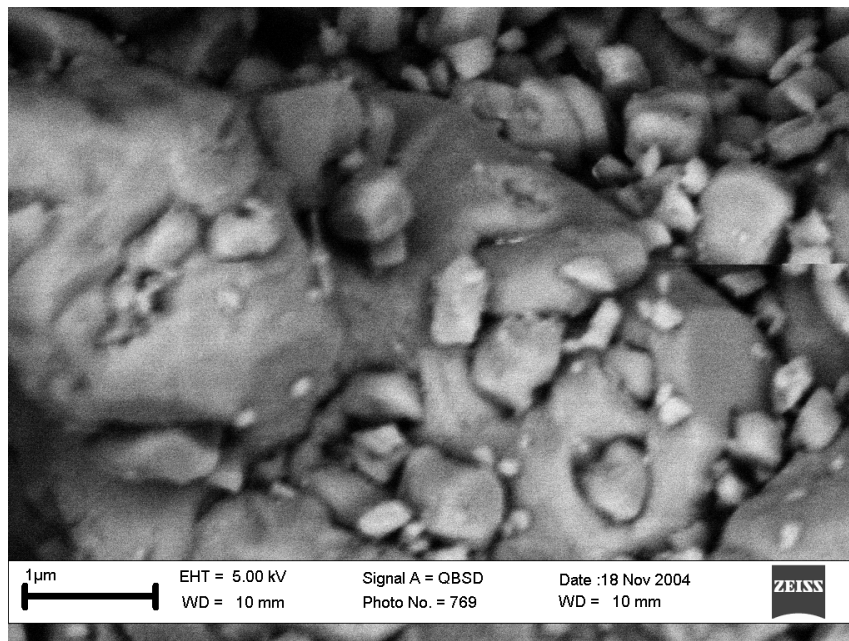Figure 3.28 SEM image of unreacted Faxe Bryozo particles

Figure 3.29 SEM image of Faxe Bryozo particles sulfated at 823 K for 90 min. ($x \approx 1$ %) (other conditions: P: 0.11 MPa; inlet SO2: 1800 ppm; O2: 3 %; CO2: 30 %; N2: balance).
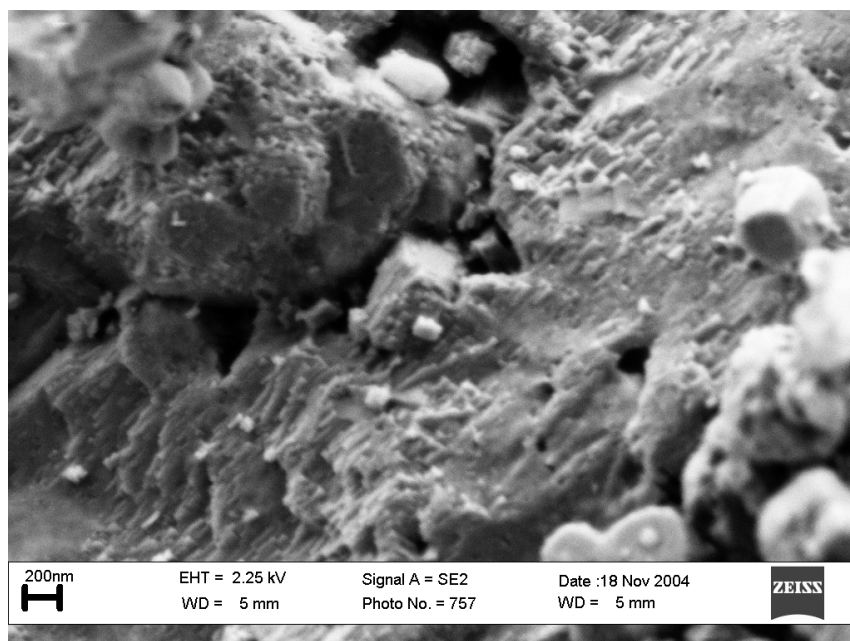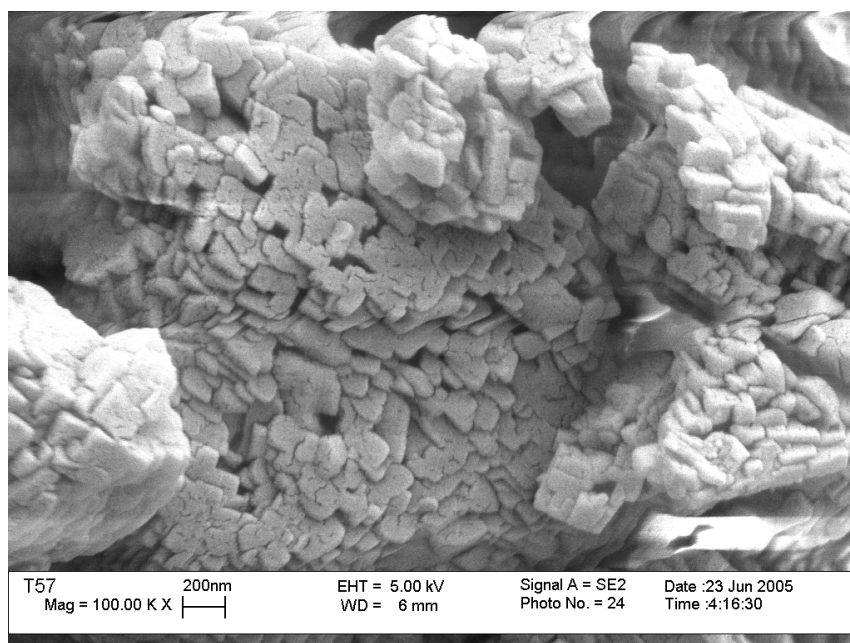
Figure 3.30 SEM images of Faxe Bryozo particles sulfated at 873 K for 10 min. ($x \approx$ 0.5 %) (other conditions: P: 0.11 MPa; inlet SO_2: 1800 ppm; O_2: 3 %; CO_2: 30 %; N_2: balance)

Figure 3.31 SEM image of Faxe Bryozo particles sulfated at 973 K for 10 min. ($x \approx$ 4.5 %) (other conditions: P: 0.11 MPa; inlet SO_2: 1800 ppm; O_2: 3 %; CO_2: 30 %; N_2: balance)
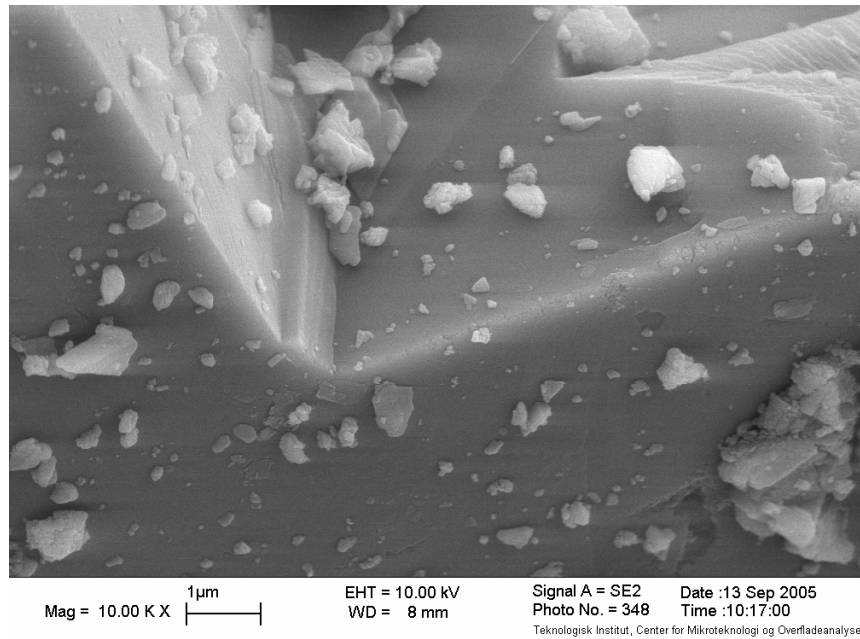
Figure 3.32 SEM image of unreacted Obajana Limestone particles
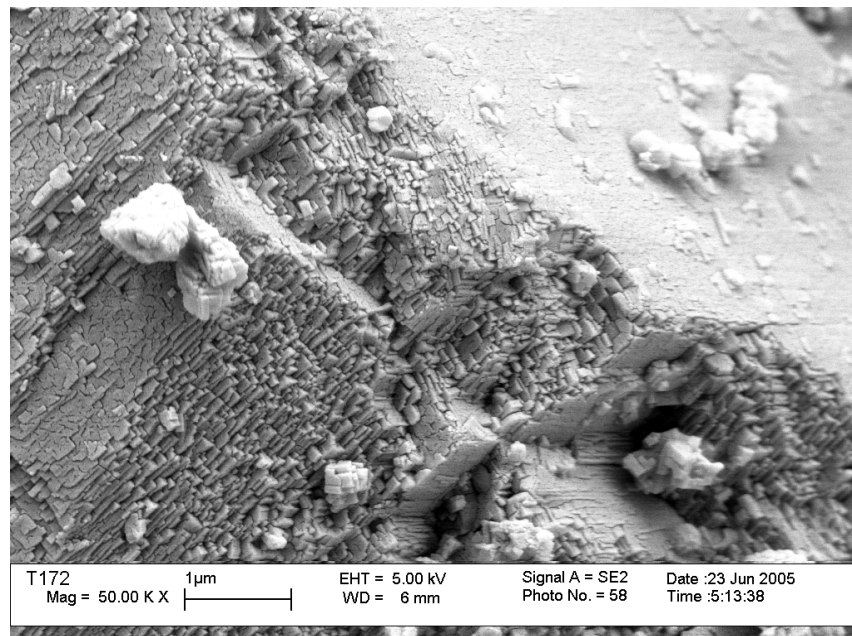
Figure 3.33 SEM image of Obajana Limestone particles sulfated at 973 K for 60 min.
($x \approx 5$ %) (other conditions: P: 0.11 MPa; inlet SO_2: 1800 ppm; O_2: 3 %; CO_2: 30 %;
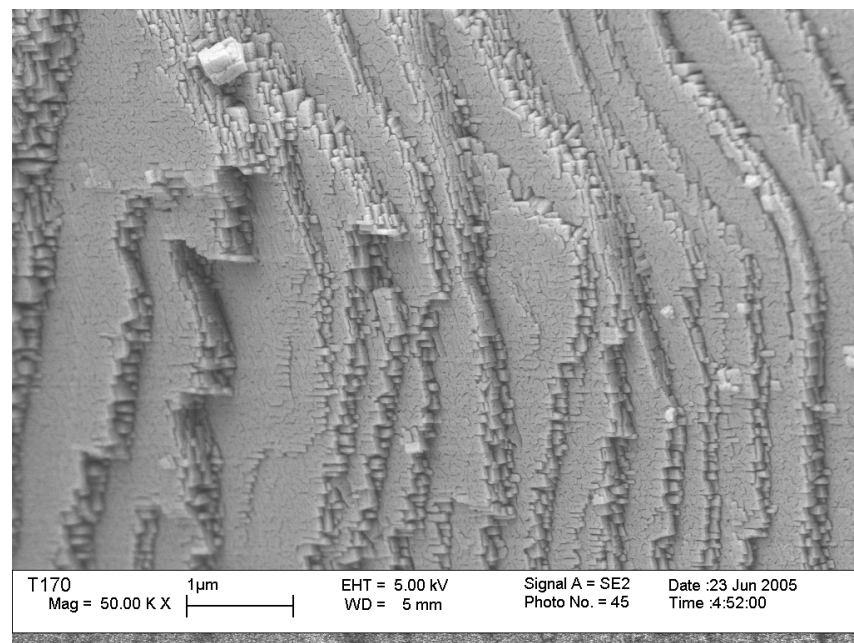N_2: balance)
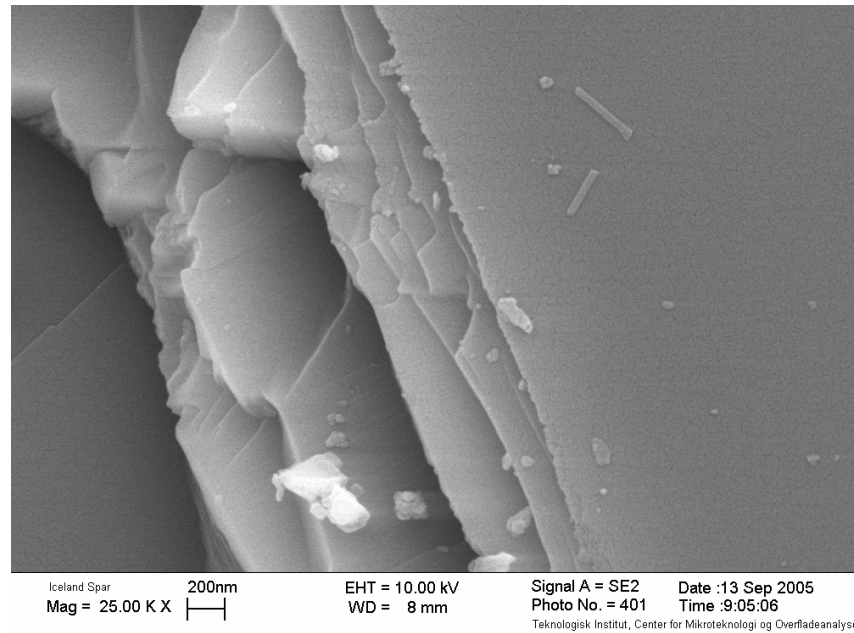
Figure 3.34 Unreacted Iceland Spar

Figure 3.35 SEM image of Iceland Spar particle sulfated at 973K for 30 min. ($x \approx$ 2.7 %) (other conditions: P: 0.11 MPa; inlet SO_2: 1800 ppm; O_2: 3 %; CO_2: 30 %; N_2: balance)
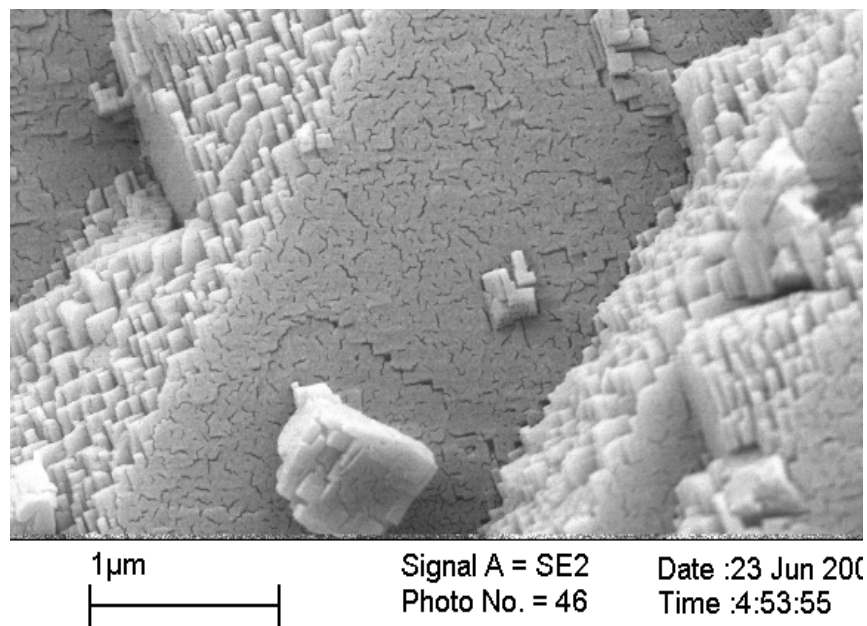
Figure 3.36 SEM image of Iceland Spar particle sulfated at 973K for 30 min. ($x \approx 2.7$ %) (other conditions: P: 0.11 MPa; inlet SO_2: 1800 ppm; O_2: 3 %; CO_2: 30   %; N_2: balance)

3.6   Discussions

The experimental results allow us to propose a mechanism for the direct sulfation of limestone and give a qualitative assessment of its validity. Various subjects concerning the direct sulfation of limestone are discussed, including phenomena observed in this and earlier studies such as porosity in the product layer, variation in the apparent reaction orders of SO_2, O_2, and CO_2, the controlling mechanism and the influence of water.

3.6.1 Mechanism of the direct sulfation of limestone

3.6.1.1   Sulfation process

As shown above, the direct sulfation of limestone involves nucleation and crystal grain growth of the solid product (anhydrite) (it will just be mentioned as nucleation and growth hereafter). The occurrence of nucleation means that the sulfation of the limestone may be divided into two stages. The first stage is the initial sulfation which extends from the start of the sulfation reaction to the initiation of nucleation of the formed solid product since the nucleation process requires the sulfate concentration at the surface to reach a critical level for the formation of stable nuclei. The second stage involves further sulfation and the growth of

the formed nuclei. It can be imagined that a thin layer may exist at the surface of the unreacted core that acts as a kind of parent layer for both nucleation and subsequent growth. The surface of the parent layer is the gas–solid reactant interface as well as the reaction front for the sulfation reaction. Formed sulfate ions (SO_4^{2-}) diffuse in solid state through the parent layer to the root of the product crystal grains and feed the growth process. This process is illustrated schematically in Figure 3.37.
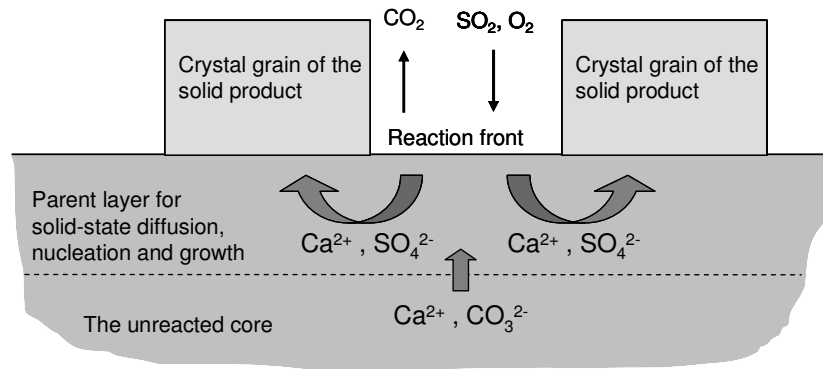

Figure 3.37 Schematic illustration of the sulfation process.

The parent layer is most likely a solid solution of the formed product anions in the parent structure of calcite considering the presence of solid–state diffusion process of the formed product ions. This means that the surface of the parent layer is no more pure calcite. The activity of carbonate ions (defined here as the ratio between the actual carbonate concentration and the carbonate concentration in pure calcite crystal) at the surface may thus deviate from the value of about 1 for pure calcite.

In addition to the commonly known steps such as gas film diffusion, pore diffusion in the particle and product layer, and chemical reaction (Levenspiel 1962, Szekely et al. 1976), the sulfation of limestone thus involves two extra steps: solid–state diffusion and the nucleation–growth process. The sequence of these steps is illustrated in Figure 3.38.
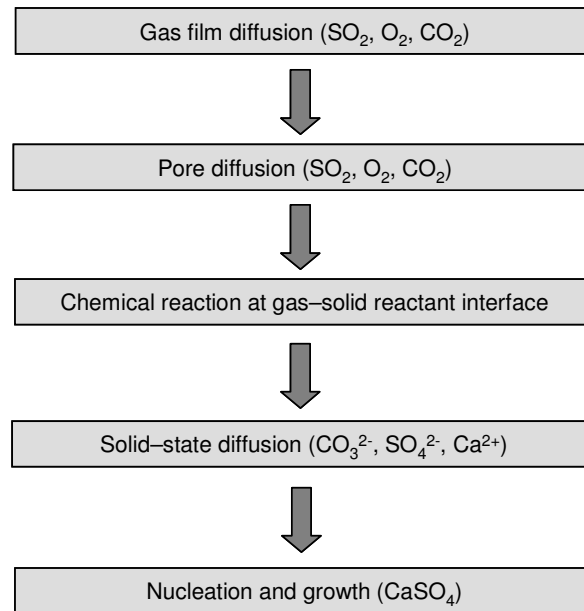
Figure 3.38 General sequential steps involved in the direct sulfation of limestone.

With the progress of the sulfation, the unreacted core shrinks. The free surface area of the parent layer—the surface area of the parent layer that is directly available for the sulfation reaction—decreases because of both the shrinkage of the unreacted core and the shielding effect of the formed nuclei/crystal grains of the solid product.

3.6.1.2   Nucleation and growth

As described above, the sulfation process involves nucleation and growth of the solid product. The above SEM images demonstrate that the nucleation and growth are oriented (West 1999). Oriented nucleation usually takes place when the nuclei of the new phase and the substrate have a close two-dimensional or three-dimensional match in their crystal lattice structures (usually termed epitaxy and topotaxy, respectively) (West, 1999). The product crystal grains are directly connected to the substrate (calcite) in lattice level and grow in a definite direction which is determined by the direction of the lattice surface on which the nucleation and growth take place. This oriented nucleation and growth is particularly clear with Iceland Spar. Iceland Spar is a natural and pure calcite crystal in relatively large sizes. The SEM image of ground particles (Figure. 3.34) shows clearly fractures and the smooth cleavages. The formation of crystal grains of the solid product takes place only at fractures that are perpendicular to the cleavages and with same orientation (Figures 3.35 and 3.36). The situation is similar with Obajana Limestone. Faxe Bryozo consists of small and randomly

orientated calcite grains; this is the reason for the apparently random orientation of the product crystal grains. The special preferred orientation of the product crystal grains indicates that they are directly rooted on the crystal lattice of calcite. That is to say, the crystal lattices of the product crystal grains and the substrate (calcite) are directly connected. The preference of particular sides for the nucleation is due to crystallographic reasons: the nucleation of the solid product prefers the sides/faces of the substrate (calcite) that have similar lattice structure such as the distance between the cations (Ca^{2+}) and crystallographic angles. Examination of the crystal lattice structures of calcite and anhydrite reveals a very close two-dimensional lattice match (epitaxy) (distance between cations (Ca^{2+}) and angles) between the {-1,1,0} lattice plane of anhydrite and the {1,0,4} lattice plane of calcite as illustrated in Fig. 3.39. (More details can be read in the article "Oriented Nucleation and Growth of Anhydrite during Direct Sulfation of Limestone" appended to this thesis.) The growth is upward, most probably also determined by the fact that the lattice match between the nuclei and the substrate is two-dimensional.
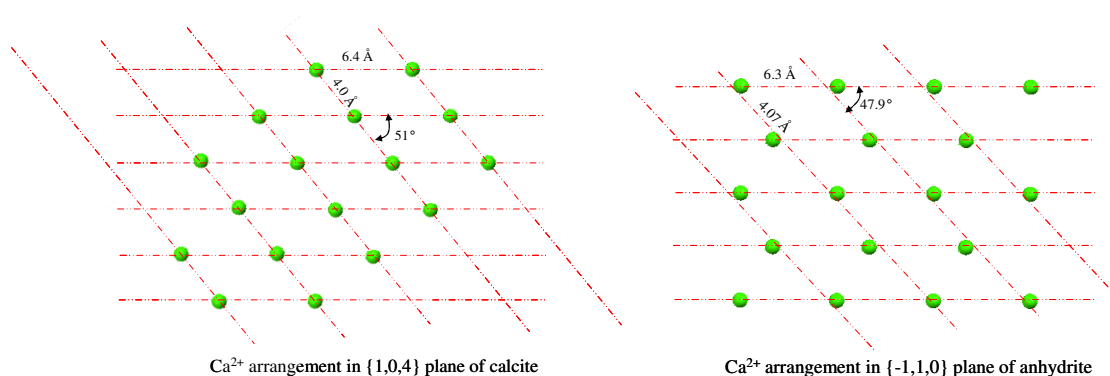

Figure 3.39 Illustration of the lattice sizes of anhydrite and calcite at their   respective lattice plane of   {-1,1,0} and {1,0,4}.

3.6.1.3   Solid–state diffusion

For nucleation and the subsequent growth of the solid product, the product ions must diffuse to the nucleation/growth sites in solid state. The diffusion process possibly takes place in the way illustrated in Figure 3.40.

The diffusion proceeds by point defects (West 1999) which are most likely vacancies of cations and anions in the crystal lattice of both the product and the substrate (calcite). As illustrated in Figures 3.37 and 3.40, sulfate ions are first formed at the surface of the parent

layer. The sulfate ions then diffuse to the root of the grain and fill the available vacancies in the root. The continuous supply of sulfate ions formed by the sulfation reaction at the surface of the parent layer to the root provides a driving force for the formation of a new layer of the crystal at the outer surface of the crystal grain because the ions that jump out of the lattice sites to the surface of the grain (the jumping-out of the lattice ions to the surface is a coupled process with the formation of point defects) are less likely to jump back due to the continuous filling-up of vacancies at the root. It is possible that movement of the ions partly may proceed synchronized. The movement of cations (Ca^{2+}) is considered to take place in the same way as that for sulfate ions. During this process, carbonate ions have to diffuse to the surface of the parent layer to facilitate the continuation of the sulfation reaction.

With the growth of the grains, the grains may at last detach from the substrate (calcite) because of various stresses, allowing new nuclei to form at places where the sulfate ion concentration reaches the critical level. The formed product layer is thus a collection of crystal grains of the solid product.
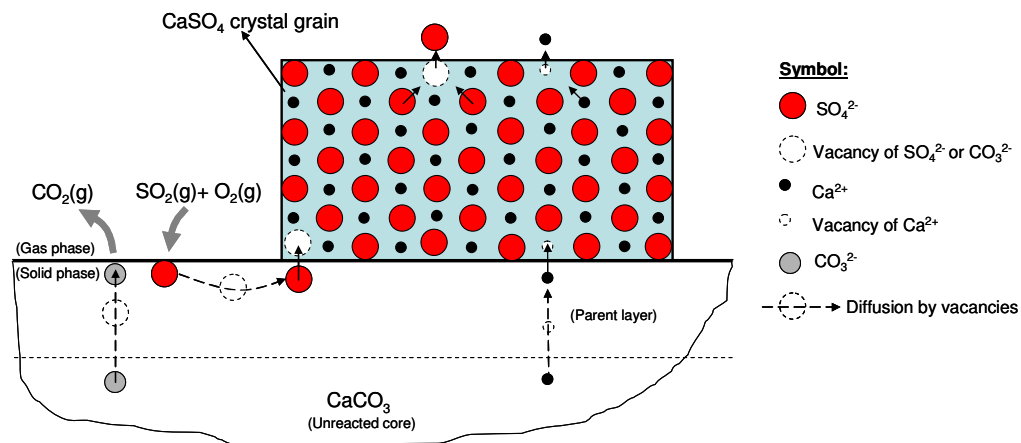

Figure 3.40 Illustration of the probable solid–state diffusion process for the nucleation-growth process involved in the direct sulfation of limestone.

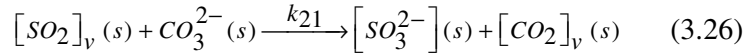### 3.6.1.4   Chemical reaction at the gas–solid reactant interface

In the mechanism described above, the chemical reaction is assumed to take place mainly at the free surface of the parent layer. Based on experimental observations and some theoretical considerations, the chemical reaction is suggested to proceed by the following multi–step mechanism:

Step 1: adsorption of SO_2 in active sites at the surface of the parent layer:

$$SO_2(g) + [\ ]_v(s) \underset{k_{12}}{\overset{k_{11}}{\rightleftharpoons}} [SO_2]_v(s) \qquad (3.25)$$
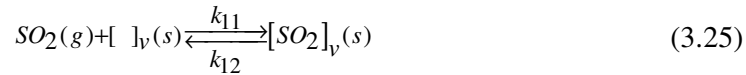
Step 2: conversion of the adsorbed SO_2 to sulfite ions:

$$[SO_2]_v(s) + CO_3^{2-}(s) \xrightarrow{k_{21}} [SO_3^{2-}](s) + [CO_2]_v(s) \qquad (3.26)$$

Step 3: formation of oxygen radicals in gas phase or at the solid surface by dissociative adsorption:

$$O_2(g) \underset{k_{32}}{\overset{k_{31}}{\rightleftharpoons}} 2O(g/s) \qquad (3.27)$$

Step 4: oxidation of sulfite ions to sulfate ions:

$$[SO_3^{2-}](s) + O(g/s) \xrightarrow{k_{41}} [SO_4^{2-}](s) \qquad (3.28)$$
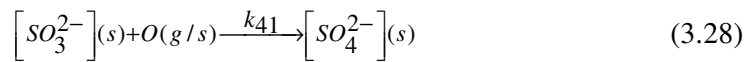
Step 5: desorption of CO_2:

$$[CO_2]_v(s) \underset{k_{52}}{\overset{k_{51}}{\rightleftharpoons}} CO_2(g) + [\ ]_v(s) \qquad (3.29)$$
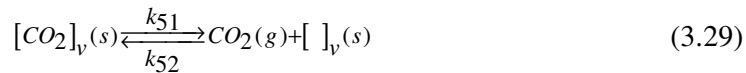
For the mechanism suggested above the following assumptions and considerations are made:

Adsorption of SO_2:

It was observed that oxidation of SO_2 in the gas phase at the highest temperature (973 K) applied in the experiments is unnoticeably small without the presence of limestone particles, even though thermodynamically the conversion of SO_2 to SO_3 in the gas phase is favored at such temperatures (Schenk and Steudel 1968). This reveals that during the sulfation reaction the oxidation of SO_2 takes place after it is adsorbed on the limestone.

Vacancies of missing carbonate ions in the crystal lattice of calcite at the surface of the parent layer are assumed to be active sites for the adsorption of SO_2. The presence of vacancies in ionic crystalline materials is known to be one of the basic conditions for solid–state diffusion (West 1999). The space of a vacancy is normally larger than the space that is occupied by a carbonate ion because of the loss of attraction from negative charges. At the surface of the parent layer, the size of vacancies of carbonate ions is expected to be even larger due to the unsaturated nature of the cations (i.e. Ca^{2+}). Vacancies at the surface are probably active sites for the adsorption of SO_2, based on considerations of the size of the vacancy, the probable benefit for lattice

energy by the adsorption and especially the dependence of the subsequent diffusion of the formed anions on the vacancies.

Formation of sulfite:

During the process of oxidation of SO_2 to sulfate (SO_4^{2-}), sulfite (SO_3^{2-}) (not $CaSO_3$ in a separate phase) is most likely first formed as an intermediate based on the following observations:

- The absorption of SO_2 on the limestone was observed in this study to proceed in the absence of oxygen.

- Investigation of the intrinsic kinetics of the direct sulfation of limestone showed that the conversion rate of limestone was not influenced by variation in O_2 concentration in the very initial stage.

- Tullin et al. (1993) detected the presence of trace amount of sulfite in the sulfated samples by Fourier Transform Infrared Spectroscopy (FTIR).

The formed sulfite ions are considered to be distributed in the crystal lattice of calcite and do not exist in a separate phase as crystalline calcium sulfite ($CaSO_3$). Crystalline calcium sulfite is likely to form if the sulfite ion concentration reaches the critical level, which, however, will usually not happen with sufficient oxygen in the gas.

Formation of oxygen radicals:

The sulfite ions are oxidized by the oxidant: oxygen radicals (O) or oxygen in other forms. In this study, there is no clear evidence concerning the form in which oxygen participates in the reaction. Oxygen radicals may come from thermal dissociation of oxygen in the gas phase. Oxygen radicals or oxygen in other forms may also form from dissociative adsorption of oxygen at solid surfaces (Roberts and Smart 1981, Henrich 1993, Cordero and Cantelli 1999, Palmer and Neurock 2002). In the mechanism suggested above, the oxidant is assumed to be oxygen radicals formed by thermal dissociation in the gas phase and/or by dissociative adsorption at the solid surface.

Formation of sulfate:

As with the formation of sulfite, sulfate ions formed initially are most likely distributed in the crystal lattice of calcite. Calcium sulfate in a separate phase ($CaSO_4$) is first formed when it is nucleated.   The existence of anhydrite crystal grains was confirmed by powder patterns of X–ray diffraction.

3.6.2 Porosity in the product layer

The product layer formed during the direct sulfation reaction has been shown to be porous (Hajaligol et al. 1988, Liu et al. 2000). Snow et al. (1988) proposed that the porosity was a result of out–flow of CO_2 formed by the sulfation reaction, partly based on the observation of a dense product layer produced during the indirect sulfation reaction (sulfation reaction between SO_2 and calcinated limestone), in which CO_2 is not formed. However, observations in this study indicate that the porosity in the product layer results from the formation of crystal grains of the solid product as shown in Figures 3.28–36 and illustrated in Figure 3.37. Porosity in the product layer reflects the presence of free spaces and voids between crystal grains of the solid product, which are clearly visible in Figure 3.31. The formation of CO_2 seems therefore to be irrelevant in the development of porosity in the product layer.

The non–relevance of CO_2 formation to porosity in the product layer is also evidenced by the observations of Duo et al. (2000) on the sulfation of calcinated limestone (indirect sulfation reaction). The dense product layer formed during the indirect sulfation reaction was believed to reflect the absence of gas (CO_2) evolution during the reaction. However, Duo et al. (2000) showed that the product layer produced by the sulfation of calcinated limestone can also be porous when the calcinated limestone is sintered at high temperatures to form larger dense particles. This fact again demonstrates that the formation of CO_2 during the sulfation reaction is not relevant to porosity in the product layer. In fact, the critical factor seems to be size: the sizes of grains and pores. The product layer formed during the sulfation of calcinated limestone is usually dense because the calcinated limestone particles typically consist of micro–grains of a size around 0.2 µm. The size of micro–pores between the micro-grains is typically around 0.1 µm (Dam–Johansen 1987, Dam–Johansen et al. 1991a–d, Duo et al. 2000). The combination of the small sizes of micro-pores and micro-grains makes the pore blocking by product crystal grains very easy. Sintering/coalescing of the product crystal grains readily takes place as they are so close together.

Porosity in the product layer can be influenced by various factors such as conversion, limestone morphology, temperature, and gas composition. With increasing conversion, the free spaces and voids between product crystal grains decrease due to growth of grains and probably coalescence as well. This process explains the observations of decreasing porosity and pore size with increasing conversion (Hajaligol et al. 1988, Liu et al. 2000). The product

layer is expected to be more porous for limestones that consist of small calcite grains like Faxe Bryozo, because the random orientation of calcite grains also causes a random orientation of the product crystal grains, which in turn creates more voids. The influence of temperature can be twofold. Temperature has a significant influence on the nucleation process. Porosity and pore size generally increase with increasing temperature due to the formation of fewer but larger nuclei/crystal grains at higher temperatures. Figures 3.29 and 3.30 demonstrate well the effect of temperature, as crystal grains are visible at the surface of the particles sulfated to a conversion of about 0.5 % at 873 K (Figure 3.30), but not at the surface of the particles sulfated to a conversion of about 1 % at 823 K (Figure 3.29). However, at sufficiently high temperatures, sintering of the product crystal grains can become significant, which can cause a decrease in porosity and/or pore size.

3.6.3 Variation in the apparent reaction orders of SO_2, O_2, and CO_2

As observed in this and earlier studies, the apparent reaction order of SO_2 varies with reaction conditions and is significantly lower than unity; O_2 and CO_2 may or may not show influence depending on the reaction conditions. The observations of the influence of these gases were mostly made in the second stage of the sulfation where nucleation and crystal grain growth of the solid product were started. The measured sulfation/conversion rate was thus inevitably influenced by the nucleation–growth process, which in conjunction with the resistance of solid–state diffusion and the nature of gas–solid reactions are most likely the reasons for the varying influences of these gases under different reaction conditions.

The direct consequence of the occurrence of the nucleation and growth of the solid product is the reduction of calcite surface area that is directly available for the sulfation reaction. The conversion rate measured at any given time is partly determined by the fraction of the uncovered surface area of the calcite grains. The apparent reaction order may thus vary significantly depending on the temperature and the conversion.

The presence of significant resistance of solid–state diffusion causes a significant deviation of the calcite surface from the pure state and thus also a lower sulfation rate at the uncovered calcite surface than at pure calcite surface because of the lowered carbonate activity. The influence of the gaseous reactants is expected to decrease with increasing solid–state diffusion resistance. The resistance of solid–state diffusion is expected to be more significant at lower temperatures because of its generally high activation energy, usually significantly higher than 100 kJ/mol. A relevant example is the activation energy for the self

diffusion of carbonate ions in calcite lattice which was measured by Haul and Stein (1955) to be about 243 kJ/mol. The much lower apparent reaction order of SO_2 measured in this study than in others (Yang et al. 1975, Iisa et al. 1992a, Krishnan et al. 1993, Qiu et al. 2000) may partly be due to a more significant influence of solid–state diffusion at the relatively low temperatures used in this study.

According to the above suggested reaction mechanism, the sulfation rate is determined by Steps 1, 2 and 5, while Steps 3 and 4 are only steps which convert sulfite ions into the final product: sulfate ions. The rate expressions for Steps 1, 2 and 5 can be established as follows:

Step 1: $r_1 = k_{11} C_{SO_2} \theta_v - k_{12} \theta_{SO_2}$ (3.30)

Step2: $r_2 = k_{21} \theta_{SO_2} a^s_{CO_3^{2-}}$ (3.31)

Step 5: $r_5 = k_{51} \theta_{CO_2} - k_{52} \theta_v C_{CO_2}$ (3.32)

Here, $\theta_v + \theta_{SO_2} + \theta_{CO_2} = 1$;

By assuming that Steps 1 and 5 are in equilibrium, Eq. (3.31) can be rewritten as follows:

$$r_2 = \frac{k_{21} K_1 C_{SO_2} a^s_{CO_3^{2-}}}{1 + K_5^{-1} C_{CO_2} + K_1 C_{SO_2}}$$ (3.33)

r_2 represents the sulfation rate at the uncovered calcite surface. In Eqs. 3.31 and 3.33, $a^s_{CO_3^{2-}}$ (carbonate activity at the uncovered calcite surface) is a parameter that reflects the influence of solid–state diffusion. $a^s_{CO_3^{2-}}$ is expected to decrease before the initiation of the nucleation process. Once the nucleation process has begun, $a^s_{CO_3^{2-}}$ will not decrease further because the nucleation–growth process acts as a buffer that prevents any further decrease in $a^s_{CO_3^{2-}}$. With the growth of the product grains, $a^s_{CO_3^{2-}}$ is expected to increase because of the reduced diffusion distance of sulfate ions from the uncovered calcite surface to product grains. Variations in $a^s_{CO_3^{2-}}$ are believed to be one of the main reasons for the variation of the apparent reaction orders of SO_2, O_2 and CO_2 with reaction conditions.

For SO_2, an increase in SO_2 concentration results an increase in the sulfation rate, which in turn causes a decrease in $a^s_{CO_3^{2-}}$ because of the resistance of solid–state diffusion. The

apparent observation is thus a reaction order of SO_2 lower than unity which varies with reaction conditions.

The effect of O_2, according to the above suggested mechanism, is due to its influence on the concentration of sulfite ions at the uncovered calcite surface, which seems to explain quite well the observed effects of O_2 at different conditions.

In the initial stage, it was observed that higher O_2 concentrations had initially negligible but at longer reaction time slightly negative influence on the sulfation rate. It may be related to the fact that nucleation is not supposed to initiate in this very initial stage. The formed intermediate sulfite ions and the final product ions, i.e. the sulfate ions take the lattice sites of carbonate ions at the surface of calcite grains and accumulate mostly at the surface because of the relatively low solid–state diffusivity. The activity of carbonate ions at calcite surface decreases with increasing conversion. The sulfation rate may not be significantly influenced by the variation in O_2 concentration simply because both sulfite and sulfate ions stay mostly at the surface.

At longer reaction time, the slightly negative influence of higher O_2 concentrations may be caused by the increased sulfate concentration because sulfate ions are significantly larger than the size of sulfite ions and thus may diffuse slower than sulfite ions. The decrease of carbonate activity may be slightly more with the formation of more sulfate ions than with the formation of sulfite ions. This difference may be "felt" when the decrease in carbonate activity is slowed down to a certain level. However, it can not be excluded that the lowed conversion rate at higher O_2 concentration at longer reaction time was caused by initiation of nucleation due to the faster increase in sulfate concentration at higher O_2 concentrations.

At higher conversions, the sulfation rate was observed to be significantly promoted by higher O_2 concentrations. The influence of O_2 became negligible after O_2 concentration was reached a certain level. This may be explained by the nucleation and growth process. After the nucleation and growth process are started, sulfate ions diffuse immediately toward the nuclei/grains after they are formed, whereas sulfite ions stay. A higher sulfite ion concentration at the uncovered calcite surface means a lower carbonate activity and thus also a lower sulfation rate. The increase in sulfation rate with increasing O_2 concentration is thus caused by the increase in carbonate activity. O_2 shows zero–order behavior when sulfite concentration approaches to zero. The influence of O_2 on sulfite ion concentration at calcite grain surface seems also to give a reasonable explanation of the observed increase in the

apparent reaction order of SO_2 with increasing O_2 concentrations, as in the growth stage the resistance of solid–state diffusion may be reduced with the decrease in sulfite ion concentrations at higher O_2 concentrations.

CO$_2$ has significant influence on solid–state diffusion in calcite (Beruto et al. 1986, Tetard et al. 1999) most likely because of its influence on the formation of extrinsic carbonate vacancies in the crystal lattice of calcite. With increasing CO_2 partial pressure the number of extrinsic carbonate vacancies in the crystal lattice of calcite is reduced, which in turn causes a corresponding decrease in solid–state diffusivity. $a_{CO_3^{2-}}^s$ is thus expected to decrease with increasing CO_2 concentration, and consequently the sulfation rate as well. The influence of CO_2 was observed to become limited at high temperatures (Snow et al. 1988, Iisa et al. 1990, Illerup et al. 1993), which may in parts be explained by the fact that with increasing temperature the number of extrinsic point defects usually gets less significant compared to the number of intrinsic point defects (West 1999).

The apparent influence of CO_2 on the sulfation reaction is most likely a combined effect of CO_2 on solid–state diffusivity and Step 5 (Equation 3.29) in the reaction mechanism.

Compared to the established theory, an important difference in the above proposed sulfation mechanism is the assumption of the deviation (decrease) of carbonate concentration or activity at calcite grain surface from that of pure calcite. Introduction of carbonate activity as a variable into the rate expression enables direct consideration of the influence of solid–state diffusion on the sulfation reaction and provides the necessary bridge between the reaction kinetics and solid–state diffusion.

3.6.4 Controlling mechanism

A reaction process is considered to be controlled by a certain step when that step is so slow that any increase in the rate of other steps that are in series does not result in any significant increase in the overall reaction rate. As discussed earlier, the direct sulfation of limestone involves 5 general steps, i.e. gas film diffusion, pore diffusion in the particle and product layer, chemical reaction, solid–state diffusion and the nucleation–growth process. The sulfation process may thus be controlled by each of these steps or by a combination of these steps.

Under the conditions in this study—relatively low temperatures and very low conversions, the sulfation process is most likely under mixed control by chemical reaction and solid–state diffusion. Calculations and the measured apparent activation energies indicate that resistances of gas film diffusion and pore diffusion are negligible.

The mixed control by both solid–state diffusion and chemical reaction is practically "guaranteed" by the nucleation–growth process. The resistance of solid–state diffusion is clearly significant in the experiments performed in this study judged by the observed nucleation of the solid product (anhydrite) at relatively low conversions (for example < 0.5 % at 873 K) in this study. Otherwise, the calcite grain would be sulfated in a pseudo–homogeneous way, as the diffusion of the formed sulfate ions into the inner part of the calcite grain would be fast if solid–state diffusion resistance was insignificant; the conversion rate would also be more or less constant at low conversions. This is obviously not the case. However, control by solid–state diffusion alone may never be realized because nucleation of the solid product will be initiated before the carbonate activity at the uncovered surface of the calcite grain ($a_{CO_3^{2-}}^s$) drops to zero due to thermodynamic reasons. Chemical reaction can influence the sulfation reaction as long as $a_{CO_3^{2-}}^s$ doesn't drop to zero. The significant influence of chemical reaction rate is reflected by the significant effects of SO_2 on the overall sulfation rate.

3.6.5 Influence of water

As observed in this study, water may promote or hinder the direct sulfation of limestone depending on the sulfation stage. A probable explanation of the effect of water is its influence on solid–state diffusion by the formation of hydroxide ions (OH^-). Hydroxide ions may be formed by the dissociation of H_2O in conjunction with the dynamic exchange of CO_2 between the CO_2 in the gas phase and CO_2 in calcite (Haul and Stein 1955):

The dynamic exchange of CO_2:

$$\left[CO_3^{2-}\right](s) \rightleftarrows \left[O^{2-}\right](s) + CO_2(g) \tag{3.34}$$
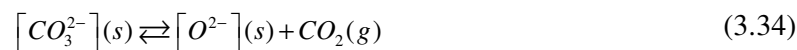
The formation of hydroxide groups:

$$\left[O^{2-}\right](s) + H_2O(g) + \left[\ \ \right] \rightleftarrows 2\left[OH^-\right](s) \tag{3.35}$$
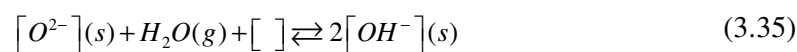
The movement of cations (Ca^{2+}) is an important part of the nucleation–growth process and may contribute a significant part of the resistance of solid–state diffusion. The formation of hydroxide ions and their adsorption in anion sites (carbonate) (Eastman and Culter 1966,

Razouk et al. 1973) in the crystal lattice of calcite may result in the formation of more cation (Ca^{2+}) vacancies, as hydroxide ions are of single valence. The increase of the number of cation vacancies improves the diffusion of the cations and thus solid–state diffusion in general. However, hydroxide ions may also occupy carbonate vacancies at the surface, resulting in a lower sulfation rate.

At the initial stage, nucleation was not started. The relevant diffusing ions were the anions. Formation of more cation vacancies may in this case produce no positive effects. The observed negative influence of water may thus be caused by the occupation of carbonate vacancies by hydroxide ions at the surface, which resulted in both lower diffusivity of the anions and fewer number of active sites.

After nucleation was started at higher conversions, addition of water may promote the sulfation process if solid–state diffusion resistance is more dominant, or hinder the sulfation process if resistance of chemical reaction is more dominant.

Addition of water to the gas in this and earlier studies (yang et al. 1975) was observed to increase the apparent reaction orders of SO_2 and O_2. This phenomenon is in good agreement with water's probable improvement on solid–state diffusion. The direct sulfation of limestone is most likely under mixed control as discussed above by both chemical reaction and solid–state diffusion. An improvement on solid–state diffusion makes the chemical reaction more dominant in the mixed control. The increase in the apparent reaction order of SO_2 is probably a reflection of the increased control by chemical reaction.

3.6.6 Influence of the nucleation and growth process on conversion rate of limestone

As illustrated in Figure 3.17, the conversion rate of Faxe Bryozo decreased sharply in the initial few seconds but significantly slower in the following period. The transition between these two periods was quite abrupt. As discussed above, there are most likely two main causes for the decrease in the conversion rate of the limestone. One is the decrease in carbonate activity, and the other is the reduction in calcite surface area by the shielding effect of solid product grains. In the initial stage before the initiation of nucleation, the decrease of the conversion rate with increasing conversion is mainly caused by the decrease in carbonate activity. After the initiation of nucleation, the decrease of the conversion rate with increasing conversion is mainly caused by the shielding of calcite surface area by the formed nuclei/grains of the solid product. During the process of nucleation and growth, carbonate

activity at calcite surface may increase due to the reduced diffusion distance of the formed sulfate ions. The transition from the first period to the second period is most likely the completion of nucleation and the start of growth judged by the similarity of the influences of SO_2, CO_2, O_2 and H_2O on the sulfation process at the start of the second period to the influences of these gases on the sulfation process after longer reaction times.

3.7 Modeling

Based on the above discussions, the sulfation process may be divided into three stages as illustrated in Figure 3.41. The three stages are the initial sulfation, nucleation and growth. The clear dividing of the three stages is an idealized simplification. In reality there may be a certain overlapping between these stages.
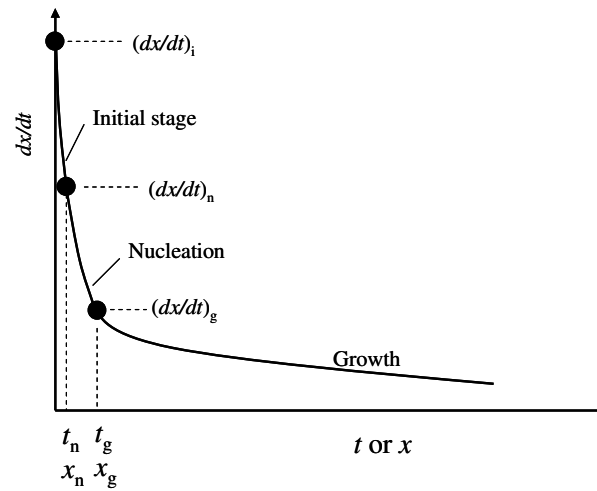
Figure 3.41 Illustration of three stages of the sulfation process

In the following sections mathematical models are proposed to model the initial and the growth stages. Modeling of the nucleation stage was not tried because of lack of usable experimental data.

3.7.1 Modeling of the initial sulfation process

The initial sulfation process before nucleation, as discussed above, most likely involves diffusion of sulfate/sulfite ions formed at the calcite grain surface towards the inner part of calcite grains and diffusion of carbonate ions towards the surface of calcite grains to participate the sulfation reaction. This process may be described by a reaction–diffusion process as illustrated in Figure 3.42.
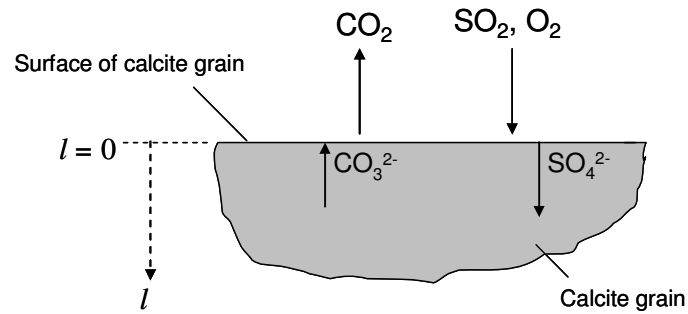
Figure 3.42 Illustration of the reaction–diffusion process before the
initiation of nucleation of the solid product

In the reaction–diffusion process, the sulfation reaction takes place at the gas–solid interface. The reaction causes a significant decrease in the carbonate activity at the surface of calcite grains because of the relatively low solid–state diffusivity.

Ionic diffusion in the calcite grain can be reasonably assumed to be equal–molar due to the facts that solid–state ionic diffusion takes place by point defects (Frenkel 1926, Wagner and Schottky 1930) and the requirement of electric neutrality. Fick's law is widely used to describe solid–state ionic diffusion (Manning 1968, Hayes 1985, Kirkaldy and Young 1987, Tilley 1987, Glicksman 2000). Though calculations indicate that the diffusion treated in this study takes place in a relatively thin layer of about 5–10 nm (corresponding to about 15–30 layers of carbonate ions in calcite crystal lattice), it is assumed that the ionic diffusion process in this case still follows Fick's law.

By assuming that the consumption rate of carbonate ions at the surface of calcite grains by the sulfation reaction is equal to the diffusion rate of carbonate ions at the surface of calcite grains, the following partial differential equation with three boundary conditions can be established. Due to the relatively low solid–state diffusivity, it is sufficient to consider the diffusion in a thin layer in slab form near the surface of calcite grains.

$$\frac{\partial a(l,t)}{\partial t} = (D_s)\frac{\partial^2 a(l,t)}{\partial l^2} \tag{3.36}$$

$$\text{BC1: } a(l,0) = 1 \tag{3.37}$$

$$\text{BC2: } \frac{\partial a(l,t)}{\partial l} = 0 \quad at\ l \to \infty \tag{3.38}$$

$$\text{BC3: } \frac{\partial a(l,t)}{\partial l} = (\frac{r^0}{D_s C_{CO_3^{2-}}^0})a(l,t) \quad at \ l = 0 \qquad (3.39)$$

BC1 means pure calcite at the start.

BC2 means that carbonate activity does not vary at sufficiently high thickness (l). Calculations indicate that under the applied reaction conditions l can be taken as to be "∞" when l is thicker than about 10 nm.

BC3 means that the diffusion rate of carbonate ions to the calcite grain surface is equal to the reaction rate at the calcite grain surface.

Considering the relatively low conversions, shrinking of the unreacted core of the limestone is negligible. The conversion of the limestone can thus be calculated by the following equation:

$$x = \int_0^t S_t M_{CaCO_3} r^0 a(0,t) \, dt \qquad (3.40)$$

By fitting the experimental data obtained in the pilot entrained flow reactor to this model, the diffusion coefficient of carbonate ions (D_s) and the intrinsic sulfation rate (r^0) at different reaction conditions can be assessed.

D_s and r^0 at the three temperatures (873, 923 and 973 K) in a gas consisting of 1800 ppm SO_2, 3% O_2, 15 % CO_2 and 81.8 % N_2 are assessed first. The values of D_s and r^0 at which the summed standard deviation between the experimental data and the model predicted data becomes least are taken as the solutions.

To minimize the uncertainty that may easily be caused by using only two data points, the conversion data obtained at 873 K at the residence time of 0.53 s was used. As shown in Figure 3.4, the gas temperatures at SO_2 injection point 1 were about 2–3 K lower than the set point of the reaction temperatures. However, the influence of this few degrees is not supposed to be significant judged from the trend of the variation of the conversion with reaction time at 873 K as shown in Figure 3.43.

Figures 3.44–3.45 show respectively the plots of the obtained values of D_s and r^0 (in the form of $\ln(D_s)$ and $\ln(r^0)$) against $1/T$.
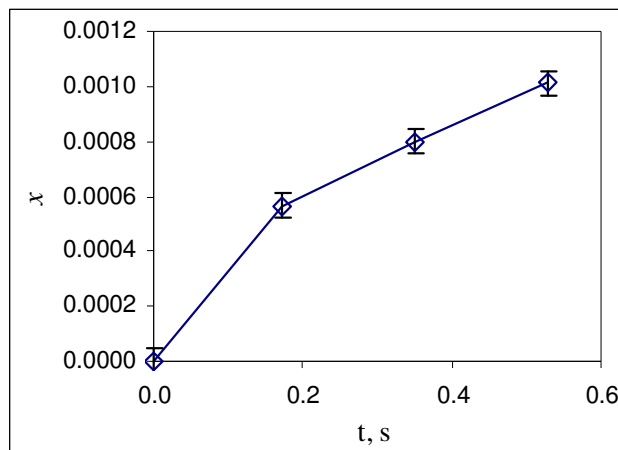
Figure 3.43 Variation of conversion of Faxe Bryozo with reaction time at 873 K (standard conditions if not specified: P: 0.1 MPa; SO_2: 1800 ppm; O_2: 3 %; CO_2: 15 %; N_2: balance)
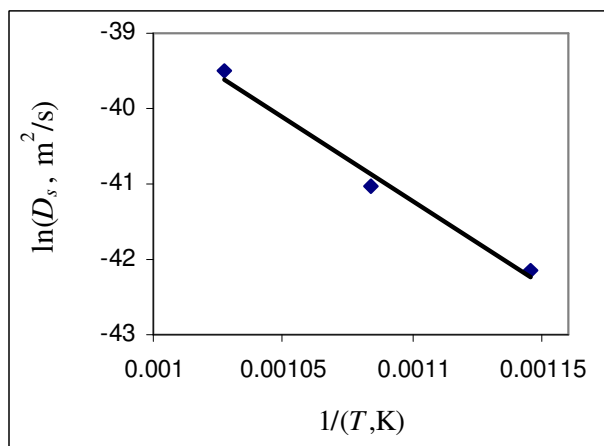

Figure 3.44 Variation of D_s with temperature in a gas consisting of 1800 ppm SO_2, 3 % O_2, 15 % CO_2 and 81.8 % N_2.
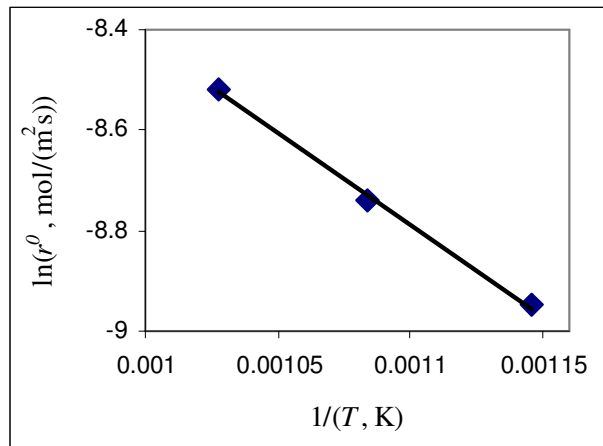
Figure 3.45 Variation of the intrinsic sulfation rate with temperature in a gas consisting of 1800 ppm SO_2, 3 % O_2, 15 % CO_2 and 81.8 % N_2.

The lines in the above two figures can be represented by the following expressions:

$$D_s = 5.8 \cdot 10^{-8} e^{\frac{-185600}{\Re T}} \qquad (\text{m}^2/\text{s}) \qquad (3.41)$$

$$r^0 = 0.0085 e^{\frac{-30400}{\Re T}} \qquad (\text{mol}/(\text{m}^2\text{s})) \qquad (3.42)$$

These results suggest that the solid–state diffusivity at calcite surface has an activation energy of about 185.6 kJ/mol, while the intrinsic sulfation rate has an activation energy of about 30.4 kJ/mol.

The influences of SO_2 and CO_2 to the intrinsic rate are expressed by the following empirical equation:

$$r^0 = A e^{\frac{-30400}{\Re T}} C_{SO_2}^n C_{CO_2}^m \qquad (\text{mol}/(\text{m}^2\text{s})) \qquad (3.43)$$

The reaction orders of SO_2 and CO_2 are assessed by further fitting of the rate data at different SO_2 and CO_2 concentrations. By assuming that the reaction orders of SO_2 and CO_2 and activation energies for both D_s and r^0 do not vary with gas concentrations and the temperature, the reaction orders of SO_2 and CO_2 can then be determined by the principle of best fit.

For SO_2, by assuming a value for n, Equation 3.43 can be expressed in the following form:

$$r^0 = A' e^{\frac{-30400}{\Re T}} C_{SO_2}^n \qquad (\text{mol}/(\text{m}^2\text{s})) \qquad (3.44)$$

With known n, A' can be calculated by the result obtained at 1800 ppm SO_2, 3 % O_2 and 15 % CO_2 (Equation 3.42). r^0 at 900 ppm SO_2 and the same O_2 and CO_2 concentrations as in the case of 1800 ppm SO_2 is then calculated. With known D_s and r^0, the sulfation process can be simulated by using the above model. The standard deviation between the model predicted data and the experimental data is calculated. The above calculations are performed at various values of n. The reaction order at which the summed standard deviation between the experimental data (at both 873 and 973 K) and model predicted data becomes least is taken as the final solution. The same procedure is used to get the reaction order of CO_2.

The above calculations result in reaction orders of approximately 1 for SO_2 and approximately -1 for CO_2, which gives the following final expression for the intrinsic rate:

$$r^0 = 0.7\,e^{\frac{-30400}{\Re T}}\, C_{SO_2}\, C_{CO_2}^{-1} \qquad (\text{mol/(m}^2\text{s)}) \qquad\qquad (3.45)$$

This expression for the intrinsic sulfation rate corresponds to a dominant influence of $K_5^{-1}C_{CO_2}$ in the denominator of Equation 3.33.

The solid–state diffusivity obtained here (for example about $4.5\ 10^{-19}$ m^2/s at 873 K) is several orders of magnitude higher than the self–diffusivity of carbonate ions in calcite lattice predicted by the following correlation presented by Haul and Stein (1955). At 873 K this equation predicts a diffusivity of about $1.4\ 10^{-22}$ m^2/s.

$$D_L = 4.5 \bullet 10^{-8}\, e^{\frac{-242790}{\Re T}} \quad (\text{m}^2\text{/s}) \qquad\qquad (3.46)$$

This large difference may be explained by the theory of grain-boundary diffusion (Barnes 1950, Fisher 1951, Hoffman and Turnbull 1951). According to this theory, solid–state diffusion at grain boundary/surface is significantly (can be up to several orders of magnitude) higher than lattice diffusion in the inner part of the grain. The diffusion process in our case takes place in a thin layer of about a few nm at the calcite grain surface. The relatively high carbonate ion diffusivity assessed by the model simulation seems to conform well to the theory of grain-boundary diffusion.

This theoretic reaction–diffusion model seems to give satisfactory simulations of the initial sulfation process. Figures 3.46–3.48 show comparisons between model simulations and experimental data.
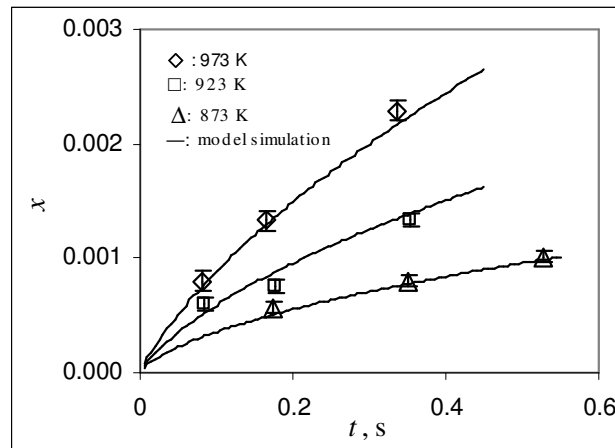
Figure 3.46 Variation of conversion of Faxe Bryozo with reaction time at different temperatures (standard conditions if not specified: P: 0.1 MPa; SO_2: 1800 ppm; O_2: 3 %; CO_2: 15 %; N_2: balance)
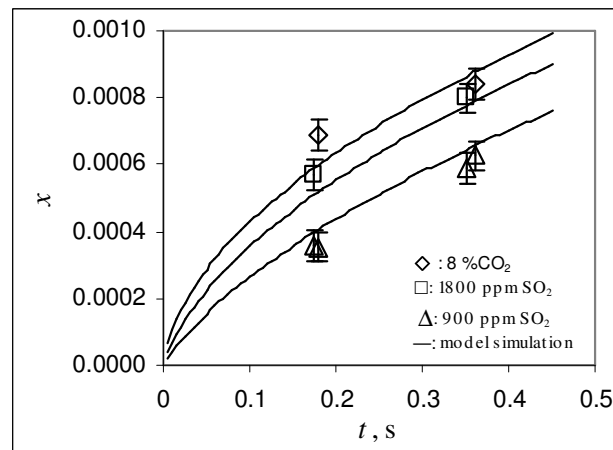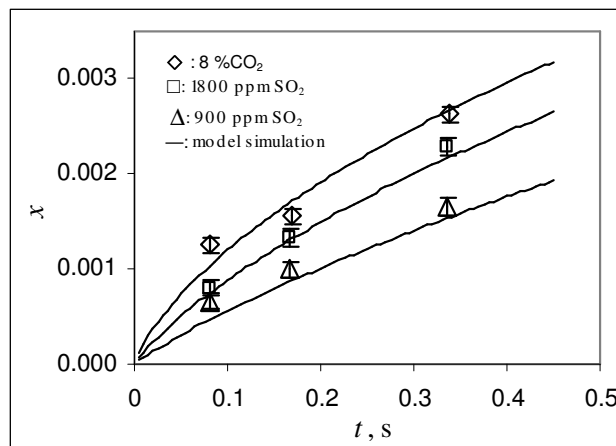

Figure 3.47 Variation of conversion of Faxe Bryozo with reaction time at 873 K and different SO_2 and CO_2 concentrations (standard conditions if not specified: P: 0.1 MPa; SO_2: 1800 ppm; O_2: 3 %; CO_2: 15 %; N_2: balance)

Figure 3.48 Variation of conversion of Faxe Bryozo with reaction time at 973 K and different SO_2 and CO_2 concentrations (standard conditions if not specified: P: 0.1 MPa; SO_2: 1800 ppm; O_2: 3 %; CO_2: 15 %; N_2: balance)

It is a compromise to use a carbonate diffusivity that varies only with temperature. The reality is that the carbonate diffusivity may vary to certain degree with gas concentrations especially with CO_2 concentrations and solid composition which varies with the conversion of the solid.

According to the suggested reaction mechanism, the intrinsic sulfation rate is determined by Step 1, 2 and 5. The intrinsic rate is the rate at zero conversion and without the influence of solid–state diffusion. The relatively high reaction order of about 1 for SO_2 seems to be quite natural. The reaction order of about -1 for CO_2 may be the combined result of the influences of CO_2 on Step 5 and the number of active sites which are most likely carbonate vacancies at calcite surface.

Figure 3.49 shows the variation of carbonate activity at calcite surface calculated by the above model. This figure demonstrates that sulfate ions, probably together with some intermediate sulfite ions, become the dominant anions at calcite surface after less than half seconds reaction time. The most dramatic drop of carbonate activity takes place at the first 0.1–0.2 seconds.
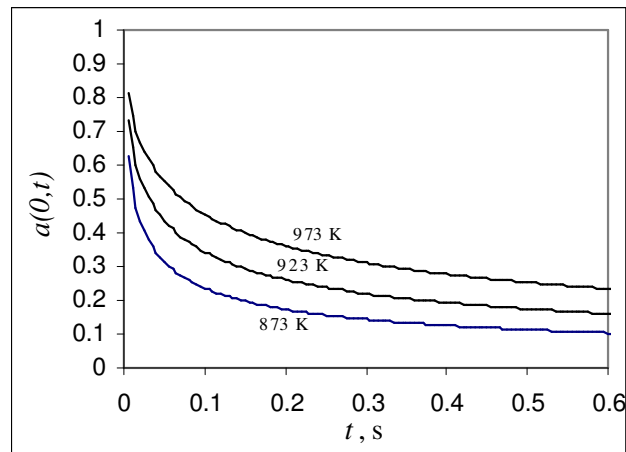
Figure 3.49 Model calculated variation of carbonate activity at the surface of Faxe Bryozo with sulfation time at different temperatures (other conditions: P: 0.11 MPa; SO_2: 1800 ppm; O_2: 3 %; CO_2: 30 %; N_2: balance)

3.7.2 Modeling of the growth process

A plot of $\ln(dx/dt)$ against x' (as shown in Figure 3.50) (x' is the conversion increase from the point SO_2 was detected by the online SO_2 analyzer. The true conversions should be slightly higher when the conversion during the full absorption period is taken into consideration) demonstrates that there is a good linear relationship between $\ln(dx/dt)$ and the conversion in the growth stage. The linearity generally holds to x' around 0.2 % (the true conversion is estimated to be around 0.25) at 823 K.
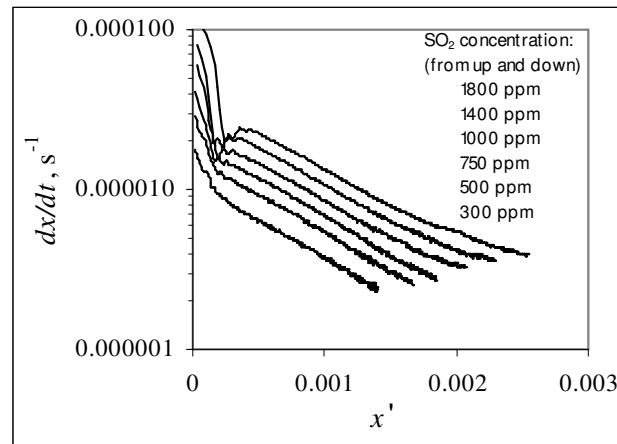
Figure 3.50 Variation of conversion rate of Faxe Bryozo with conversion at 823 K (standard conditions if not specified: P: 0.11 MPa; O_2: 3 %; CO_2: 30 %; N_2: balance)

At such conversion level, the sulfation process can be described by the following empirical equation:

$$\frac{dx}{dt} = (\frac{dx}{dt})_g \, e^{-B(x-x_g)} \qquad (s^{-1}) \tag{3.47}$$

Integration of Equation 3.47 results the following equation for the conversion of limestone as a function of time:

$$x = (\frac{1}{B})\ln(1 + B(\frac{dx}{dt})_g \, (t - t_g)) + x_g \tag{3.48}$$

The parameter B and $(dx/dt)_g$ can be read or assessed from the plots of $\ln(dx/dt)$ against x at different gas concentrations and temperatures. With Faxe Bryozo the following correlations are obtained for B and $(dx/dt)_g$.

$$B = 0.73 \, e^{\frac{44800}{\Re T}} \, C_{O_2}^{-0.12} \, C_{CO_2}^{0.4} \quad (\text{Dimensionless}) \tag{3.49}$$

$$(dx/dt)_g = 124 \, e^{\frac{-83300}{\Re T}} \, C_{SO_2}^{0.7} \, C_{O_2}^{0.3} \, C_{CO_2}^{-0.2} \qquad (s^{-1}) \tag{3.50}$$

The parameter B represents the relative pace by which the conversion rate decreases with increasing conversion caused by shielding of calcite surface area by the grains of the solid product. This parameter was not significantly influenced by SO_2 concentration, but significantly influenced by temperature and CO_2 concentrations and slightly influenced by O_2. B increases with decreasing temperature, probably because of formation of more nuclei at

lower temperatures (Duo et al. 2000). B increases with increasing CO_2 concentrations probably due to the same reason as for temperature. A significant increase in solid–state diffusion resistance at higher CO_2 concentrations (Beruto et al. 1986, Tetard et al. 1999) may cause formation of more nuclei.

The effect of O_2 on B may be related to its influence on the formation of sulfite ions. With the growth of the solid product grains, carbonate activity at the free calcite surface increases because of the shorter diffusion distance of sulfate ions, which compensates partly for the effect of reduced free calcite surface area. The relative decrease in conversion rate becomes smaller if the relative increase in the carbonate activity is larger. With decreasing O_2 concentration, sulfite concentration at the free calcite surface may increase, which makes the increase in carbonate activity by the shortened diffusion distance less significant and thus a larger decrease in conversion rate.

The influence of gas concentrations and temperature on $(dx/dt)_g$ when judged in terms of the apparent reaction orders and the apparent activation energy is quite similar to the results evaluated by using the average conversion rates at significantly higher conversions. This is a good support to the proposed completion of nucleation and start of growth at the turning point of the conversion rate vs. time curves.

Figures 3.51–3.53 show comparisons between experimental data and model simulations. Figures 3.51–3.52 show the variation of conversion of Faxe Bryozo with reaction time at different gas concentrations and different temperatures, respectively. Figure 3.53 shows the variation of conversion of Obajana limestone with reaction time at different temperatures. In these figures, x'' and t'' are the conversion increase starting from the point of $(dx/dt)_g$ as illustrated in Figure 3.41 and reaction time starting from t_g, respectively. The agreement between experimental data and model simulations are quite good with x'' up to about 0.2–0.3 % (the total conversion around 0.25–0.4 %). At higher conversions, the model generally undershoots.

Model simulations of the conversion of Obajana Limestone shown in Figure 3.53 are made by changing the pre–exponential constant in Equation 3.50 from 124 to 10 and keeping the other parameters unchanged. Obajana Limestone is a hard and crystalline limestone with relatively low porosity. The success of model simulation with parameters obtained with Faxe Bryozo indicates that the growth mechanisms with different limestones may be similar.
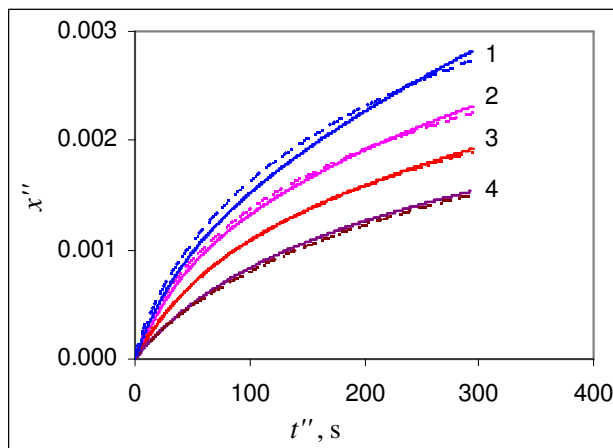
Figure 3.51 Variation of conversion of Faxe Bryozo with reaction time at 823 K and different gas concentrations (solid lines: experimental results; dashed lines: model simulations; 1: 750 ppm SO_2, 30 % O_2; 2: 1800 ppm SO_2; 3: 1000 ppm SO_2; 4: 500 ppm SO_2. Other conditions if not specified: P: 0.11 MPa; O_2: 3 %; CO_2: 30 %; N_2: balance)

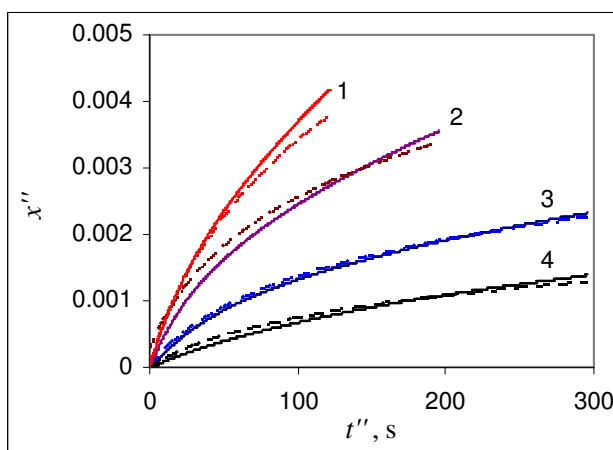Figure 3.52 Variation of conversion of Faxe Bryozo with reaction time at different temperatures (solid lines: experimental results; dashed lines: model simulations; 1: 873 K, 8 % CO_2; 2: 873 K, 30 % CO_2; 3: 823 K; 4: 773 K. Other conditions if not specified: P: 0.11 MPa; SO_2: 1800 ppm; O_2: 3 %; CO_2: 30 %; N_2: balance)
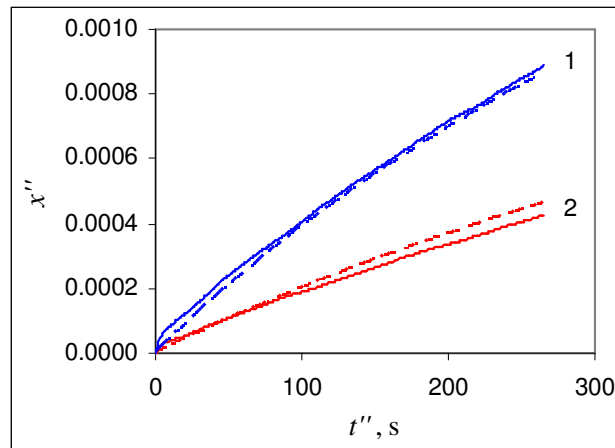
Figure 3.53 Variation of conversion of Obajana Limestone with reaction time at different temperatures (solid lines: experimental results; dashed lines: model simulations; 1: 873 K; 2: 823 K. Other conditions if not specified: P: 0.11 MPa; SO_2: 1800 ppm; O_2: 3 %; CO_2: 30 %; H_2O: 7.5 %; N_2: balance)

Figure 3.54 shows plots of the variation of sulfation rate with reaction temperature by using the intrinsic rate expressions presented in the literature, the intrinsic rate expression assessed in this study (Eq. 3.45) and the rate expression for $(dx/dt)_g$ (Eq. 3.50) at atmospheric pressure and in a gas consisting of 1800 ppm SO_2, 3 % O_2 and 15 % CO_2. The intrinsic sulfation rates predicted by the rate expressions presented in the literature are 40–200 times lower than the intrinsic rates predicted by Eq. 3.45, but quite close to the rates predicted by Eq. 3.50 for $(dx/dt)_g$ with a difference of only about 2–4 times, which indicates that the kinetic parameters obtained by those authors by extrapolation or by using rate data at conversions of a few percent (a few percent is actual a quite high conversion in this context) are actually for the growth period rather than for the initial sulfation.
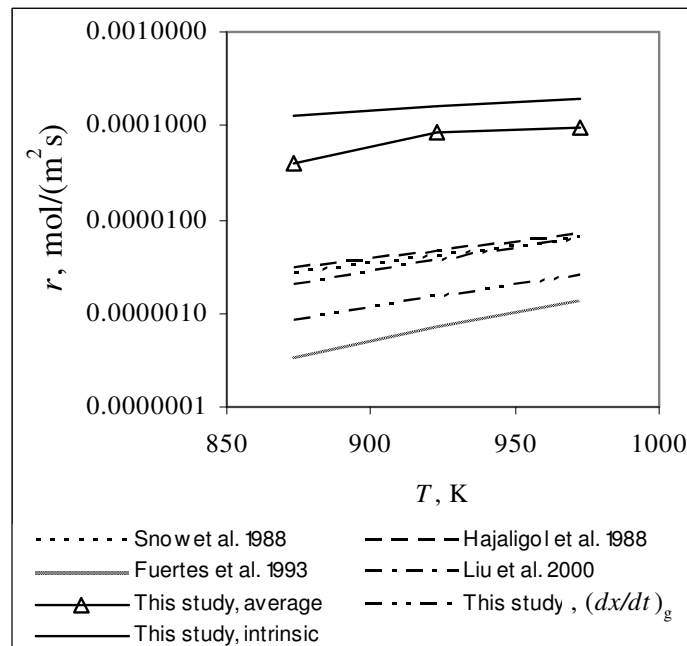
Figure 3.54 Comparison between the sulfation rates predicted by the intrinsic rate expressions presented in the literature, the intrinsic rate expression assessed in this study and the rate expression for $(dx/dt)_g$ at different temperatures (other conditions: P: 0.1 MPa; SO_2: 1800 ppm; O_2: 3 %; CO_2: 15 %; N_2: balance)

3.8 Conclusion

3.8.1 Mechanism of the direct sulfation of limestone

The direct sulfation of limestone at low conversions has been studied in both a bench scale fixed–bed reactor and a pilot entrained flow reactor. The direct sulfation of limestone is found to involve oriented nucleation and crystal grain growth of anhydrite—the final solid product. The whole sulfation process can be divided into three stages: the initial stage before nucleation of the solid product, nucleation of the solid product and subsequent growth of the formed nuclei.

Solid–state diffusion of ions of the solid reactant (calcite/limestone) and the solid product plays a key role in the sulfation process. During the sulfation process, carbonate ions diffuse in solid–state from the inner part towards the surface to participate the reaction, while the formed sulfate ions diffuse in solid–state towards the inner part of calcite grains or the

nucleation/growth sites of the solid product. At lower temperatures the sulfation process is usually under mixed control by both chemical reaction and solid–state diffusion. The significant solid–state diffusion resistance results in a decrease of carbonate activity at calcite grain surface to a value significantly lower than the value of about 1 for pure calcite.

The sulfation reaction that takes place at the gas–solid reactant interface may involve steps such as the adsorption of SO_2 in active sites on the surface of the solid reactant, the formation of sulfite ions (SO_3^{2-}) as an intermediate, further oxidation of the formed sulfite ions to form sulfate ions, and desorption of CO_2. The active sites are most likely carbonate vacancies at the surface of calcite grains. The rate of the sulfation reaction may be influenced by various gases such as SO_2, O_2, CO_2 and H_2O either by affecting gas adsorption/desorption (such as SO_2 and CO_2) or by affecting carbonate activity at the surface of calcite grains (such as CO_2, O_2) and solid–state diffusivity (such as CO_2 and H_2O).

The apparent conversion rate of limestone depends on factors such as the fraction of the uncovered surface area of calcite grains and the sulfation rate at the uncovered surface of calcite grains. The variation of the apparent reaction orders of SO_2, O_2 and CO_2 is most likely caused by the variation of the fraction of the uncovered calcite grain surface area and the influence of solid–state diffusion with reaction conditions.

The product layer formed during the direct sulfation of limestone is a collection of crystal grains of the solid product ($CaSO_4$). The presence of spaces and voids between the crystal grains is the main reason for porosity in the product layer. The decrease in porosity and pore size with increasing conversion is due to the reduction in these spaces and voids caused by growth of the crystal grains of the solid product and probably also sintering.

3.8.2 Sulfation kinetics

The intrinsic rate of the direct sulfation of limestone is significantly promoted by higher SO_2 concentrations and lower CO_2 concentrations, but is zero order with respect to O_2. The significant influence of CO_2 on the intrinsic rate is most likely the combined effects of CO_2 on the adsorption of CO_2 from the active sites and the formation of carbonate vacancies in calcite grains, while the zero–order behavior of O_2 is most likely related to the formation of sulfite ions as an intermediate in the sulfation reaction mechanism.

At temperatures up to 973 K, the intrinsic sulfation rate, assessed by model simulations, has reaction orders of about 1 for SO_2 and about -1 for CO_2 and an activation energy of about 30.4 kJ/mol. For Faxe Bryozo the following intrinsic rate expression is obtained:

$$r^0 = 0.7\, e^{\frac{-30400}{\Re T}}\; C_{SO_2}\, C_{CO_2}^{-1}.$$

The kinetics of the direct sulfation of limestone at low conversions is characterized by its two distinct periods: a first period of a few seconds with relatively high but fast decreasing conversion rate and a second period with relatively low but slowly decreasing conversion rate. The appearance of these two distinct periods is most likely related to the nucleation and crystal grain growth of anhydrite ($CaSO_4$), the solid product. The first period include an initial sulfation stage and a following stage with the nucleation of the solid product, while the second period is most likely the period for the growth of the product nuclei formed in the first period.

The conversion rate of the limestone in the first period decreases sharply with increasing conversion rate, most likely caused by the drop of carbonate activity at the surface of calcite grains due to the low solid–state diffusivity in the initial stage and by the shielding of calcite grain surface by the nuclei of the solid product in the last stage of this period. The conversion rate in the initial stage is significantly promoted by higher SO_2 and lower CO_2 concentrations but not influenced by variation in O_2 concentration. The negligible influence of O_2 is most likely due to the formation of sulfite ions as an intermediate. The significant influence of CO_2 is most likely related to its influence on the formation of point defects (carbonate vacancies) and thus solid–state diffusivity.

The conversion rate of the limestone in the second period decreases slowly, most likely because of the reduction of limestone surface area caused by the growth of crystal grains of the solid product. The conversion rate in this period is significantly promoted by higher SO_2 and O_2 concentrations and lower CO_2 concentrations. The significant promoting effect of O_2 in this period is most likely related to the affect of O_2 on carbonate activity at the surface of calcite grains because of its influence on sulfite concentration at the surface. At high O_2 concentrations (> approximately 15 %), the apparent reaction order of O_2 drops to zero, most likely because sulfite ion concentration approaches zero.

The apparent activation energies of about 83 kJ/mol for the conversion rate at the initial growth stage and 103 kJ/mol for the conversion rate at higher conversions represent the combined effects of temperature on chemical reaction with an activation energy of about 30 kJ/mol and solid–state diffusion with an activation of about 186 kJ/mol.

The solid–state diffusivity of carbonate ions at the calcite grain surface assessed in this study is several orders of magnitude higher than the self–diffusivity of carbonate ions in calcite lattice, which conforms well to the theory of grain–boundary diffusion.

3.8.3 Modeling

The kinetics of the initial sulfation stage before nucleation of the solid product is successfully modeled by a theoretic reaction–diffusion model. The kinetics of the growth process is successfully modeled by a simple empirical model mainly based on the growth mechanism of the solid product grains. These are two examples that demonstrate the importance of understanding the mechanism of the sulfation process to a successful modeling.

Chapter 4   Enhancement of the direct sulfation of limestone by additives

This Chapter presents experimental results of the enhancement of direct sulfation of limestone by various additives. Mechanisms of the enhancement are assessed based on the obtained experimental results. The contents in this chapter are also presented in the paper "Enhancement of the Direct Sulfation of Limestone by Alkali Metal Salts, Calcium Chloride and Hydrogen Chloride" by Guilin Hu, Kim Dam–Johansen, Stig Wedel and Jens Peter Hansen, published in I&EC Research, 2007.

4.1   Introduction

The direct sulfation of limestone is relatively slow at low temperatures. As shown in the literature survey in Chapter 3, this reaction can be enhanced by addition of various additives such as different alkali metal salts, $CaCl_2$ and HCl. In this project, with the main purposes to explore possible ways to enhance the sulfation reaction taking place in the cyclone preheater and to get better understanding of the enhancement mechanisms, the influence of various additives on the direct sulfation of limestone were studied at relatively low temperatures around 723–923 K, which are typical temperatures in the cyclone preheater. The influences of various factors such as thermal treatment, additive dosage and temperature are investigated. The mechanisms of the enhancements are assessed based on the obtained results.

4.2   Experimental

4.2.1 Reactor set-up

The experiments were performed in the fixed–bed reactor. Details about the reactor and the experimental procedure are described in Chapter 3.

4.2.2 Preparation of the materials

The limestone used for the experiments is Faxe Bryozo. (Details about this limestone are presented in Chapter 3.) The additives were introduced into the limestone samples by impregnation. For the impregnation, the relevant additive was first dissolved in water and then mixed with the limestone particles to form a slurry. The slurry was then heated to

evaporate most of the demineralised water. The still wet sample was further dried in an electrically heated oven at 393 K for approximately 12 hours. The dried sample was gently ground and sieved again. The fraction between 0.18-0.25 mm was used for the experiments. Calculations indicate that intra–particle diffusion resistance under the applied reaction conditions was insignificant with such particle sizes. Table 4.1 shows the tested additives and the dosages.

Table 4.1 Dosage of the used additives

Additive name	Dosage, mol %
NaCl	0.5-4
Na_2CO_3	1
Na_2SO_4	1
Li_2CO_3	1
KCl	2
K_2CO_3	1
$CaCl_2$	1
HCl (gas)	1000 ppm in the gas

4.2.3 Experimental conditions

In this investigation reaction conditions were kept within the following ranges:

- Temperature:723–923 K
- SO_2 concentration: 900–1800 ppm
- O_2 concentration: 1–3 vol. %
- CO_2 concentration: 15–30 vol. %
- H_2O concentration: 2–6 vol. %.

These conditions cover typical conditions in the cyclone preheater.

4.3 Results

4.3.1 Data treatment

For calculation of the conversion rate and conversion of the limestone sample, the following equations were used:

Conversion rate of the limestone at any time:

$$\frac{dx}{dt} = \frac{P\,V(y_{SO_2,in} - y_{SO_2,out})M_{CaCO_3}}{\Re\,T\,W\,\eta} \quad (\text{s}^{-1}) \tag{4.1}$$

Increase in conversion during the time interval of sampling (Δt) at any time:

$$\Delta x = \frac{P\,V(y_{SO_2,in} - y_{SO_2,in})M_{CaCO_3}\,\Delta t}{\Re\,T\,W\,\eta} \tag{4.2}$$

The conversion of the limestone at time t is obtained by summing Δx.

In the first half minute of each run, the outlet SO_2 concentration is significantly influenced by residence time distribution (RTD) in the system. After this short period, the change of the outlet SO_2 concentration is relatively slow; the RTD influence becomes insignificant. In the presented conversion rate data in the following sections, values in the first minute are therefore not included.

By using data from two set of experiments repeated under identical reaction conditions (900 data pairs), the standard variance of the conversion rate was calculated to be about ±2.5 % of the rate value. This variance is expected to hold for all conversion rates presented in this chapter.

4.3.2 Influence of different additives

Figure 4.1 shows the conversion rate vs. time curves obtained with Faxe Bryozo doped with the additives listed in Table 4.1. The sulfation process was enhanced by all the tested additives. With the most effective ones (Li_2CO_3 and Na_2CO_3), the conversion rates were increased about 6–8 times when compared to the conversion rate of the undoped sample. These curves show also that the behaviors of these additives differed. The conversion rates of the samples doped with Li_2CO_3, Na_2CO_3 K_2CO_3, Na_2SO_4 and $CaCl_2$ were relatively high at the start, but decreased relatively fast with reaction time. In contrast, conversion rates with the samples doped with NaCl and KCl were not as high as with the above 5 additives at start, but kept almost constant for a long time. For long duration sulfation, NaCl and KCl are therefore competitive with Li_2CO_3, Na_2SO_4 and Na_2CO_3.
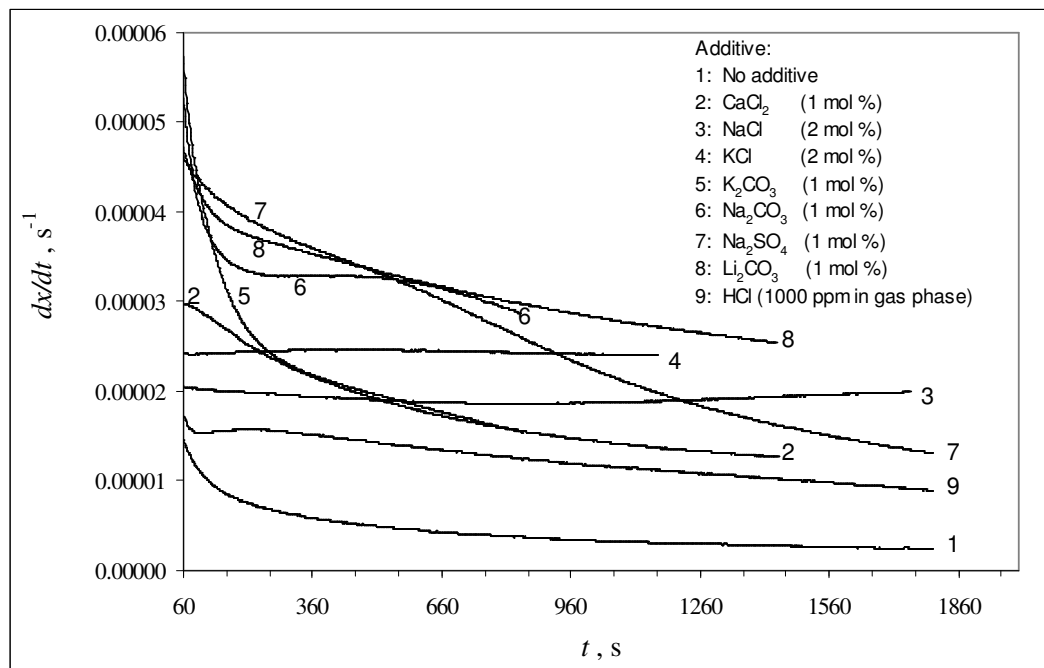
Figure 4.1 Conversion rate vs. time curves of Faxe Bryozo doped with different additives (other conditions: T: 823 K; P: 0.11 MPa; inlet SO_2: 1800 ppm; O_2: 3 %; CO_2: 30 %; N_2: balance)

The observed significant enhancing effects of the tested alkali metal salts and HCl on the direct sulfation of limestone are in good agreement with the experimental results obtained by Fuertes and Fernandez (1996) and Partanen et al. (2005)

4.3.3 Influence of thermal pre–treatment

It was observed during the study that the conversion rate of a doped limestone sample was strongly influenced by its thermal history before the sulfation reaction. To see such effect, the doped limestone samples were tested after they were thermally pre–treated at 923 K for 1 hour in a gas consisting of 30 % CO_2, 3% O_2 and 67 % N_2. As shown in Figure 4.2, the thermal pre–treatment radically changed the situation. The thermal pre–treatment made NaCl the most effective additive, and Li_2CO_3 and $CaCl_2$ the most ineffective ones. An interesting phenomenon is the appearance of upcurved conversion rate vs. time curves with maximum (it will just be mentioned as "upcurved" later on) obtained with the samples doped with NaCl, KCl, Na_2CO_3 and Na_2SO_4. The upcurved form means that the sulfation reaction was somehow accelerated in the period before the maximum point.
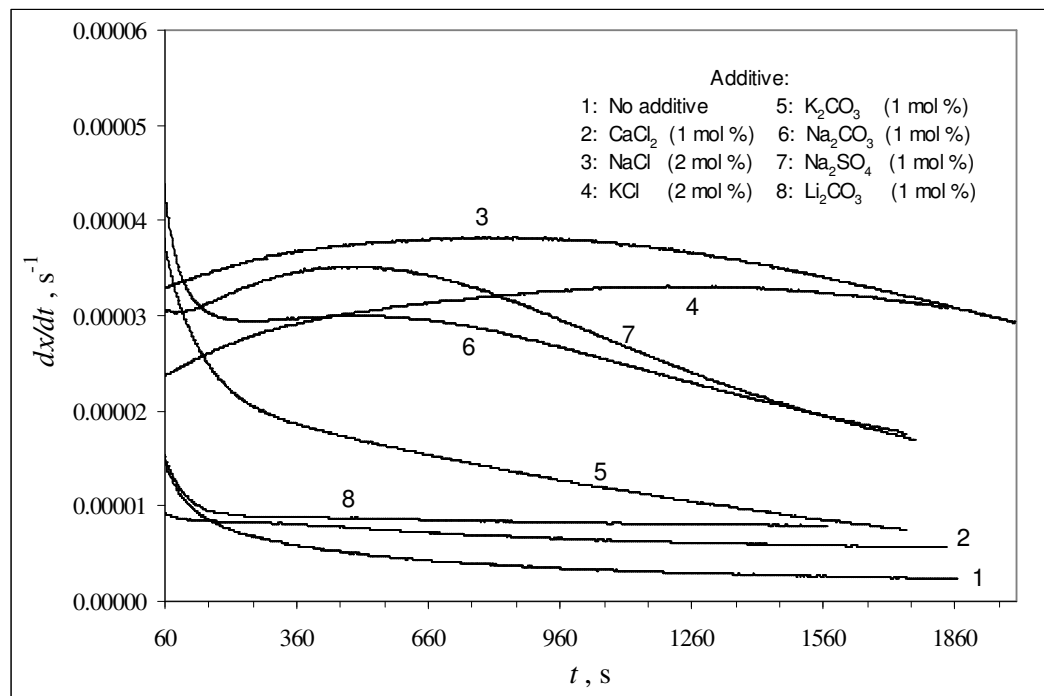
Figure 4.2 Conversion rate vs. time curves of doped and thermally treated Faxe Bryozo (other conditions: thermal pre–treatment before sulfation: 923 K for 1 h; T: 823 K; P: 0.11 MPa; inlet SO_2: 1800 ppm; O_2: 3 %; CO_2: 30 %; N_2: balance)

NaCl was studied further to explore the influence of duration and temperature level of the thermal pre–treatment. As shown in Figures 4.3–4.4, the enhancing effect of NaCl on the sulfation process was significantly increased with increasing temperature of the thermal pre–treatment, whereas no extra benefit was obtained with durations of the thermal pre–treatment longer than 1 hour.
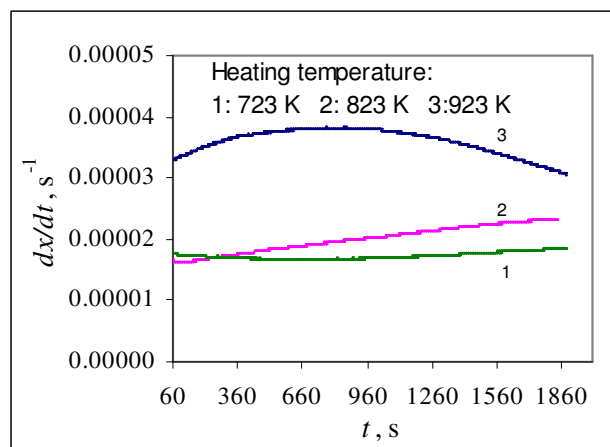
Figure 4.3 Influence of the temperature of the thermal pre–treatment on the conversion rate of Faxe Bryozo doped with 2 % NaCl (other conditions: T: 823 K; P: 0.11 MPa; inlet SO_2: 1800 ppm; O_2: 3 %; CO_2: 30 %; N_2. balance)
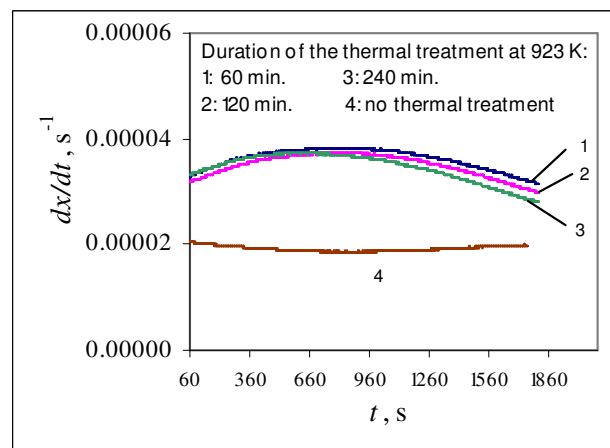
Figure 4.4 Influence of the duration of the thermal pre–treatment on the conversion rate of Faxe Bryozo doped with 2 % NaCl (other conditions: T: 823 K; P: 0.11 MPa; inlet SO_2: 1800 ppm; O_2: 3 %; CO_2: 30 %; N_2: balance)

4.3.4 Influence of additive dosage

The additive dosage may also influence the enhancement. To study this, limestone samples with varying NaCl dosage and thermally pre–treated (923 K for 1 hour) were tested.

As shown in Figure 4.5, higher dosages did not improve the enhancing effect. A too high dosage, on the contrary, caused a weaker enhancement.
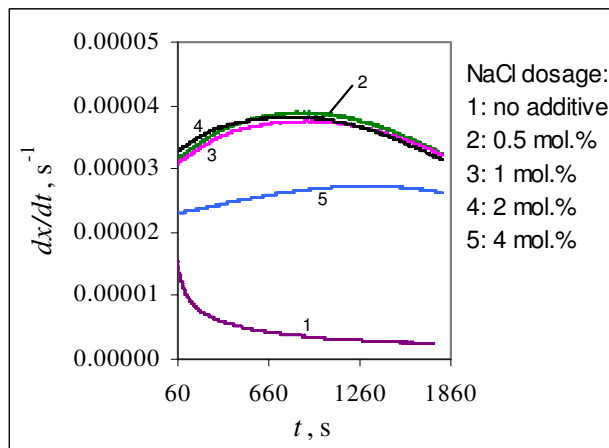
Figure 4.5 Influence of NaCl dosage on the conversion rate of Faxe Bryozo (other conditions: thermal treatment before sulfation: 923 K for 1 h; T: 823 K; P: 0.11 MPa; inlet SO_2: 1800 ppm; O_2: 3 %; CO_2: 30 %; N_2: balance)

4.3.5 Final product

The sulfated limestone samples were analyzed by X–ray powder diffraction to confirm the formed solid product. The powder patterns shown in Figure 4.6 demonstrate that the final solid product of the sulfation reaction with addition of the different additives is anhydrite ($CaSO_4$)—the same as without addition of the additives.
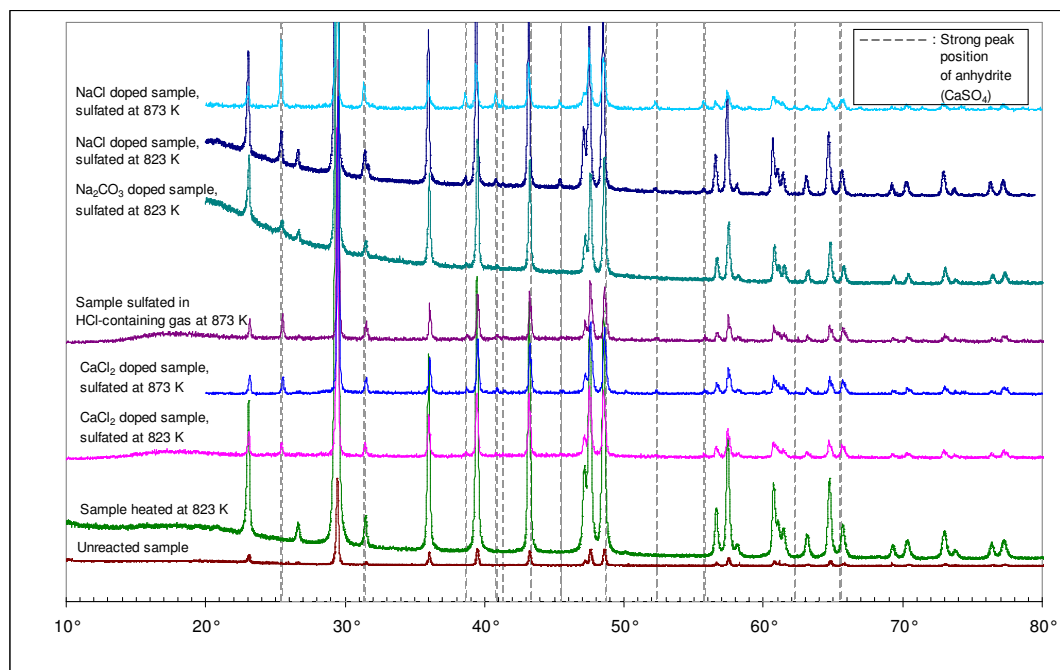
Figure 4.6 Powder patterns of sulfated Faxe Bryozo doped with different additives

4.3.6 Morphological change of the sulfated limestone particles

Particles of Faxe Bryozo, doped and sulfated, were examined by scanning electron microscope (SEM) to see morphological changes, which may help to understand the mechanisms for the special kinetic behaviors of the sulfation of doped limestone particles.

4.3.6.1   Alkali metal salts

SEM examinations show that the sulfation of the limestone samples doped with the alkali metal salts involves nucleation and crystal growth of the solid product–anhydrite. Analysis (line–scanning) of the sulfated samples doped with NaCl and KCl by EDS (energy dispersive spectrometry) X–ray microanalysis (see appendix 4–2, 4–3, 4–4) show that the crystals formed at the surface contain high percentage of sulfur and calcium, which in conjunction with the powder patterns shown in Figure 4.6 confirms that the crystals are anhydrite crystals.

Na⁺–containing salts:

SEM examinations showed that relatively large and seriously deformed product crystals are formed with the samples doped with NaCl, Na_2CO_3 and Na_2SO_4. SEM images obtained with NaCl–doped samples are presented here as a representative to demonstrate this

phenomenon. The samples were doped with 2 % NaCl and thermally pre–treated at 923 K for 60 minutes before the sulfation. Figures 4.7–4.9 show respectively the sampling positions in the conversion rate vs. time curve, SEM image of the unsulfated particles and SEM images of the sulfated particles.
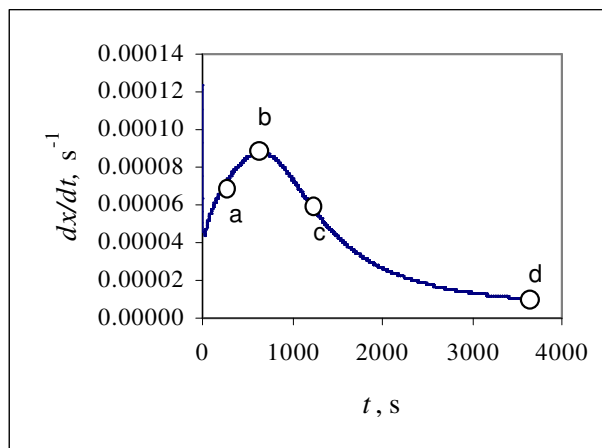

Figure 4.7 Conversion rate vs. time curve of Faxe Bryozo showing sampling points for SEM examination of the sulfated sample (other conditions: additive: 2 mol % NaCl; thermal pre–treatment before sulfation: 923 K for 1 hour; T: 873 K; P: 0.11 MPa; inlet SO_2: 1800 ppm; O_2: 3 %; CO_2: 30 %; N_2: balance)
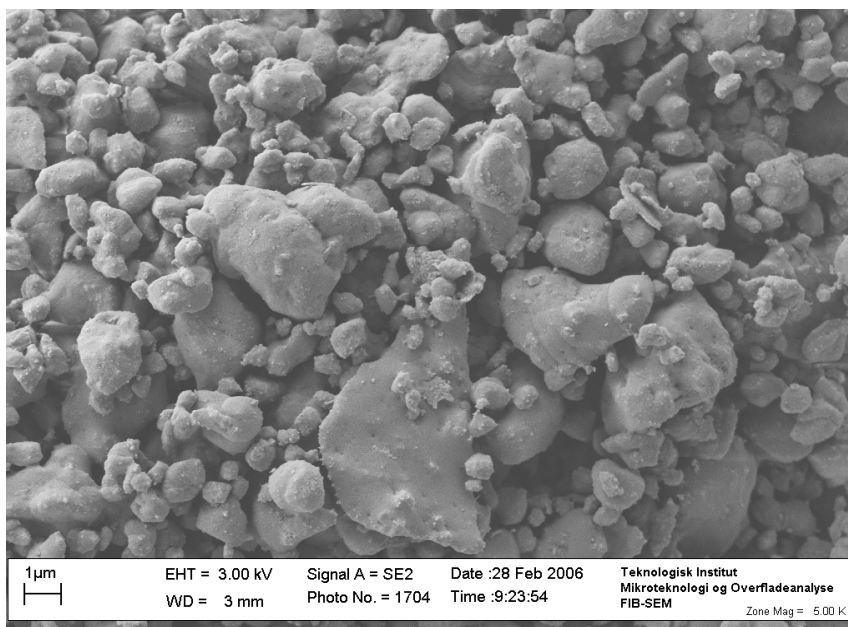
Figure 4.8 Faxe Bryozo particles doped with 2 % NaCl and thermally treated at 923 K for 1 hour
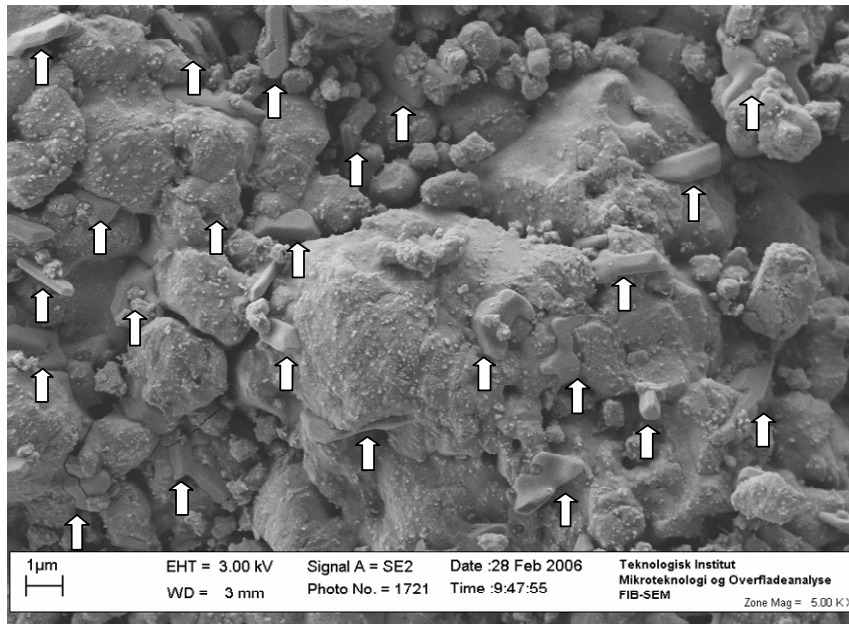
Figure 4.9a SEM images of NaCl–doped Faxe Bryozo particles sulfated at 873 K for 5 minutes with $x = 1.9$ % (corresponding to position a in Figure 4.7; the crystal grains are indicated by the white arrows)
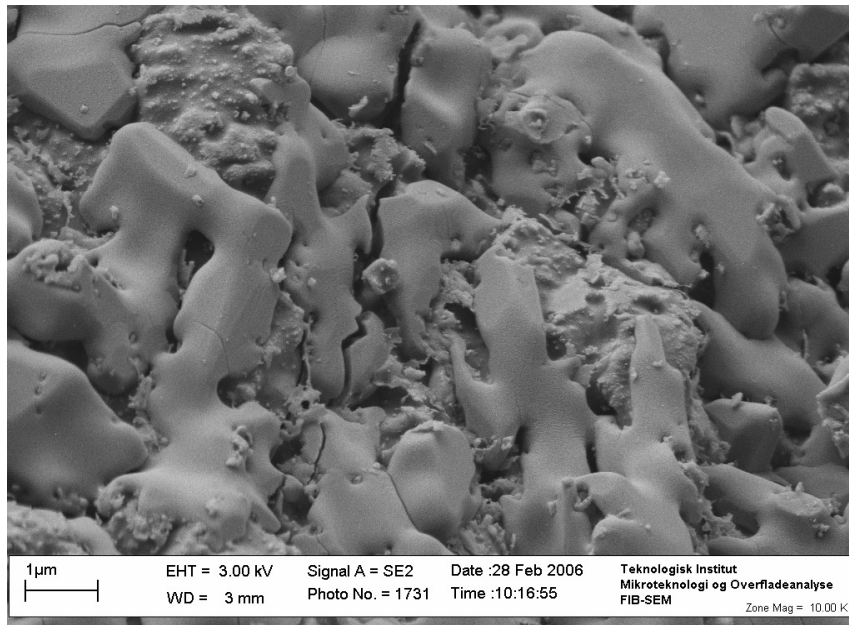
Figure 4.9b SEM images of NaCl–doped Faxe Bryozo particles sulfated at 873 K for 10 minutes ($x = 4.4$ %, corresponding to position b in Figure 4.7)
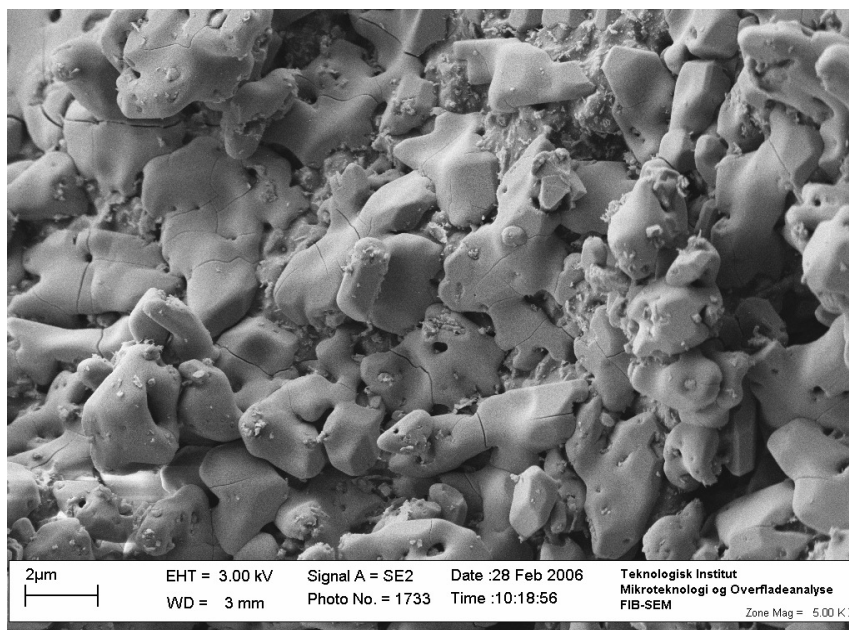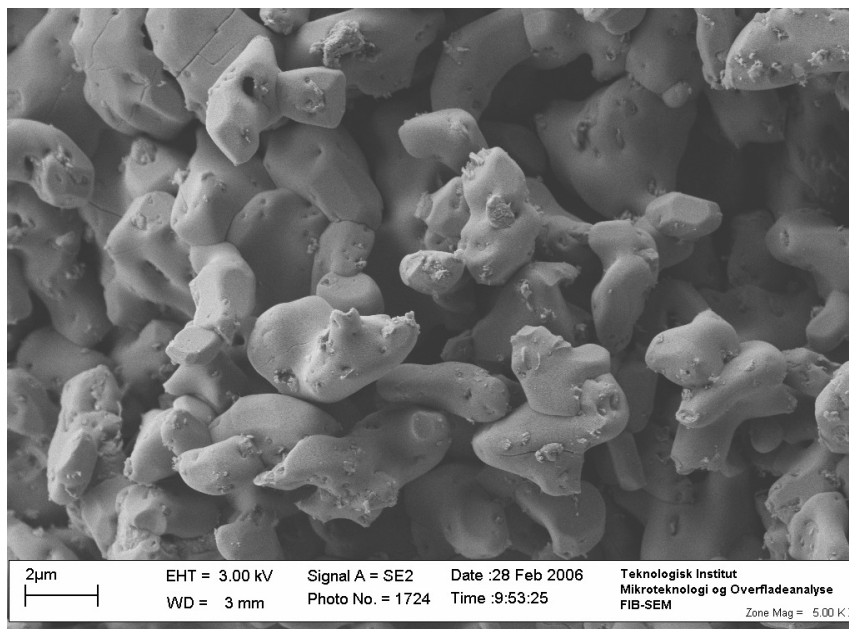
Figure 4.9c SEM images of NaCl–doped Faxe Bryozo particles sulfated 873 K for 20 minutes (x = 9.0 %, corresponding to position c in Figure 4.7)

Figure 4.9d SEM images of NaCl–doped Faxe Bryozo particles sulfated at 873 K for 60 minutes (x = 14.8 %, corresponding to position d in Figure 4.7)

Figures 4.9a–d clearly demonstrate the initial formation of product nuclei/crystal grains (indicated by the white arrows) scattered around the particle surface with relatively long

distance from each other (Figure 4.9a), the progressive covering of the limestone surface by the growing solid product crystals (Figures 4.9b–c) and the total covering of the limestone particles/grains by coalesced product crystals (Figure 4.9d). The product crystals are seriously deformed.

Li_2CO_3

The effect of Li_2CO_3 seems to depend very much on the thermal pre–treatment before sulfation. With the sample thermally pre–treated at 923 K for 1 hour, as demonstrated in Figure 4.10, the limestone particles are seriously sintered. The product crystals are also seriously deformed as in the case of NaCl. Without the thermal pre–treatment, as demonstrated in Figure 4.11, the sintering of the limestone particles is insignificant. Relatively well shaped product crystals are formed.
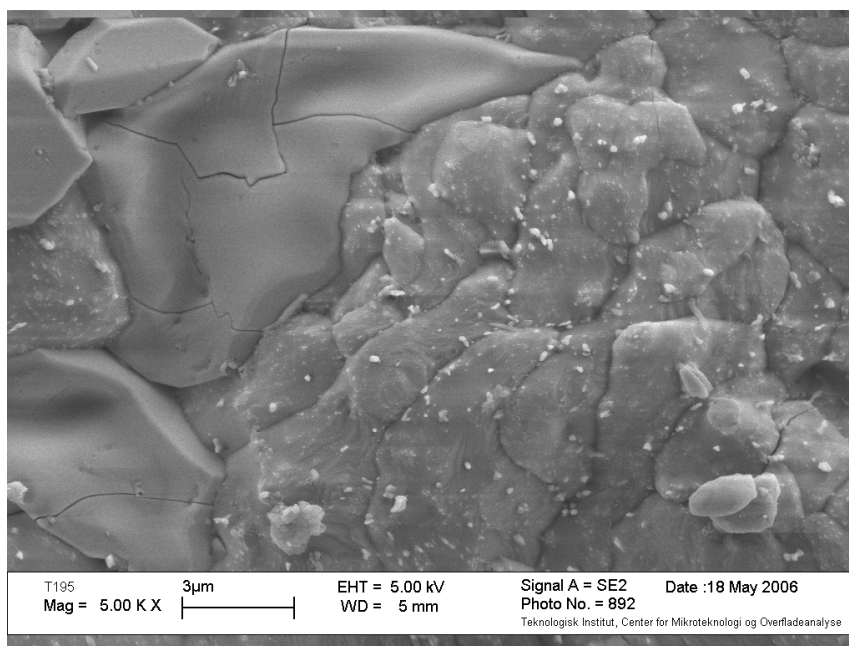

Figure 4.10 SEM image of Faxe Bryozo doped with 1 % Li_2CO_3 and sulfated to a conversion of about 1.5 % at 823 K (other conditions: thermal pre–treatment before sulfation: 923 K for 1 hour; P: 0.11 MPa; inlet SO_2: 1800 ppm; O_2: 3 %; CO_2: 30 %; N_2: balance)
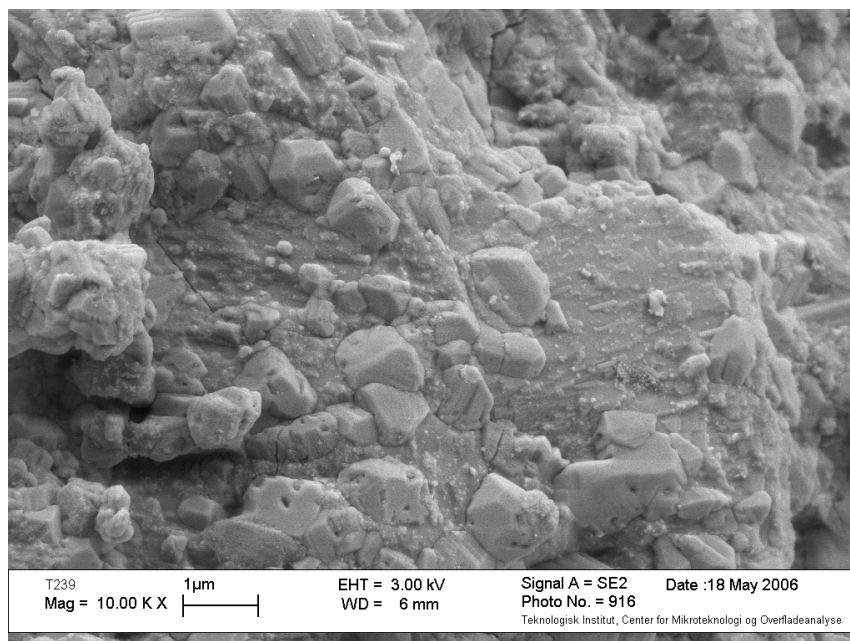
Figure 4.11 SEM image of Faxe Bryozo doped with Li_2CO_3 and sulfated to a conversion of about 4.6 % at 823 K (other conditions: additive: 1 mol % Li_2CO_3, no thermal pre–treatment; P: 0.11 MPa; inlet SO_2: 1800 ppm; O_2: 3 %; CO_2: 30 %; N_2: balance)

KCl:

Addition of KCl caused the formation of relatively large and well shaped product crystals, which is demonstrated in Figure 4.12. Sintering of the limestone particles is similar to the effect of NaCl.
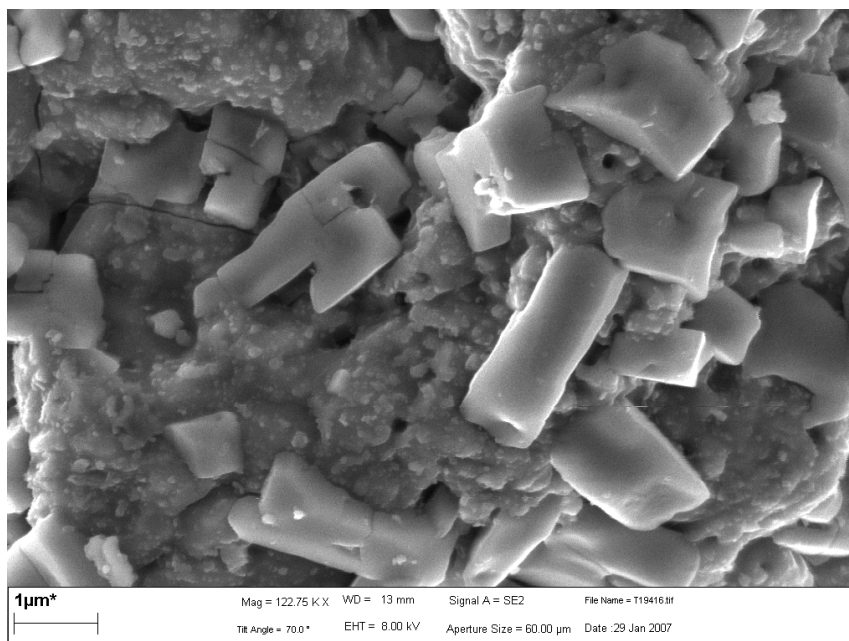
Figure 4.12 SEM image of Faxe Bryozo doped with 2 % KCl and sulfated at 823 K for 30 minutes (x = ca. 6 %) (other reaction conditions: thermal pre–treatment before sulfation: 923 K for 1 hour; P: 0.11 MPa; inlet SO_2: 1800 ppm; O_2: 3 %; CO_2: 30 %; N_2: balance)

4.3.6.2   CaCl$_2$

To see the effect of $CaCl_2$, the sample was first doped with 1 mol % $CaCl_2$ and thermally pre–treated at 923 K for 1 hour, and then sulfated at 823 K for about 30 minutes. Figures 4.13–4.14 show the SEM images of the surface of $CaCl_2$–doped Faxe Bryozo particles before and after the sulfation, respectively. Addition of $CaCl_2$ caused a serious sintering of the limestone particles and the formation of relatively large product crystals, as demonstrated in these two figures. Analysis (line–scanning) of the relevant particles by EDS X–ray microanalysis (see appendix 4–5) shows that the crystals contain high percentage of sulfur and calcium. Figures 4.15a–b are sulfur mapping images of particles from the same sample used for Figure 4.14 by energy–dispersive X–ray analysis (EDXA). Figure 4.15a is the SEM image, while Figure 4.15b is the sulfur mapping image of the same area shown in Figure 4.15a. These two images show clearly a match between the sulfur distribution pattern and the slice shaped crystals. The EDS X–ray microanalysis, sulfur mapping and powder patterns shown in Figure 4.6 confirm that the formed crystals are anhydrite crystals.

In contrast to the totally deformed solid product crystals with the limestone samples doped with Li^+ and Na^+–containing salts, the solid product crystals here are well shaped in slice form. The situation is the same with the samples reacted at 873 K and the samples without the thermal pre–treatment at 923 K.
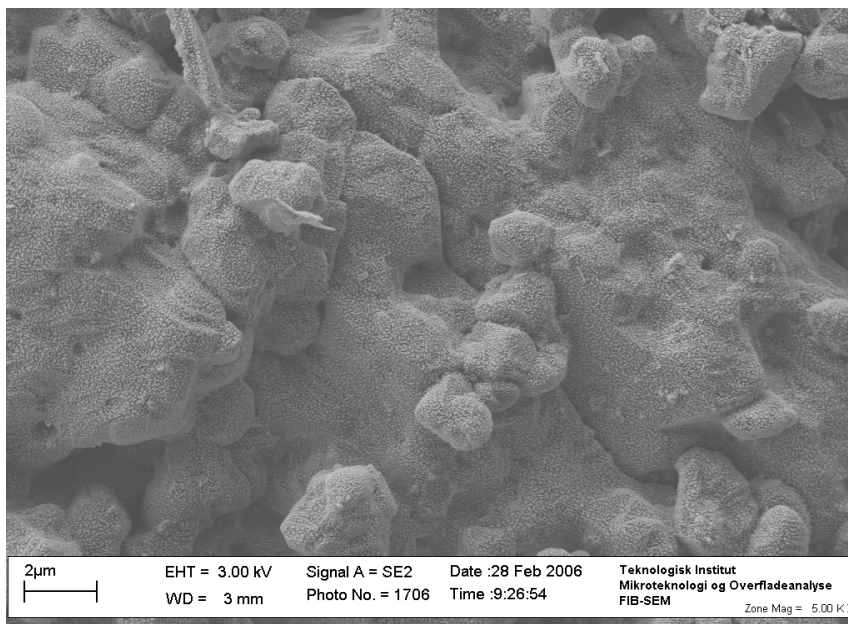

Figure 4.13 SEM image of Faxe Bryozo particles doped with 1 % $CaCl_2$ and thermally pre–treated at 923 K for 1 hour (Notice: the tiny light dots all over the surface are gold coated on the particle for SEM examination).
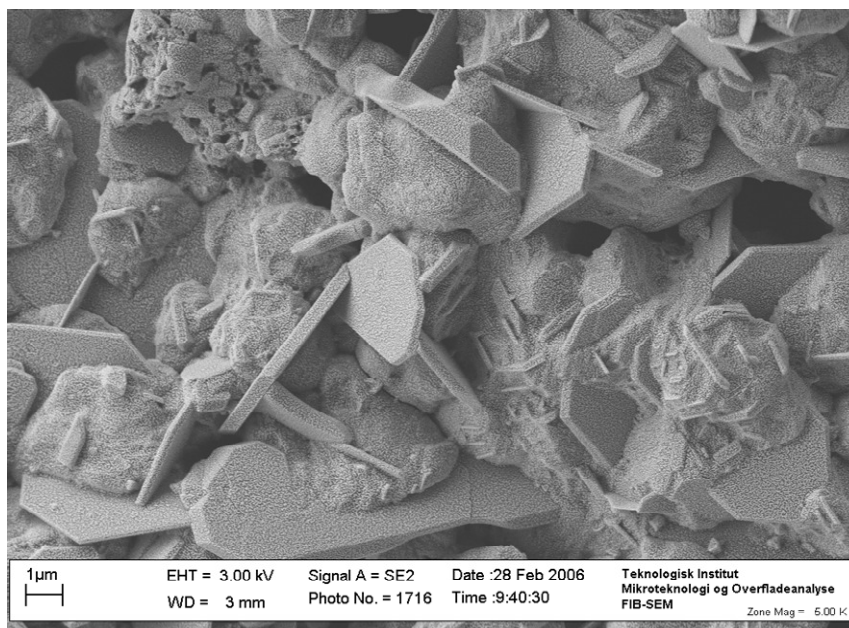
Figure 4.14 SEM image of Faxe Bryozo particles doped with 1 % CaCl$_2$ and sulfated at 823 K to a conversion of ca. 1.3 % (other conditions: thermal pre–treatment before sulfation: 923 K for 1 h; P: 0.11 MPa; inlet SO$_2$: 1800 ppm; O$_2$: 3 %; CO$_2$: 30 %; N$_2$: balance) (Notice: the tiny light dots all over the surface are gold coated on the particle for SEM examination).

(a)   (b)
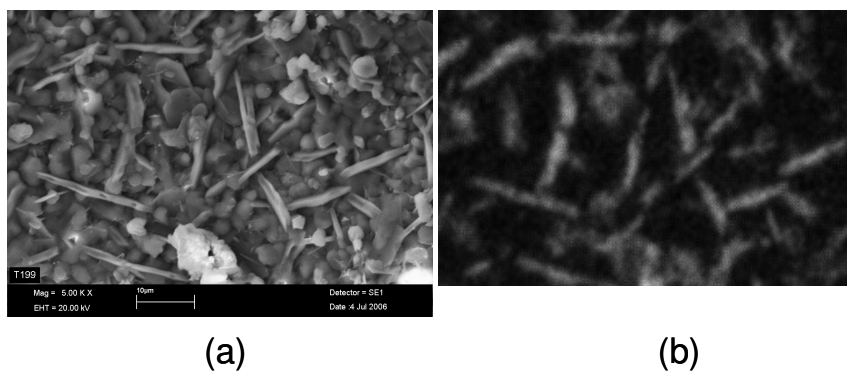
Figure 4.15 Images of EDXA sulfur mapping of Faxe Bryozo particles doped with 1 % CaCl$_2$ and sulfated at 823 K to a conversion of ca. 1.3 % (other conditions: thermal pre–treatment before sulfation: 923 K for 1 h; P: 0.11 MPa; inlet SO$_2$: 1800 ppm; O$_2$: 3 %; CO$_2$: 30 %; N$_2$: balance) (Notice: the tiny light dots all over the surface are gold coated on the particle for SEM examination) (a: SEM image, b: sulfur mapping).

4.3.6.3   HCl

Figure 4.16 shows the SEM image of the surface of Faxe Bryozo particles sulfated at 823 K in the presence of about 1000 ppm HCl in the gas. This figure reveals that the addition of HCl in the gas phase resulted in the formation of a melt–like product phase. Situation is similar with samples sulfated at 873 K. This phenomenon is in good agreement with the observations made by Partanen et al. (2005). X–ray powder diffraction confirmed the formation of anhydrite crystal though no individual crystals of anhydrite are visible. Analysis (point analysis) of the relevant particles by EDS X–ray microanalysis (see appendix 4–6) shows that the melt–like product layer contains high percentages of sulfur, calcium and chlorine.
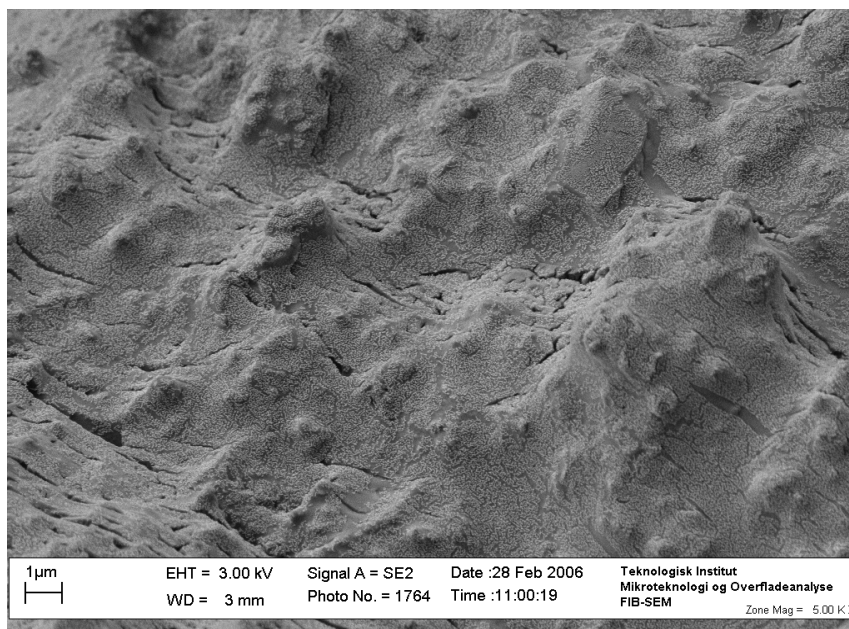

Figure 4.16 SEM image of the surface of Faxe Bryozo particles sulfated in the presence of 1000 ppm HCl in the gas at 823 K to a conversion of about 2.7 % (other conditions: P: 0.11 MPa; inlet SO_2: 1800 ppm; O_2: 3 %; CO_2: 30 %; N_2: balance) (Notice: the tiny light dots all over the surface are gold coated on the particle for SEM examination).

4.3.7 Influence of gases

4.3.7.1 SO_2, O_2 and CO_2

The influences of SO_2, O_2 and CO_2 on the sulfation of NaCl–doped limestone samples were evaluated by their apparent reaction orders. To ensure a close reaction conditions (such as same conversion and same product layer structure), pre–sulfated samples corresponding to position (b) and (d) in Figure 4.7 were used for the evaluation. The reaction orders of SO_2, O_2 and CO_2 were evaluated by a step decrease of the concentration of the relevant gas in a single run with the same sample.

Figure 4.17 shows that the apparent reaction order of SO_2 was significantly influenced by the temperature. The apparent reaction order of SO_2 increased from about 0.2 at 823 K to about 0.5 at 923 K. Conversion seems to have only slight influence on the apparent reaction order.

Figure 4.18 shows the apparent reaction orders of O_2 and CO_2 at 823 K. Both reaction orders decreased with increasing conversion, which means weaker influence of O_2 but stronger influence of CO_2 with increasing conversion.
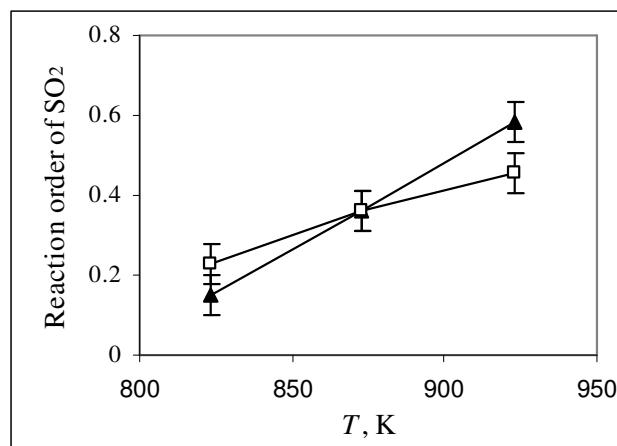

Figure 4.17 Variation of the apparent reaction order of SO_2 with reaction temperature with NaCl–doped and pre–sulfated Faxe Bryozo (▲: with the sample doped with 2 % NaCl, thermally treated at 923 K for 1 h and pre–sulfated to 4 % conversion; □: with the sample doped with 2 % NaCl, thermally pre–treated at 923 K for 1 hour and pre–sulfated to 15 % conversion) (other conditions: P: 0.11 MPa; inlet SO_2: 900–1800 ppm; O_2: 3 %; CO_2: 30 %; N_2: balance)
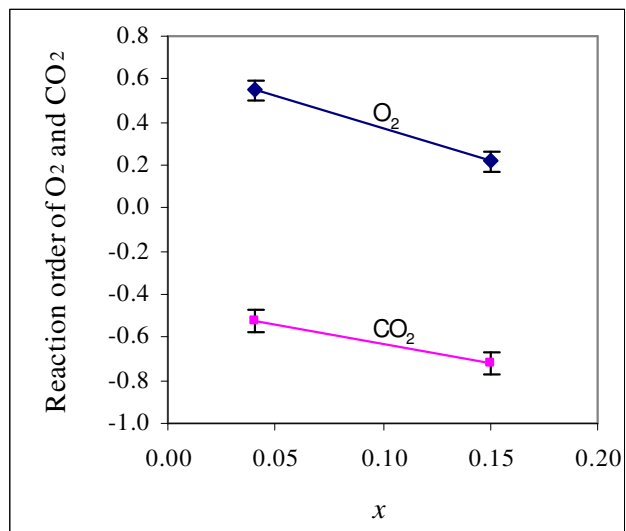
Figure 4.18 Variation of the apparent reaction orders of O_2 and CO_2 with the conversion of NaCl–doped and pre–sulfated Faxe Bryozo (other conditions: additive: 2 % NaCl; thermal pre–treatment before sulfation: 923 K for 1 hour; T: 823 K; P: 0.11 MPa; inlet SO_2: 1800 ppm; O_2: 3–6 % (3 % for measuring the reaction order of CO_2); CO_2: 15–30 % (30 % for measuring reaction order of O_2); N_2: balance)

4.3.7.2 H_2O

The influence of water was investigated with limestone samples doped with 2 % NaCl at both 823 K and 923 K and with water concentration varied from 2 to 6 vol. %. It showed that the effect of water addition depends very much on reaction temperature and conversion. Figure 4.19 shows that at 823 K water promoted the sulfation reaction. Variation in water concentration in the investigated concentration interval had little influence.
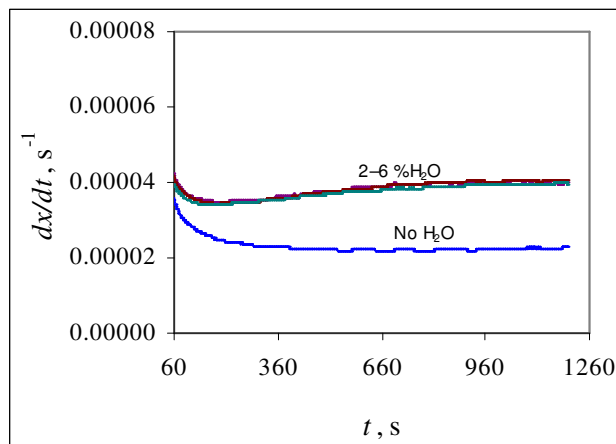
Figure 4.19 Influence of water addition on the conversion rate of Faxe
Bryozo doped with 2 % NaCl at 823 K (other conditions: P: 0.11 MPa; inlet
SO$_2$: 1800 ppm; O$_2$: 3 %; CO$_2$: 30 %; N$_2$: balance)

At 923 K, as shown in Figure 4.20, water had negative influence on the conversion rate in
the initial period. The influence of variation in water concentration in the investigated
concentration interval was not significant. However, the decay of the conversion rate with the
reaction time in the presence of water was not as fast as without water. After a longer reaction
time the conversion rate with water addition surpassed the conversion rate without water
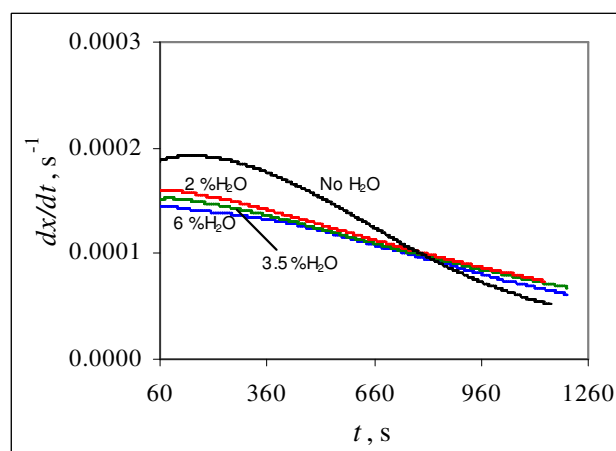addition.

Figure 4.20 Influence of water addition on the conversion rate of
Faxe Bryozo doped with 2 % NaCl at 923 K (other conditions: P: 0.11 MPa;
inlet SO$_2$: 1800 ppm; O$_2$: 3 %; CO$_2$: 30 %; N$_2$: balance)

4.3.8 Influence of temperature

Figure 4.21 shows the influence of temperature on the conversion rate vs. time curves of Faxe Bryozo doped with 2 % NaCl and thermally pre–treated at 923 K for 1 hour. The temperature apparently has two effects on the sulfation reaction. One is the general increase in the conversion rate with increasing temperature; the other is the form of the conversion rate vs. time curve. As shown earlier, samples doped with NaCl and some other additives produced upcurved conversion rate vs. time curves. Figure 4.21 shows that with increasing temperature, the conversion rate vs. time curve becomes more curved; the maximum point appears at an earlier time as well.
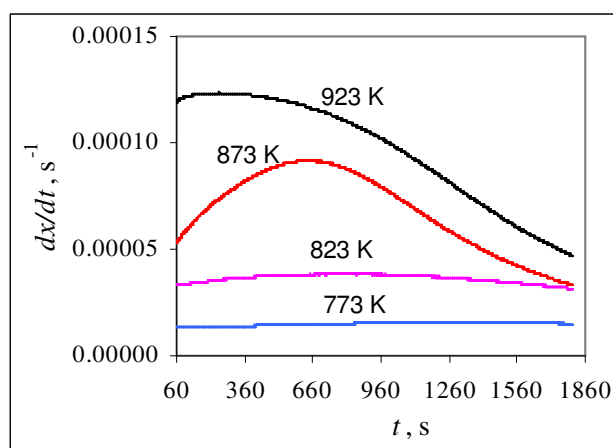

Figure 4.21 Influence of temperature on the conversion rate of Faxe Bryozo doped with 2 % NaCl (other conditions: thermal pre–treatment before sulfation: 923 K for 1 h; P: 0.11 MPa; inlet SO_2: 1800 ppm; O_2: 3 %; CO_2: 30 %; N_2: balance)

To evaluate the apparent activation energy, the pre–sulfated samples—the same samples used for measuring of the apparent reaction orders of SO_2 and CO_2 to ensure closely reaction conditions. Figures 4.22–4.23 show the results. As it can be seen in these two figures, the apparent activation energy is significantly influenced by SO_2 concentration in the gas. With the sample pre–sulfated to a conversion of about 4.4 %, the apparent activation energy decreases from about 98 kJ/mol to about 77 kJ/mol when the SO_2 concentration is decreased from 1800 ppm to 900 ppm. Similarly, with the sample pre-sulfated to a conversion of about 14.8 %, the apparent activation energy decreases from about 100 kJ/mol to about 90 kJ/mol

when SO_2 concentration is decreased from 1800 ppm to 900 ppm. Limestone conversion has also certain influence on the apparent activation energy. The apparent activation energy is generally increased with increasing conversion.

Figure 4.22 Influence of temperature on the conversion rate of Faxe Bryozo doped with NaCl in a gas containing 1800 ppm SO_2 (▲: with the sample doped with 2 % NaCl, thermally pre–treated at 923 K for 1 h and pre–sulfated to 4.4 % conversion; □: with the sample doped with 2 % NaCl, thermally treated at 923 K for 1 hour and pre–sulfated to 14.8 % conversion) (other conditions: P: 0.11 MPa; O_2: 3 %; CO_2: 30 %; N_2: balance)
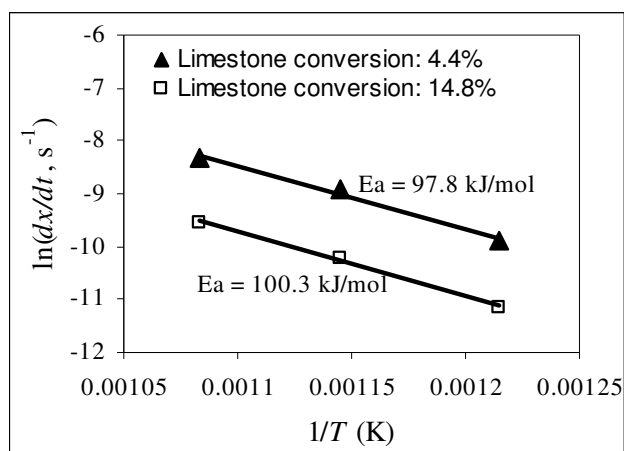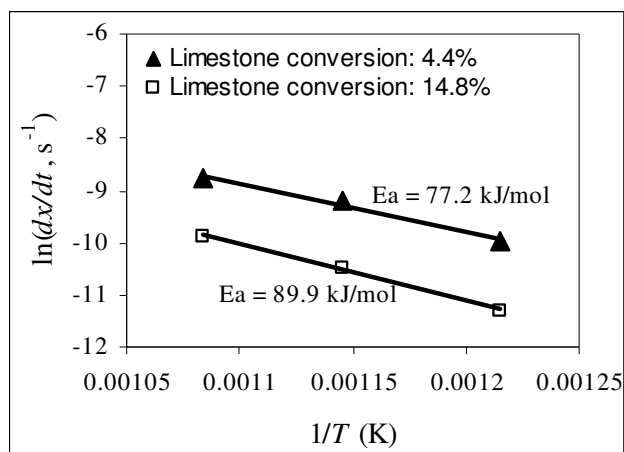
Figure 4.23 Influence of temperature on the conversion rate of Faxe Bryozo doped with NaCl in a gas containing 900 ppm SO_2 (▲: with the sample doped with 2 % NaCl, thermally treated at 923 K for 1 h and pre–sulfated to 4.4 % conversion; □: with the sample doped with 2 % NaCl, thermally pre–treated at 923 K for 1 hour and pre–sulfated to 14.8 % conversion) (other conditions: P: 0.11 MPa; O_2: 3 %; CO_2: 30 %; N_2: balance)

4.4   Discussions

As shown above, the direct sulfation of Faxe Bryozo in the presence of additives produced upcurved conversion rate vs. time curves, was significantly influenced by the thermal pre–treatment, and produced the same solid product in varying physical forms depending on additive types. In the following sections, these phenomena are discussed and the mechanisms of the enhancement by the tested additives are assessed.

4.4.1 Mechanisms of the enhancing effect of the additives

4.4.1.1   NaCl

4.4.1.1.1 Mechanism of the enhancement

SEM images presented above show that in the presence of NaCl the direct sulfation of limestone involved nucleation and crystal grain growth of the solid product as well. However, compared to the situation without additives, the nucleation and growth process in the presence of NaCl differs in various aspects:

(i)   The number of nuclei formed in the presence of NaCl is significantly fewer than without the additive; the distance between the formed nuclei is relatively long.

(ii)   The product crystal grains formed in the presence of the additive are seriously deformed and almost totally lost the characteristic orthorhombic form of anhydrite crystals.

(iii)   The product crystals grow laterally and coalesce when in touch.

(iv)   The nucleation and growth of the product crystals are not orientated any more.

These changes caused by NaCl indicate a significantly increased ionic mobility in both the solid reactant (calcite) and the solid product (anhydrite), most probably by the mechanism of formation of more extrinsic point defects (West 1999) in the crystal lattices of calcite and anhydrite by the incorporation of single valent Na^+ and/or Cl^- ions in their lattice structures. The increased ionic mobility in calcite makes it possible for product ions to migrate longer distances to reach the nucleation and growth sites, while the increased ionic mobility in the product crystal grains is the main reason for the deformation of the product crystal grains and their easy coalescence. The high ionic mobility in the product crystals and the probably less stable lattice structure at the surface of calcite because of the significantly increased ionic mobility are most likely the main reasons for the non–orientated nucleation and growth. Considering the significant enhancing effect of $CaCl_2$ (as shown in Figure 4.1) the effect of NaCl should contain the contributions of both Na^+ and Cl^- ions. As shown in Figures 4.1 and 4.2, the enhancing effects of Na_2CO_3 and Na_2SO_4 changed (decreased) only about 10–20 % after a thermal pre–treatment at 923 K for 1 hour, whereas the enhancing effect of NaCl increased about 100 % after the same thermal pre–treatment. This is most likely due to the enhanced effect of Cl^- by the thermal pre–treatment.

The increase in ionic mobility in the solid product crystals is most likely caused by the diffusion of sodium ions (Na^+) from the calcite phase into the solid product phase during the nucleation and growth process, as line–scanning of the samples doped with NaCl with EDS X–ray microanalysis (see appendix 4–2, 4–3) showed clearly the presence of Na^+ in the product crystals, even in a higher concentration than in the limestone. It was observed that the thermal pre–treatment before sulfation significantly enhanced the sintering of the product crystals, which indicates an enhanced transport of Na^+ to the product phase by the thermal pre–treatment.

The sulfation reaction may take place on both the surface of calcite and the surface of product crystals. The observed conversion rate is the sum of the contributions from the sulfation reaction on both surface types. The increase in ionic mobility in both calcite and the solid product may increase carbonate concentration at both surfaces and thus also the reactivity of these two surfaces. The enhancement by the additive thus most likely comes from three major contributions: the first from the increased reactivity on the calcite surface, the second from the increased reactivity on the product surface and the third from the slower shielding of the more reactive calcite surface (it is reasoned below) because of the formation of fewer product nuclei.

4.4.1.1.2 Controlling mechanism

As it has been concluded earlier in Chapter 3, the direct sulfation of limestone at temperatures lower than about 973 K is under mixed control by both chemical reaction and solid–state diffusion. It seems that addition of NaCl does not change this situation under the used reaction conditions, indicated by the variations of the apparent reaction order of SO_2 and the apparent activation energy with the reaction conditions shown in Figures 4.17 and 4.22–23. The significant increase in the apparent reaction order of SO_2 with increasing temperature may be due to reduced resistance of solid–state diffusion at higher temperatures. The significant influence of SO_2 concentration on the apparent activation energy may be due to the influence of SO_2 concentration on the relative dominance between chemical reaction and solid–state diffusion. A higher SO_2 concentration means a higher chemical reaction rate and thus an increased resistance of solid–state diffusion (indicated by a higher apparent activation energy), vice versa.

4.4.1.1.3 Reasons for the upcurved conversion rate vs. time curves

The upcurved form of the conversion rate vs. time curves of the NaCl–doped limestone samples could be caused by a combination of the progressive shielding of the more reactive calcite surface by the solid product crystals and the presence of significant resistance of solid–state diffusion.

In the sulfation process, sulfate ions formed at the uncovered calcite surface diffuse into the product crystals. The rate by which the formed sulfate ions diffuse into a product crystal may be roughly assumed to be proportional to the length of the boundary of the crystal and the sulfate concentration gradient around the crystal. The sulfation rate at the uncovered

calcite surface is proportional to the uncovered calcite surface area and the concentration of carbonate ions at the uncovered calcite surface. A balance between the formation of sulfate ions at the uncovered calcite surface and the diffusion of the formed sulfate ions into the product crystal is supposed to exist. With increasing product crystal size, the uncovered calcite surface area shrinks.

Initially, the conversion is relatively low. The crystals are small and cover only a small fraction of the calcite surface. The increasing conversion rate with increasing conversion or reaction time is most likely caused by two major reasons. One is the higher percentage of increase in the size of the crystals than the percentage of reduction in the uncovered calcite surface area. The other is the significant resistance of solid–state diffusion. The rate by which the formed sulfate ions diffuse into the product crystal increases with the increase in the size of the product crystals, which in turn results in a decrease of the concentration of sulfate ions at the uncovered calcite surface and thus a higher concentration of carbonate ions. This increased concentration of carbonate ions results in a higher sulfation rate at the uncovered calcite surface which keeps in balance with the rate by which the sulfate ions diffuse into the crystal. The apparent result is thus an increasing conversion rate.

After the conversion reaches a certain level, the product crystals become large and cover a large percentage of the calcite surface. The conversion rate now decreases with increasing conversion because the percentage of reduction in the uncovered calcite surface area is now significantly larger than the percentage of increase in the size of the product crystal. The increase in the reaction rate caused by the increased concentration of carbonate ions is now not sufficient to compensate for the reduction in the uncovered surface area because the concentration of carbonate ions is limited to that in pure calcite.

The maximum rate may be the transition point between these two situations. As shown in Figures 4.7 and 4.9b, the maximum in the conversion rate vs. time curve appeared when the calcite surface was only half covered by product crystals. This indicates that the reactivity of the calcite surface was higher than the surface of the product crystals, which is also expected to be.

The increasing reactivity of the uncovered calcite surface and the gradual shielding of limestone surface by the solid product crystals with increasing conversion are therefore most likely the two key factors for the upcurved form of the conversion rate vs. time curves. However, the shape of a conversion rate vs. time curve may depend on a number of factors such as the relative dominance of chemical reaction and solid–state diffusion, the

morphological properties of the limestone particles, the ionic mobility in the product phase, the number of nuclei and the sulfation rate at the product surface.

Figure 4.21 shows conversion rate vs. time curves of NaCl–doped samples at different temperatures. This figure demonstrates the movement of the maximum towards the left side with increasing temperature and the significantly flattened and almost invisible peak at temperatures lower than about 823 K. The explanation could be that at sufficiently high temperatures (> about 923 K), chemical reaction begins to become the dominant control mechanism. At temperatures lower than about 823 K, solid–state diffusion becomes the dominant control mechanism.

4.4.1.2   Other alkali metal salts

Other alkali metal salts tested in this study were not investigated as thoroughly as NaCl. With the limestone samples that were doped with Na_2CO_3 and Na_2SO_4, SEM examinations showed that the reacted surfaces of these samples are to a high degree similar to the samples doped with NaCl. The thermal pre–treatment was also observed to slightly enhance the sintering of the product crystals. Figure 4.2 shows that the conversion rate vs. time curves with samples doped with Na_2CO_3 and Na_2SO_4 have an upcurved form just as NaCl–doped samples. Though the performances of these Na^+–containing salts were not exactly the same, their general behaviors are quite similar, which may be indication of a similar enhancement mechanism for these additives.

With the limestone samples doped with Li_2CO_3, SEM examinations showed that the product crystals formed at 823 K are well shaped when the doped sample was not thermally pre–treated at 923 K, but highly deformed when the doped sample was thermally pre–treated at 923 K, which indicates that the diffusion of Li^+ into the product phase was greatly affected by the thermal pre–treatment. The dependence of the effect of Li^+ on the temperature may be due to the influence of temperature on the way of incorporation of Li^+ ions into the crystal lattice of calcite. The size of Li^+ ions is significantly smaller than the size of Ca^{2+} ions. Li^+ ions may occupy the interstitial sites or the sites of Ca^{2+} in the crystal lattice of calcite. Temperature most likely has strong influence on the site type Li^+ ions are going to occupy, which may subsequently affects the diffusion of Li^+ ions into the product phase.

With the limestone sample doped with KCl, relatively large and well shaped product crystals are formed. Analysis with EDS X–ray microanalysis did not show significant amount of K in the product crystals, either. These observations indicate that diffusion of K^+ into the product crystals during the nucleation and growth process is limited, most likely due to the fact that the size of K^+ is significantly larger than the size of Ca^{2+}. Thus, KCl most likely affects the sulfation reaction by increasing solid–state mobility only in the solid reactant.

The observations with Li^+, Na^+, and K^+–containing salts indicate that these salts may enhance the sulfation reaction by different mechanisms. Li^+–containing salts may promote the sulfation reaction by increasing solid–state mobility in both the solid reactant and product or just in the solid reactant depending on reaction conditions such as a thermal pre–treatment before sulfation, while Na^+–containing salts promote the sulfation reaction by increasing solid–state mobility in both the solid reactant and product. K^+–containing salts seem to promote the sulfation reaction by increasing solid–state mobility only in the solid reactant. Na^+ has a similar size to that of Ca^{2+}, whereas Li^+ and K^+ are respectively significantly smaller and larger than Ca^{2+}. An easy incorporation of aliovalent ions into a crystal requires similarity in ion sizes (West, 1999), which may explain the differences between the enhancement mechanisms of these alkali metals salts. The different anions in the salts may also have certain influence on the enhancement. It is particularly true with Cl^- considering both the effect of $CaCl_2$, the significantly stronger enhancing effect of KCl than K_2CO_3 with or without the thermal pre–treatment and the significantly stronger enhancing effect of NaCl than Na_2CO_3 and Na_2SO_4 with the thermal pre–treatment.
.

4.4.1.3   CaCl$_2$

The mechanism of the enhancement by $CaCl_2$ is different from that of alkali metal salts judged by SEM images of the reacted limestone particles (Figure 4.14). The enhancing effect of $CaCl_2$ appears to be solely due to the increased ionic mobility in the limestone, indicated by the relatively long distance between the product crystals. The ionic mobility in the limestone may be increased due to the formation of more cation vacancies by the incorporation of the single valent chloride ions (Cl^-).

The well shaped form of the product crystals shown in Figure 4.14 indicates that ionic mobility in product crystals was not increased noticeably by the additive, most likely because

of the difficulties of the incorporation of chloride ions into the crystal lattice of the solid product (anhydrite) which is evidenced by analysis with EDS X–ray microanalysis. Point analysis of the sulfated Faxe Bryozo particles doped with $CaCl_2$ (see appendix 4–7) demonstrates clearly the presence of Cl^- in the limestone but not in the product crystals. A probable reason for this phenomenon could be difficulties for Cl^- ions to diffuse into product crystals because of too large differences in both the size and the structure of Cl^- and SO_4^{2-}.

With the same sample for Figure 4.14, an upcurved conversion rate vs. time curve was observed at 873 K as shown in Figure 4.24. The upcurved form may be explained by the same reasons for samples doped with NaCl.
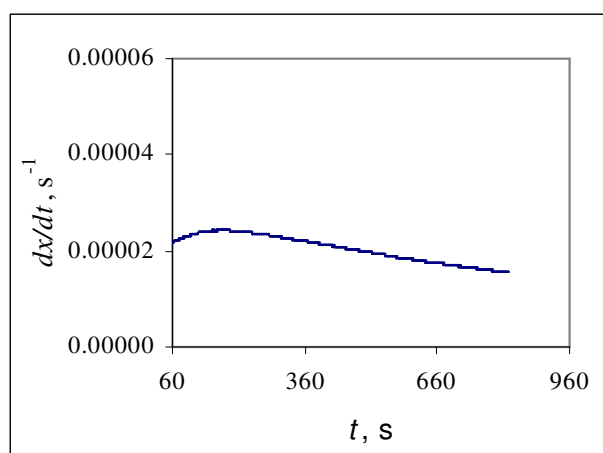

Figure 4.24 Conversion rate vs. time curve of $CaCl_2$–doped Faxe Bryozo at 873 K (other conditions: additive: 1 mol % $CaCl_2$; thermal pre–treatment before sulfation: 923 K for 1h; P: 0.11 MPa; inlet SO_2: 1800 ppm; O_2: 3 %; CO_2: 30 %; N_2: balance)

Partanen et al. (2005) suggested that a eutectic between $CaCO_3$, $CaSO_4$ and $CaCl_2$ might be formed at a temperature above 853 K based on thermodynamic model calculations. However, SEM examinations of the $CaCl_2$–doped Faxe Bryozo particles that were sulfated at 873 K showed that such a eutectic apparently was not formed under the reaction conditions used in this study, possibly because of too low a concentration of $CaCl_2$.

4.4.1.4   HCl

The sulfation of Faxe Bryozo, as shown in Figure 4.1, was enhanced by the presence of HCl in the gas phase. SEM examinations (Figure 4.16) revealed that the addition of HCl in the gas phase resulted in the formation of a melt–like product layer. However, as it can be

seen in Figure 4.1, the conversion rate vs. time curve with HCl addition is upcurved with the maximum rate appeared at a relatively earlier reaction time, which could mean a progressive covering of the more reactive calcite surface by the melt–like product phase.

Partanen et al. (2005) observed the formation of $CaCl_2$ by the chlorination reaction between limestone and HCl in the gas. In this study, it was observed that the conversion rate jumped instantly to a significantly higher level after the addition of HCl was stopped and maintained at this new level for a relatively long time. This phenomenon and the presence of high percentage of chlorine as determined by analysis with EDS X–ray microanalysis (see appendix 4) indicate the existence of chlorination of the limestone—a competing reaction to the sulfation of the limestone.

A comparison between the results with $CaCl_2$ addition and the results with HCl addition indicates that the formation of the melt–like product layer may be related to the simultaneous formation of $CaCl_2$ and $CaSO_4$, which probably creates conditions for the formation of the eutectic suggested by Partanen et al. (2005).

However, the formation of a eutectic may not always mean a faster conversion rate. The conversion rates enhanced by the alkali metal salts are generally much higher than HCl. Blocking of the internal surface area for the sulfation reaction by the melt–like product layer and the presence of the competing reaction—the chlorination of the limestone may be part of the reasons.

4.4.2 Thermal pre–treatment

The results shown earlier demonstrate that a thermal pre–treatment of the doped limestone samples had large influence on the enhancing effects of the additives. Three major effects of the thermal treatment have been observed.

The first is the increase in reactivity of the limestone, most probably due to the formation of more point defects because of increased incorporation of the additive in the crystal lattice of calcite by the thermal pre–treatment.

The second is the decrease in total surface area of the samples caused by sintering during the thermal pre–treatment. Table 4.2 shows that after a thermal pre–treatment at 923 K for 1 hour the total surface area was significantly reduced with samples doped with Li_2CO_3 and Na_2CO_3 but less significantly with others.

Table 4.2 Total surface areas of the undoped and some of the doped samples before and after thermal pre–treatment at 923 K for 1 hour (only 15 minutes for the undoped sample)

Sample	Measured total surface area* (m^2/g)	
	Before the thermal pre–treatment	After the thermal pre–treatment
Blank Faxe Bryozo	0.79	0.62 (heated for 15 min.)
Faxe Bryozo + NaCl	0.62	0.51
Faxe Bryozo + KCl	0.55	0.50
Faxe Bryozo + Li_2CO_3	0.62	0.22
Faxe Bryozo + Na_2CO_3	0.56	0.23
Faxe Bryozo + K_2CO_3	0.47	0.41
Faxe Bryozo + Na_2SO_4	0.6	0.46

* Determined by BET (Micrometrics ASAP 2000).

The third is the influence on the ionic mobility of the solid product, which is well illustrated by SEM images of the sulfated Faxe Bryozo particles doped with Li_2CO_3 in Figures 4.10–4.11. Without the thermal pre–treatment (Figure 4.11), relatively well shaped product crystal grains of around 1 micrometer diameter were formed on the particle surface, whereas with the sample thermally pre–treated (Figure 4.10), the product crystal grains are seriously deformed, an indication of significant increase in ionic mobility in the product phase. Samples doped with NaCl, Na_2CO_3 and Na_2SO_4 showed enhanced sintering of the product phase when the samples were thermally pre–treated before sulfation. However, the same effect was not observed with samples doped with KCl and $CaCl_2$. These phenomena demonstrate that the thermal pre–treatment has great influence on the diffusion of Li^+ and Na^+ ions into the product phase but not for K^+ and Cl^- ions during the nucleation and growth process. The thermal pre–treatment may increase the concentration of Li^+ and Na^+ ions in the calcite lattice or affect the lattice site types in calcite which is occupied by these ions.

The apparent conversion rate of a doped sample depends on all the above three aspects. For example, as shown in Figures 4.1–4.2, the significantly reduced conversion rate of the sample doped with Li_2CO_3 and thermally pre–treated before the sulfation may be explained by the significantly reduced total surface area and the significantly increased ionic mobility in the solid product by the thermal pre–treatment, whereas the significantly increased conversion rate with the sample doped with NaCl and thermally treated before the sulfation may be explained by the significantly increased ionic mobility and a limited decrease in the total surface area by the thermal pre–treatment.

Figure 4.4 demonstrates that a thermal pre–treatment longer than 1 hour did not apparently produce any extra benefit with the NaCl–doped samples. There may be various reasons for this. It could be due to the limitation on the incorporation of the additive in the crystal lattice of calcite determined by its solid–state solubility in calcite.

Figure 4.3 shows that significantly higher conversion rates were achieved with the sample doped with 2 % NaCl and thermally treated at 923 K than the same samples thermally pre–treated at lower temperatures. This may again be explained by the formation of more point defects by the incorporation of larger amount of the additive in the crystal lattice of calcite at a higher temperature.

In general, the phenomena observed with the thermal pre–treatment is in good accordance with the suggested main reason for the enhancement of the direct sulfation of limestone by the additives, i.e. the increased ionic mobility in the solid reactant (the limestone) or in both the solid reactant and the solid product (anhydrite).

4.4.3 Additive dosage

It is shown in Figure 4.5 that higher NaCl dosages apparently produced no positive effects. The detailed reasons are not quite clear. It could be that the lowest dosage (0.5 %) used for the experiments was still more than the amount that can be incorporated into the crystal lattice of calcite at the applied reaction and thermal pre–treatment temperatures. It could also be that it was only an apparent result of the combined effects of additive incorporation and reduction in total surface area. A too higher additive dosage (as in the case of 4 % NaCl in Figure 4.5) may cause negative effect by for example pore blocking, coating effect or a too significant decrease in total surface area.

4.4.4 Influence of water

Water is shown in Figure 4.19 to have positive effects on the sulfation reaction with limestone samples doped with NaCl at the reaction temperature of 823 K. However, at 923 K as shown in Figure 4.20 the conversion rate of the limestone samples in the presence of water was initially lower than without water but higher than without water after a longer reaction time. This special behavior may be related to the influence of hydroxide ions on the chemical reaction and the ionic movement during the sulfation process just as in the case without the additives. At lower temperatures, the resistance of solid–state diffusion may be more

dominant than that of chemical reaction. An increase in the diffusivity of Ca^{2+} caused by hydroxide ions may result in a higher conversion rate. The observed promoting effect of water at 823 K (Figure 4.19) could be such a case. With the increase in the reaction temperature, the relative resistance of solid–state diffusion decreases. To a certain point, the resistance of chemical reaction may get to a more dominant position than that of solid–state diffusion. In such a situation the formation of hydroxide ions may reduce the conversion rate because of probable occupation of the active sites (anion vacancies at the surface of calcite grains), which may explain the reduced conversion rate in the presence of water at the earlier sulfation stage.

Figures 4.25–4.26 show SEM images of Faxe Bryozo particles doped with 2 % NaCl and sulfated with and without water at 923 K for 25–30 minutes. Compared to the totally coalesced product layer in the absence of water, the solid product crystals were better shaped and less coalesced with water addition; pores and uncovered limestone surface are visible. The higher conversion rate in the presence of water after a longer reaction time shown in Figure 4.20 may partly be explained by the existence of pores and uncovered limestone surface.
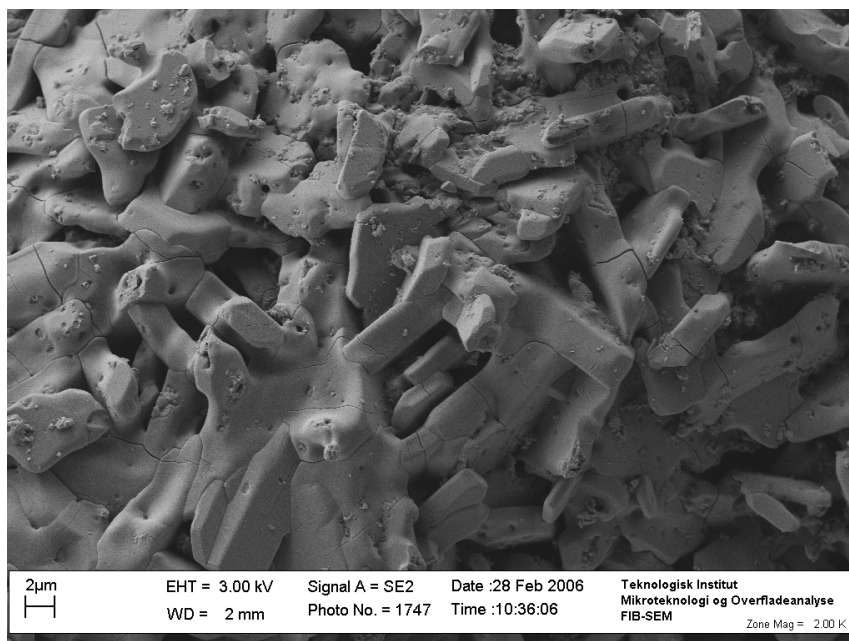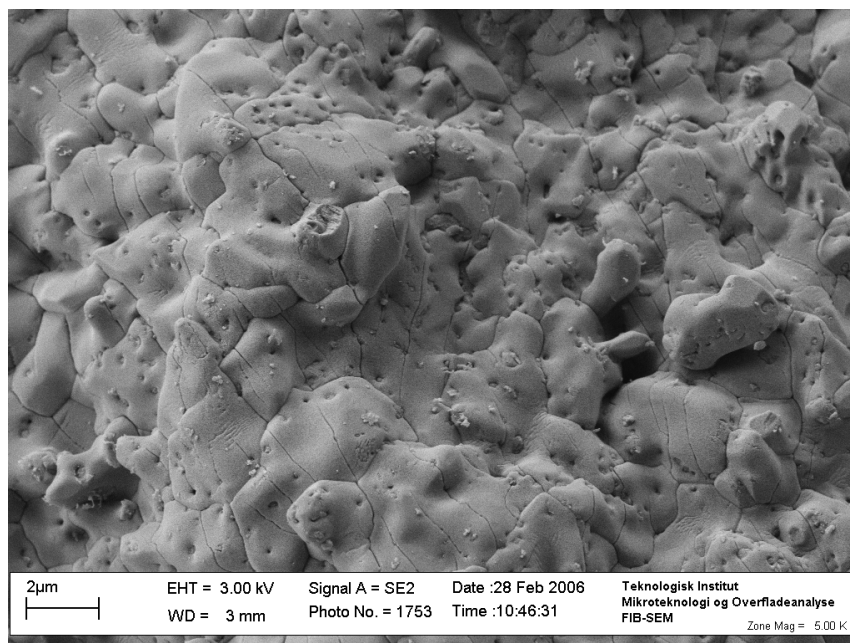
Figure 4.25 SEM image of the surface of Faxe Bryozo doped with 2 % NaCl and sulfated at 923 for about 25 minutes (x = ca. 15 %) in the presence of water   in the gas (other conditions: P: 0.11 MPa; inlet SO_2: 1800 ppm; O_2: 3 %; CO_2:   30 %; N_2: balance)

Figure 4.26 SEM image of the surface of Faxe Bryozo doped with 2 % NaCl and sulfated at 923 for about 20 minutes (x = ca. 15.5 %) without water in the gas (other conditions: P: 0.11 MPa; inlet SO_2: 1800 ppm; O_2: 3 %; CO_2: 30 %; N_2: balance)

The less coalesced product crystals in the presence of water could be related to a significantly depressed effect of sodium ions on the ionic mobility in the product crystals either by a reduced transport of Na^+ into the product crystals or by a neutralization of the effect of Na^+ in the product crystals by the formation of hydroxide ions.

In general, the influence of water on the direct sulfation reaction is complicated and highly dependant on the actual reaction conditions such as the used additive, reaction temperature and conversion. The above discussion is to a high degree speculative and needs to be confirmed by experimental results.

4.5   Conclusions

The direct sulfation of limestone has been observed to be significantly enhanced by various Li^+, Na^+ and K^+–containing inorganic salts (Li_2CO_3, $NaCl$, Na_2CO_3, Na_2SO_4, KCl, K_2CO_3), $CaCl_2$ and HCl. The additives causes also the conversion rate vs. time curves to become upcurved with a maximum and the solid product (anhydrite) to be formed in different physical forms depending on the additive types and reaction conditions. These phenomena are explained by the increased ionic mobility in the solid phases by the additives. Depending on the additive types, ionic mobility may be increased in both the solid reactant (limestone) and the solid product (anhydrite) or just in the solid reactant.

The sulfation process in the presence of the alkali metal salts involves nucleation and growth of the solid product crystals similar to the case without additives. Na^+–containing salts enhance the sulfation process by increasing ionic mobility in both the solid reactant (calcite) and the solid product (anhydrite), while Li^+–containing salts may enhance the sulfation process by increasing ionic mobility in both the solid reactant (calcite) and the solid product (anhydrite) or just in the solid reactant depending on reaction conditions. K^+–containing salts enhance the sulfation process by increasing ionic mobility only in the solid reactant. An increase in ionic mobility in the solid reactant results in the formation of fewer but larger nuclei/crystals of the solid product, while a significant increase in ionic mobility in the solid product crystals causes the product crystals to lose their normal orthorhombic form and coalesce easily. The increase in ionic mobility in the solid product is caused by the diffusion of Li^+ and Na^+ ions into the product phase during the nucleation and growth process. A progressive covering of the surface of limestone particles/grains by the (coalesced) product crystals generally takes place during the sulfation process.

In the presence of $CaCl_2$, the sulfation process involves nucleation and crystal growth of solid product as well. $CaCl_2$ enhances the sulfation process by increasing only ionic mobility in the solid reactant (calcite). The ionic mobility in the solid product is not increased significantly by $CaCl_2$ mainly because of the difficulties for chloride ions to diffuse into the product phase. The significant increase in ionic mobility solely in the solid reactant results in the formation of relatively large, individual and well shaped anhydrite crystals.

The enhancement by HCl in the gas phase is related to a eutectic which is formed by the simultaneous formation of $CaCl_2$ by the chlorination reaction of limestone and $CaSO_4$ by the sulfation of limestone.

The upcurved conversion rate vs. time curve of the doped limestone is a combined result of increasing reactivity of the uncovered limestone surface with increasing conversion and a gradual shielding of the limestone surface by the product crystals or eutectics.

The thermal experience of the doped limestone particles before the sulfation reaction has significant influence on the sulfation kinetics mainly because of its influence on the physical/chemical properties of the doped limestone (such as total surface area and solid–state diffusivity/mobility) and the later diffusion of the relevant additive ions into the product phase during the sulfation process.

In the presence of additives such as alkali metal salts, the influence of water is complicated. Water may promote or inhibit the sulfation process depending on conditions such as temperature and conversion. The effect of water is probably related to the formation of hydroxide ions and their influence on ionic mobility and the ionic movements during the sulfation process, such as the diffusion of sodium ions into the product phase.

The results obtained in this study shows that the rate of the direct sulfation of limestone at temperatures around 823 K can be enhanced about 6–8 times by the addition of alkali metal salts in a relatively low dosage. This means that with proper engineering the application of additives may make the direct sulfation of limestone practical for the desulfurization of flue gases at a temperature significantly lower than 973 K. This may be especially valuable for those industrial processes that generate sulfur containing flue gases at a relatively low temperature such as in cement production.

Chapter 5   Concluding remarks

The two reactions —pyrite oxidation and limestone sulfation—which determine SO_2 emissions from the cyclone preheater used in the dry process for cement production have been studied through extensive literature surveys and extensive experimental work.

A careful analysis of literature data indicates that pyrite transformation in an oxygen–containing atmosphere can take place by direct oxidation or by a two–step process—pyrite first decomposes to form pyrrhotite which is then oxidized—depending on actual reaction conditions. With sufficient oxygen in the gas, the rate of pyrite transformation usually begins to take off at a temperature higher than about 800 K most likely because of the start of the two–step process.

The experiments showed that the direct sulfation of limestone starts with a quite fast initial rate which decreases rapidly to a relatively low level after a few seconds reaction time because of the significant resistance of solid–state diffusion and the occurrence of nucleation and crystal grain growth of the formed solid product. The initial sulfation of limestone, which is important for SO_2 absorption in the cyclone preheater because of the short particle residence time, was shown to be significantly promoted by lower CO_2 concentrations and a gas without water. Various additives such as different kinds of Li^+, Na^+ and K^+–containing inorganic salts, $CaCl_2$ and HCl can also significantly enhance the sulfation reaction at temperatures around 700–900 K. The enhancing effects of Na^+ and K^+–containing salts can be particularly valuable for enhancing SO_2 absorption in the cyclone preheater because these two ions are often present in the raw meal in significant amounts.

It is believed that SO_2 emissions from the cyclone preheater can be significantly reduced by optimizing process conditions and addition of additives based on the above experimental observations.

Experimental results obtained in this study show that the direct sulfation of limestone involves nucleation and crystal grain growth of the solid product and is significantly hindered by solid–state diffusion. Most of the kinetic phenomena observed with this reaction is related to the influence of solid–state diffusion and the nucleation and growth process.

For modeling of the direct sulfation of limestone, shrinking unreacted core model (Levenspiel 1962, Szekely et al. 1976) has been frequently used. Generally, the concept of

shrinking unreacted core is considered applicable for the direct sulfation of limestone. However, the simplified shrinking unreacted core model that are described in Szekely (1976) and Levenspiel (1962) are insufficient for the direct sulfation of limestone, especially the initial sulfation stage; this is because these models do not consider the significant influence of solid–state diffusion and the nucleation–growth process at the surface of the unreacted core. Model simulations are often used for the extraction of kinetic parameters and for the judgment of controlling mechanisms. The use of the simplified shrinking unreacted core model for the modeling of the direct sulfation of limestone without considering the above two aspects may lead to erroneous results and conclusions. For example, the effective diffusivity in the product layer was often evaluated across the whole thickness of the product layer. However, considering (1) that the resistance of solid–state diffusion is most likely the major diffusion resistance and (2) that this resistance of solid–state diffusion is probably located at the surface of the unreacted core at low conversions and in a relatively thin layer near the unreacted core at high conversions, the effective diffusivity evaluated in such a way is no more than a model parameter and does not represent any physical properties of diffusion in the gas phase or in the solid phase. It was also shown that the intrinsic kinetics assessed by various authors using the simplified unreacted core model is far away from the reality.

The two models suggested in this study are mainly based on the well clarified general sulfation mechanism. Though relatively simple, they are able to give good simulations of the sulfation process of limestone at low conversions. This may be seen as an example of model building based on a well understood mechanism. At higher conversions, a more sophisticated shrinking unreacted core model that can consider the influence of solid–state diffusion and the nucleation–growth process is needed.

It is worthwhile to point out that the important role of solid–state diffusion and the nucleation–growth process in the kinetic behaviors of the direct sulfation of limestone maybe not a unique case. Nucleation and subsequent growth are usually a common mechanism for the formation of the new solid product phase for many gas–solid reactions involving formation of crystalline solid products. Solid–state diffusion is an interrelated process to the nucleation–growth process. The significant influence of solid–state diffusion is therefore a quite natural result considering the usually significantly lower solid–state diffusivity than gas phase diffusivity. It is believed that an improvement of our general knowledge about nucleation and growth of solid materials and solid–state diffusion will greatly benefit our

understanding of reaction kinetics of gas–solid reactions similar to the direct sulfation of limestone.

Finally, concerning pyrite oxidation and limestone sulfation, there is still a long way to go to get clarified the detailed reaction mechanisms, though this Ph. D. study has clarified the general processes of these two reactions.

Concerning pyrite oxidation it is still necessary to produce better kinetic data for making it possible to predict the kinetic behaviors of a pyrite particle in an oxygen–containing atmosphere. The reaction mechanism at the pyrite surface needs as well to be clarified in order to understand and simulate the effect of sulfur gas to the decomposition reaction of pyrite.

Concerning the direct sulfation of limestone, the suggested chemical reaction mechanism, though being able to explain most of the observed kinetic phenomena, still needs to be confirmed by more convincing evidence. To make the understanding of the kinetics of the whole sulfation process more complete, more work is still needed to clarify the kinetic behavior of the nucleation process.

Notations

A: constant, $mol^{(1-n-m)}/(m^{(2-3(n+m))}s)$

A′:   constant, $mol^{(1-n)}/(m^{(2-3n))}s)$

a: solid–state activity of carbonate ions (ratio between actual carbonate ion concentration and carbonate ion concentration in pure calcite crystal), dimensionless

B: constant, dimensionless

C: concentration, mol/m^3

D: diffusion coefficient, m^2/s

E_a: activation energy, J/mol

ΔH_r : enthalpy change of reaction, J/mol

h :   heat transfer coefficient of the gas film, $J/(m^2\ K\ s)$

K: equilibrium constant (unit depending on rate expressions)

k: reaction rate constant (unit depending on rate expressions)

l: diffusion distance, m

M: molar weight, g/mol

P: total pressure, Pa

p: partial pressure, Pa

$\Re$:   gas constant, J/(mol K)

R: particle radius, m

r: surface reaction rate, $mol/(m^2\ s)$

S_t: total surface area, m^2/g

t: reaction time, s

T: temperature, K

V: gas flow, m^3/s

w: solid feeding rate, g/s

W: bed weight, g

x: conversion of solid reactant, dimensionless (limestone)

y: molar fraction

λ: thermal conductivity of the product layer, J/(m s K)

τ :   time for complete conversion of a particle, s

η :   fraction of $CaCO_3$ in limestone

ρ : density, kg/m^3

θ_v : fraction of vacant active sites for the adsorption of SO_2 and CO_2

θ_{SO_2} fraction of active sites occupied by SO_2

θ_{CO_2} fraction of active sites occupied by CO_2

$[\ ]_v$: vacant active site

$[SO_2]_v$: active site occupied by SO_2

$[CO_2]_v$: active site occupied by CO_2

$[OH^-]$: carbonate site occupied by hydroxide ions

$[SO_3^{2-}]$: carbonate site occupied by sulfite ions

$[SO_4^{2-}]$: carbonate site occupied by sulfate ions

Superscript:

n, m: reaction order

s: surface

0:     intrinsic, pure state

Subscript:

B: solid reactant

c: core

f: fluid/gas

g: growth

i: intrinsic

L: lattice

n: nucleation

s: solid–state

References

Allen GC, Paul M. and Hallam KR. Can. J. Appl. Spectrosc. 1995, 40(6).

Alvarez E and Gonzalez JF. Fuel. 1999, 78:341-348.

Arnold RG. Econ. Geol. 1962, 75:72-90.

Baker EH. J. Chem. Soc. 1962, 464-470.

Barker WW and Parks TC. Geochim. Cosmochim. Acta. 1986, 50:2185-2194.

Barnes RS. Nature. 1950, 166:1032-1033.

Beruto D, Giordani M and Botter R. J. Physique, Colloque C1, Supplement au n°2. 1986, 47: C1-527-531

Bog S, Rosenqvist T. Trans. Farady Soc. 1959, 55:1565-1569.

Borgwardt RH, Bruce, KR and Blake J. An investigation of product–layer diffusivity for CaO sulfation. Ind. Eng. Chem. Res. 1987, 26:1993-1998.

Borgwardt RH, Bruce KR and Blake J. Ind. Eng. Chem. Res. 1987, 26:1993-1998.

Boyabat N, Özer, AK, Bayrakceken S and Gülaboglu M S. Fuel Processing Technol. 2003, 85:179-188.

Bulewicz EM, Kandefer S and Jurys C. J. Inst. Energy. 1986, pp188-195.

Chuang YY, Hsieh KC and Chang YA. Metall. Trans. B. 1985, 16B:277-285.

Coats AW and Bright NFH. Can. J. Chem. 1966, 44:1191-1195.

Cole DA, Simmons GW, Herman RG, Klier K and Czako-Nagy I. Fuel, 1987, 66:1240-1248.

Cordero F and Cantelli R. Physica C. 1999, 312:312–224

Dam–Johansen et al. 1991a: Dam-Johansen K and Østergaard K. Chem. Eng. Sci. 1991, 46(3):827-837.

Dam–Johansen et al. 1991b: Dam-Johansen K and Østergaard K. Chem. Eng. Sci. 1991, 46(3):839-845.

Dam–Johansen et al. 1991c: Dam-Johansen K and Østergaard K. Chem. Eng. Sci. 1991, 46(3):847–853.

Dam–Johansen et al. 1991d: Dam-Johansen K and Østergaard K. Chem. Eng. Sci. 1991, 46(3):855–859.

Dam-Johansen K. "Absorption of SO2 on dry limestones", Ph. D. thesis (in Danish), 1987, Department of Chemical Engineering, the Technical University of Denmark.

Darken LS and Gurry RW. J. Am. Chem. Soc. 1946, 68:798-816.

David RL. "CRC Handbook of Chemistry and Physics". 2003, 84th ed., 4-63, CRC Press.

de las Heras C, Martin de Vidales JL, Ferrer IJ and Sanchez C. J. Mater. Res. 1996, 11(1):211-220.

Dickson FW, Shields LD and Kennedy GC. Econ. Geol. 1962, 57:1021-1030.

Dunn et al. 1989a: Dunn JG, De GC and O'Connor BH. Thermochim. Acta, 1989, 145:115-130.

Dunn et al. 1989b: Dunn, J G, De GC and O'Connor BH. Thermochim. Acta, 1989, 155:135-149.

Dunn et al. 1992a: Dunn JG and Mackey LC. J. Ther. Anal. 1992, 38:487-494.

Dunn et al. 1992b: Dunn JG. Gong W and Shi D. Thermochimica Acta. 1992, 208:293-303.

Dunn et al. 1993a: Dunn JG and Mackey LC. J. Therm.Anal. 1993, 39:1255-1271.

Dunn et al. 1993b: Dunn JG. Gong W and Shi D. Thermochim. Acta. 1993, 215:247-254.

Dunn JG and Mackey LC. J. Therm. Anal. 1991, 37:2143-2164.

Duo W, Laursen K, Lim J and Grace J. Powder Technology. 2000, 111:154–167

Eastman PF and Cutler IB. J. Am. Cera. Soc. 1966, 49(10):526–530.

Eneroth E and Koch C Bender. Min. Eng. 2003, 16:1257-1267.

Eymery JP. Eur. Phys. J. AP. 1999, 5:115-121.

Fegley B and Lodders K. Icarus. 1995, 115:159-180.

Ferrer IJ and Sanchez C. J. Appl. Phys. 1991, 70(5):2641-2647.

Fisher JC. J. Appl. Phys. 1951, 22:74-77.

Frenkel JI. Z. physic. 1962, 35:652.

Fuertes AB and Fernandez MJ. Thermochim. Acta. 1996, 276:257-269.

Fuertes AB, Velasco G, Fuente E and Alvarez T. Fuel process. Technol. 1994, 38:181-192.

Fuertes AB, Velasco G, Fuente E, Parra JB and Alvarez T. Fuel process. Technol. 1993, 36:65-71.

Gao F and Li F. J. Fuel Chem. Technol. 1989, 17(2):175-182.

Glicksman ME. "Diffusion in solids: field theory, solid–state principle, and applications". John Wiley & Sons, Inc., 2000.

Greulich E. Z. Anorg. Chem. 1927, 168:197-202.

Groves SJ, Williamson J and Sanyal A. Fuel. 1987, 66:461-466.

Gurvich LV, Veyts IV and Alcock CB. "Thermodynamic Properties of Individual Substances", 4th ed. Vol. 1, Part 2. Hemisphere Publishing Corporation, 1989.

Hajaligol MR, Longwell JP and Sarofim AF. Ind. Eng. Chem. Res. 1988, 27:2203-2210.

Hansen JP. Ph. D. thesis, Department of Chemical Engineering, Technical University of Denmark, August 2003.

Hansen JP, Jensen LS, Wedel S and Dam-Johansen K. Ind. Eng. Chem. Res. 2003, 42:4290-4295.

Haul R and Stein LH. Transactions of the Faraday Society. 1955, 51:1280-1290.

Hayes W and Stoneham AM. "Defects and defect processes in nonmetallic solids". John Wiley & Sons, Inc., 1985

Helble JJ, Srinivasachar S and Boni AA. Prog. Energy Combust. Sci. 1990, 16:267-279.

Henrich VE. Applied Surface Science. 1993, 72:277–284

Hepola J. Acta Polytechnica Scandinavica, Chemical Technology and Metallurgy Series No. 193, Helsinki 1990.

Hewlett PC. Lea's Chemistry of Cement and Concrete, 4th edition, Butterworth–Heinemann, Oxford, 1998.

Hill KJ and Winter ERS. J. phys. Chem. 1956, 60:1361-1362.

Hoare IC, Hurst HJ and Stuart WI. J. Chem. Soc. Faraday Trans. I. 1988, 84 (9):3071-3077.

Hoffman RE and Turnbull D. J. Appl. Phys. 1951, 22:634-639.

Hong Y and Fegley B. Ber. Bunsenges. Phys. Chem. 1997, 101(12):1870-1881.

Hong Y and Fegley B. Planet. Space Sci. 1998, 46(6/7):683-690.

Hubbard FH and McGill RJ. Mineral. Mag. 1984, 48:251-256.

Huffman GP, Huggins FE and Levasseur AA. Fuel, 1989, 68:485-490.

Iisa et al. 1992a: Iisa K, Hupa M and Yrjas P. Twenty-Fourth Symposium (International) on Combustion/The combustion Institute, 1992, pp1349-1356.

Iisa et al. 1992b: Iisa K and Hupa M. J. Inst. Energy. 1992, 65:201-205.

Iisa K, Tullin C and Hupa M. 11th International Conference on Fluidized Bed Combustion, ASME, 1991, pp83-90.

Iisa Kand Hupa M. Twenty-Third Symposium (International) on Combustion/The Combustion Institute, 1990, pp943-948.

Illerup JB, Dam-Johansen K and Lunden K. Chem. Eng. Sci. 1993, 48(11):2151-2157.

Jellinek F. "Sulfides", chapter 19 in "Inorganic Sulphur Chemistry", edited by G. Nickless, Elsevier Publishing Co. Ltd., 1968.

Jensen LS. "NOx from cement production—Reduction by primary measures", PhD thesis, 1999, Department of Chemical and Biochemical Engineering, Technical University of Denmark.

Johnston J. J. Am. Chem. Soc. 1910, 32:938-946.

Jorgensen FRA and Moyle FJ. J. Therm. Anal. 1982, 25:473-485.

Kirkaldy JS and Young DJ. "Diffusion in the condensed state". The Institute of Metals, 1987.

Komraus JL, Popiel ES and Mocek R. Hyperfine Interact. 1990, 58:2589-2592.

Kopp OC and Kerr PF. Am. Mineral. 1958, 44:1079-1097.

Krishnan SV and Sotirchos SV. The Can. J. Chem. Eng. 1993, 71:244-255.

Kubaschewski O. "Iron-Binary Phase Diagrams", Springer-Verlag, Berlin, 1982, pp125, Iron-Sulphur.

Kullerud G and Yoder HS. Econ. Geol. 1959, 54:533-572.

Lambert JM, Simkovich G and Walke PL. Metall. Mater. Trans. B. 1998, 29B:385-396.

LeClaire AD. Philos. Mag. 1951, 42:468.

Levenspiel O. "Chemical reaction engineering", John Wiley and Sons Inc., New York, 1962.

Levenspiel O. "Chemical reaction engineering", John Wiley and Sons Inc., New York, 1999.

Liu H, Katagiri S, Kaneko U and Okazaki K. Fuel. 2000, 79:945-953.

Ljungström E and Lindqvist O. International conference on fluidized bed combustion, 7th conference, Philadelphia, Penn. 1982, pp465-472.

Manning JR. "Diffusion kinetics for atoms in crystals". D. Van Nostrand Company, Inc., 1968

McLennan AR, Bryant GW, Stanmore BR and Wall TF. Energy and Fuel. 2000, 14:150-159.

Meng L and Liu MS. Mater. Sci. Eng. 1999, B60:168-172.

Meng L, Liu YH and Huang W. Mater. Sci. Eng. 2002, B90:84-89.

Meng L, Liu YH and Tian L. Mater. Res. Bull. 2003, 38:941-948.

Meyer B. "Elemental Sulphur", chapter 7 in "Inorganic Sulphur Chemistry", edited by G. Nickless, Elsevier Publishing Co. Ltd., 1968.

Mitchell J. J. Am. Chem. Soc. 1923, 123:1055-1068.

Murthy KS, Howes JE and Nack H. Am. Chem. Soc. 1979, 13(2):197-204.

Nishihara K and Kondo Y. Mem. Fac. Eng. Kyoto Univ. 1959, 21:214-218.

Palmer MS and Neurock MJ. Phys. Chem. B. 2002, 106:6543–6547

Pannetier G and Davignon L. Bull. Soc. Chim. 1961, 72:1513.

Partanen J, Backman P, Backman R and Hupa M. Fuel. 2005, 84:1685-1694.

Pelovski Y and Petkova V. J. Therm. Anal. Calorimetry. 1999, 56:95-99.

Perry HR, Green DW and Maloney JO. "Perry's Chemical Engineers' Handbook", seventh edition, McGraw-Hill, 1997.

Prasad A, Singru RM and Biswas AK. Phys. Stat. Sol. (a). 1985, 87:267-271.

Qiu K and Lindqvist O. Chem. Eng. Sci. 2000, 55:3091-3100.

Razouk RI, Mikhail RS and Ragai J. J. Appl. Chem. Biotechnol. 1973, 23:51–61.

Roberts MW and Smart RSC. Surface Science. 1981, 108:271–280

Samal GI. Geterogennye Khim. Reaktsii, Inst. Obshch. i Neorgan Khim. Akad. Nauk Belorussk. SSR, 93, 1965.

Schenk PW and Steudel R. "Oxides of Sulphur", chapter 11 in "Inorganic Sulphur Chemistry", edited by G. Nickless, Elsevier Publishing Co. Ltd., 1968.

Schorr JR and Everhart JO. J. Am. Ceram. Soc. 1969, 52(7):351-354.

Schwab GM and Philinis J. J. Am. Chem. Soc., 1947, 69(11):2588-2596.

Scott SD and Barnes HL. Econ. Geol. 1971, 66:653-669.

Smyth FH and Adams LH. J. Am. Chem. Soc. 1923, 45:1167-1184.

Snow MJH, Longwell JP and Sarofim AF. Ind. Eng. Chem. Res. 1988, 27:268-273.

Spartinos DN and Vayenas CG. Chem. Eng. Process. 1991, 30:97-106.

Srinivasachar S and Boni AA. Fuel. 1989, 68:829-836.

Srinivasachar S, Helble JJ and Boni AA. Prog. Energy Combust. Sci. 1990, 16:281-292.

Szekely J, Evans JW and Sohn HY. "Gas-Solid Reactions", Academic Press, New York, 1976.

Taylor HFW. Cement Chemistry, 2nd edition, Telford, London, 1997.

ten Brink HM, Eenkhoorn S and Hamburg G. Fuel. 1996, 75(8):945-951.

ten Brink HM, Smart JP, Vleeskens JM and Williamson J. Fuel. 1994, 73(11):1712-1717.

Tetard F, Bernache-Assollant D and Champion, E. J. Therm. Anal. Calorimetry. 1999, 56:1461-1473

Tilley RJD. "Defect Crystal Chemistry and Its Application". Blackie & Son Limited, 1987.

Toulmin P and Barton PB. Geochim. Cosmochim. Acta. 1964, 28:641-671.

Tuffrey NE, Richards GG and Brimacombe JK. Metall. Mater. Trans. B. 1995, 26B:959-970.

Tullin C, Nyman G and Ghardashkhani S. Energy & Fuels. 1993, 7:512–519.

Udintseva VS and Chuforov GI. J. Appl. Chem. USSR, 1941, 14:3.

Ulerich NH, Newby RA and Keairns DL. Thermochim. Acta. 1980, 36:1-16.

Van Houte G and Maon JC. J. Air Pollut. Control Assoc. 1978, 28(10):1030-1033.

Van Houte G and Delmom B. J. Chem. Soc. Faraday Trans. 1, 1979, 75:1593-1605.

Van Houte G, Rodrique L, Genet M and Delmom B. Environ. Sci. Technol. 1981, 15(3):327-332.

Varma A and Morbidelli M. "Mathematical methods in chemical engineering", Oxford University Press, New York, 1997.

Vuthaluru HB, Eenkhoorn S, Hamburg G and Heere PGT. Fuel Processing Technol. 1998, 56:21-31.

Wagner C and Schottky W. Z. Phys. Chem. B. 1930, 11:163-210.

Warner NA and Ingraham TR. Can. J. Chem. 1960, 38:2196-2202.

West AR. Basic Solid State Chemistry. John Wiley & Sons, Ltd., 1999.

West JR. Ind. Eng. Chem. 1950, 42(4):713-718.

Yang RT, Cunningham PT, Wilson WI and Johnson SA. Adv. Chem. Ser. (1975), 139(Sulfur Removal Recovery Ind. Processes, Symp., 1974), pp149-157.

Yrjas P, Iisa K and Hupa M. Fuel. 1995, 74(3):395-400.

Zevenhoven et al. 1998a: Zevenhoven R, Yrjas P and Hupa M. Fuel. 1998, 77(4):285-292.

Zevenhoven et al. 1998b: Zevenhoven CAP, Yrjas PK and Hupa M. Ind. Eng. Chem. Res. 1998, 37:2639-2646.

Zhong Q. Thermochim. Acta. 1995, 260:125-136.

Zhukovskii VM, Montilo IA and Babadzhan AA. Tr. Ural. Nauch. Issled. Proekt. Inst. Med. Prom. 1965, 8:387.

Appendixes

Appendix 1: Particle distribution of Faxe Bryozo used for experiments in the pilot entrained flow reactor

MALVERN INSTRUMENTS

MASTERSIZER 2000

Result Analysis Report

Sample Name: Kemitek - Average	**SOP Name:** Dekanter-starch	**Measured:** 29. juni 2006 11:54:41
Sample Source & type: Factory = Paris	**Measured by:** BioCentrum	**Analysed:** 29. juni 2006 11:54:42
Sample bulk lot ref: 123-ABC	**Result Source:** Averaged	

Particle Name: Starch	**Accessory Name:** Hydro 2000SM (A)	**Analysis model:** General purpose	**Sensitivity:** Enhanced
Particle RI: 1.530	**Absorption:** 0	**Size range:** 0.020 to 2000.000 um	**Obscuration:** 18.36 %
Dispersant Name: Water	**Dispersant RI:** 1.330	**Weighted Residual:** 0.557 %	**Result Emulation:** Off

Concentration: 0.1301 %Vol	**Span :** 0.913	**Uniformity:** 0.323	**Result units:** Volume
Specific Surface Area: 0.335 m²/g	**Surface Weighted Mean D[3,2]:** 17.915 um	**Vol. Weighted Mean D[4,3]:** 167.619 um	

d(0.1): 98.974 um   **d(0.5):** 159.930 um   **d(0.9):** 244.922 um
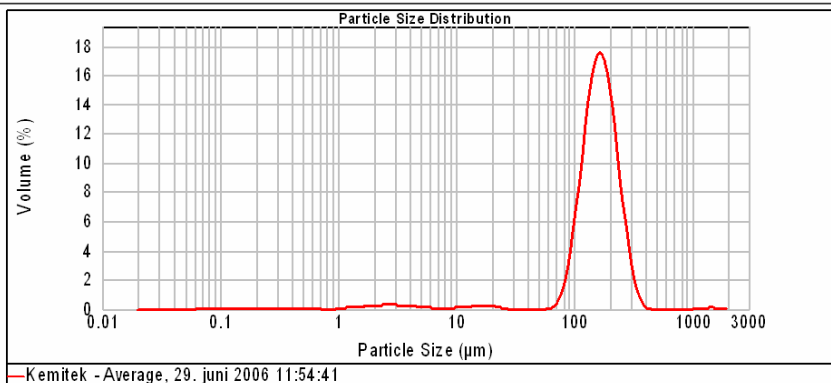
Kemitek - Average, 29. juni 2006 11:54:41

| Size (µm)	Volume In %	Size (µm)	Volume In %	Size (µm)	Volume In %	Size (µm)	Volume In %	Size (µm)	Volume In %	Size (µm)	Volume In %
0.010		0.105		1.096		11.482		120.226		1258.925	
0.011	0.00	0.120	0.04	1.259	0.09	13.183	0.15	138.038	12.73	1445.440	0.09
0.013	0.00	0.138	0.05	1.445	0.11	15.136	0.19	158.489	15.23	1659.587	0.09
0.015	0.00	0.158	0.05	1.660	0.16	17.378	0.22	181.970	15.76	1905.461	0.06
0.017	0.00	0.182	0.05	1.905	0.20	19.953	0.21	208.930	13.89	2187.762	0.01
0.020	0.00	0.209	0.05	2.188	0.24	22.909	0.17	239.883	10.31	2511.886	0.00
0.023	0.00	0.240	0.05	2.512	0.26	26.303	0.05	275.423	6.30	2884.032	0.00
0.026	0.00	0.275	0.05	2.884	0.27	30.200	0.00	316.228	3.19	3311.311	0.00
0.030	0.00	0.316	0.05	3.311	0.26	34.674	0.00	363.078	1.08	3801.894	0.00
0.035	0.00	0.363	0.04	3.802	0.24	39.811	0.00	416.869	0.22	4365.158	0.00
0.040	0.00	0.417	0.04	4.365	0.20	45.709	0.00	478.630	-0.00	5011.872	0.00
0.046	0.00	0.479	0.03	5.012	0.16	52.481	0.00	549.541	0.00	5754.399	0.00
0.052	0.00	0.550	0.03	5.754	0.12	60.256	0.00	630.957	0.00	6606.934	0.00
0.060	0.00	0.631	0.02	6.607	0.09	69.183	0.09	724.436	0.00	7585.776	0.00
0.069	0.00	0.724	0.00	7.586	0.06	79.433	0.70	831.764	0.00	8709.636	0.00
0.079	0.03	0.832	0.00	8.710	0.06	91.201	2.17	954.993	0.00	10000.000	0.00
0.091	0.03	0.955	0.00	10.000	0.08	104.713	5.22	1096.478	0.00		
0.105	0.04	1.096	0.02	11.482	0.11	120.226	8.42	1258.925	0.05		

Operator notes:

Appendix 2: Porosity of Faxe Bryozo particles

The porosity of Faxe Bryozo (particle size 0.045–0.125 mm) was determined by mercury intrusion (Micromeritics, MicroAutopore II 9220). The following figure is the intrusion curve.

Considering that Faxe Bryozo particles are agglomerates of primary particles of around 2–3 micrometer in average diameter, it is assumed that intrusion volume from the pore size less than 1 micrometer (corresponding the intrusion pressure around 170 pisa (1 pis = 6890 Pa) is the pore volume in the particles. The intrusion volume into the particles is thus about 0.33–0.15 = 0.18 ml/g.

Considering a density of 2.7 g/ml for calcite the porosity of Faxe Bryozo is calculated to be about 30 %.

It is expected that porosity for particles of the size 0.63–0.18 mm and 0.18–0.25 mm is approximately the same, i.e. around 30 %.

Cumulative Intrusion vs Pressure
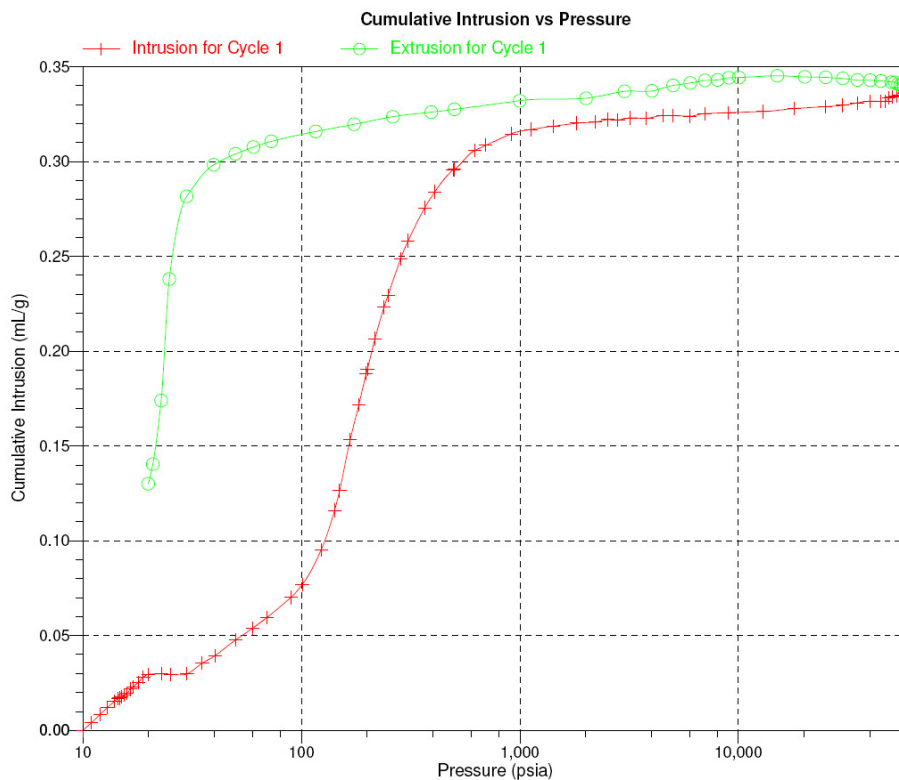
Appendix 3: Estimation of intra–particle diffusion resistance

The influence of intra–particle diffusion resistance in a spherical particle can be evaluated with the following generalized Thiele modulus for a first order reaction (Froment and Bischoff, Chemical reactor analysis and design, Chapter 3, 1999, John Wiley & Son):

$$\phi = \frac{R}{3} \sqrt{\frac{S \; k}{D_e}}$$

Here:

ϕ :   Thiele modulus;

R: radius of the particle, m;

S: total surface area, m^2/m^3;

k: rate constant, m/s;

D_e: effective diffusion coefficient, m^2/s
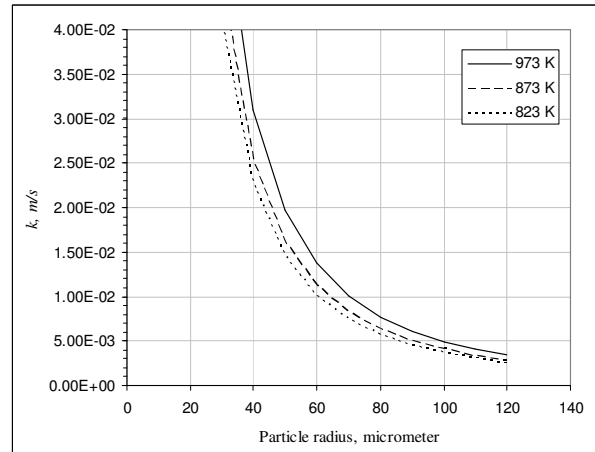
The resistance of intra–particle diffusion is considered to be insignificant if the Thiele modulus is smaller than about 0.5.

The maximum value of k for $\phi = 0.5$ can be calculated as follows:

$$k = \frac{9 \, \phi^2 \, D_e}{R^2 \, S}$$

The diffusion coefficient of SO_2 in the nitrogen/air is about $1.1 \; 10^{-5}$ m^2/s at 273 K (Massman, W. J. 1998, Atmospheric Environment, vol. 32, no. 6, pp1111–1127) (Considering N_2 is the major constituent in the reaction gas, this value is used directly). At other temperatures the diffusion coefficient can be calculated by using the value at 273 K times a factor of $(T/273)^{1.81}$.

The total surface area for Faxe Bryozo is about 0.79 m^2/g. With a porosity about 0.3, the total surface area per cubic meter is calculated to be about $1.5 \; 10^6$ m^2/m^3.

The above figure shows the variation of maximum value of k with particle size of Faxe Bryozo.

Appendix 4: EDS X–ray microanalysis results

4–1: Iceland Spar sulfated at 973K for 30 min. (limestone conversion ca. 2.7 %) (other conditions: P: 0.11 MPa; inlet SO_2: 1800 ppm; O_2: 3 %; CO_2: 30 %; N_2: balance)
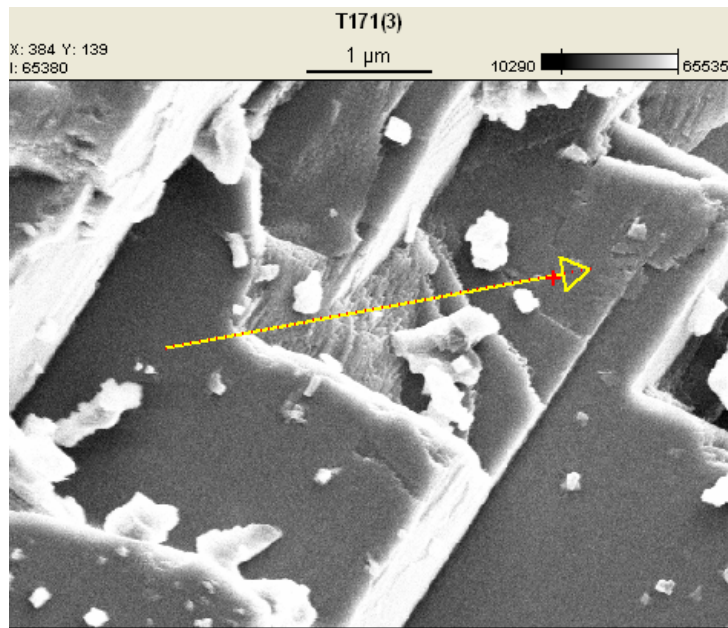
SEM image showing the scanning line starting from the smooth cleavage and crossing areas with product crystals
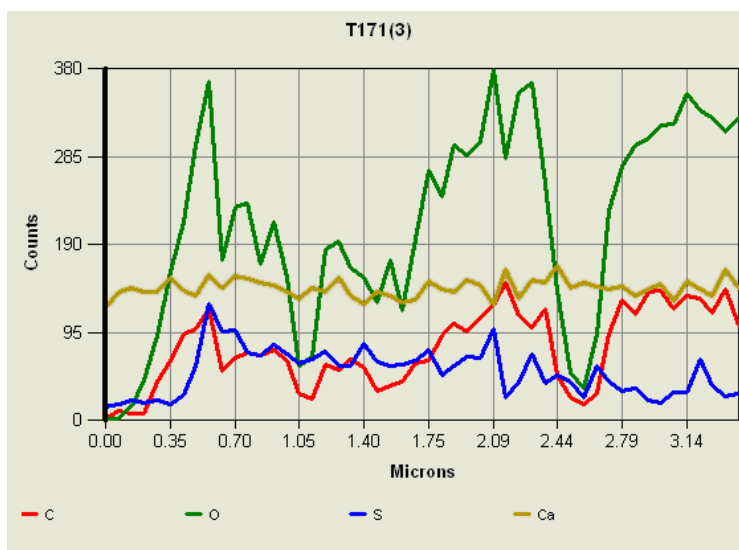
Line scanning showing significant amount of sulfur at the place where scanning line crosses the fractures with crystals.

4–2: Faxe Bryozo doped with 2 % NaCl and sulfated at 873 K for 5 minutes (limestone conversion ca. 1.9 %) (other conditions: thermal treatment before sulfation: 923 K for 1 h; P: 0.11 MPa; inlet SO_2: 1800 ppm; O_2: 3 %; CO_2: 30 %; N_2: balance)
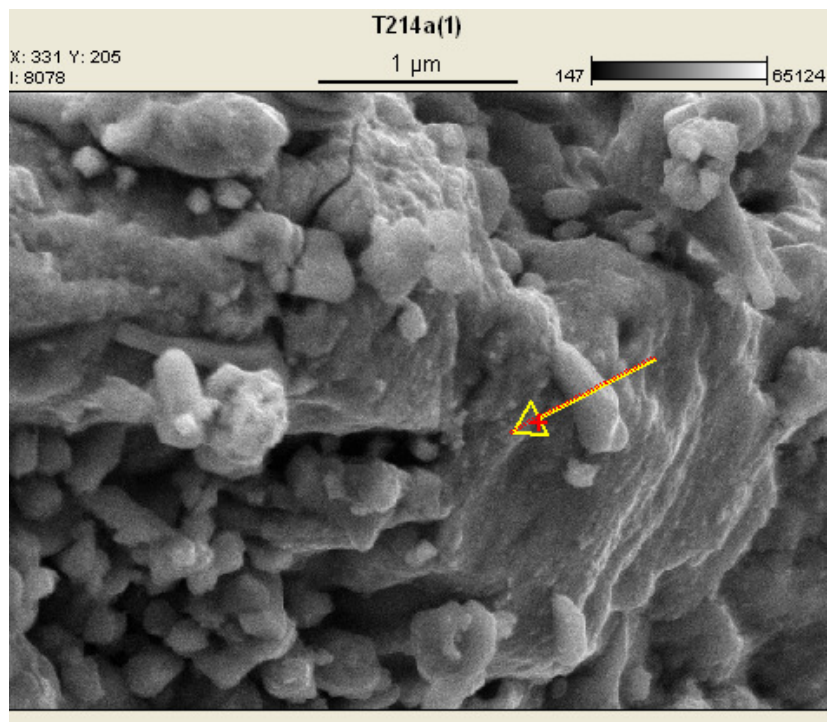
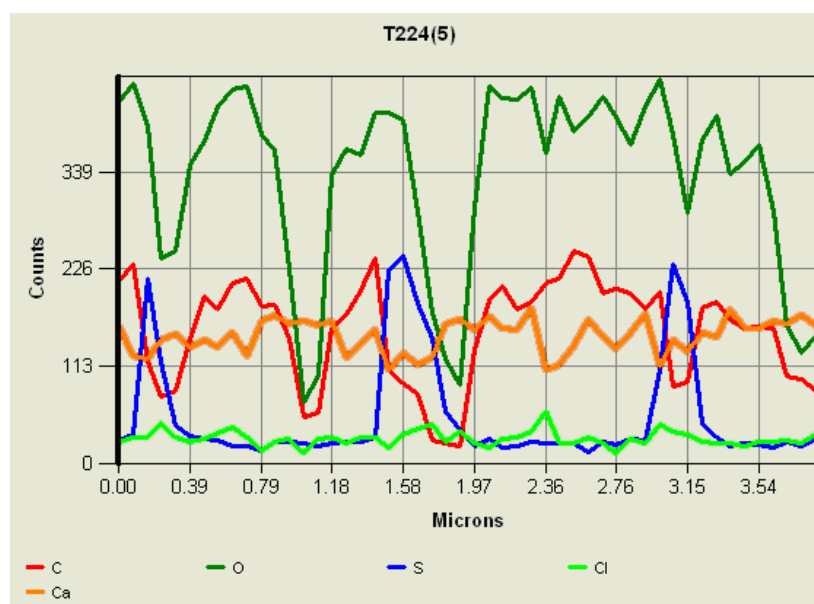

SEM image showing the scanning line crossing one crystal
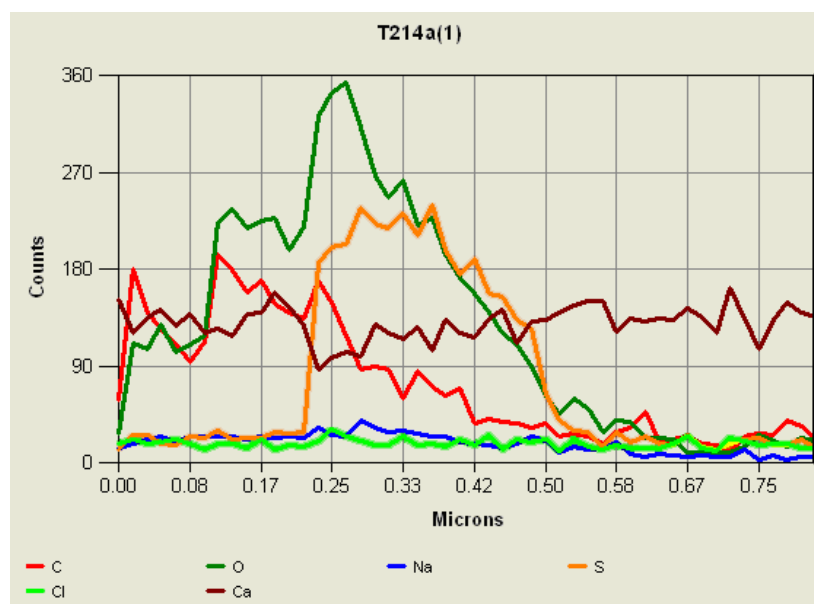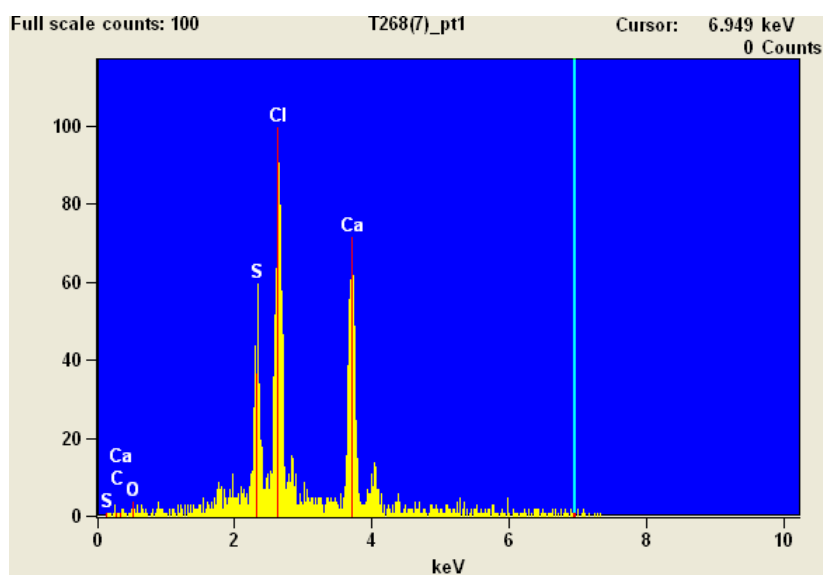

Line scanning showing high percentages of sulfur and calcium at the place where scanning line crosses the crystal.

4–3: Faxe Bryozo doped with 2 % NaCl and sulfated at 873 K for 10 minutes (limestone conversion ca. 4.4 %) (other conditions: thermal treatment before sulfation: 923 K for 1 h; *P*: 0.11 MPa; inlet SO₂: 1800 ppm; O₂: 3 %; CO₂: 30 %; N₂: balance)
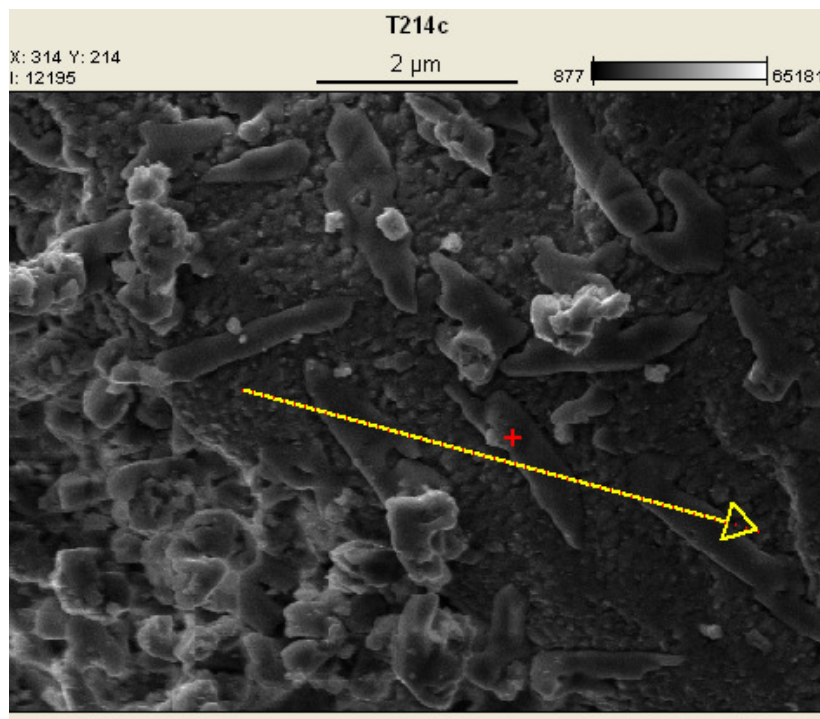
SEM image showing the scanning line crossing three crystals
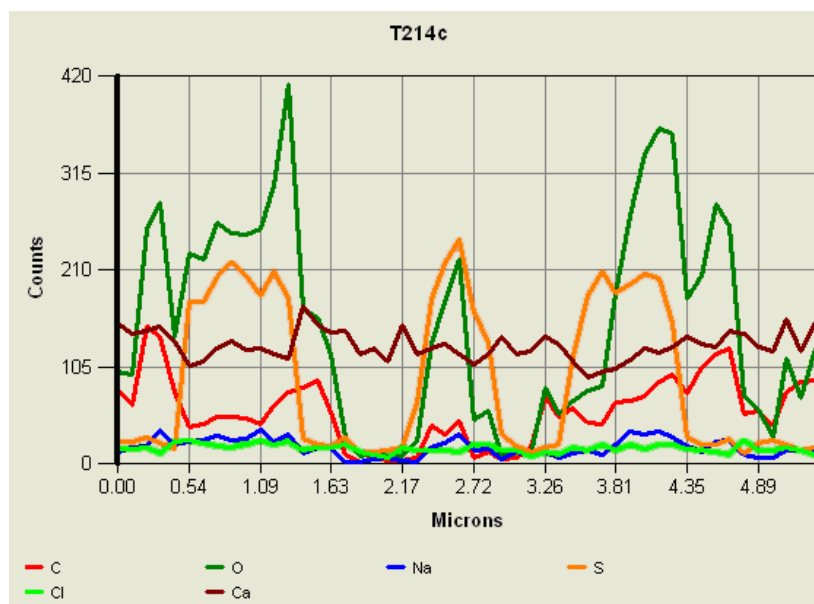
Line scanning showing high percentages of sulfur and calcium at the place where scanning line crosses the crystals.
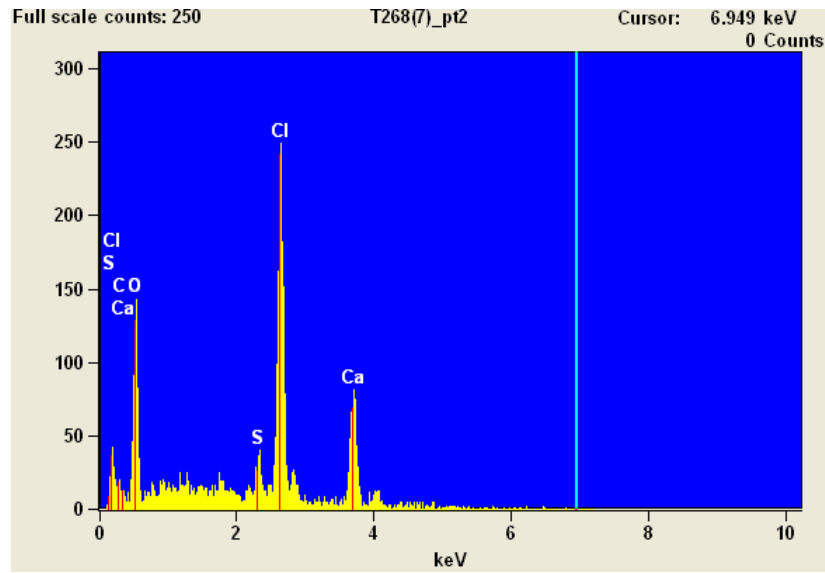
4–4: Faxe Bryozo doped with 2 % KCl and sulfated at 823 K for 30 minutes (limestone conversion ca. 6 %) (other conditions: thermal treatment before sulfation: 923 K for 1 h; P: 0.11 MPa; inlet SO_2: 1800 ppm; O_2: 3 %; CO_2: 30 %; N_2: balance)
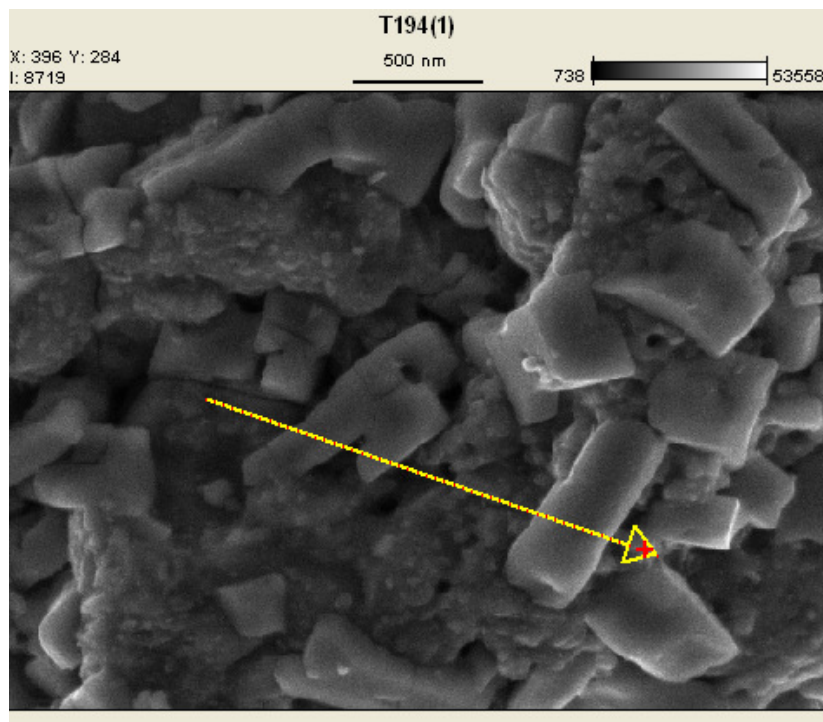
SEM image showing the scanning line crossing two crystals
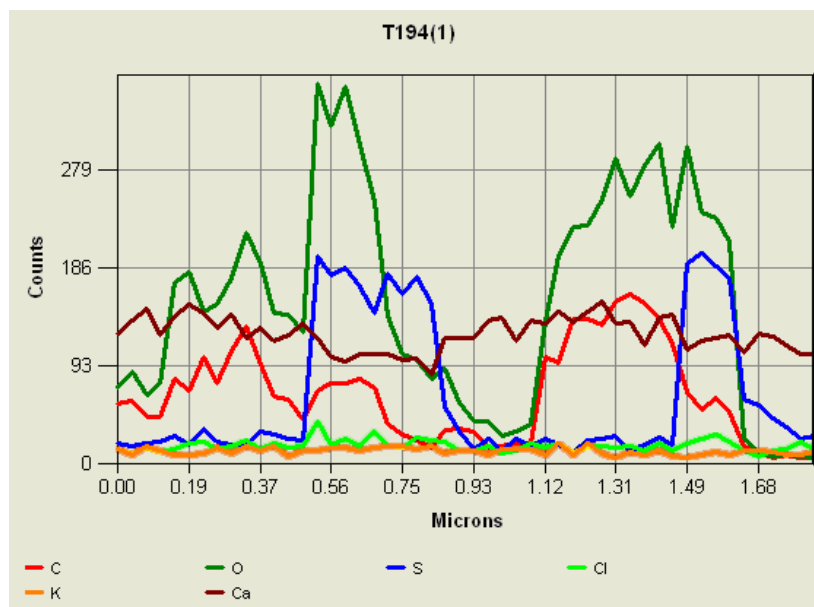
Line scanning showing high percentages of sulfur and calcium at the place where scanning line crosses the crystals.

4–5: Faxe Bryozo doped with 1 % CaCl$_2$ and sulfated at 873 K for 15 minutes (limestone conversion ca. 1.8 %) (other conditions: thermal treatment before sulfation: 923 K for 1 h; P: 0.11 MPa; inlet SO$_2$: 1800 ppm; O$_2$: 3 %; CO$_2$: 30 %; N$_2$: balance)
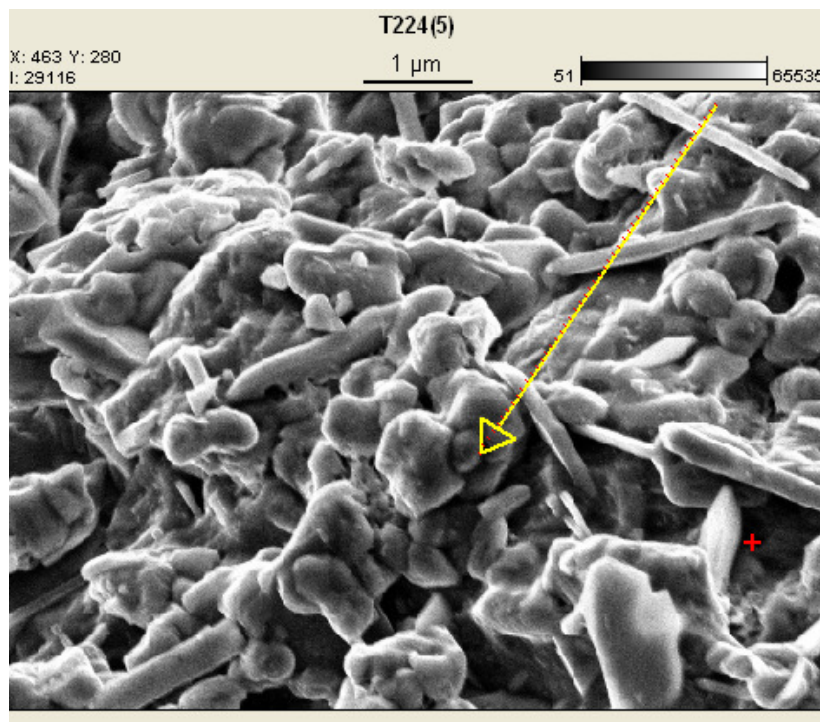
SEM image showing the scanning line crossing three crystals

Line scanning showing high percentages of sulfur and calcium at the place where scanning line crosses the crystals.

4–6: Faxe Bryozo sulfated at 873 K for 25 minutes with about 1000 HCl in the gas (limestone conversion ca. 5.7 %) (other conditions: *P*: 0.11 MPa; inlet SO₂: 1800 ppm; O₂: 3 %; CO₂: 30 %; N₂: balance)
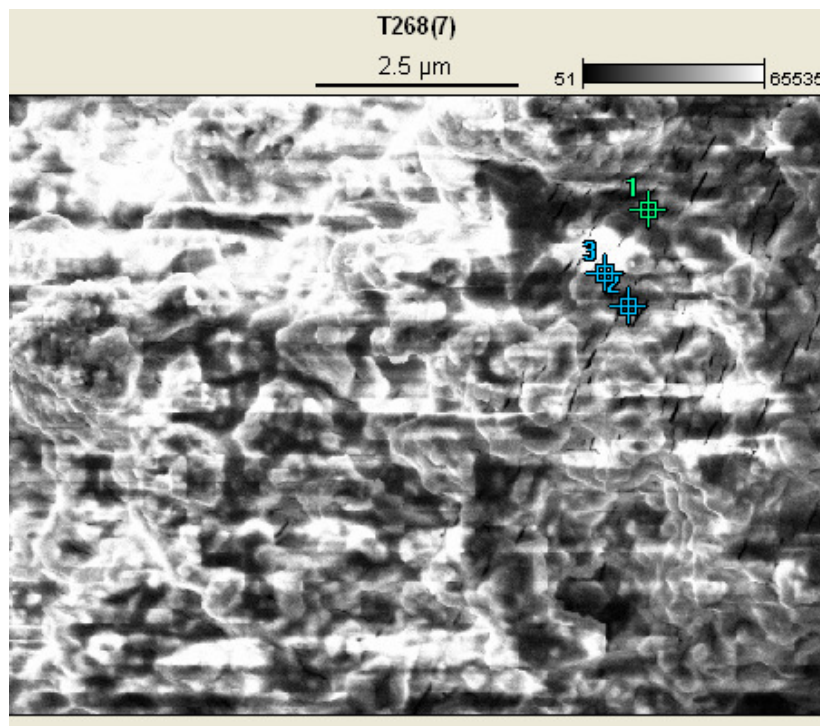
SEM image showing 3 analyzed points

Result for point 1 showing high percentages of sulfur, chlorine and calcium

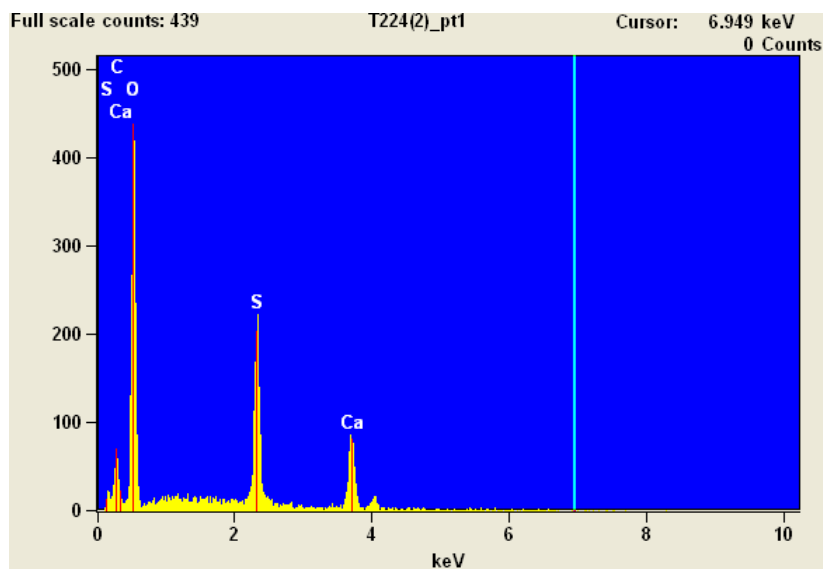Result for point 2 showing high percentages of sulfur, chlorine and calcium
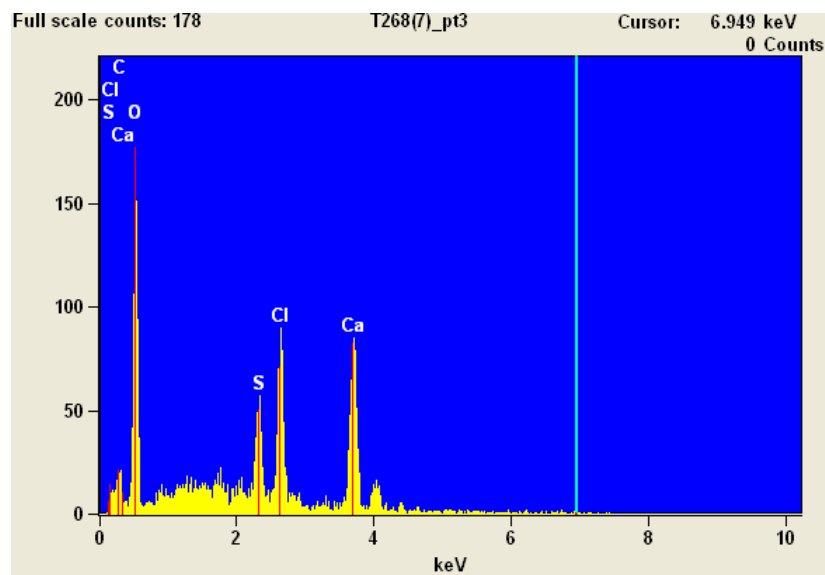
Result for point 3 showing high percentages of sulfur, chlorine and calcium

4–7: Faxe Bryozo doped with 1 % CaCl$_2$ and sulfated at 873 K for 15 minutes (limestone conversion ca. 1.8 %) (other conditions: thermal treatment before sulfation: 923 K for 1 h; _P_: 0.11 MPa; inlet SO$_2$: 1800 ppm; O$_2$: 3 %; CO$_2$: 30 %; N$_2$: balance)
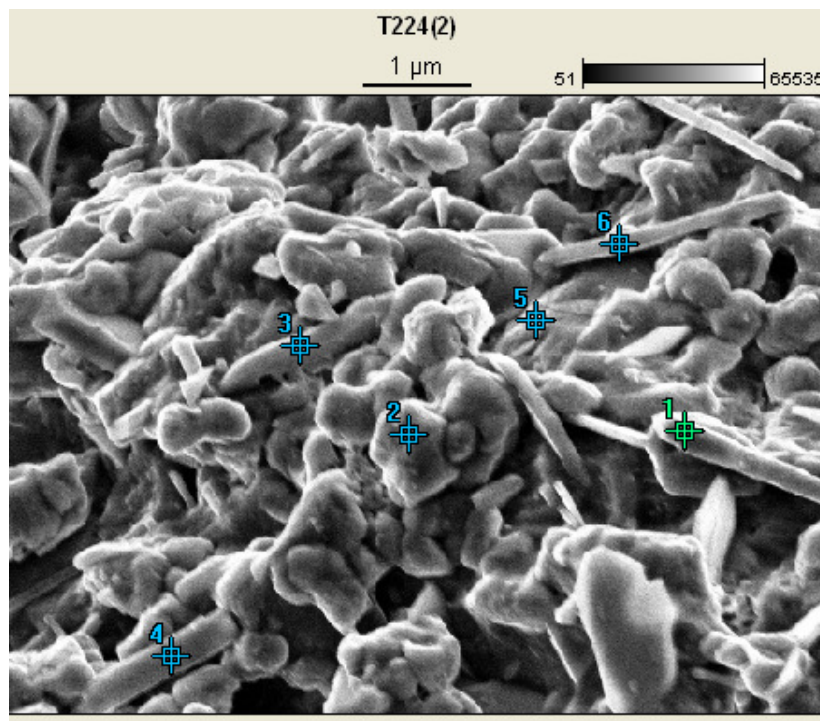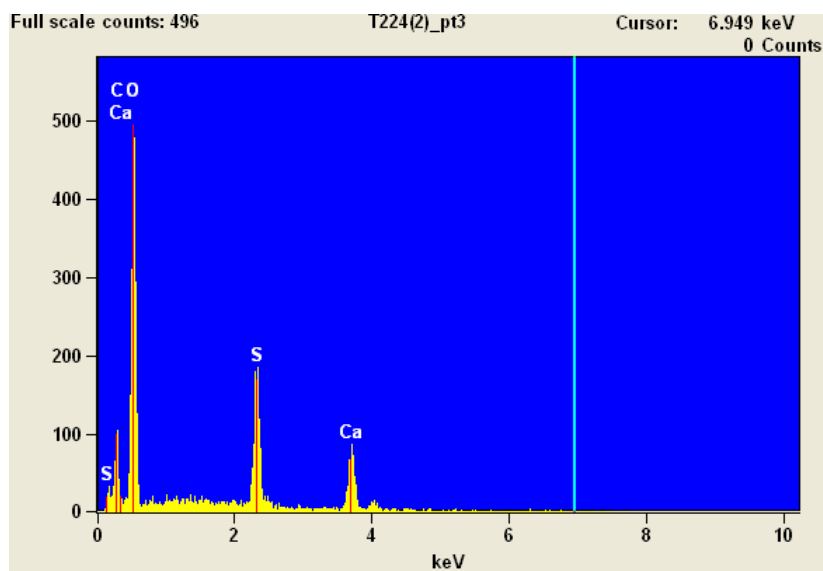

SEM image showing 6 analyzed points

Result for point 1 (product crystal) showing high percentages of sulfur and calcium, but no chlorine.
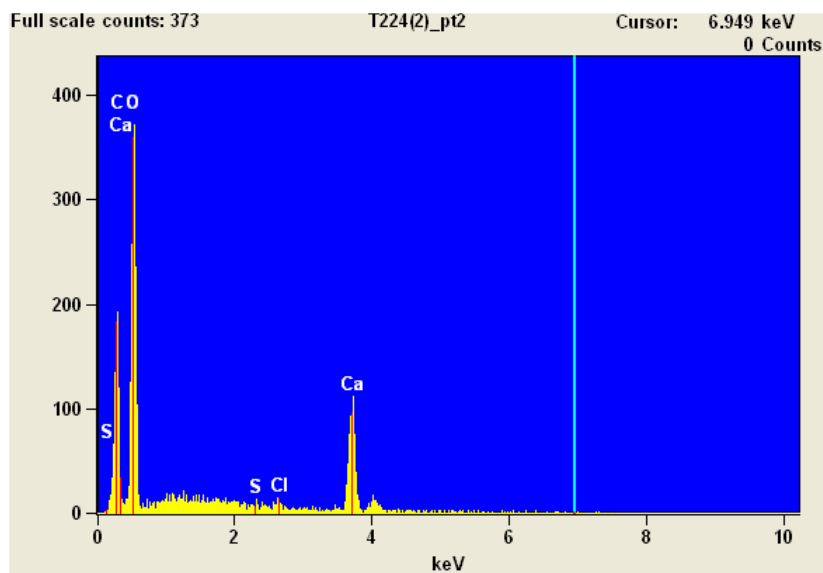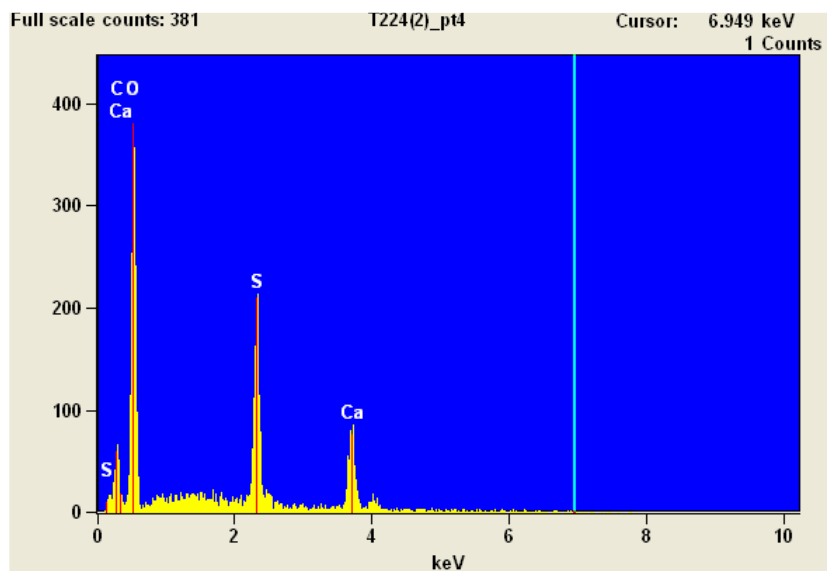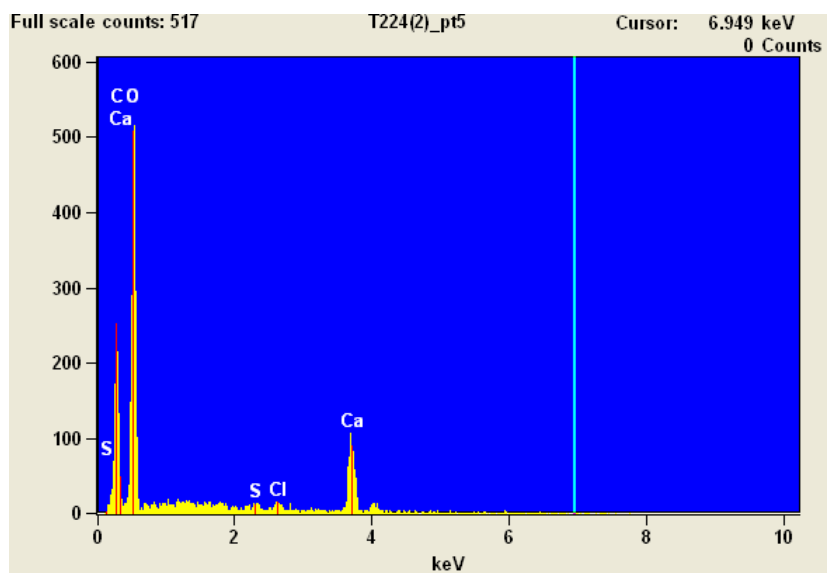
Result for point 2 (limestone) showing high percentages of calcium and small amounts of sulfur and chlorine.
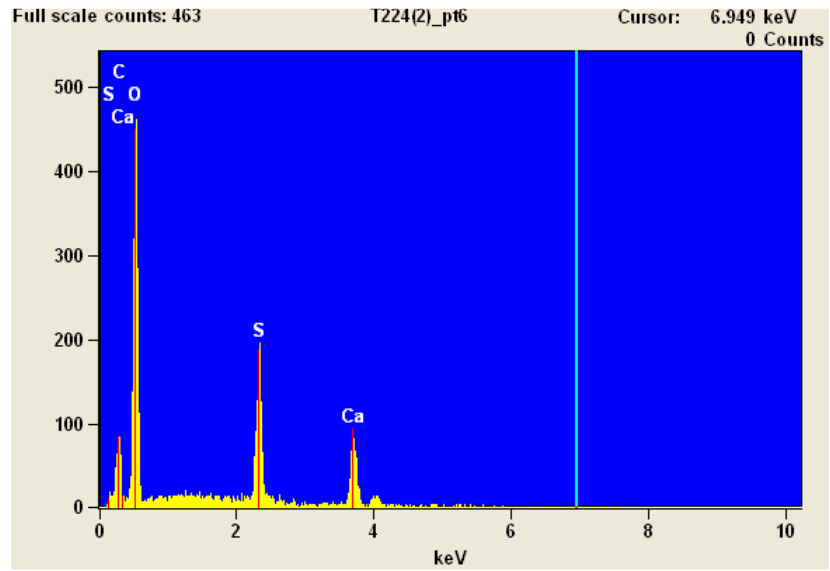

Result for point 3 (product crystal) showing high percentages of sulfur and calcium, but no chlorine.

Result for point 4 (product crystal) showing high percentages of sulfur and calcium, but no chlorine.

Result for point 5 (limestone) showing high percentages of calcium and small amounts of sulfur and chlorine.

Result for point 6 (product crystal) showing high percentages of sulfur and calcium, but no chlorine.

Appendix 5: Published and submitted articles.

1. "Decomposition and Oxidation of Pyrite" by Guilin Hu, Kim Dam–Johansen, Stig Wedel and Jens Peter Hansen, Progress in Energy and Combustion Science, 2006, Vol. 32, pp295-314.

2. "Review of the Direct Sulfation Reaction of Limestone" by Guilin Hu, Kim Dam–Johansen, Stig Wedel and Jens Peter Hansen, Progress in Energy and Combustion Science, 2006, Vol. 32, pp386-407.

3. "Direct sulfation of limestone" by Guilin Hu, Kim Dam–Johansen, Stig Wedel and Jens Peter Hansen, AIChE J., 2007, Vol. 53, No. 4, pp948-960.

4. "Enhancement of the Direct Sulfation of Limestone by Alkali Metal Salts, Calcium Chloride and Hydrogen Chloride" by Guilin Hu, Kim Dam–Johansen, Stig Wedel and Jens Peter Hansen, Industrial & Engineering Chemistry Research, in press, 2007.

5. "Initial Kinetics of the Direct Sulfation of Limestone" by Guilin Hu, Lei Shang, Kim Dam–Johansen, Stig Wedel and Jens Peter Hansen (paper submitted to AIChE J., June 2007).

6. "Oriented nucleation and growth of anhydrite during direct sulfation of limestone" by Guilin Hu, Kim Dam-Johansen and Stig Wedel (paper submitted to Crystal Growth and Design, April 2007).